# High Sensitivity Detection of Nucleic Acids Using Electrochemistry and Spectroscopy

*A thesis submitted as a fulfilment of the requirements for the degree of Doctorate of Philosophy*

*Author:* **Mohammad A. Elshahawy B.Sc.**

*Supervisor*: **Prof. Robert J. Forster**

*School of Chemical Sciences*

*Dublin City University*

*January 2016*

# Declaration

I hereby certify that this material, which I now submit for assessment on the programme of study leading to the award of Doctorate of philosophy is entirely my own work, and that I have exercised reasonable care to ensure that the work is original, and does not to the best of my knowledge breach any law of copyright, and has not been taken from the work of others save and to the extent that such work has been cited and acknowledged within the text of my work.

Signed: (Candidate) ID No.:

Date:

# Acknowledgements

Maybe I have not got the proper chance to express my sentiments about my time studying at DCU, so I am seizing this opportunity to express my uttermost gratitude to all my colleagues in our research group and the whole school of chemical science, who supported and are still supporting me throughout the course of my study. I am thankful for their inspiring guidance, invaluably constructive criticism and useful advice and for sharing their truthful and illuminating views on the project. I was blessed by this friendly environment and welcoming attitude. I enjoyed your company during the last three years. I will always remember with a smile the Christmas dinners, the grill-less "barbecue" lunches and the unanticipated post-meetings coffee mornings.

I would like to thank my project supervisors Prof. Robert Forster for his unceasing guidance and enormous efforts. I am immeasurably very grateful for all what he has done to me, in times when I was feeling so disoriented and lost, and for what he is still providing. Also to Prof. Tia Keys for her vital contribution to my work and study. I will always be thankful.

Special thanks to Elaine, my cheerful mentor and the supporting boss who is younger than me, also all colleaues in the BDI Kellie, Andrea, Hazel, Aisling, Una, Aurèlien, Eoin, Anita, Colm, Bincy and the whole Electrochemistry tribe for the continuous support and help. And for the pleasant times socializing although I wished they were more frequent.

I am also very grateful for the synthesis clan who allowed me inside their sacred temple and showed me their special tricks. Aaron, Ciarán and the most patient teacher of all times the young professor Christopher. Thanks a lot for your help and guidance.

Endless thanks to my fellow undergraduate demonstrators, and to Pat. It was a pleasure working with you. Demonstration was surprisingly a very delightful and interesting experience for me.

I would like to mention here also great friends I met in DCU, Brian, Fadwa, Suzanne, Leannee, Kerrie, Ruth, Ahmed, Hanna, Andy, keana and all the rest of the beautiful faces that will never leave my memory. I enjoyed our time eating and chatting. You taught me a lot about the Irish and European cultures.

I will never forget the cooking evenings and movie nights. I enjoyed the company of Kerileng, Samantha and Nabil in our Africa mini society and its wonderful times. I am proud I still can pronounce the names of those authentic delicious African dishes that I would not dare to write!

My working hours in the lab could not have been smoother, full of cooperation and support without the presence of the best lab mates one can ask for. Thanks, a lot Seàn, Siva, Aggie and my younger sister Nicola, my presence among you was a pleasure.

I was also very lucky to have the best neighbours in the DCU accommodation, Thanks Nilesh and Marisol for the wonderful family time we had together.

Hajra, one paragraph in the acknowledgement will not suffice for expressing how grateful I am for your continuous support and advice. I enjoyed our talks with Sergio about all subjects of life, science, art, literature, history, health, diet and religion during lunchtime. I am so happy for the friendship we developed, which I hope it lasts forever.

I also would like to thank the ISOC friends, the Muslim community in DCU for the wonderful times we spent together, all the Interfaith Centre personnel, and all the lovely people I met there from all religions and backgrounds. Glen, Abdullah, Abdelsalam, Fatima, Summaya, Opaid, Ali and Fahim. Also Shady, Aymen, Salem, Khaled, Jihad, Abdulaleem and many others that I will always remember even I did not mention here.

I want to thank my work colleague, expatriation fellow and cousin Abdellatif and wish him the best of luck. Also my dear friends who never stopped contacting and supporting me. Ahmed, Amr, Mohammad, Moataz and Ramy I will always be indebted.

My family and extended families: you are the most precious beings in my life. Thanks for your patience and support. My beloved mother Nabila, sisters Eman, Amany, Alaa, Albatoul and my brother Ahmad. Your feelings always traversed desert sands, seas and lands. Its warmth embraced me in cold days and kept me going for years. I love you all even I do not repeat it a lot. Finally, I remember my late father who taught me to follow my passion and pursue my dreams. May God rest your soul in peace and mercy for eternity and more.

“This thesis is dedicated to my family, with love. Thank you for all your support.”

# Table of Contents

# Table of Acronyms

| | |
|---|---|
| µ | Micro |
| 4ATP | 4-aminothiophenol |
| 6-Fam | 6-Carboxyfluorescein |
| a | Atto |
| Å | Angstrom |
| AgCl | Silver chloride |
| AMBER | Assisted model building with energy refinement |
| $A_p$ | Peak area |
| APNA | Aromatic peptide nucleic acid |
| BPE | 1,2-di(4-pyridyl) ethylene |
| C | Coloum |
| cal | Calori |
| CAN | Circulating nucleic acid |
| CBZ | Carboxybezyl |
| CD | Circular dichroism |
| cm | Centimeter |
| D | Diffusion coefficient |
| DFT | Density function theory |
| DLS | Dynamic light scattering |
| DMSO | Dimethylsulfoxide |
| DNA | Deoxyribonucleic acid |
| DPV | Differential pulse voltammetry |
| E | Potential |
| E° | Standard potential |
| EC | Electric conductivity |
| EDTA | Ethylenediaminetetraacetic |
| EDX | Energy-dispersive X-ray spectroscopy |
| F | Faraday constant |
| f | Femto |
| FDA | Food and drug administration |
| Fmoc | Fluorenylmethyloxycarbonyl |
| G | Moleculer conductance |
| GA | Geometric area |

| | |
|---|---|
| h | Hour |
| $H_2O_2$ | Hydrogen peroxide |
| $H_2PtCl_6$ | Hydrogen hexachloroplatinate (IV) |
| H2SO4 | Sulphuric acid |
| HBTU | N,N,N′,N′-Tetramethyl-O-(1H-benzotriazol-1-yl)uronium hexafluorophosphate |
| I | Electric current |
| $i_p$ | Peak current |
| ITO | Indium tin oxide |
| J | Current density |
| $K_a$ | Association constant |
| KCl | Potassium Chloride |
| $K_d$ | Dissociation constant |
| KOH | Potassium hydroxide |
| $LiClO_4$ | Lithium perchlorate |
| LNA | Locked nucleic acid |
| LOD | Limit of detection |
| LSV | Linear sweep voltammetry |
| M | Molar |
| MHz | Megahertz |
| MM | Molecular mechanics |
| mol | Mole |
| MV | Methylviologen |
| MWCNT | Multiwall carbon nanotubes |
| n | Nano |
| $N_2$ | Nitrogen |
| NaCl | Sodium Chloride |
| NaOH | Sodium Hydroxide |
| NMR | Nuclear magnetic resonance |
| OLED | Organic light emitting diodes |
| p | Pico |
| PA | Polyacetylene |
| PANI | Polyaniline |
| PANI-NA | Polyaniline nucleic acid |

| | |
|---|---|
| PCR | Polymerase chain reaction |
| PDPA | Polydiphenylamine |
| PNA | Peptide nucleic acid |
| Ppy | Polypyrrole |
| PT | Polythiophene |
| PtNPs | Platinum nanoparticles |
| Q | Charge |
| QM | Quantum mechanics |
| R | Universal gas constant |
| RF | Roughness factor |
| RMSD | Relative mean square deviation |
| RNA | Ribonucleic acid |
| S | Siemens |
| s | Seconds |
| SAM | Self-assembled monolayer |
| SCC | Somatic cell count |
| SEM | Scanning electron microscopy |
| SERRS | Surface-enhanced resonance Raman scattering |
| SERS | Surface enhanced Raman scattering |
| STM | Scanning tunnelling microscopy |
| T | Absolute temperature |
| t | Time |
| t-Boc | tert-Butyloxycarbonyl |
| TFA | Trifluoroacetic acid |
| THF | Tetrahydrofuran |
| $T_M$ | Melting temperature |
| Tris | Tris hydroxymethylaminomethane |
| V | Volt |
| $V_{bias}$ | Voltage bias |
| Γ | Surface coverage |
| ΔG | Binding energy |
| Δi | Current difference |

"The superiority of a learned man over a devout worshipper is like that of the full moon to the rest of the stars in brightness" *Mohammad, 7th century AC.*

# Abstract

**High sensitivity detection of Nucleic Acids using Electrochemistry and Spectroscopy**

*Author: Mohammad Elshahawy B.Sc.*

The ability to detect and quantify specific biomarkers can lead to the development of very powerful tools for the diagnosis and prognosis of disease. For example, electrochemical nucleic acid biosensors provide an easy, rapid, portable and economic tool for the diagnosis of diseases from cancer to cardiovascular disease. This thesis reports on highly sensitive DNA sandwich assays where the probe strand is labelled with an electrocatalytic nanoparticle to sensitively signal the binding event. Specifically, an electrode is functionalised with capture strands that are complementary to approximately 50% of the target. Once the target is hybridised to the capture strand, a probe strand, that is labelled with an electrocatalytic nanoparticle and is complementary to the unbound section of the target, is allowed to hybridise, i.e., the immobilisation of the nanoparticles is mediated by the presence of the target. The magnitude of the electrocatalytic current depends on the concentration of the target and wide dynamic ranges and low LODs can be achieved. The dynamic range achieved was between 1 aM and 100 nM and limit of detection of $1.5 \times 10^{-13}$ M was reached. The electrocatalytic nanoparticles comprise a hemispherical platinum core with a silver shell. These particles are highly electrocatalytic and show some promise as labels in surface enhanced Raman spectroscopy.

The rate of heterogeneous electron transfer from the underlying electrode to the bound nanoparticle can influence the observed electrocatalytic current especially if the target sequence contains many bases. To investigate the possibility of improving the conductivity of the DNA strands, a polyaniline (PANI) based conducting nucleic acid analogue was designed and modelled in silico. Then it was electrochemically synthesized using a novel step-wise addition of individual bases and its binding to natural DNA was assessed. Finally, the current generated from an electrocatalytic nanoparticle bound through hybridisation was examined. The PANI-NA layer was characterized using electrochemical techniques, imaging of the attached nanoparticle and single molecule scanning tunnelling microscopy. The measurement of current densities of the electrodes modified with a PANI-NA capture strand immobilizing electrocatalytic nanoparticles was found to be 16 times the current densities obtained with conventional DNA capture strand at similar concentrations.

# Chapter 1

# Introduction and Literature Review

"The more I increase in knowledge, the more I increase in knowledge about my ignorance" *Al-Shafi'i, 8th century AC.*

# 1 Chapter 1: Introduction and literature review

## 1.1 Introduction

There has been always a need to develop accurate and unequivocal methods of early diagnosis and monitoring of disease conditions. Using of vital sign provided useful and quick method of diagnosis. For example, temperature to diagnose fever, heartbeats and measuring the blood pressure to diagnose cardiovascular diseases. However, other conditions like infectious diseases need the analysis of the affected tissue or perform microscopial count for parasite cells present in body fluids or studying the morphology of the tissues, as in case of cancer cells, to determine its malignancy. Some of these tests require taking a biopsy from the patient, which is an invasive process that cannot be performed frequently especially if the affected cells are in remote places like bone marrow. Moreover, they are time consuming measurements especially in critical conditions that needs quick and early intervention. More sophisticated methods of diagnosis, which are less invasive and provide quicker results have been developed. These methods utilize chemical, spectral and electronic techniques to measure disease-specific chemical biomarkers in blood or other body fluids. For example, the measurement of blood glucose levels to diagnose and monitor diabetes[1], measurement of the concentration of different enzymes and proteins that are associated with tissue injury[2] or cancer specific biomarkers[3]. Detecting disease-associated nucleic acids as biomarkers has attracted the attention decades ago, DNA detection and sequencing developed in a fast

pace to the extent that even whole genome sequencing is now possible[4,5] and these technologies are continuing to evolve and their economic feasibility is improving over time.

One of the most promising disease biomarkers is the circulating nucleic acids CNA. They can be deoxy ribonucleic acid (DNA), messenger ribonucleic acid (mRNA) and mircro ribonucleic acid (microRNA). They are released by cells into the systemic circulation of patients[6]. The release is believed to be due to the apoptosis or necrosis of affected cells like in case of viral infections[7], cardiovascular diseases[8] or different types of cancer[6]. The diagnostic value of CNAs originates from their high specificity and the association of their plasma concentration with the degree of the progression of the disease and the amount of affected cells.

The objective of this thesis is to develop a highly sensitive DNA electrochemical biosensor that detects small concentrations of DNA using the sandwich assay method. In sandwich assays, as depicted in Figure 1.1 the probe strand is labelled with an electrocatalytic nanoparticle to signal the binding event. The composition of the nanoparticles can affect its electrocatalytic activity and spectroscopic properties. The electric conductivity of DNA especially when the target DNA is long can affect the charge transfer rate from the underlying electrode to the DNA-mediated immobilized particle. The use of a DNA analogue which can conduct electrons could increase the overall electrocatalytic current and hence increase the sensitivity of the electrochemical DNA sandwich assay sensor.

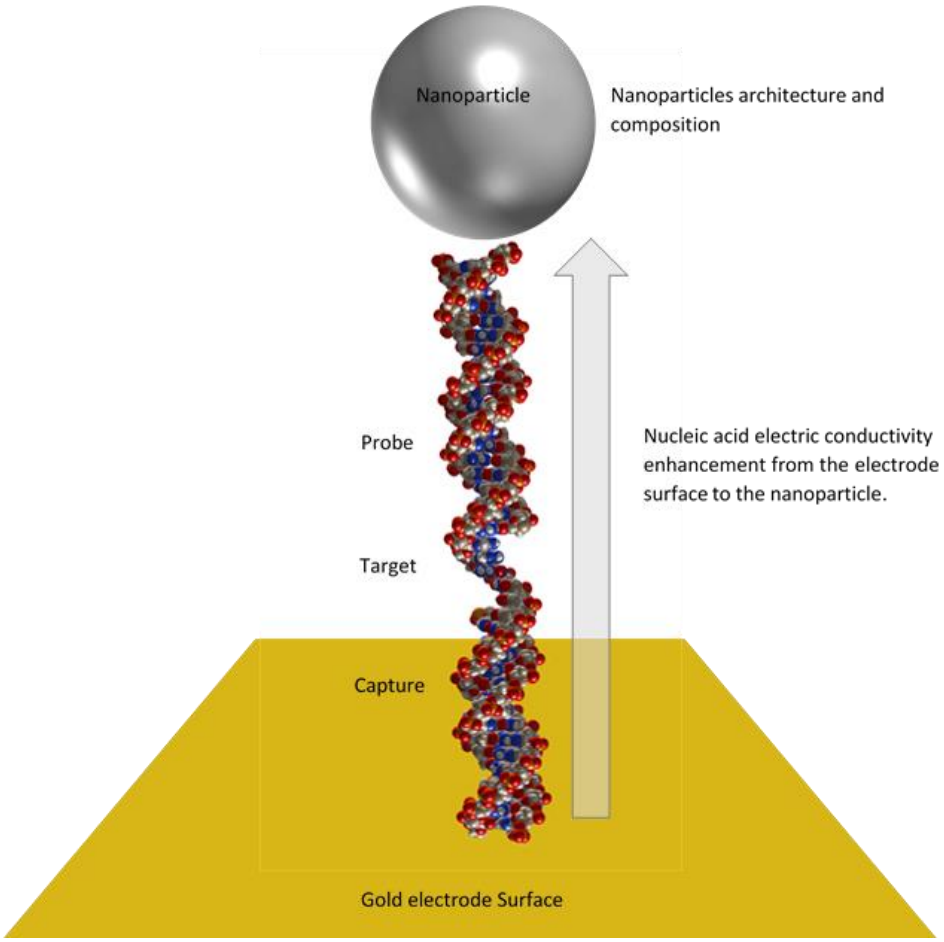


*Figure 1.1 DNA nanoparticle sandwich assay structure composed of captured strand immobilized on electrode surface, bound to target strand which is bound from the other end to probe strand that is tagged with a nanoparticle.*

This chapter reviews the existing literature and provides a context for the data presented. Specifically, an introduction to DNA detection and electrochemical biosensors and sandwich assay detectors is given, followed by a review of platinum and silver nanoparticles and their use in electrochemical biosensing. Also the previous attempts to design DNA analogues will be discussed and then a review on conductive polymers focused on polyaniline is given.

Later in this chapter, the relevant computational and experimental as electrochemical, spectral methods and techniques used in this thesis along with related equations and theoretical backgrounds will be overviewed.

Chapter 2 describes the fabrication of platinum particles synthesized by electrochemical deposition in defective dodecyl thiol self-assembled monolayer SAM. A silver coat was then deposited on one side of the particles and DNA detected. In addition, it reports the improvement in the surface enhanced Raman spectroscopy signal of DNA obtained from these particles when immobilized inside a gold micro cavity array.

Chapter 3 discusses the computational modelling of different DNA analogues that have conductive polymers as backbones. The modelling software and the algorithms used were validated by comparing the quality of the calculated values and the generated models with previously reported structures. Then three different conductive polymers namely polypyrrole, polythiophene and polyaniline were modelled as a backbone carrying nucleotides. Polyaniline-based analogue showed the highest binding affinity to a natural DNA complementary sequence and hence was chosen to be synthesized and characterized in chapter 4.

Chapter 4 reports the novel stepwise method of electrochemically polymerizing single monomer units to control the composition of the analogue and create a specifically coded strand that is complementary to the target DNA strand of interest. Then, the characterization of the electrode surface and testing of the binding of this DNA analogue to a natural complementary sequence is discussed. Also, the ability to improve the resulting electrocatalytic current from sandwich assay is presented.

Finally, chapter 5 presents the broader context of the results obtained and discusses potential next steps for the approaches reported, possible future applications and improvements for the developed particles and analogue.

## 1.2 DNA detection

DNA-based detection methodologies are highly selective. DNA can be used as biomarkers for disease diagnosis including cancer, cardiovascular disease and the detection of specific pathogens[9]. Polymerase chain reaction or PCR is regarded as the gold standard for DNA detection and quantitation[10]. PCR was first developed about thirty years ago and has developed significantly in performance in terms of sensitivity and speed namely the quantitative PCR, multiplex PCR[11] and 'real-time' PCR[12] assays that can simultaneously detect different target sequences in the same sample. Although it is a sensitive and accurate analytical method, it needs a lot of time, instrumentation and has a high cost.

Human diagnostics have a very high barrier to entry making applications in veterinary medicine attractive for proving a biosensor concept. For example, bovine mastitis is considered to be one of the main problems in dairy production in many countries[13]. But it is difficult to detect before the disease is relatively advanced and the animal shows significant syndroms. Due to its economic impact[14,15], a large volume of research has been carried out to determine the associated pathogens, prevalence and early diagnosis and detection[16]. Staphylococcus aureus mastitis is one of the most important mastitis pathogens in cattle. Detection of infection, before clinical symptoms appear, requires sensitive yet highly selective method of detection and quantitation of a biomarker specific for the disease that discriminates against the widely found Staphylococcus aureus epidermis. Many analytical techniques detect the Staphylococcus aureus mastitis and its associated disease biomarkers in milk[17].

Immunoassays, such as enzyme-linked immunosorbent assay (ELISA), can provide a relatively fast and inexpensive method to detect pathogens like mastitis, but suitable antibodies must be available for each specific inflammation related biomarkers or the causative microorganism. However, microbial culture of the milk of ELISA-positive cows is always required for confirmation[18]. Other methods of analysis have been employed to detect mastitis in milk samples such as electric conductivity (EC)[19], somatic sell count (SCC)[20], colour tests for detection of blood[21] or enzymes elevated during mastitis in the milk, determination of volatile substances by gas sensors, such as sulphides, ketones, amines and acids[22], lactate sensors, haemoglobin detectors in milk by surface Plasmon resonance[23]. There have also been major developments in nucleic acid testing for the identification pathogens.[24]

This thesis reports an electrochemical biosensor that has the potential to detect a specific sequence of DNA found only in Staph. Aureus mastitis at very low concentrations in milk before the animal shows any significant clinical symptoms. Ideally, it could be integrated within a sample-to-answer device to provide a result quickly that allows early management of the condition in affected cases.

## 1.3 Electrochemical biosensors

### 1.3.1 Definition of electrochemical biosensors.

Electrochemical biosensors are a subclass of chemical sensors. A biosensor is an integrated receptor-transducer device, which is capable of providing selectively quantitative or semi-quantitative analytical information using a biological recognition element[25] It combines the sensitivity as indicated by low limits of detection (LOD), of electrochemical transducers with the high specificity of biological recognition processes.[25]

### 1.3.2 Composition of the typical electrochemical biosensor:

Biosensors typically are composed of three parts[26].

a) The sensory elements (biological recognition element) that can be composed of enzymes, proteins, antibodies, nucleic acids, cells, tissues or receptors that selectively binds with the target analyte and produces an electrical signal that is related to the concentration of the analyte under study[26].

b) The transducer or detector element that transforms the binding event into a measurable, quantified and readable signal output. The transducing microsystem may be optical, electrochemical, thermometric, piezoelectric or magnetic.

c) The signal processor that records and displays the signal in a comprehensible and user-friendly way.[26]

### 1.3.3 Nucleic acid electrochemical biosensors

A nucleic acid electrochemical biosensor is a type of biosensors that use a nucleic acid as the probe or recognition element and uses an

electrochemical technique to transduce the recognition even and convert it into a readable signal.

Electrochemical nucleic biosensors are mainly used to detect a complementary strand of nucleic acid for the probe immobilized in different samples and for many applications. They have immense value in gene-expression[27] studies, genotyping[28], pharmacogenomics[29], pathogen classification, drug discovery, sequencing[30] and molecular diagnostics. That is why during the previous decade, the field of nucleic acid electrochemical biosensors has witnessed a significant development[31].

### 1.3.4 Types of nucleic acid electrochemical biosensors:

### 1.3.5 Amperometric electrochemical biosensors.

Amperometry is based on measuring the current resulting from an electrochemical process i.e. oxidation or reduction of an electro-active species. It is normally performed by maintaining a constant potential at a Pt, Au or C based working electrode or on an array of electrodes. The magnitude of the resulting current is related to the bulk concentration of the electroactive species or its production or disappearance rate within the adjacent catalytic layer[25]. Electrocatalysis is attractive since a large current can be generated from relatively few binding events while the background current is very low giving a high signal-to-noise ratio. Catalysis can be due to an enzyme, polymer, nanoparticle or carbon nano-material. In some cases the catalysis is indirect and involves recruiting a redox active couple which produces the electrochemical signal upon exposure to one of the catalytic products. The biocatalytic reaction rates are preferred to be first order, i.e., where the steady-state current is directly dependent on the analyte concentration. The

theory underpinning amperometric measurements will be covered later in the electrochemical process section.

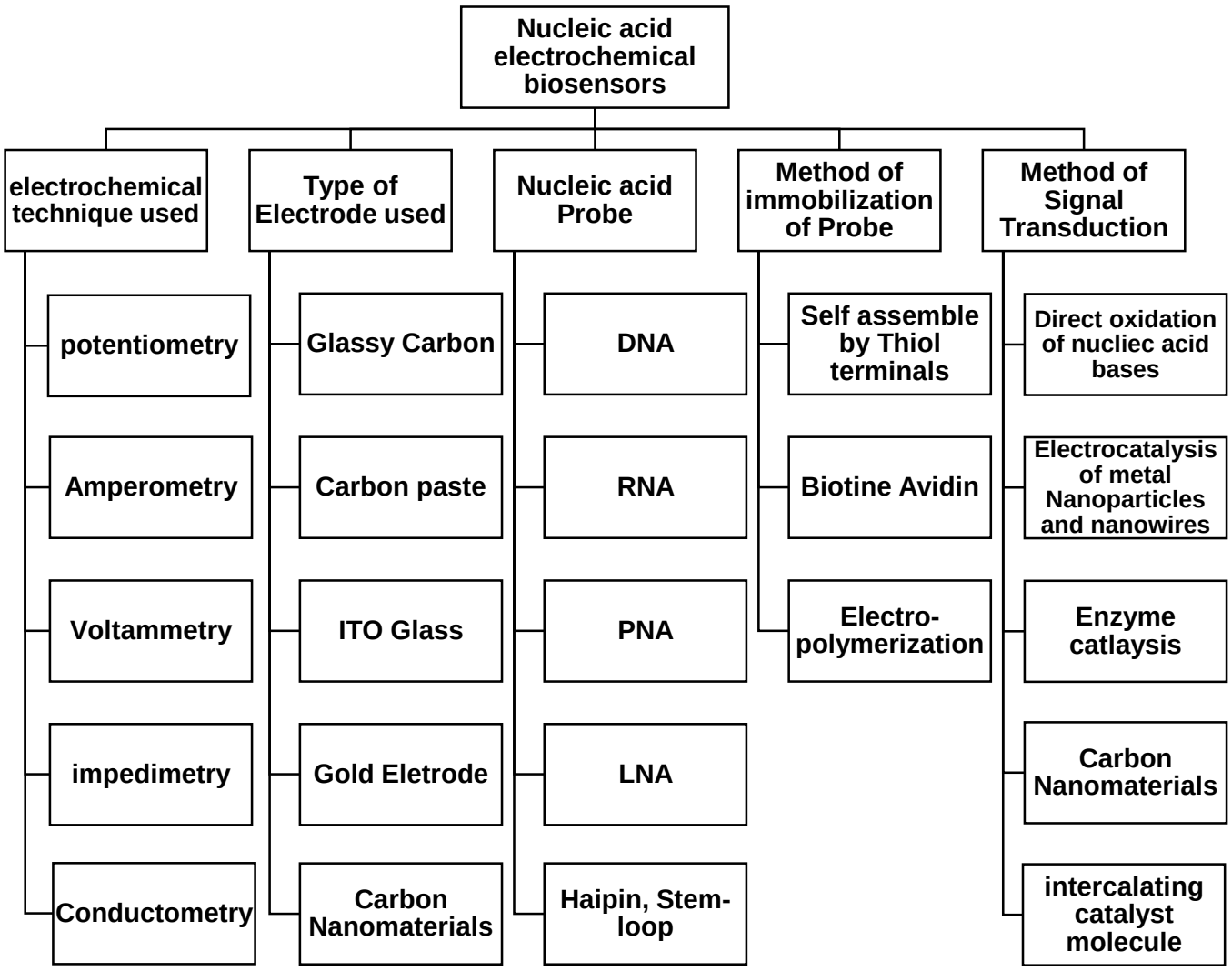


*Figure 1.2 types of techniques and components used in electrochemical biosensors. Adapted from reference*[32] *Bora, U.; Sett, A.; Singh, D. Nucleic Acid Based Biosensors for Clinical Applications.* Biosens J ***2013***, 1*, 104.*

## 1.4 Platinum and silver nanoparticles in DNA electrochemical biosensors.

The interesting physical and chemical properties of nanoparticles makes them useful for electroanalytical applications. Due to the massive increase in the surface area of the metal upon decreasing the particle size, the interfacial properties are greatly enhanced. Catalysis on metallic nanopartilces involves adsorption of the substrate onto the particle's surface. In addition, the surface plasmon properties are greatly affected by the size of the particle. Gold nanoparticles are very widely used due to its plasmonic and catalytic properties and can be used to tag biological materials[33]. Iron oxide nanoparticles contain paramagnetic properties that can be used in many applications including magneto responsive therapy[34], and silver and platinum particles have good catalytic properties[33] as well as plasmonic properties[35,36]. In this work, platinum particles coated with silver are utilised.

### 1.4.1 Platinum Nanoparticles

Platinum particles have excellent catalytic properties, high resistance to corrosion and high stability[37]. A very informative review has been published by Yang *et al.*[37] discussing different methods of synthesis, ways of optimization of size and control of shape and monodispersity[38]. The main interest for the platinum nanoparticles is in fuel cells, as it provides a large surface area for catalysing the redox reaction in hydrogen and methanol fuel cells[38].

Platinum nanoparticles have been utilised in the field of electrochemical biosensors to detect many analytes[34,39]. For example glucose biosensors that use platinum particles as a catalyst for glucose oxidase enzyme[40], cholesterol

biosensors[41] detection of $H_2O_2$ by immobilization of haemoglobin on Pt particles[42] and nucleic acid biosensors[43].

A DNA biosensor was reported by our group that employs region-selective decorated platinum nanoparticles. The particles were synthesized using electrochemical deposition[44]. The electrochemical deposition of platinum can be carried out using single potential step and double potential steps. The double potential step produces more uniform particles in terms of size[45]. Both techniques were used in the current work. Those platinum particles are used to tag a thiolated probe strand oligonucleotide that is complementary to one end of the target DNA strand, which is immobilized at a gold electrode surface using a thiolated capture strand that is complementary to the other end of the target DNA strand. The platinum catalyses the reduction of hydrogen peroxide in a three-electrode electrochemical cell, and the associated amperometric signal is monitored and recorded.[45]

### 1.4.2 Silver nanomaterials in DNA detection

Silver nanomaterials have been used alone or in combination with other metals in constructing electrochemical biosensors due to its catalytic, electric and plasmonic properties[46]. One of the ways of electrochemical detection utilizes the relative ease of silver oxidation. Wang *et al.*[47] developed a method that uses catalytic silver deposition on gold particles attached to target single strand DNA to form a silver shell on the gold particles, followed by detection of the binding event of this tagged target to an immobilized capture strand on electrode surface by chronopotentiometric stripping of the deposited silver. The silver provides a high enhancement (125 times higher) for this electrochemical signal. Zhang *et al*.[48] used silver nanoparticles electrodeposited on multiwall carbon nanotubes MWCNT layer covered with

a layer of poly(trans-3-(3- pyridyl) acrylic acid) as a catalyst to improve the redox signal of DNA-intercalated adriamycin by differential pulse voltammetry (DPV).

Silver nanomaterials have interesting plasmonic properties that can produce surface enhanced Raman scattering SERS effect which attracted the attention decades ago because it is believed that it can reach a single molecule sensitivity[49]. Kneipp *et al*. reported SERS label-free detection of denaturated DNA molecules[50] and a single nucleotide adenine base using colloidal silver in water[51]. Bell *et al*. detected RNA and DNA mononucleotides in a similar way[52]. Mirkin *et al*.[53] used silver enhancement of gold particles by hydroquinone mediated silver deposition in a three-component DNA sandwich assay. The detection was a multiplexed assay using different Raman active labels for different DNA sequences. The sensor is depicted in Figure 1.3.

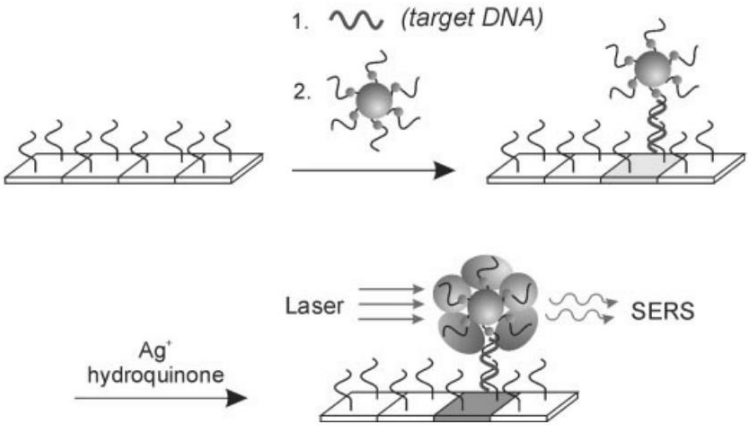


**Scheme 1.**

*Figure 1.3 sandwich assay using gold particles covered by silver layer and Raman active label and used in SERS detection of DNA. Adapted from reference[53]: Cao, Y. C.; Jin, R.; Mirkin, C. A. Nanoparticles with Raman spectroscopic fingerprints for DNA and RNA detection.* Science ***2002***, 297*, 1536-1540.*

Silver nanoparticles were used by Braun *et al*.[54] in a three component DNA sandwich assay in which a smooth silver surface whose microstructures are

small and produces only very low levels of SERS enhancement. Attached to it a label molecule (F). Upon the arrival of the probe bound silver particle, a SERS hot spot is created around the particle, and enhancement factor of the Raman scattering for the surface bound label molecule could be obtained that reached $5\times10^5$. The structure of the biosensor is depicted in Figure 1.4.

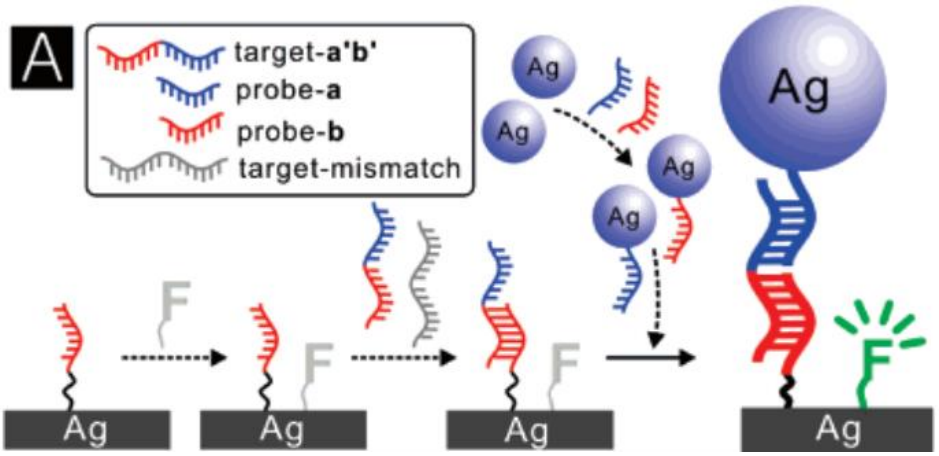


*Figure 1.4 Schematic illustration for the detection of single-stranded DNA by SERS. A target strand (a'b') is captured by probes on Ag nanoparticles and AgFilm-F, resulting in the creation of the SERS-active structure in the form of a-Ag nanoparticle/a'b'/b-AgFilm-F. Target DNA detection is confirmed by collecting the SERS signal of surface-bound Raman label, F. Adapted from reference [54]: Braun, G.; Lee, S. J.; Dante, M.; Nguyen, T.; Moskovits, M.; Reich, N. Surface-enhanced Raman spectroscopy for DNA detection by nanoparticle assembly onto smooth metal films.* J. Am. Chem. Soc. ***2007***, 129*, 6378-6379.*

Other silver nanostructures have been used to enhance the Raman scattering like nanorods[55] nanowires[56], and different shapes that can be synthesized chemically or electrochemically[57].

## 1.5 Gold micro-cavity arrays

The use of gold micro-cavity arrays can be interesting due to its plasmonic properties[58]. Gold micro-cavity arrays were utilised in the current work as a substrate for DNA mediated immobilization of silver-coated platinum particles to enhance SERS signal.

Bartlett *el al*.[59] used templates prepared by assembling closepacked arrays of monodisperse polystyrene spheres to prepared highly ordered three-dimensional macroporous thin films of gold and platinum, by electrochemical deposition of the metals from salt solution. The deposition starts from the bottom of the electrode and the metal is added to fill the gaps between the spheres. The deposition is continued to the desired height. The void spaces or cavities are created after dissolving the polystyrene spheres using a suitable organic solvent.

The gold micro-cavity arrays have some interesting properties based on the highly ordered surface structure. For example, the increased surface area improves the electrochemical signal when used as working electrode, and gives a way to prepare miniaturized electrodes with high effective surface area[60]. The sub-micron features of the metal improve the optical and plasmonic properties[58]. For example, the micro-cavity array provides a good substrate for SERS. The enhancement is particularly strong if the Raman active molecules are present in certain regions of the cavities. The position and intensity of enhancement of those hot spots depends on the size of the cavity, degree of completeness of the spherical void space inside, height of the walls, position and angle of the incident excitation beam[61]. In Figure 1.6 position of those hot spots is illustrated according to the theoretical calculation using the Mie solutions to Maxwell's equations.

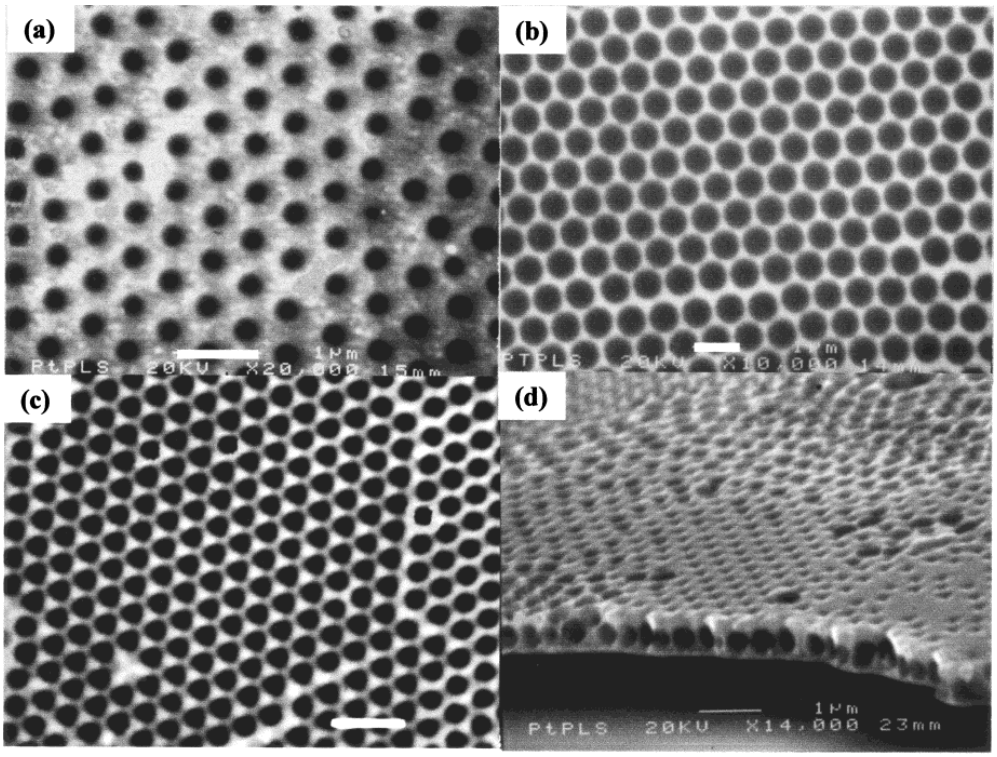


*Figure 1.5 SEM images of regions of macroporous platinum films grown with a thickness gradient by electrochemical deposition through templates assembled from either 500- or 750-nm-diameter polystyrene spheres. a) A platinum film deposited through a template of 500-nm-diameter spheres with a layer thickness of about 17 nm and about 180-nm pore mouth diameter; (b) Pt film which is about 130 nm thick deposited through a template made of 750- m polystyrene spheres and the pore mouth diameter is 570 nm (c) Pt film produced using 500 nm latex sphere template with rounded triangular pore mouth diameter about 200 nm and about 370 nm thick; (d) image of a fractured platinum film one of the template-sphere diameter thick, template sphere diameter 500 nm. Adapted Reference[59]: Kelf, T.; Sugawara, Y.; Cole, R.; Baumberg, J.; Abdelsalam, M.; Cintra, S.; Mahajan, S.; Russell, A.; Bartlett, P. Localized and delocalized plasmons in metallic nanovoids.* Physical Review B ***2006***, 74*, 245415.*

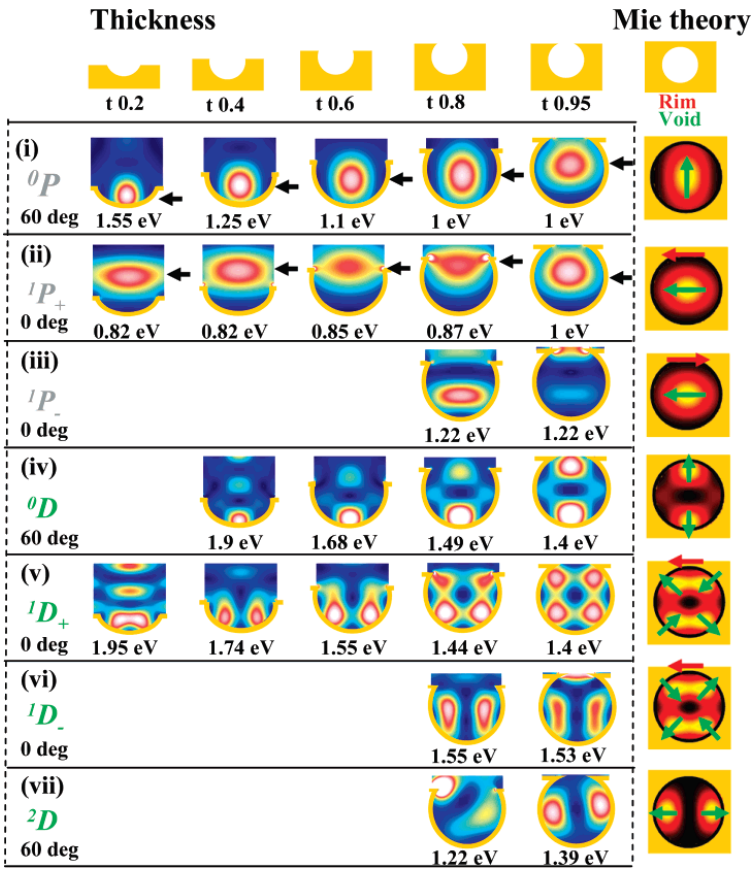


*Figure 1.6 Spatial intensity distributions at increasing thickness, with (right) field profiles from Mie theory. Theoretical position of the maximum optical field. Adapted from reference [61]: Cole, R. M.; Baumberg, J. J.; García de Abajo, F Javier; Mahajan, S.; Abdelsalam, M.; Bartlett, P. N. Understanding plasmons in nanoscale voids.* Nano Letters ***2007***, 7*, 2094-2100.*

It has been proven that the SERS and surface-enhanced resonance Raman scattering (SERRS) response and intensity differs if the Raman active substance is attached to the surface or inside the cavities[62]. As a combination of the enhancement expected from a cavity and a nanoparticle, our group reported a DNA-mediated immobilization of platinum nanoparticles in gold nano-cavity array of a diameter of 600 nm[63]. Despite the fact that a platinum particle in a gold cavity might not be the optimum condition of the highest enhancement that could be achieved, two fold enhancement of the SERS was observed in this study[63].

## 1.6 Conducting Nucleic acid

DNA electric conductivity has been studied extensively for its role in the signalling and DNA repair functions in living cells[64], and also the potential use of DNA as a conductor in nanoscale circuits and devices[65]. The electron transfer process is believed to occur through the π-stacking of nucleotides[66]. The phosphate-sugar backbone does not have a role in the electron transfer. As an improvement for the electron transfer along DNA molecules, the backbone can also be modified so as it becomes electro conducting[67]. One way to attain this can be by synthesizing an artificial analogue for DNA that replaces the phosphate deoxyribose backbone with a conducting backbone with a conjugated π system. The backbone conductivity will improve the overall conductivity, perhaps increasing the current response and consequently the sensitivity of nucleic acid based electrochemical biosensors. In this review we will discuss the native DNA structure and the previous efforts to modify this structure.

### 1.6.1 DNA structure

DNA is the biological polymer that carries the genetic information for the expression of proteins to carry out physiological and structural functions in the cells and tissues of living organisms. The double helix structure of DNA, Figure 1.7, was described by Watson and Crick in 1953[68]. It is composed of four different nucleotides, two are purine derivatives namely adenine (A) and guanine (G), and the other two belong to the pyrimidines namely Thymine (T) and Cytosine (C). They are connected to a phosphate sugar moiety composed of deoxyribose sugar, which is formed of five membered ribofuranose ring. In the polymeric chain, sugar monomers are linked via

phosphodiester group from the carbon number 3' and 5'. That is why one end of the DNA chain is named 5' end and the other is called 3' end. In Figure 1.8 the sequence of 3'-GCAT-5' showing numbering and the four different nucleotides is presented. DNA molecules exist mainly in the form of a duplex of two DNA strands complexed together in an antiparallel fashion. However, DNA multiple strands complexes were discovered, for example DNA triplexes and quadruplexes i.e three and four strands bound together.[69]

The sequence recognition properties depends on the base pairing of the heterocyclic nucleotides through formation of two hydrogen bonds in the case of A-T pairing and three hydrogen bonds between C-G base pairing. In either cases, the pyrimidine-purine pairing is coplanar and stacked on top of each other to form a hydrophobic domain at the core of the duplex. The double strand complex winds around its core axis to form a helical shape. The winding creates two helical grooves along the DNA duplex strand called major groove and minor groove due to their difference in width and depth[70]. Unlike the core of the DNA duplex, the phosphodiester-deoxyribose backbone that carries the nucleotides is hydrophilic. The phosphate group carries a negative charge that is responsible for many physical and chemical properties of DNA for example its behaviour in electrophoresis (migration towards the anode).

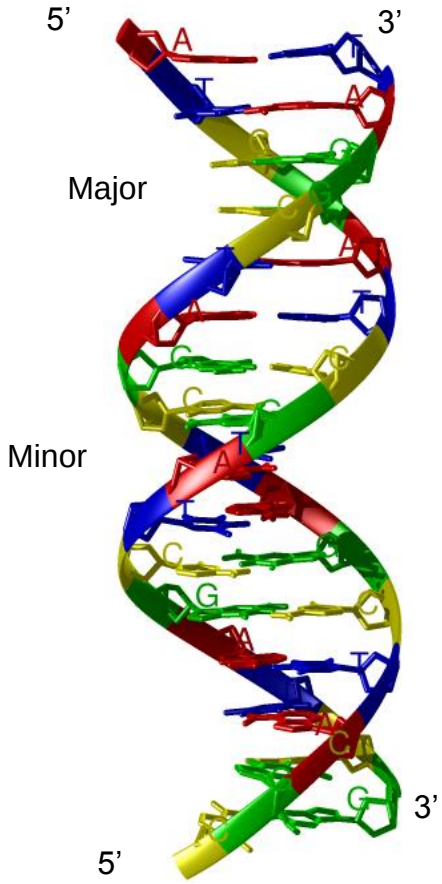


*Figure 1.7 DNA B-form duplex helix, ceated using the templates provided with the Hyperhem (8.0.9) Molecular Modeling package.*

The DNA helix can adopt different conformations depending on the medium or chemical modifications like Form A and B which differ in the helix length and the grooves dimensions. The prevalent form in physiological conditions is B-form. While form A is more prevalent in dehydrated samples[71].

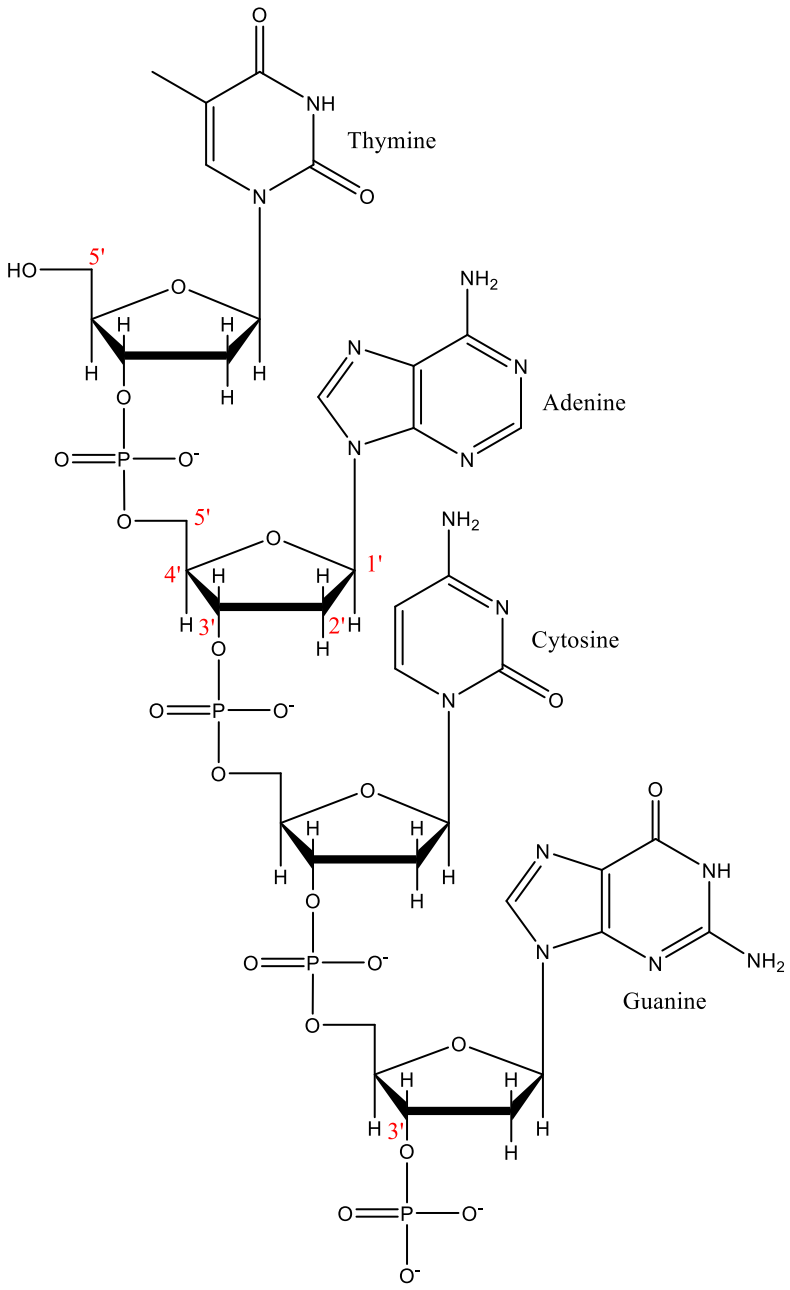


*Figure 1.8 DNA of the sequence 3'-GCAT-5' showing numbering and four different nucleotides.*

### 1.6.2 DNA modifications

There are many different modifications to the DNA that can be found in the previous literature. The main focus will be on modifications that involve backbone modification specially that involve adding aromatic rings to the backbone of the nucleic acid. Also discussing some of the most widely recognized nucleic acid analogues.

Nucleic acids selective binding to complementary target DNA or RNA inside the cell makes it a potential therapeutic agent that can prevent the translation of transcription of a certain gene. This will consequently inhibit the production of the associated protein and prevent its action. This type of analogues are referred to as the antisense agents[72]. That was the motivation for the efforts to design and produce antisense agents with higher binding affinity to natural nucleic acids.

One of the earliest modifications was the introduction of sulphur atom to the phosphodiester group to form what is known as phosphorothioate nucleoties[73] This oligonucleotide analogue exhibits good DNA and RNA recognition properties and enhanced *in vivo* stability. A hallmark of the phosphorothioate linked DNA is that it forms duplex structures with RNA that are recognized by RNase leading to degradation of the target RNA by the enzyme[74]. Phosphorothioate oligonucleotides were the first antisense drugs to receive FDA approval for the treatment of a number of diseases[75].

Freier *et al*. published a comprehensive review about DNA modifications[76]. In this review, about 200 modifications were discussed. The number of the modified bases ranged from 1 to 10. Thymine was chosen to be the modified base. Some of the modifications involved adding different groups to the sugar ring and modification of the pyrimidine ring of thymine. Other modifications were related to the phosphodiester and 5' methylene group connects the deoxyribose sugar rings that forms the (-O-$PO_2$-O-$CH_2$-) structure.

Several modifications were tested in which these four atoms long chain (-O-$PO_2$-O-$CH_2$-) and were replaced with a non-phosphorous containing backbone. In Figure 1.9 (A) replacement of the phosphate backbone with four CH2 groups, flexible glycol and ether linkages were very destabilizing to the

duplex formation and caused the melting temperature ($T_M$) values to be less than the natural DNA. When C=C double bonds and C≡C triple bonds were incorporated into the backbone, destabilization was less pronounced but none of the oligonucleotides with only carbon backbone hybridize to complementary RNA with the same affinity as unmodified DNA. In contrast to these all carbon backbones, the thioformacetal backbone (-S-$CH_2$-O-$CH_2$-) increased $T_M$ 0.8°C per substitution. Other oligonucleotides containing unsubstituted urea, carbamate and amide linkages were synthesized[76]. Different number of atoms like three-atom and five-atom amide linkages between sugar rings were proved to be destabilizing. The four atoms modifications that has urea, carbamate and amide backbones were also destabilizing except two amides did not destabilize the duplex formation, both of which had the amide moiety located in the middle position. A single oligonucleotide uniformly modified with amide 3 was also investigated. Its $T_M$ was slightly lower than that of the unmodified DNA control suggesting that the flexibility of intervening phosphates is required to obtain improved hybridization compared to natural DNA.

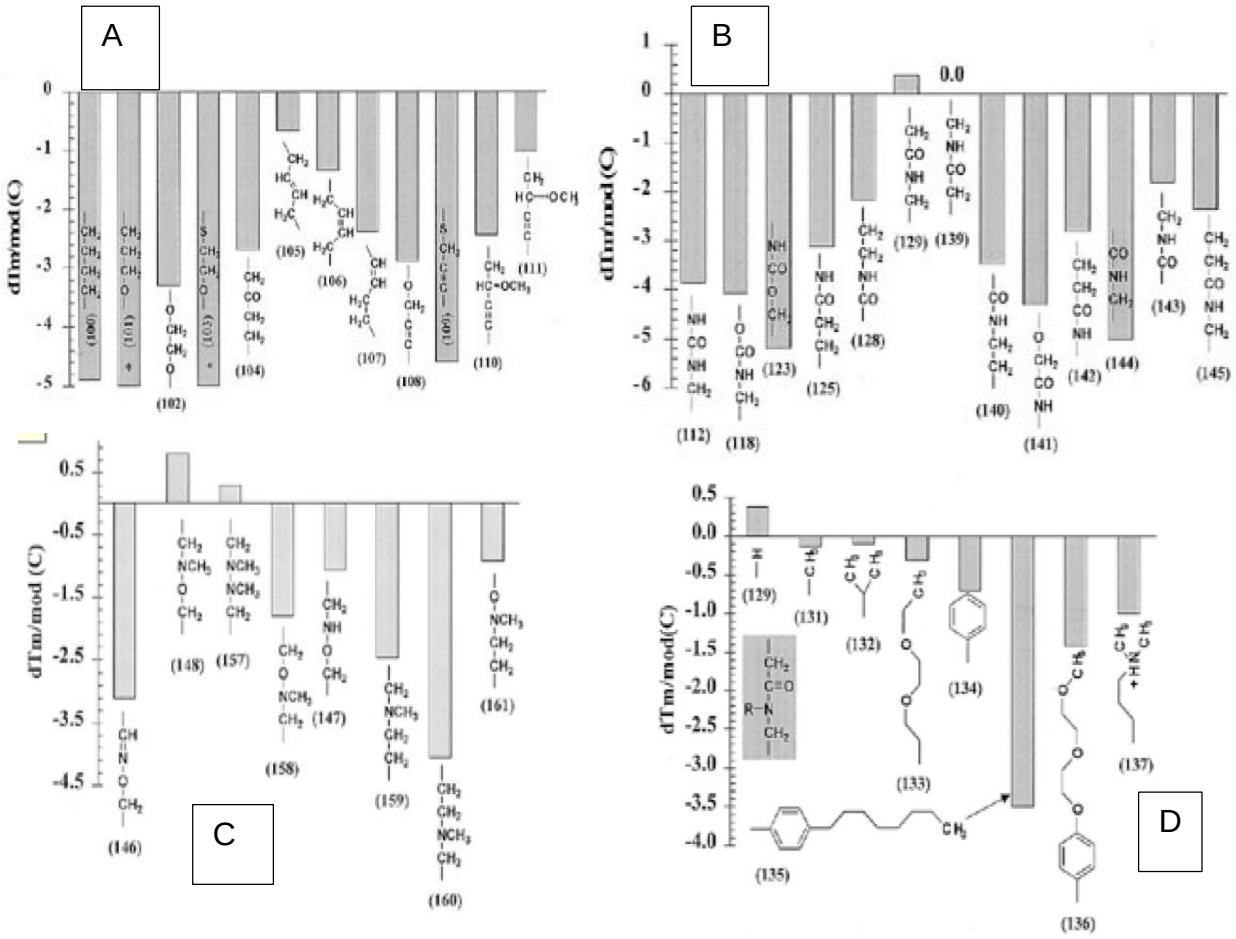


*Figure 1.9 Average $\Delta T_M$ (°C) per substitution for oligonucleotides containing non phosphorous backbone modifications. (**A**) Glycols, ethers and all carbon backbones; (**B**) urea, carbamate and amide backbones. (C) amines, hydroxylamines and hydrazino backbones; (D) N-substituted amide 3 backbones. Figure Adapted from reference [76]: Freier, S. M.; Altmann, K. H. The ups and downs of nucleic acid duplex stability: structure-stability studies on chemically-modified DNA:RNA duplexes.* Nucleic Acids Res. ***1997***, 25*, 4429-4443.*

Other four-atom link between sugar rings, non phosphorous backbones were investigated. Among these amine, hydroxylamine and hydrazino backbones, only two were stabilizing. These were the methylene (methylimino) and the dimethylhydrazino. Effect of *N*-substituted of amide was investigated. Although small substituents on the nitrogen of amide were tolerated, none improved hybridization compared to the amide itself and large substituents were very destabilizing.

As seen from the previous study, the amide linkage and sulphur were found to be the most successful modification in the backbone with the highest increase in melting temperature. The stability of these modifications is likely due to a tendency of the backbone in the single strand to pre-organize in conformations favourable for duplex formation. The beneficial effect of a rigid bond in the middle position was also observed for the C=O group in amide and trans C=C double bond which was the least destabilizing of the all carbon backbones[77].

### 1.6.3 Locked Nucleic acid (LNA).

The extent of pre-organization of the nucleic acid analogues is a factor in controlling the hybridisation rate and the stability of the duplex formed. One of the analogues that possesses better binding properties than natural nucleic acids is the locked nucleic acid (LNA). The sugar moiety contains a methylene bridge between the oxygen at 2' carbon and the 4' carbon or the furanose ring as shown in Figure 1.10. Its superior properties is believed to be attributed to this strained structure that locks it to a more favourable conformation. These properties emphasizes the importance of having a rigid backbone in the right conformation. Unlike the PNA which carries no charge on the backbone, LNA's backbone has a negative charge similar to DNA and RNA. It was first developed by Koshkin *et al*. and they described its synthesis[78] and hybridization[79] properties in 1998.

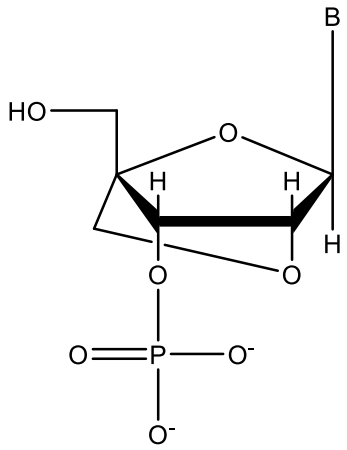


Locked nucleic acid (LNA)

*Figure 1.10 Chemical structure of a monomer of locked nucleic acid (LNA).*

### 1.6.4 Peptide nucleic acid (PNA)

Nielsen *et al*.[80] in University of Copenhagen in 1991 incorporated an amide group into the backbone to successfully produce the peptide nucleic acid analogue (PNA). Figure 1.11 shows that the PNA backbone is composed of glycine ethyl-based polyamide units. The molecule was designed and modelled by computer originally to bind to the major groove of a DNA duplex and form a triplex. Upon hybridization with the complementary duplex strands, the newly designed PNA could displace the homologues DNA strand and bind to the complementary strand. The DNA-PNA duplex was found to be more stable and have higher melting temperature and binding[81].

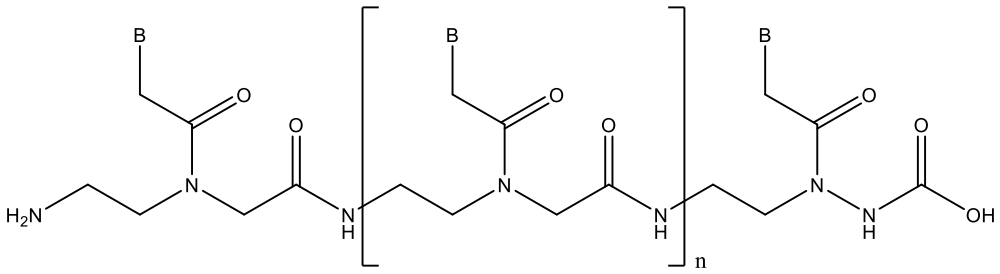


Peptide nucleic acid PNA

*Figure 1.11 Chemical structure of peptide nucleic acid PNA*

The synthesis of PNA monomers was described by Dueholm *et al*.[82]. The nucleotides used are acetic acid derivatives of natural nucleotides, that form an amide bond to the amine side of poly glycine ethyl backbone. The thymine-yl acetic acid derivative synthesis is depicted in Figure 1.12 from thymine and 1-bromoacetic acid.

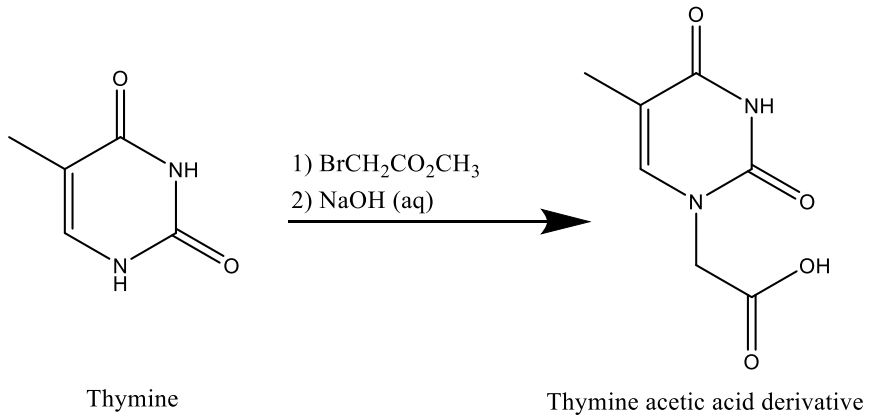


*Figure 1.12 Synthesis of thymine-ly acetic acid.*

The synthesis of PNA oligonucleotides can be carried out in a fashion similar to the peptide synthesis using modified Merrifield solid phase synthesis scheme. The general procedure of solid phase synthesis was depicted in Figure 1.13. Different strategies of synthesis depend on the protecting groups used were developed.

There are two types of amino groups in the A, C and G monomers. The backbone amino group and the exocyclic amino groups on the nucleotide rings. The protecting group used with the exocyclic amino groups should withstand the cleavage conditions of the backbone protecting group to prevent the connection of nucleotides from the wrong amino group. Christensen *et al*.[83] used tertiary butyloxycarbonyl t-Boc group to protect the backbone amino groups, while the nucleotide amino groups were protected by carboxybezyl CBZ protecting group. The deprotection of the t-Boc group was carried out using trifluoroacetic acid and the final deprotection of the

nucleotides was carried out using hydrofluoric acid. Thomson *et al*.[84] also prepared the PNA using solid phase synthesis but replaced the tBoc group with Fmoc to protect the backbone amino group. The deprotection was carried out using piperidine. While Sugiyama *et al*.[85] prepared PNA using Fmoc to protect the backbone amino groups and t-Boc group to protect the exocyclic amino group for the nucleobases.

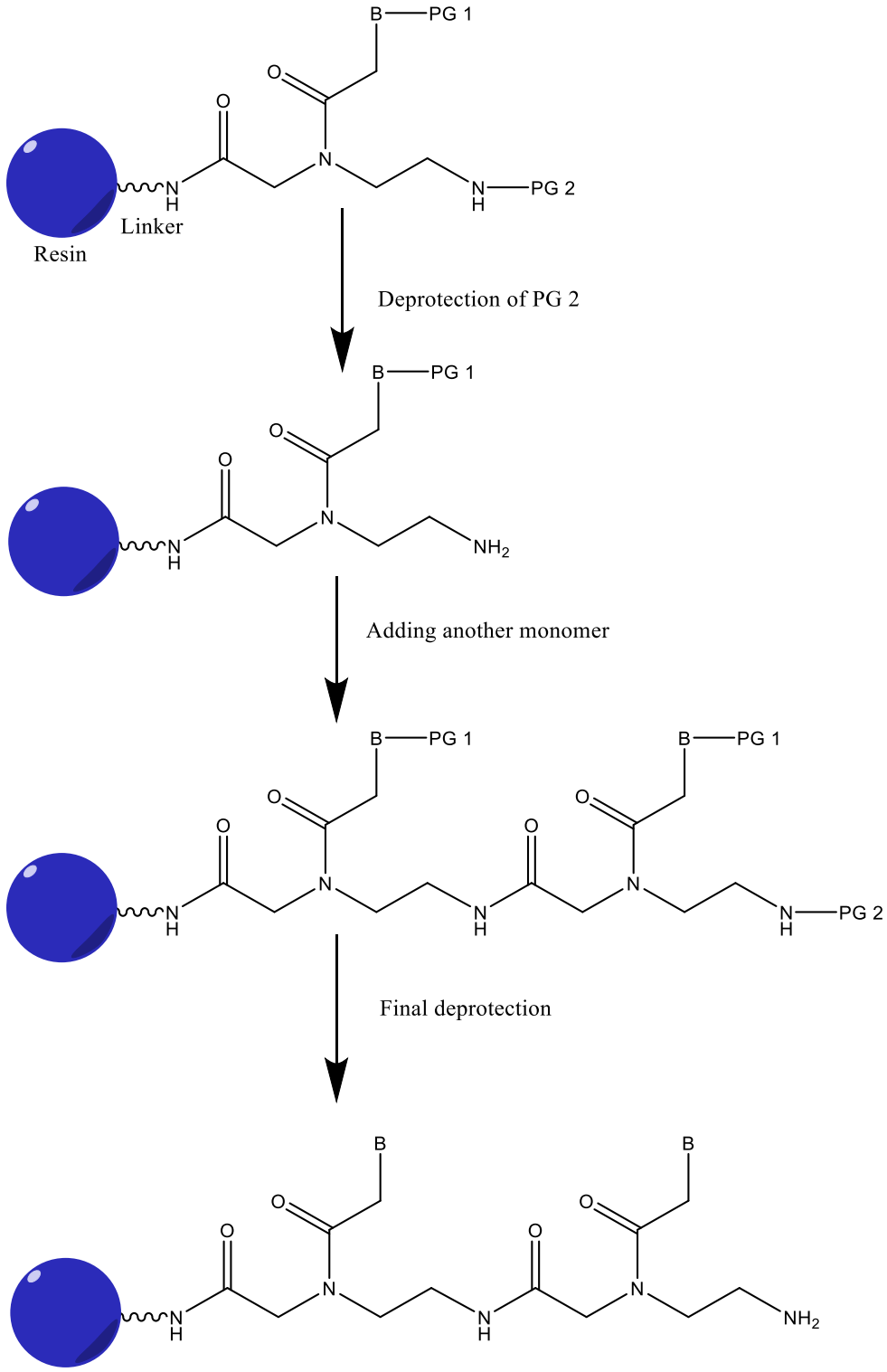


*Figure 1.13 General scheme of solid phase synthesis of PNA.*

In this thesis, the solid phase synthesis procedures described here was adapted to suit an electrochemical stepwise synthesis of a nucleic acid analogue with a conductive polymer backbone. The t-Boc was

used to protect the backbone amino group. However, the coupling of backbone units was carried out electrochemically.

### 1.6.5 Aromatic modification to DNA backbone.

Although PNA has superior DNA binding properties, it suffers from poor cellular uptake. Also PNAs are acyclic and therefore conformationally quite flexible. It was expected that increased structural rigidity of the PNA backbone in a way that improves the preorganization of the oligomers to form duplex or triplex complexes.

To address the previous issues, Tsantrizos *et al*.[86] reported the introduction of a benzene ring into the structure of PNA and termed it aromatic PNA or APNA. They suggested that if analogues were designed to be more hydrophobic that their cell membrane penetrating properties could be enhanced. Also the aromatic ring can provide rigidity to the backbone and the conformation of the single strand will favour binding if the stereochemistry is controlled[87].

Figure 1.14 depicts the APNA designed in Tsantrizos group.

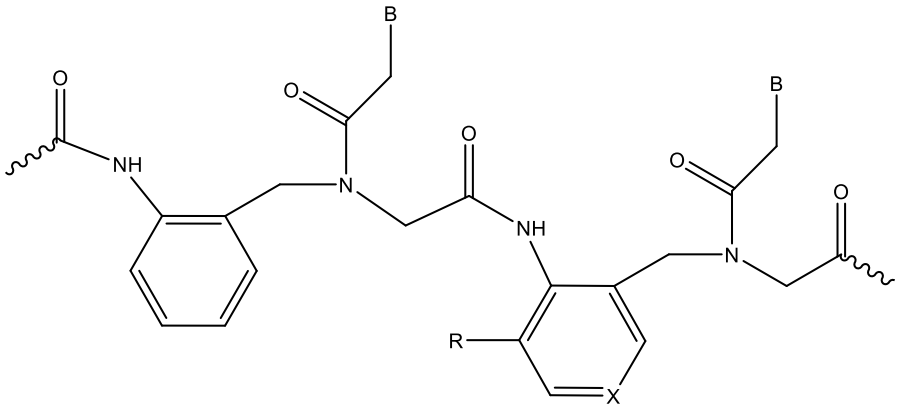


*Figure 1.14 APNA with positions of modifications, adapted from reference[88]: Fader, L. D.; Myers, E. L.; Tsantrizos, Y. S. Synthesis of novel analogs of aromatic peptide nucleic acids (APNAs) with modified conformational and electrostatic properties.* Tetrahedron ***2004***, 60*, 2235-2246.*

Binding studies of those analogues in chimeric strands (which have both PNA and APNA bases) showed good binding to both DNA and RNA to form duplexes and triplexes[87]. The increase of the number of APNA monomers in the sequence was well tolerated[88]. However, upon preparing a strand that is formed solely of APNA that consisted of a decamer of the homopolymer, it was found to be insoluble in aqueous solvents, which prevented the hybridization studies using UV absorption spectroscopy or circular dichroism spectropolarimetry (CD). Other modifications to the backbone of PNA especially using pyridine moiety were attempted[88]. Adding a heteroatom like nitrogen in the X position to form the pyridine analogue of APNA, and an exocyclic carboxylic group in R position as illustrated in Figure 1.14. Those modifications rendered the structure more hydrophilic and did not affect the binding abilities compared to the previously synthesized APNA.

Also the number of methylene groups that is separating the tertiary amine from the carbonyl carbon in the backbone was changed[88], and it was found that any change from the normal number of separating atoms between the nucleotides in native DNA molecules (five toms separation between each nucleotide) caused the binding properties of the analogue to decrease. In PNA the number of separating atoms is retained at five and and the same number is achieved in LNA and APNA.

The number of separating methylene group in the linker that attaches the nucleobase to the backbone was also altered[88]. It was found that any change from the total number of two atoms between the nucleobase nitrogen and the backbone nitrogen caused destabilization to the duplex, which also agrees with the results presented above.

## 1.7 Conductive polymers and polyaniline review

### 1.7.1 Introduction

Conductive polymers started to attract the attention of scientists many decades ago[89] In the mid-1970s, the discovery of doped polyacetylene[90] marked the beginning of modern conductive polymers and polyacetylene its discovery was awarded the Nobel Prize for Chemistry in 2000[89]. As illustrated in Figure 1.15, many different conjugated conductive polymers have been synthesised to suit different applications[91].

In the current work, polyaniline was prepared as a backbone for a conductive DNA analogue, polypyrrole and polythiophene were modelled and tested for the suitability for the same task. For this reason, the review is focused on polyaniline.

### 1.7.2 Applications of conductive polymers

The interest in organic conductive polymers is due to their electric conductivity, optical and mechanical properties[89]. Although conductive polymers can in theory act as lightweight conductors that can replace metals in many electrical applications this has not been achieved yet. Since the 1980s, conductive polymers have been applied for corrosion protection of metals. That is due to the relative ease of synthesis both via chemical and electrochemical methods coupled with their electrical conductivity[92]. Also, a lot of work has been done to utilise the electrochemical switching properties between oxidized and reduced forms especially for polypyrrole to act as a means of energy storage when metal polymer complex is used[93]. Photonic

properties of conducting polymers are mainly either photovoltaic, i.e. use light to induce charge separation and hence act as solar cell material, or electrochemically induce luminescence which can be used as light emitting diode[89] The efficiency of conductive polymer based organic solar cells is still way behind single crystal silicon semiconductor based solar cells[89]. However, the cost of the silicon cells remains high limiting its wide spread usage. Thanks to the intensive research efforts that produces different types of polymers and modifications to conductive polymers, the efficiency of polymer based solar cells is increasing year after year[94].

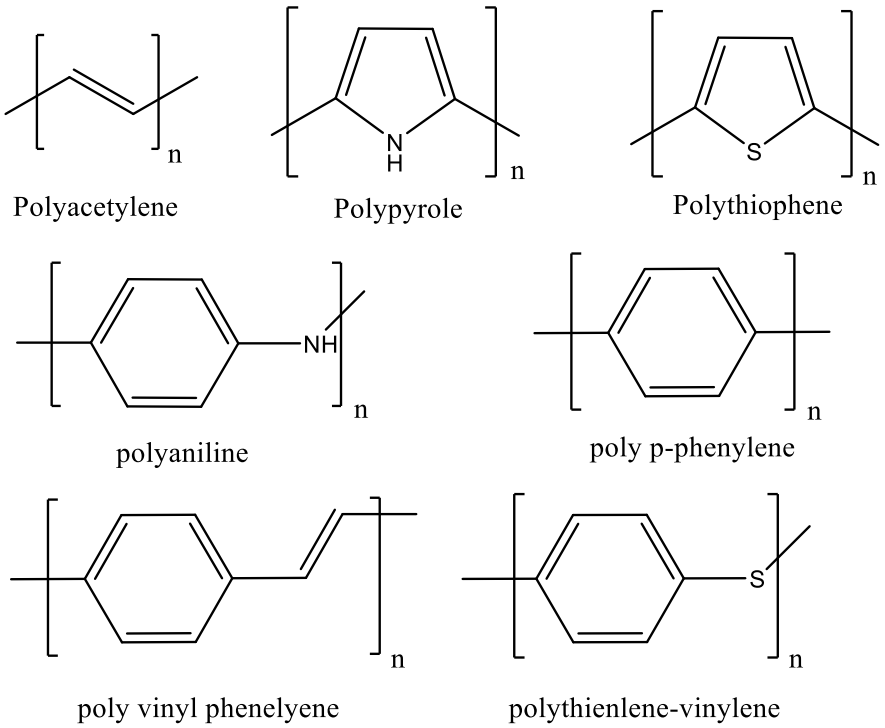


*Figure 1.15 Different chemical structure of known conductive polymers.*

The electrically induced light emission of conductive polymers is basically the reverse of the photovoltaic properties. In which the conductive polymer is designed to emit photons upon applying voltage to it. The field of organic light emitting diodes (OLED) witnessed a great advancement since its discovery by Richard Friend and coworkers[95]. The efficiency of these devices started

very low then after intense research efforts the OLED based display devises are widely marketed[96].

The mechanical properties of conductive polymers is a result of the influx and out flux of ions to the matrix of the polymer upon changing oxidation state. More futuristic applications can be employ those mechanical properties like artificial muscles, smart membranes and smart drug delivery systems[97].

### 1.7.3 Properties of conductive polymers

#### 1.7.3.1 Electric conductivity

The extent of electronic conductivity depends on the ease of transition of electrons from the valence band to the conductance band. In the case of conductors, the valence band overlaps with the conduction band, i.e., $E_g \approx 0$ eV, where $E_g$ is the gap potential, so the conduction band always occupied partially by electrons. In case of the semiconductors, there is a gap between the valence and conduction bands but this gap is narrow with $E_g \approx 1.0$ eV; which allows the possibility of exciting electrons from the valence band to the conduction bands in room temperature. On the other side, in case of insulators, the separation between the valance and conduction band is large with $E_g \geq 10$ eV. That is why it is impossible to excite electrons from the valance band to conduction band in normal conditions using normal potentials. The band gap, $E_g$, of conducting polymers lies in the region around 1.0 eV, that is why conducting polymers may be regarded as semiconductors.

Conducting polymers comprise 1D chains that can form crystalline ordered structure and other amorphous disordered regions between ordered crystals[91]. The charge transfer along single polymer chain depends on the quasi infinite π system extended along the fibres and mediated by electronic states like solitons, polarons and bipolarons[91].

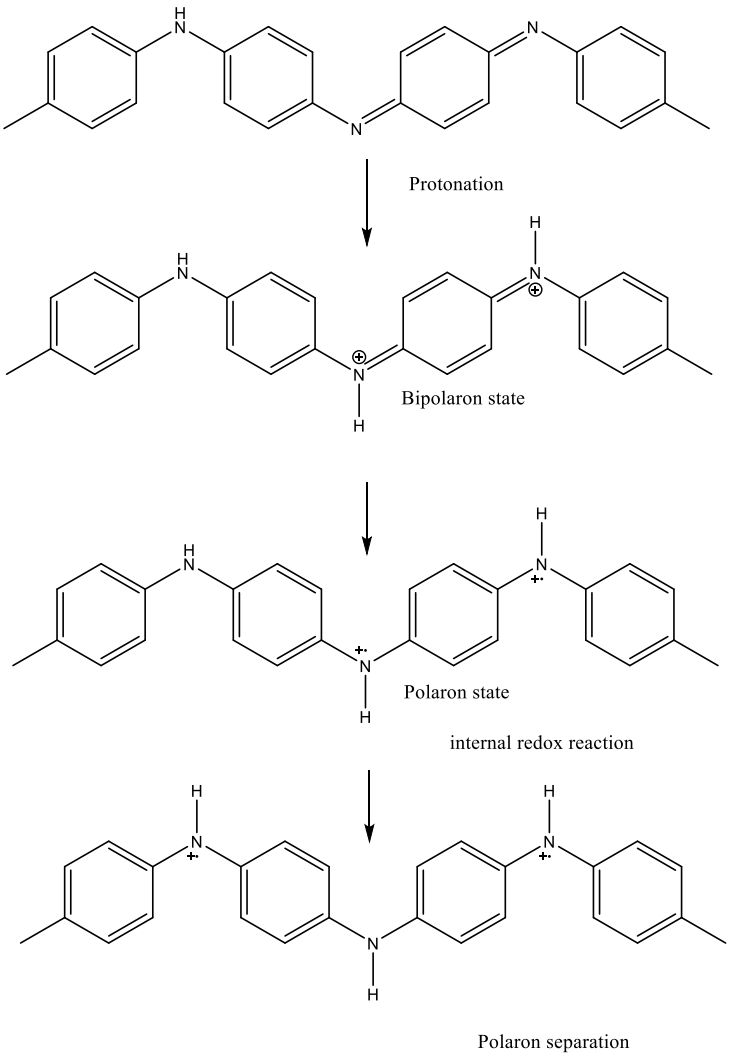


*Figure 1.16 bipolaron formation and separation in emeraldine salt. Figure adapted from reference[98] : Stafström, S.; Bredas, J.; Epstein, A.; Woo, H.; Tanner, D.; Huang, W.; MacDiarmid, A. Polaron lattice in highly conducting polyaniline: theoretical and optical studies. Phys. Rev. Lett. 1987, 59, 1464.*

Figure 1.16 depicts the formation and propagation of the conductive bipolaron along polyaniline fiber[98]. Conduction in conjugated polymers is not only related to the charge transfer along the conjugated system, but also the need for electrons to hop from one ordered crystalline region to another crystalline region by resonance tunneling through localized states in the disordered regions[91]. Those regions with different arrangement of polymer

fibers, their distribution and their relative concentrations in the bulk of the material can significantly influence its physical and electrical properties[91].

| Conducting polymers | Conductivity (Ω-1 cm-1) | Type of doping |
|---|---|---|
| Polyacetylene (PA) | 200 - 1000 | n, p |
| Polydiphenylamine (PDPA) | 500 | n, p |
| Polyaniline (PANI) | 5 | n, p |
| Polypyrrole (Ppy) | 40 - 200 | p |
| Polythiophene (PT) | 10 - 100 | p |

*Table 1 Conductivity of common organic conducting polymers adapted from reference [99]*

### 1.7.3.2 Role of doping in conductive polymers

The discovery of increased conductivity of conjugated polymers upon doping was a key turning point in the research in this area. Doping in most of the cases is oxidizing the conductive polymer by adding an anion that can remove an electron from the Pz orbital, which increases the mobility of electrons in these delocalized orbitals. Thus, the conjugated p-orbitals form a linear electronic band[91]. Polyaniline is inherently conducting. However, it has three discreet oxidation states that differ radically in their electric conductivity. Leucoemeraldine is the fully reduced state of polyaniline and pernigraniline state which is fully oxidized form, and emeradine form with is half oxidized half reduced and it is the only conductive state of polyaniline. Figure 1.17 shows the chemical structures of polyaniline oxidation states. Doping of emeraldine salt improves the conductivity, and also alters the physicochemical properties of the bulk polymer.

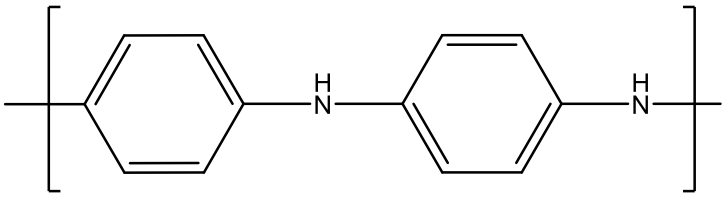

Leucoemeraldine

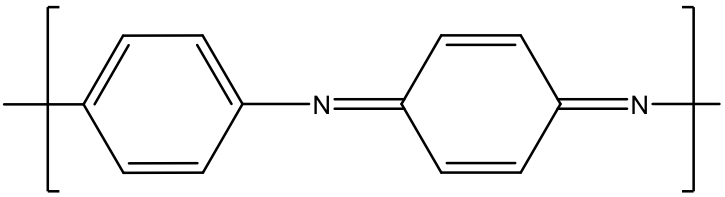

Pernigraldine

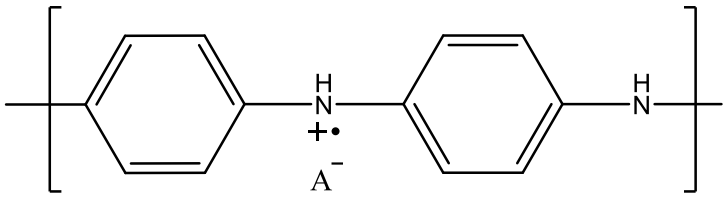

emeraldine salt

*Figure 1.17 Doping states of polyaniline*

### 1.7.1 Synthesis of polyaniline

Polyaniline is commonly prepared by chemical or electrochemical oxidative polymerization procedures[89]. In this thesis, electrochemical polymerization is used to synthesize the conductive polyaniline nucleic acid analogue, that is why the mechanism and formation methods are discussed.

#### 1.7.1.1 Electrochemical polymerization

Normally the electrochemical polymerization of aniline is carried out in an acidic medium[89]. The low pH is favourable to solubilize the monomers and to generate the emeraldine salt during synthesis which favours the formation of a thick layer. However, electrochemical polymerization in neutral media has been reported[100].

Polyaniline can be synthesized using constant potential techniques like amperomety or potential scanning techniques like cyclic voltammetry.

Because the oxidation potential of the monomers is around 0.9 V and the over oxidation of the polyaniline to the fully oxidized pernigraldine form is at approximately 1.1 V, the electrochemical polymerization should be carried out with care as this form is non-conductive. The mechanism of electrochemical polymerization of polyaniline is depicted in Figure 1.18.

The steps of are described as follows:

Step 1: Anodic oxidation of monomer and formation of a radical cation which forms resonant forms at the ortho and para position of aniline although it occupies the para position most of the time.

Step 2: Two oxidised radical species of aniline couple to form a dimer. One of them the radical is on the nitrogen atom and the other has the radical unpaired electron on the para position. This dimer is a dicationic species, which turns into a neutral dimer upon deprotonation.

Step 3: Further oxidation of the neutral dimer that results in the formation of a radical cation on the amino group nitrogen atom, which in turn couples with an aniline radical cation with the unpaired electron centred in the para-position. This process is repeated and results in propagation of the chain.

Step 4: The neutral polymer can be oxidized and doped with the anion from the acidic media to produce emeraldine salt.

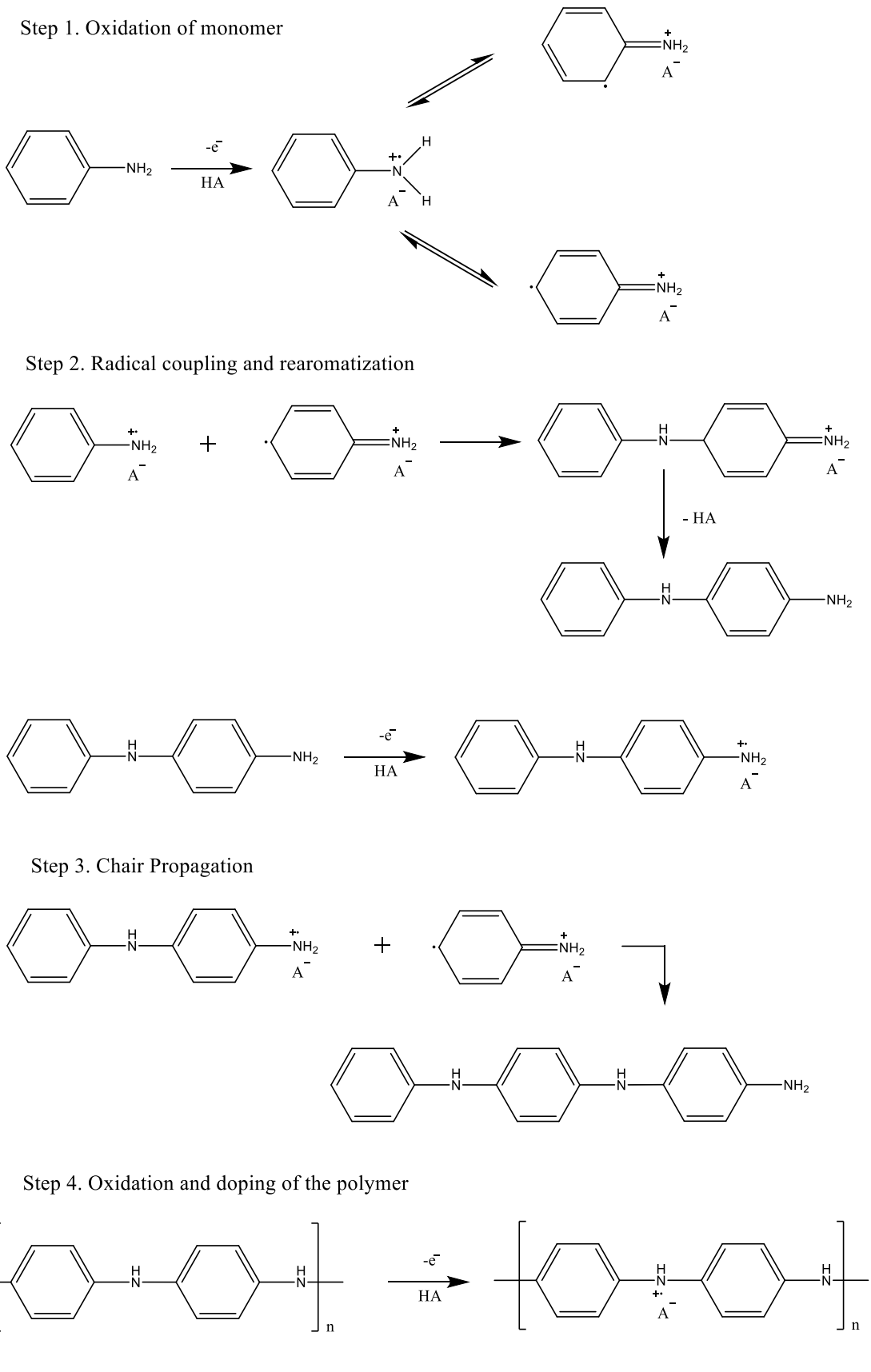


*Figure 1.18 Mechanism of electrochemical polymerization of aniline adapted from reference[89]: Wallace, G. G.; Teasdale, P. R.; Spinks, G. M.; Kane-Maguire, L. A.* Conductive electroactive polymers: intelligent polymer systems; *CRC press: 2003.*

#### 1.7.1.2 Other methods of synthesis

Chemical polymerization of aniline produces bulk quantities of the polyaniline and it is the major way of producing polyaniline commercially. It requires a chemical oxidant in solution and ammonium persulphate is the mostly used oxidant[89]. Ceric ammonium sulphate[101], potassium dichromate[102] and hydrogen peroxide[103] have been used as oxidants.

Polyaniline was prepared by photochemical initiation of oxidation by using layers of Ru complexes[104] as initiators and methylviologen $MV^{2+}$ [105]. Upon photo excitation of Ru complex for example $[Ru(bipy)_3]^{2+}$ it reaches the triplet exited state which allows the electron transfer between the exited complex and the $MV^{2+}$ and creates $[Ru(bipy)_3]^{3+}$ which is a powerful oxidizing agent that commences the aniline oxidation reaction.

Horseradish peroxidase is an enzyme that has been used as an oxidant for the synthesis of polyaniline[106]. It has the advantage of being able to produce polyaniline at higher pH than the chemical polymerization method and allowing biological templates like DNA to influence the growth of polyaniline.

### 1.7.2 STM and single molecule conductance of polyaniline

Scanning tunnelling microscopy is one of the techniques that can be used to probe the conductivity of single molecules. To measure the conductance of a single molecule, it must be wired in a reliable way to two electrodes[107]. Typically, the conductance measured depends on the intrinsic physicochemical properties of the molecule and the interconnect which may be influenced by the electrode material and the local environment in which the experiment is being carried out[108].

Conductivity is defined as the reciprocal of electrical resistivity, and is a measure of the ability of a certain material to conduct an electric current. In the large scale, the conductivity, σ, is defined as:

*Equation 1*

$$\sigma = \left(\frac{I}{V}\right) \times \left(\frac{L}{A}\right)$$

where I is the electrical current, V is the applied bias voltage, L is the length of the conducting material, and A is its cross sectional area. For a single molecule, A and L are hard to precisely define. That is why a more well-defined quantity is the conductance, G, given by:

*Equation 2*

$$G = \frac{I}{V}$$

Figure 1.19 (a) describes the setup for a single molecule conductance experiment. A voltage bias $V_{bias}$ is applied between the two electrodes that drives a current $I_s$ which is measured and the G value is calculated. In Figure 1.19 (b), the direct conductance between the two electrodes or the through a metal wire gold for example, is called the quantum point contact. Its conductance $G_0$ = 77.4 μS, corresponding to 100% transmission of electrons. The values measured for organic molecules are normally much smaller than this value. P-benzenedithiol[109] for example which should be one of the highly conductive organic molecules due to its length and good contact with gold electrodes through the dithiol has a first conductance peak at 0.83 μS.

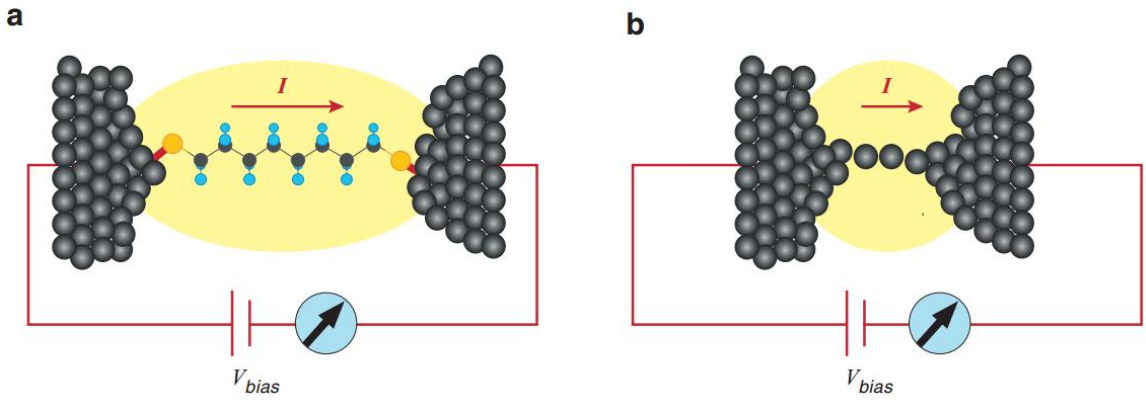


*Figure 1.19(a) Current through a molecule covalently bound to two electrodes. $V_{bias}$ (b) Current through a metal atom attached to two electrodes made of the same metal. Adapted from Reference[108]: Chen, F.; Hihath, J.; Huang, Z.; Li, X.; Tao, N. Measurement of single-molecule conductance. Annu. Rev. Phys. Chem. 2007, 58, 535-564.*

### 1.7.2.1 Scanning tunnelling microscopy STM

STM is one of the scanning Probe Techniques. The probe's tip typically has one metal atom that can be placed over a molecule, and tunnelling spectroscopy measurements on the molecule can be performed, i.e., the current measured as a function of the applied potential. Moreover, the tip also can manipulate or move atoms and molecules on surfaces of the substrate.

STM was used in this thesis to characterize the single molecule conductance of the conductive DNA analogue. The sample preparation in this work was done by electrochemical deposition of a monolayer of the compound on a gold coated glass substrate. The tip moves across a terrace of the molecules and obtain information about the morphology and the electric properties of single molecules and a conductance map can be created which has molecular resolution. Figure 1.20 depicts a general setup of an STM experiment.

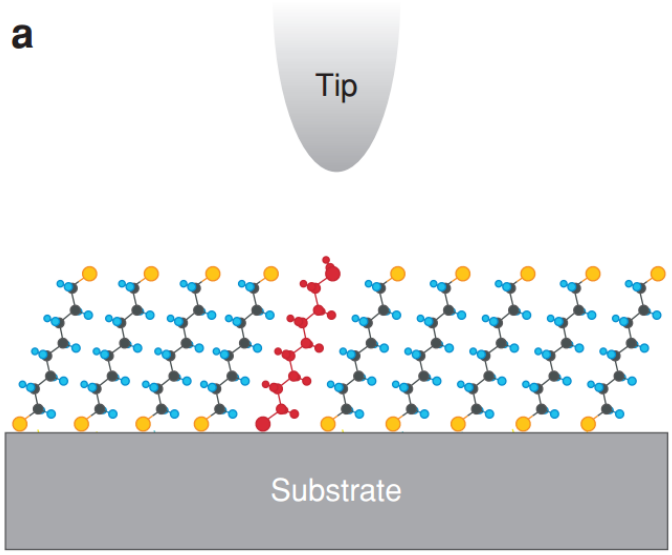


*Figure 1.20 Scanning tunnelling microscopy (STM) study of electron transport through an ordered array of molecules. Adapted from reference[108]: : Chen, F.; Hihath, J.; Huang, Z.; Li, X.; Tao, N. Measurement of single-molecule conductance. Annu. Rev. Phys. Chem. 2007, 58, 535-564.*

#### 1.7.2.2 STM break junction method

Xu & Tao[110] developed the STM break junction method that creates a large number of molecular junctions experiments by repeatedly moving the tip of the STM into and out of contact with the substrate electrode in the presence of the sample molecules. This movement is driven by a piezoelectric motor. The STM break junction method is as illustrated in Figure 1.21 as follows: (a) The tip is moved towards the substrate surface until it contacts the molecules immobilized on the substrate. One or more of the surface bound molecules can bind to the tip. (b) While the tip is being pulled up away from the substrate, the voltage bias is being applied and the current is being measured and recorded. The retraction of the tip is continued until the single molecule mediated contact is cut due to the molecules break contact with the tip of the substrate, which is associated with a sudden drop in the current $I_s$. (c) The process is repeated thousands of times to gather a large number of molecular junctions measurements.

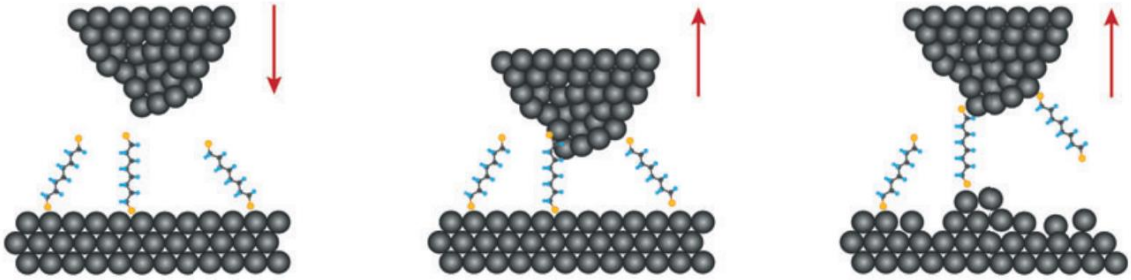

*Figure 1.21 Measurement of single-molecule conductance using a scanning tunnelling microscopy (STM) break junction method. Adapted from Reference [108]: : Chen, F.; Hihath, J.; Huang, Z.; Li, X.; Tao, N. Measurement of single-molecule conductance. Annu. Rev. Phys. Chem. 2007, 58, 535-564.*

Figure 1.22 (A) shows the process of measuring the single molecule conductivity of aniline oligomer molecule in solution, the experiment setup and the electrode configuration. Figure 1.22 (B) shows the current vs pulling distance terraces showing the three phases of the STM break junction experiments. The horizontal plateau that can be seen on the current vs distance curve represents the distance in which molecule is still connecting the tip to the substrate before the tip travels upwards a distance with is larger than the molecule length which causes it to detach and the current drops to zero, Figure 1.22. The current plateaus occur at integer multiples of a fundamental current, which is the current for a single molecule, i.e., the tip can interact with one molecule or two or three etc., thus the current values obtained in break junction can be due to the sum of a number of interacting molecules. (C) represents the sorting process. In which the large number of break junction terraces are sorted according to the $I_s$ current, and a histogram of current vs counts is created. The peaks in this histogram represent the current values with the highest frequency of occurrence. The peaks correspond to the current due to 1, 2, 3, 4, and 5 molecules in the gap. The single-molecule current is found from the slope of the current vs peak number plot (insert).

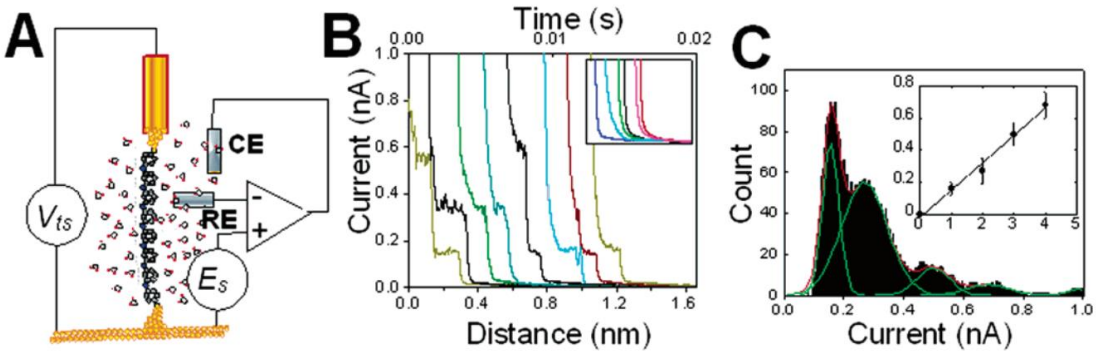


*Figure 1.22(A) Showing the gold-oligomer-gold junction with the electrode surface potential, controlled by a Pt counter electrode relative to a silver wire reference electrode and with a bias $V_{bias}$ applied across the molecule. (B) Current vs pulling distance for the hepta-aniline (C) Current distribution for the measurements in (B). adapted from reference*[111]*: Chen, F.; He, J.; Nuckolls, C.; Roberts, T.; Klare, J. E.; Lindsay, S. A molecular switch based on potential-induced changes of oxidation state.* Nano letters ***2005***, 5*, 503-506.*

The single molecule conductance of polyaniline was determined by Chen *et al*.[111]. They studied the change in conductance upon the oxidation from the leucoemeraldine form to the emeraldine salt. They detected a fifteen-fold increase (from 0.32 ± 0.03 nS to 5.3 ± 0.4 nS) on oxidation from the leucoemeraldine form to the emeraldine salt.

## 1.8 Modeling of DNA

As discussed in Section 1.6.2, even relatively small changes in the structure of DNA can significantly affect the binding energy. Therefore, it is essential to model the proposed conducting polymer backbones before attempting its synthesis. The advances in the theoretical aspects of computational chemistry produced many algorithms and approximations that, when combined with the improvements in computers hardware, enable complex calculations and simulations to be carried out in a reasonable time using personal computers. Software packages that are user friendly for chemists, e.g. HyperChem$^{TM}$ Release 8.0.9 for windows, were used in this thesis to model DNA and nucleic acid analogues and predict the binding properties of these analogues by calculating the different between the energy of the bound and the free strands. Here, a concise overview of the theoretical aspects of the algorithms and computational methods used is provided.

### 1.8.1 Computational chemistry

The term computational chemistry is used when the mathematical theory can be automated on a computer[112]. Generally these methods and applications are an approximation to the basic equation that describes the atom and its components i.e. Schrödinger wave equation. Most of the chemistry aspects have been described in a qualitative or semi-quantitative computational method. Despite being a qualitative or approximate method, it can still give very useful insights into the chemical system and enables the researchers to predict with some certainty the properties and structure of compounds.

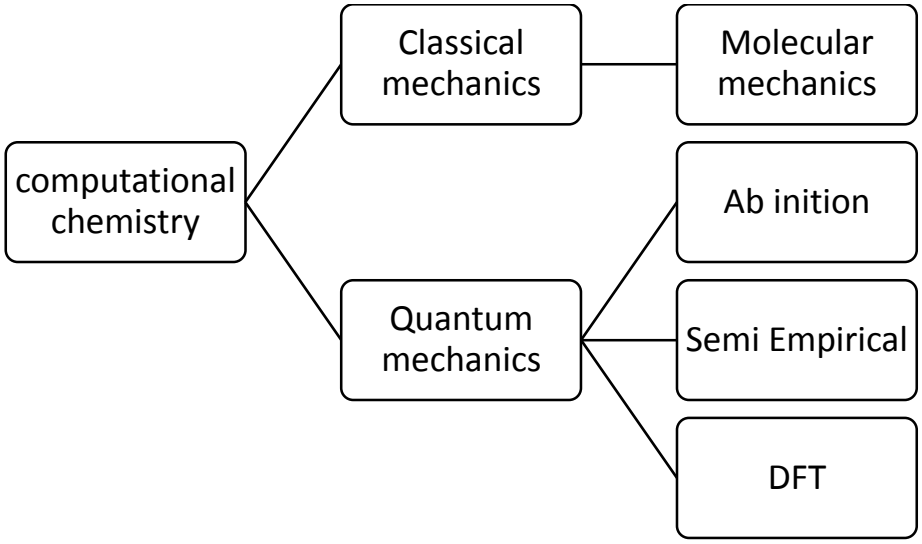


*Figure 1.23 Computational theoretical methods.*

### 1.8.2 Quantum Mechanics

As seen in Figure 1.23 computational methods can be divided into two main categories. Molecular mechanics which deals with chemical systems i.e. atoms and molecules disregarding the wave nature of electrons. This type will be discussed in more detail later. The second type (quantum mechanic) utilize the basic quantum wave function described by Schrödinger. Which is considered the correct mathematical description of the behaviour of electrons and can predict chemical properties with greater accuracy. Theoretically, quantum mechanics can predict any property of an atom or a molecule exactly. However, practically, the quantum mechanics equations could be only be solved exactly for one-electron systems, i.e. hydrogen atom. The Schrödinger wave equation is:

Equation 3 $$H\Psi=E\Psi$$

where H is the Hamiltonian operator and E is the eigenvalue corresponding to the allowed energy levels. Ψ is the wave function

The wave function Ψ is a function describes the position of the electron and nucleus. As the name implies, it describes an electron as a wave, and it is a probabilistic description of its position. It means that it can describe the probability of finding the electrons in certain locations, but it cannot predict the location and energy of the electron exactly.

Many approximations for Schrödinger equation have been developed to solve the multiple electron systems and multiple atoms i.e. molecules. Examples are Ab initio methods, Semiempirical methods and Density Function Theory DFT. These methods can only be used with molecules with limited number of atoms. The ab initio methods are limited in very small molecule that can be modelled using even super computers. Semiempirical calculations are used for larger organic molecules[112], but again they are too much complicated for modelling most of the biomolecular systems like proteins and DNA. If a molecule is too large for a semiempirical treatment, it is still possible to model its behaviour by avoiding the quantum mechanics completely and use molecular mechanics[113]. This thesis focuses on DNA molecules so the use of the quantum mechanics methods was not possible and are not considered further and the focus will be on the classical mechanic methods.

### 1.8.3 Classical molecular mechanics

Classical molecular mechanics methods were developed to treat atoms and molecules as macro units with defined properties[114]. The energy expression of atoms consists of simple algebraic equations for the energy of a compound. It does not use the complex wave function or total electron probability density. The terms of this equation represent properties of the

molecules that has been previously obtained either from spectroscopic data or more accurate ab initio calculations. A number of equations with their associated constants and terms are called a force Field. The basic assumption for the molecular mechanics method is that the parameters are fixed, which means that the properties of a particular atom or the energy of a certain molecular motion, for example the bending of a three carbon atom system, will be the same in all molecules. This requires a simple calculation which can be applied to very large molecular systems like proteins, nucleic acids, polymers, metal surfaces etc. The quality of data obtained from this technique depends on the basic data and values used to parameterize the constants in the force field equations.

### 1.8.4 Force field parameters

The energy calculation in the molecular mechanics approach is simply the sum of solutions based on classical Newtonian mechanics. These force field equations describe various aspects of the molecule, such as bond length and stretching, bond angle and bending, torsions angles between four atoms (three bonds), electrostatic interactions, van der Waals forces non-bonding interaction and hydrogen bonding. Figure 1.24 shows the force field components in the molecular mechanic method AMBER which will be reviewed later.

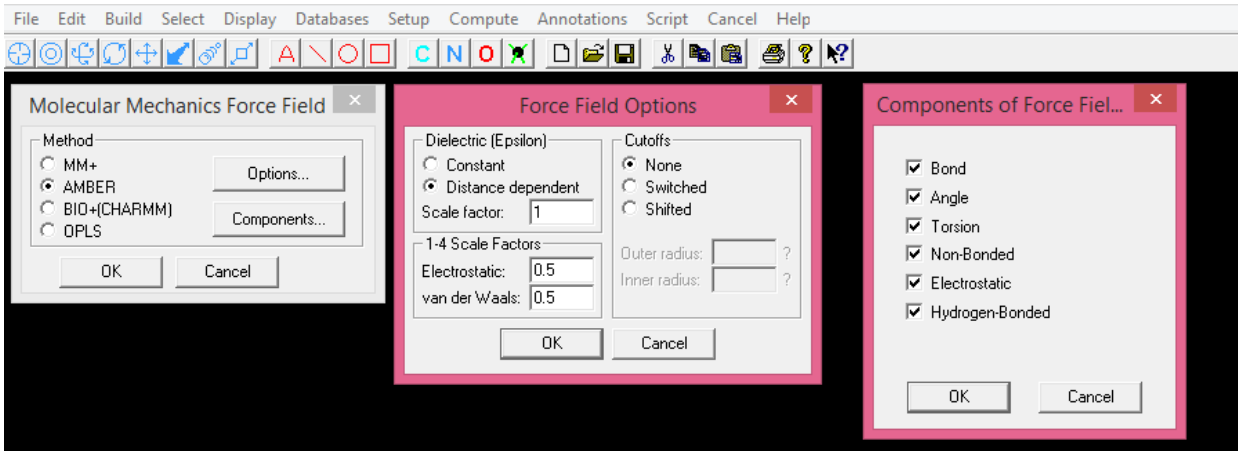


*Figure 1.24 force filed components in AMBER molecular mechanic method as seen in HyperChem molecular modelling software.*

The molecular mechanics force field equation for bond stretching treats the bond as a spring, which is best described by a harmonic oscillator equation. It is mostly described by a Morse potential that can be described in the following formula

*Equation 4*

$$D_e[1 - e^{-\alpha(l-l_0)}]^2$$

where $l$ is bond length, $D_e$ is dissociation energy and $\alpha$ is constants particular to the elements in a certain hybridization state and calculated using one of the quantum mechanical approximation methods.

Bond bending is most often described by a harmonic equation.

*Equation 5*

$$k(\theta - \theta_o)^2$$

where $\theta$ is the bond angle and $k$ is a constant. Bond rotation or torsion angle is generally described by a cosine expression as follows:

*Equation 6*

$$k[1 + cos(n\theta)]$$

Electrostatic forces are calculated using Coulomb equation

*Equation 7*

$$\frac{q_1 q_2}{4\pi\varepsilon_0 r}$$

where $q$ is the charge and $r$ is the non-bonding distance.

And Van der Waals forces:

*Equation 8*

$$4k\left(\frac{A}{r}\right)^{12} - \left(\frac{B}{r}\right)^{6}$$

Where $K$, $A$, $B$, $12$ and $6$ are constants calculated from quantum mechanics approximation method and they differ between different atoms and bonds.

### 1.8.5 AMBER

AMBER is an acronym stands for Assisted Model Building with Energy Refinement. It is the name of both a force field and a molecular mechanics simulation program[115]. It was developed specifically for proteins and nucleic acids and its parameterization is optimized for amino acids and nucleotides using either explicit solvent with periodic boundary conditions or an implicit solvent model.

The concept of AMBER dates back to 1978 when Paul Weiner joined Peter Kollman's laboratory. Since then it witnessed a lot of modification and improvements.

Case *et al*.[115] reviewed AMBER and Table 2 was adapted from the review that describes the advantages and disadvantages of using AMBER as a molecular modelling algorithm.

| Strengths | Weaknesses |
|---|---|
| Amber implements efficient simulations with periodic boundary conditions, using the PME method for electrostatic interactions and a continuum model for long-range van der Waals interactions.<br><br>Non-periodic simulations are supported, using a generalized Born or numerical Poisson-Boltzmann implicit solvent model.<br><br>Explicit support is provided for carbohydrate simulations, as well as for proteins, nucleic acids and small organic molecules.<br><br>Free-energy calculations use thermodynamic integration or umbrella sampling techniques, and are not limited to pairwise decomposable potentials.<br><br>Convergence acceleration can use locally-enhanced sampling or replica exchange techniques.<br><br>There is an extensive support for trajectory analysis and energetic post-processing.<br><br>There is a large and active user community, plus tutorials and a User's Manual to guide new users. The source code is portable and is available for inspection and modification. | One cannot do good simulations of just part of a system, such as the active site of an enzyme: stochastic boundary conditions for the water-continuum interface are missing, as are efficient means for handling long-range electrostatics and a reaction field.<br><br>The component programs lack a consistent user interface; there is only limited scripting capability to support types of calculations not anticipated by the authors.<br><br>There is limited support for force fields other than those developed by Amber contributors.<br><br>Missing features include: "dual topology" free energy calculations, reaction-path analysis, Monte Carlo sampling, torsion angle dynamics, and interactive steered molecular dynamics.<br><br>QM/MM simulations are limited to semiempirical Hamiltonians, and cannot currently be combined with the PME or generalized Born solvation options.<br><br>The codes were written by many authors over many years, and much of it is difficult to understand or modify.<br><br>Efficient parallel scaling beyond about a dozen processors may required access to special hardware or the adoption of an implicit solvent model. |

*Table 2 Strong and Weak Points of the Amber Biomolecular Simulation Programs. Adapted from reference[115]: Case, D. A.; Cheatham, T. E.; Darden, T.; Gohlke, H.; Luo, R.; Merz, K. M.; Onufriev, A.; Simmerling, C.; Wang, B.; Woods, R. J. The Amber biomolecular simulation programs.* Journal of computational chemistry ***2005***, 26*, 1668-1688.*

In brief, AMBER was chosen in the current investigations, because it is suitable to modelling of DNA and its analogues.

Cheatham at al[116] explained the limitation of using AMBER molecular modelling software in DNA modelling. The decision of using implicit or explicit solvent molecules is related to the system being used[116]. Also the ability of the empirical force field to predict accurately the interaction of DNA with specific ions in specific areas is not yet well developed. Also, the algorithm can give different values for different sequences i.e. specific sequences may have slightly different conformation than the empirical conformation of the nucleotides. Finally, the change in DNA structure i.e. chemical modification in the composition of the DNA for example designing a nucleic acid analogue might cause the results to be inaccurate, and the error in calculation depends on how far the structure of the analogue departs from the canonical structure of the DNA.

### 1.8.6 Optimization algorithms and Polak-ribiere method

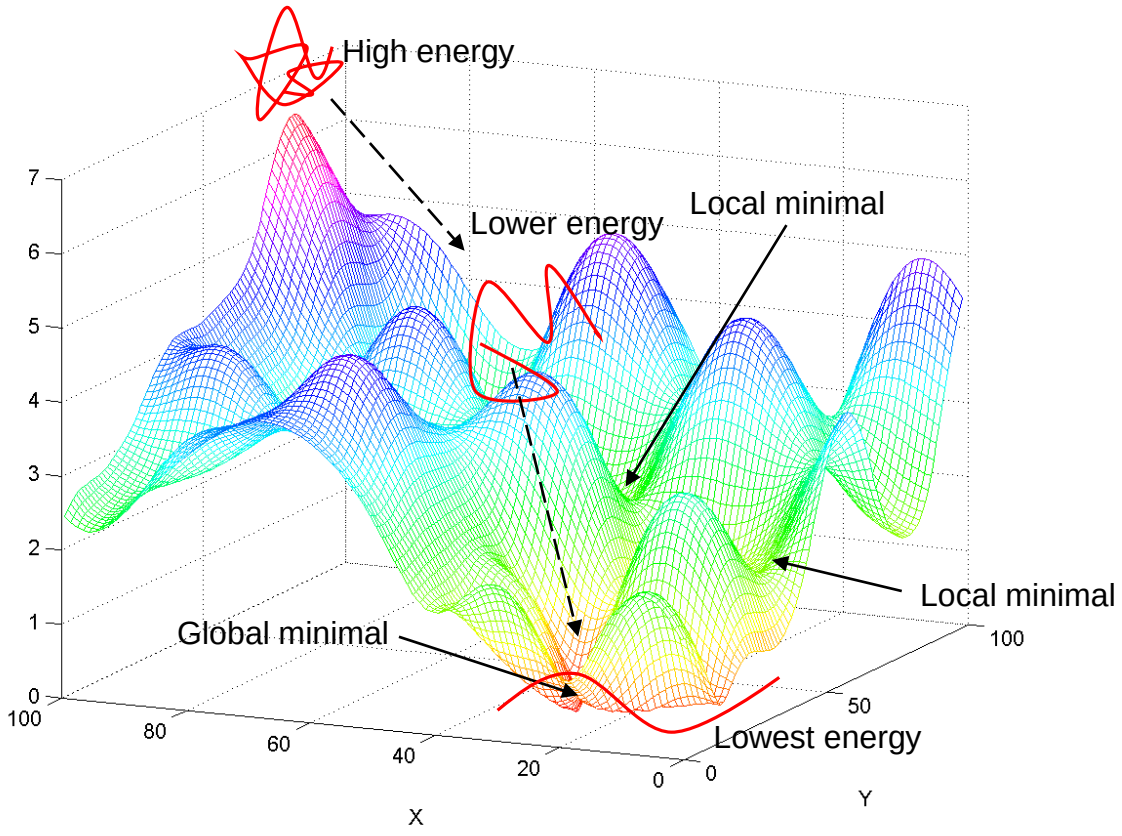


*Figure 1.25 Energy surface and location of energy minima.*

Energy minimisation algorithms are used to change to the conformation of the molecule so as to reduces the calculated energy and find the conformation with the lowest energy, which is called the global minimum.

Figure 1.25 depicts an imaginary representation of the energy values of all the possible conformations of a molecule as a surface. While the program is searching for the global minimum, other local minima can be found where it will be energetically unfavourable for the algorithm to leave, as any change in the conformation will push the energy an uphill.

There are many different algorithms for searching the values of coordinates where the minimum energy lies. One of the examples is the method of steepest descent. This algorithm works by applying small iterative changes to the structure in different directions and repeat the energy calculation upon

each change until the minimum energy is located for this small change then this direction is followed. After that another set of probable changes are tried and again the direction of the lowest energy is followed and so on.

This method needs a lot of steps to reach the global minima which can take a lot of time especially. Also, as stated above, the molecule can fall into a local minimum where small changes cannot push the molecule uphill after which the real global minimum probably lies.

Optimization methods that are most often used with molecular mechanics is the conjugate gradient method, which finds the minimum by following each coordinate in turn, rather than taking small steps in each direction. That allows the program to take less steps towards the global minimum. In addition, the probability of finding the global minimum is higher with bigger steps. The Polak-Ribiere algorithm is an adaptation of the conjugate gradient specifically for molecular mechanics. For that reason, it was chosen as the method for optimization used in this thesis.

### 1.8.7 Relative mean square deviation RMSD

RMSD is an important tool to compare the closeness of structure configuration between two molecules in terms of atomic position in the Cartesian coordinates. During the calculation two molecules of identical *chemical* structure (number and type of atoms constituting the molecule) are superimposed on each other and the root mean square deviation of position of atoms in the three dimensional space in Angstrom is calculated.

The RMSD is calculated from the following equation:

*Equation 9* $$RMSD = \sqrt{\frac{1}{n}\sum_{i=1}^{n}((v_{ix} - w_{ix})^2(v_{iy} - w_{iy})^2(v_{iz} - w_{iz})^2)}$$

where V and W are positions of two atoms in Cartesian coordinates and n is the overall number of atoms in the molecule.

The reference value of the RMSD difference has been a subject for controversy in the literature[117]. Some studies suggests that values less than 3 Å means that the two compared structures are significantly similar[117]. some studies suggests that the cut off value is 2 Å[118]. Others calculated the significant value for the RMSD statistically which can be different according to the size of the molecule, for example, Reva *et al*.[119] suggested that the probability of having RMSD value of 6 Å by chance is very small for proteins with 60-80 residues, and below this value of RMSD the two compared structures are considered significantly similar. To obtain a significant value for RMSD, we compared different experimentally measured structures of the same DNA chain and the value was considered a suitable reference for comparison.

## 1.9 Introduction to Electrochemistry

Electrochemistry has been used in this work to deposit core-shell nanoparticles, to detect DNA hybridisation, to electrochemically polymerize and probe the conductivity of the PANI nucleic acid analogue. In order to understand more about the electrochemical processes that happen at the electrode surface in the amperometric measurements, electrochemical theory and methods are reviewed.

### 1.9.1 Electrochemical Processes

Electrochemistry is the science that studies chemical reactions, which take place at the interface of an electrode in contact with an electrolyte, and the effect of the electrical energy on the chemical properties of matter. The electrode can be a solid metal or a semiconductor, and the electrolyte is an ionic conductor, which can be a solution phase or a solid state electrolyte. These reactions involve the movement of electric charges in the form of ions or electrons between the electrodes and the electrolyte. Thus, electrochemistry deals with the effect of electrical energy and the associated chemical change.

The rate of an electrochemical reaction is determined by the following factors:

1. The physical transport of the electro-active chemical species towards and away from the electrode surface.
2. Charge Transfer between the chemical species and the electrode at its surface.

The following equation is a demonstration of a simple electrochemical reaction:

*Equation 10* $O + ne^- \leftrightarrow R$

In order for the Oxidised form (O) to convert to the reduced form (R) the following steps are expected:

a) The rate of diffusion of O from the bulk solution to the electrode surface;
b) Transfer of electrons from the electrode surface to produce Red;
c) Diffusion of R away from the electrode surface into the bulk solution.

The overall reaction rate at the electrode surface and consequently the measured current depends on the slowest step among the above process i.e., the rate-limiting step.

### 1.9.2 Cyclic voltammetry

Cyclic voltammetry is one of the most widely used techniques for studying electrochemical reactions. It enables oxidation and reduction processes at an electrode to be investigated (working electrode) by applying a triangular potential-time sweep, depicted in Figure 1.26 with a given scan rate and the resulting current produced is measured. The plot between the potential applied and the current is called a voltammogram[120]. Those plots provide thermodynamic information about the redox processes, it locates the potential of the redox couple quickly and can be used to measure heterogeneous electron transfer rates, and it also gives considerable information about the effect of different conditions like media, concentration, temperature etc., on the rate of the reaction.

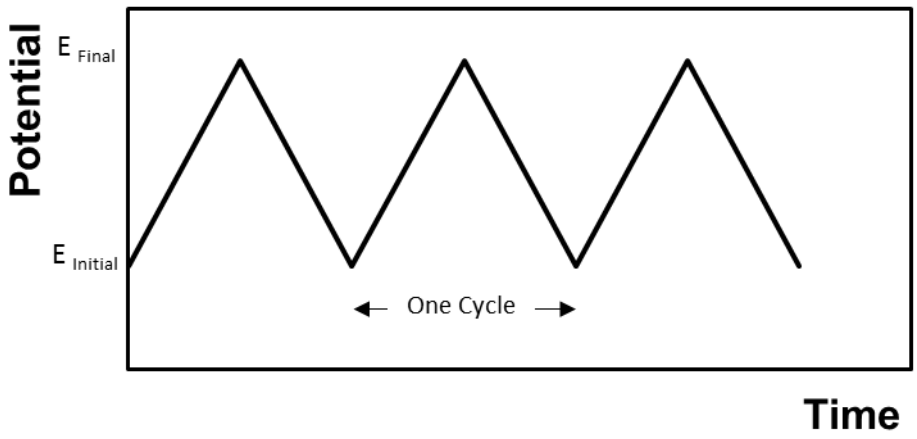


*Figure 1.26 Potential-Time plot demonstrating the potential change during a three voltammetric cycles.*

In Figure 1.27, the cyclic voltammogram of a reversible redox couple dissolved in a solution is presented, in which O represents the oxidized form that converts into the R or reduced form. The potential is swept from a point where no reduction occurs, towards the direction of the standard potential for the redox reaction (E°) at which the reduction of O occurs. The voltammogram indicates the potential region at which the redox reaction takes place in the form of a peak. This peak represents the increase of current when the potential scan reaches the characteristic E° for the redox process before reaching it, the current is in a steady state and almost flat. Upon approaching and crossing this potential, the reduction will take place and the current will increase to create a peak. As the reaction proceeds, the local concentration of O drops due to slow diffusion of molecules to the electrode surface causes the current to decrease. At the same time, the rate of heterogeneous electron transfer increases as the potential increases. Upon reversing the sweep direction, the produced molecules R at the electrode surface will be oxidized back to O and reaches 50% oxidized when the scan

reaches the E° of the redox reaction according to Nernst equation, and an inverted anodic peak will be produced.

If the Initial potential is $E_i$ and the scan rate is $\nu$, the potential at any time t can be calculated by:

*Equation 11*

$$E_{(t)} = E_i - \nu$$

The behaviour of the redox reaction can be either reversible “Nernstian” or irreversible. The Nernstian kinetics assumes that the oxidation and reduction reactions are fast and the potential directly controls the concentration of the reactants and products obeying Nernst equation:

*Equation 12*

$$E = E° + \frac{RT}{nF} ln \frac{C_o}{C_R}$$

Under conditions of semi-infinite linear diffusion, The peak current or $i_p$, which can be calculated from Randles-Sevcik equation:

*Equation 13*

$$i_p = (2.96 \times 10^5)\, n^{2/3} A C D^{1/2} \nu^{1/2}$$

where n is the number of electrons transferred in the reaction, A is the electrode surface area in $cm^2$, C is the concentration (in mol $cm^{-3}$), D is the diffusion coefficient (in $cm^2\ s^{-1}$) and $\nu$ is the scan rate in $Vs^{-1}$.

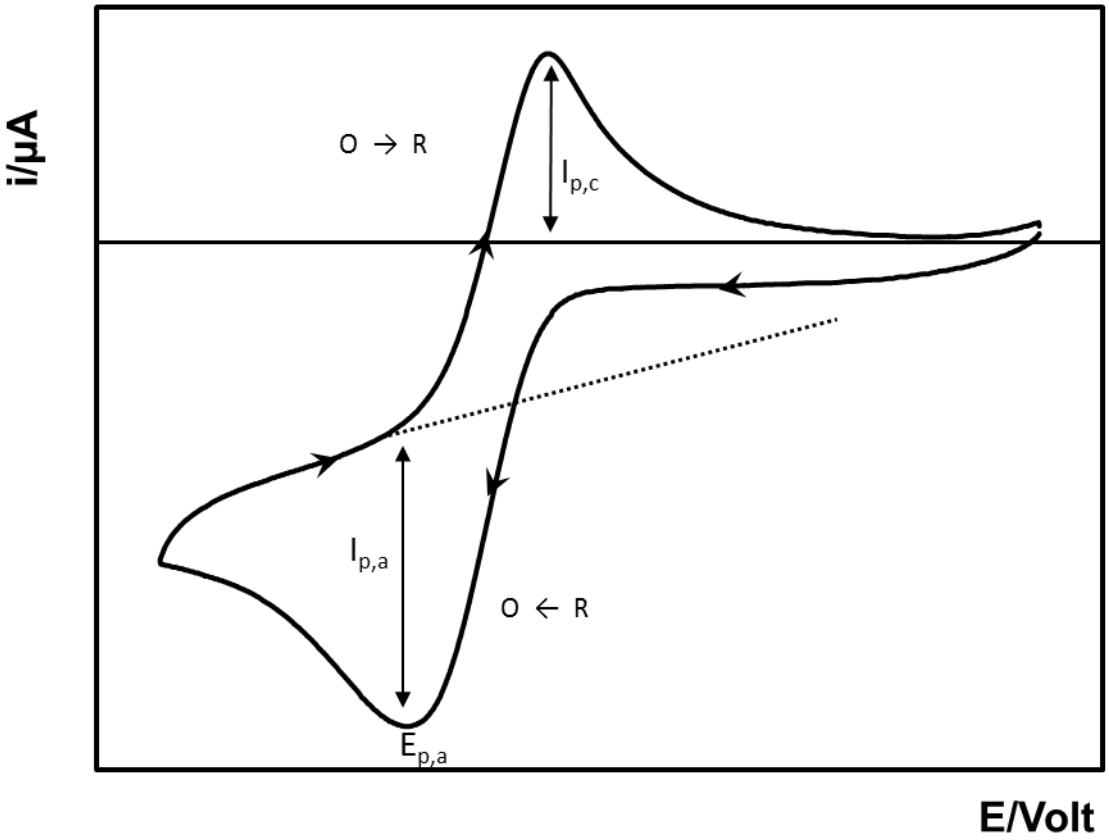


*Figure 1.27 Diagnostic features of cyclic voltammetry for a reversible reaction, $E_{p,c}$ is the cathodic peak potential, $E_{p,c}$ is the anodic peak potential, $I_{p,c}$ the cathodic peak current and $I_{p,a}$ is the anodic peak current.*

The position of the E° is located midway between the anodic and cathodic potentials, and obtained by taking the average of the two values. The separation between the anodic and cathodic peaks can give an indication of the number of electrons involved in the reversible Nernstian reaction as:

*Equation 14*

$$\Delta E_P = E_{p,a} - E_{p,c} = \frac{57}{n}$$

where n is the number of electrons.

### 1.9.3 Potentiostatic techniques:

Unlike the cyclic voltammetry, which is one of the potential sweep techniques in which the potential is varying with time, the potentiostatic techniques applies a fixed applied potential to the electrochemical cell, and the current or charge are measured and recorded. In chronoamperometry, the potential is stepped to different potential values or steps.

Upon applying the potential, a faradic current is generated due to the redox reaction. With time, the surface concentration of the electroactive species drops, and in an unstirred solution, the magnitude of the reaction will be controlled by diffusion as in Figure 1.28 and the current time plot will reflect the change in the concentration gradient of the electro active species. The change will involve the expansion of the depletion layer away from the electrode surface.

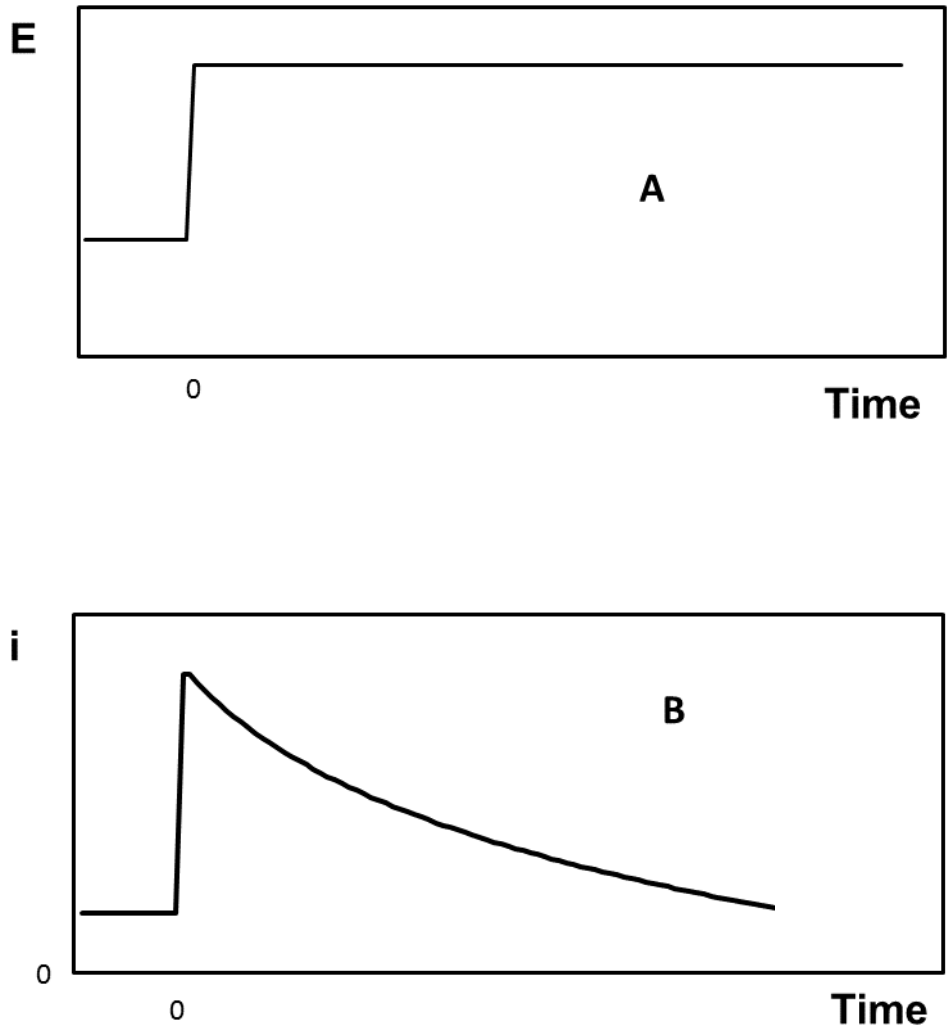


*Figure 1.28 A Potential time plot for an ampermetric experiment, in which the potential is stepped from a lower potential to a high potential that is suitable for the electrochemical diffusion controlled reaction. B, The current-time transient, in which the initial increase in current is observed upon applying the potential, and the following gradual decline.*

The current can be described by the Cottrell equation:

*Equation 15* $$i(t) = \frac{nFACD^{1/2}}{\pi^{1/2}\, t^{1/2}}$$

From the equation it is obvious that the current depends on time and the diffusion coefficient, concentration, area of electrode and faraday constant.

The charge can be also calculated and plotted against time; this is done practically by integrating the area under the current in the form:

*Equation 16* $$Q(t) = \int_0^t I\, dt$$

The importance of determining the charge is that it can be connected to the stoichiometry of the reaction by using Faraday constant, which gives quantitative information about the masses of the reacting and produced species.

## 1.10 Self-Assembled Monolayer (SAM)

Self-assembled monolayer, SAM was used in this work as means to attach of the capture strand DNA onto the electrode surface, to attach the probe strand DNA onto the nanp-particles surface, to for a defective monolayer of alkanethiol that allows the growth of platinum particles in those defects and as a surface blocking that prevents unwanted non-specific binding.

The surface of metals tend to adsorb organic molecules as it decreases the free energy between the surface and the medium[121]. Those organic molecules attaches to the surface atoms through a head group that has an affinity to the metal or metal oxide atoms on the surface[121]. Different head groups have different affinities to different surfaces or “substrates”. Compounds alkanoic acids and fatty acids can bind to meal and metal oxides

surfaces[122], and organosilicon compounds on hydroxylated surfaces like metal oxides[123]. The substrate can be in the form of a planar flat surface or spherical particles of different shapes. The most studied SAM is thiolated compounds on metals especially gold[124], and it is the type of SAM used in this work. The monolayer can change a variety of the interfacial properties of the surface depending on the properties of the adsorbed molecule for example, surface hydrophobicity, hydroxylated alkanthiole can render the surface of gold more hydrophilic[125].

Those monolayers are self-assembled which means that the molecules arrange themselves spontaneously in a densely packed structure on the surface of the substrate. This is achieved by incubating the substrate in a solution that contains the monolayer-forming compound and allowing it to attach to the substrate. The adsorbing process can also be forced by means of applying a cathodic or anodic potential that is suitable to the electrochemical nature of the adsorption reaction[126]. The quality of the monolayer, density and the number of defects is affected by many factors, including the structure of the compound, the exposure time of the surface to the solution of monolayer-forming compound, also the concentration, type of solvent, temperature, purity of the solution and cleanliness of the substrate surface[127].

The thiol head group has a high affinity to gold with which it forms a stable bond while the alkane chains interact laterally to stabilise the assembly. The stability of the SAM depends on the chain length of the alkanethiol as the shorter alkanthiols are less packed and forms a more fluid monolayer[127,121]. Alkanethiols increases the hydrophobicity of the surface, and they can be used for surface blocking especially in electrochemical biosensors.

One of the useful applications of the bonding between metals and thiolated organic molecules is the immobilization of thiolated nuclide acids on electrode surfaces[128]. Its highest impact is in the field of nucleic acid electrochemical biosensors[27]. There are reports that discuss the surface coverage of thiolated DNA on flat surfaces as well as spherical particles.[129]

The advantage of thiol-tethered DNA is that the surface coverage of the immobilised DNA can be adjusted by changing the immobilisation time and the concentration of the short chain alkyl thiols. Thiolated DNA can also bind to the gold surface by the exocyclic amino groups present on the nucleotides. However, the amine-gold bond is weaker than the thiol-gold bond. That is why, short oligonucleotides attach to the gold through the thiol group and a close-packed vertically aligned oligos can be produced. In case of long DNA molecules they can bend and attach to the gold surface through thiol bond as well as amino groups which means that the close-packed arrangement may be lost. To resolve that issue, mixed SAMs have been used by incorporating a short chain thiolated compound that can reach the surface more easily and replace the lateral amine-gold bonds with stronger thiol-gold bonds and help to restore the vertical aligning of thiol-thethered DNA chains. The small thiolated compounds can also replace the thiol bond of DNA so in this step the concentrations and incubation time should be carefully adjusted.[130]

## 1.11 Raman and SERS

Raman and SERS has been employed in this work as an alternative way to detect the DNA hybridisation. The plasmonic enhancement from silver and gold microarrays forms the basis for that detection.

Raman spectroscopy is a technique that detects the vibrational, rotational, and other low-frequency transitions in chemical compounds by observing the inelastic scattering of the photos of a monochromatic electromagnetic radiation in the visible, near infrared, or near ultraviolet range[131]. The frequency of the scattered light changes according to the nature of the interaction with the chemical compounds at the molecular level.

### 1.11.1 Principles of Raman spectroscopy

In Raman spectroscopy, the sample is irradiated by an intense laser beam in the UV-visible region and gradually increasing the frequency ($v_0$), and the scattered light is usually observed in the direction perpendicular to the incident beam. The scattered light can be one of two types: one, is the Rayleigh scattering, it is strong and has the same frequency as the incident beam ($v_0$) which represents the elastic scattering of the incident photons. That is why its frequency is the same as the excitation laser, and the other, called Raman scattering, is very weak (~ $10^{-5}$ of the incident beam intensity) and has frequencies ($v_0 \pm v_m$), where $v_m$ is a vibrational frequency of a molecule. Two possible types of frequencies can be produced ($v_0 – v_m$) and ($v_0 + v_m$) which generates peaks in the resulting spectrum which are called the Stokes and anti-Stokes lines, respectively. Thus, in Raman spectroscopy, the vibrational frequency ($v_m$) is measured and recorded as a shift from the incident beam frequency ($v_0$). The peaks that are produced from this measurement represent different bonds and chemical groups and gives a unique fingerprint for the compound. It also can give information about chemical changes for instance, appearance and disappearance of certain functional groups and bonds. It is particularly useful in characterizing interfacial structures and chemical changes involved in interfacial processes.

### 1.11.2 Surface-Enhanced Raman Spectroscopy SERS

SERS was discovered, by Fleischmann *et al*. in 1974[132] who noticed a dramatic increase in the Raman scattering of pyridine adsorbed on a roughened silver electrode. SERS was observed for a large number of compounds adsorbed on particular metals with different topography and physical environments. Coinage metals, namely silver, copper and gold were mostly used as SERS substrates, Later alkali metals and other metals have been employed too[133]. The surface features that are responsible for roughness which fall between 10-100 nm gives the largest enhancements. The metal surface or substrate can be electrode surfaces that is roughened by means of oxidation–reduction cycles, electrochemical deposition of metal nanoparticles, chemically immobilized metal nanoparticles, metal films deposited by vapor deposition or sputtering or patterned surfaced by lithographic techniques.

### 1.11.3 Principles of SERS

Two mechanisms are believed to be responsible for SERS enhancement, electromagnetic enhancement and charge-transfer or chemical enhancement[133]. Electromagnetic enhancement acts when the electromagnetic radiation interacts with the metal surface electrons to create an oscillating electron wave on the surface that is called a plasmon. Surface plasmons can either be propagating on the surface like the case of a grating, or localized and confined on the surface due to size restriction, for example in the case of a spherical particle. That is why the surface has to be suitably roughened in order for the plasmon to be created. The size of the nanostructure as well as the separation between them affects the properties of the plasmon.

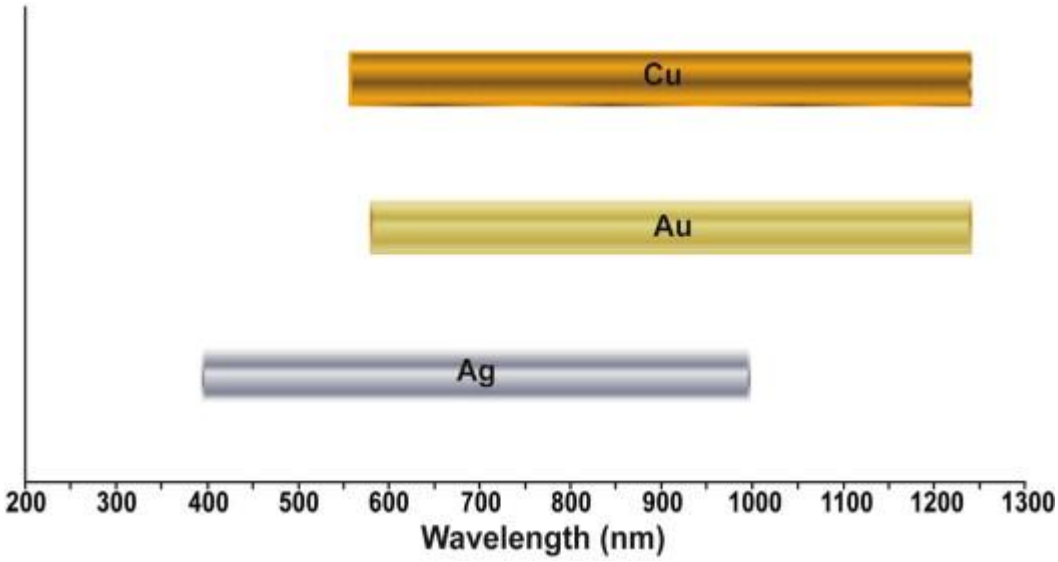


*Figure 1.29 Approximate wavelength ranges where Ag, Au, and Cu have been well-characterized and are established to support SERS. Adapted from Reference[134]: Sharma, B.; Frontiera, R. R.; Henry, A.; Ringe, E.; Van Duyne, R. P. SERS: materials, applications, and the future. Materials today 2012, 15, 16-25.*

One of the factors that affects the oscillation frequency of the plasmon is the dielectric constant of the metal. That is why the coinage metals and the alkali metals are mostly used as SERS substrates because the resonance frequency for their plasmons, which is dictated by their dielectric constant, is suitable at the electromagnetic frequencies commonly used in the excitation laser of Raman spectroscopy (mostly the visible range)[133]. Figure 1.29 shows the wavelength range where some metals can support SERS. The plasmon energy causes the Raman scattering to occur in the analyte molecule, the energy is transferred back into the plasmon, and the scattered radiation, with a different frequency from the excitation laser (Raman shift) because of the energy transferred to the molecule in the Raman process, is detected then by the spectrometer[135]. The particles or nano-structures on the rough surface act as antennas which amplifies the scattered light intensity. Other factors can affect the enhancement magnitude of the metal surface, such as the size

of structures, morphology, shape[136], distance between particles or surface features, and the adsorption orientation of the molecule.[137]

## 1.12 Conclusion

In this literature review, the importance of developing high sensitivity DNA electrochemical biosensors, that can determine the concentration of nucleic acids associated with pathological conditions quickly and accurately was discussed. Different types of electrochemical biosensors and different techniques and strategies employed in the detection process has been discussed. Also the principles of electrochemistry and how it provides a way to observe a biological binding event, SAMs and their use in nanotechnology was reviewed. SERS phenomenon, its origin, factors that affect its magnitude and its potential use in biosensors. Platinum and silver particles, their useful properties and previous studies that employed them in electrochemical biosensors was reported.

In this study, the combination of the electrocatalytic activity for platinum particles and silver enhancement for the Raman signal for DNA added to the enhancement from the gold micro-cavities was tested. Perhaps the Raman spectrum can give qualitative information about the DNA, and possible mismatches. The catalytic activity of platinum will be used to give quantitative determination for the DNA content of the sample. That relatively complex architecture of the particles will be achieved by synthesizing the platinum particles, using defective alkyl thiol SAMs as a template for electro deposition, then adding silver layer by another electrochemical deposition step on one side of the particles that is still attached to the electrode surface.

Combining two methods of detection allows them to be used as a reference for each other. Also obtaining qualitative and quantitative information about the nucleic acid is important in diagnostic applications.

A review of DNA analogues and conductive polymers was given. Also the theoretical background for molecular modelling. That is an essential part of designing and synthesis of a conducting nucleic acid analogue that can improve the electron transfer process between the nanoparticle and the electrode surface in sandwich assays.

The aim of this thesis are:

1) Fabrication of platinum particle using electrochemical deposition onto dodecane-1-thiol defective monolayer. Those particles have an electrocatalytic activity towards the reduction of hydrogen peroxide.
2) Electrochemical deposition of a hemispherical silver shell on one side of the platinum particles to improve the SERS signal of the particles immobilized in gold microarray and adds a new functionality to the particles to allow multimodal detection of DNA hybridization.
3) Improving the sensitivity of the sandwich assay by increasing the current value obtained by increasing the conductivity of the DNA tethering the particle to the electrode surface by preparing a nucleic acid analogue with conducting backbone.
4) The computational modelling of different analogues and calculating the binding energy to choose the best analogue.
5) Preparation of the conducting nucleic acid using a stepwise electrochemical polymerization method.

6) Characterization of the conducting nucleic acid analogue and measuring the single molecule conductance using scanning tunnelling microscopy STM.

# Chapter 2

# Silver-coated platinum particles

"Courage is a mean with regard to fear and confidence." *Aristotle*.

# 2 Chapter 2 Silver-coated platinum particles

## 2.1 Introduction:

As discussed in Chapter 1, electrocatalysis represents a powerful approach to enhancing the current observed upon nucleic acid hybridisation. This can lead to highly sensitive detection and avoid the need for amplification of the target by PCR. This chapter describes the fabrication of platinum particles that are asymmetrically coated with silver on one side for Raman enhancement and the other side is left uncoated for electrocatalysis. This combination of metals could lead to efficient electrocatalysis, e.g., the reduction of hydrogen peroxide. The silver shell could also enhance the Raman signal of the attached DNA when immobilized in gold micro cavities.

The particles are modified with a thiolated probe strand DNA that is complementary to a section of the target DNA. In the sandwich assay format, another thiolated capture strand DNA that is complementary to the other end of the target DNA is assembled on a gold electrode. Its function is to capture and immobilize the target strand DNA from the sample. In a final hybridization step, the probe strand DNA tagged with the asymmetrically silver-coated platinum particles attaches to the complementary part of the target DNA and hence immobilizes particles on the surface of the electrode. The electrochemical reduction of hydrogen peroxide is catalysed by the particles and gives a high amperometric response which is proportional to the surface concentration of the immobilized particles and consequently to the concentration of the target DNA present in the sample. The enhancement of the Raman response when the DNA particle complex is immobilized inside gold microcavities array is also reported.

## 2.2 Materials

All chemicals were purchased from Sigma Aldrich with analytical grade, and were used as received unless otherwise stated. All the aqueous solutions were prepared from Milli–Q water (Millipore Core), 18 MΩcm$^{-1}$. The alumina polishing powder (micropolish size 1µm and 0.3 µm) was obtained from Buehler. Piranha solution (3:1 mixture of concentrated sulfuric acid and 30% hydrogen peroxide) (*Caution: Piranha solution is dangerous and reacts violently with organic materials!*) was used to remove organic residues from substrates. The buffer denoted as 1 M NaCl-TE, contained (1.0 M sodium chloride (NaCl, ≥ 99.5 % purity), 10 mM Tris hydroxymethylaminomethane hydrochloric acid (Tris-HCl, ≥ 99 % concentration) and 1 mM ethylenediaminetetraacetic acid (EDTA, ≥ 98 % purity), pH 7.0 by adding 1.0 M NaOH) was prepared in-house and used for solution phase DNA probe assembly. The oligonucleotides were purchased from Eurogentec©™ and their purity was >98%. The base sequences are as follows:

Capture: 5'- CGG-CAG-TGT-TTA-TCA -3' – SH

Target: 5'-TGA-TAA-ACA-CTG-CCG-TTT-GAA-GTC-TGT-TTA-GAA-GAA-ACT-TA-3'

Probe: SH-5'- TA-AGT-TTC-TTC-TAA-ACA-GAC- -3'

## 2.3 Instrumentation.

### 2.3.1 Spectroscopic measurements

Raman Spectroscopy was performed using Jobin Yvon Horiba HR800 connected to a CCD detector. The laser beam (He – Ne laser) with 632.8 nm exciting radiation utilising a 300-line grating, was focused on the sample by

a 100x lens. Baseline correction and smoothing were performed using Lab Spec software.

### 2.3.2 Electrochemical experiements

All electrochemical experiments were carried out in a three-electrode cell using a CH instruments Model 660 electrochemical workstation. A three-electrode electrochemical cell was used consisting of a working electrode, a platinum wire counter electrode and a reference electrode. The working electrode was a 2 mm radius planar gold disc. Potentials are quoted with respect to silver /silver chloride (Ag/AgCl) reference electrode (3 M KCl). All solutions were deoxygenated thoroughly using nitrogen prior to use and a blanket of nitrogen was maintained over the solution during all experiments. All experiments were carried out at room temperature (22 ± 3 °C). The scan rate was 0.1 $Vs^{-1}$ unless stated otherwise.

### 2.3.3 Microscopic measurements

Scanning Electron Microscopy (SEM) and Energy-dispersive X-ray spectroscopy (EDX) images were recorded using a Hitachi S3400N scanning electron microscope to investigate the surface morphology and micro/nanostructure of the platinum nanoparticles. SEM images were taken at accelerating voltage between 5 and 30 kV. Samples were mounted on a high purity aluminium stub using conductive carbon tape.

### 2.3.4 Dynamic Light Scattering (DLS)

Experiments were performed at 25 °C on a Nanosizer NanoZS (Malvern Instruments, Malvern U.K.) using a detection angle of 173° and a 3 mW He-Ne laser operating at a wavelength of 633 nm.

## 2.4 Gold electrode fabrication and cleaning

### 2.4.1 Cleaning and polishing of gold disc electrode.

The electrode surface was first washed with deionised water and ethanol and then polished with 0.3 μM alumina paste on a flat bed for at least 10 min. Voltammetry in acidic electrolyte using (0.1 M $H_2SO_4$) was carried out to determine the microscopic area by cycling the electrode between -0.35 and 1.5 V.

### 2.4.2 Dodecanethiol monolayer self-assembly.

Freshly cleaned gold disc electrodes were immersed in a 1 mM solution of 1-dodecanethiol in absolute ethanol and monolayer self-assembly was allowed to proceed for 7 h. After the formation of the monolayer, the substrate was rinsed 4 to 5 times with ethanol and dried under a $N_2$ stream.

### 2.4.3 Construction of platinum core nanoparticles

#### 2.4.3.1 Single potential step deposition

Platinum nanoparticles were deposited into the defects within the monolayer from a 0.5 M sulphuric acid solution containing 3 mM hydrogen hexachloroplatinate (IV) hydrate ($H_2PtCl_6$) at a fixed potential of -0.273 V for 3 min. Figure 2.1 depicts the current time plot against the dimensionless plot of instantaneous and progressive electrochemical deposition.

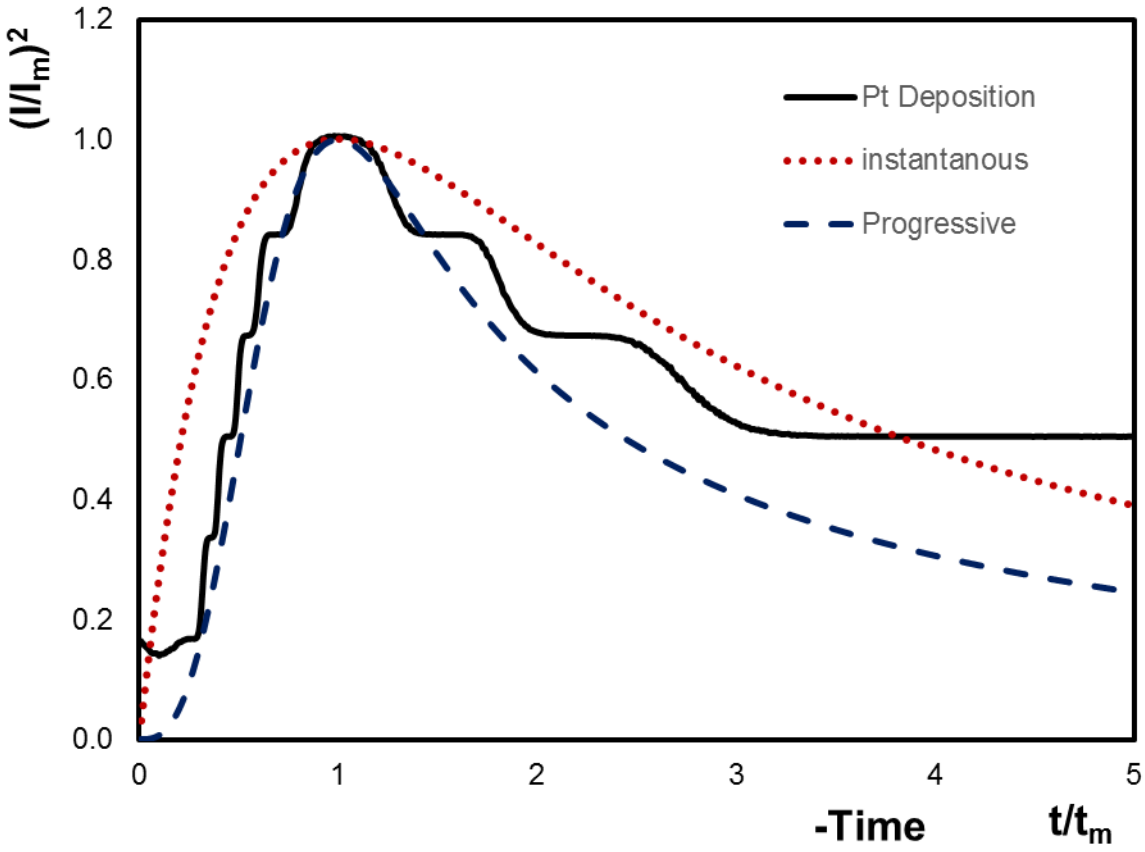


*Figure 2.1: Dimensionless current transients for the potentiostatic deposition of platinum nanoparticles from 3mM hydrogen hexachlorideplatinate (IV) hydrate solution in 0.5 sulphuric acid upon applying a potential of -0.25 V for 180 s. Dimensionless plot for instantaneous and progressive models of deposition are also shown.*

### 2.4.3.2 Double step potential deposition of platinum particles.

The concentration of the potassium hexachloroplatinate solution was 1 mM solution in 0.5 M sulphuric acid. The double potential steps were applied as depicted in Figure 2.2. The first step was at -1600 mV for 0.02 s. And second step was at -200 mV for 60 s.

The current-time transient for the double step deposition is depicted in Figure 2.3

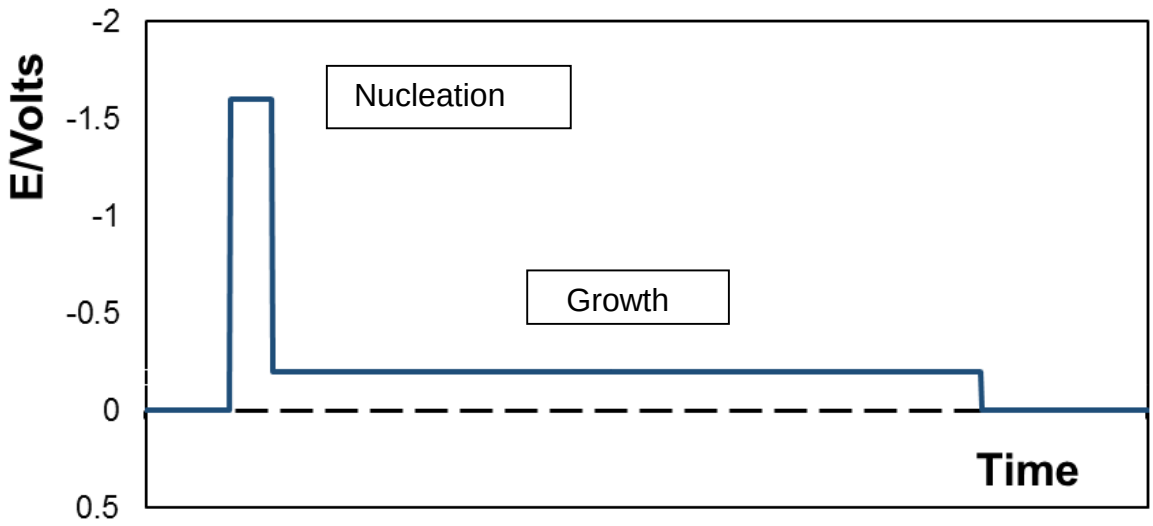


*Figure 2.2: Potential time plot for the double step potential technique used to deposit Pt particles, the nucleation step was for 2 ms at potential of -1.6 V, and a growth step for 60 s at potential of -0.2 V.*

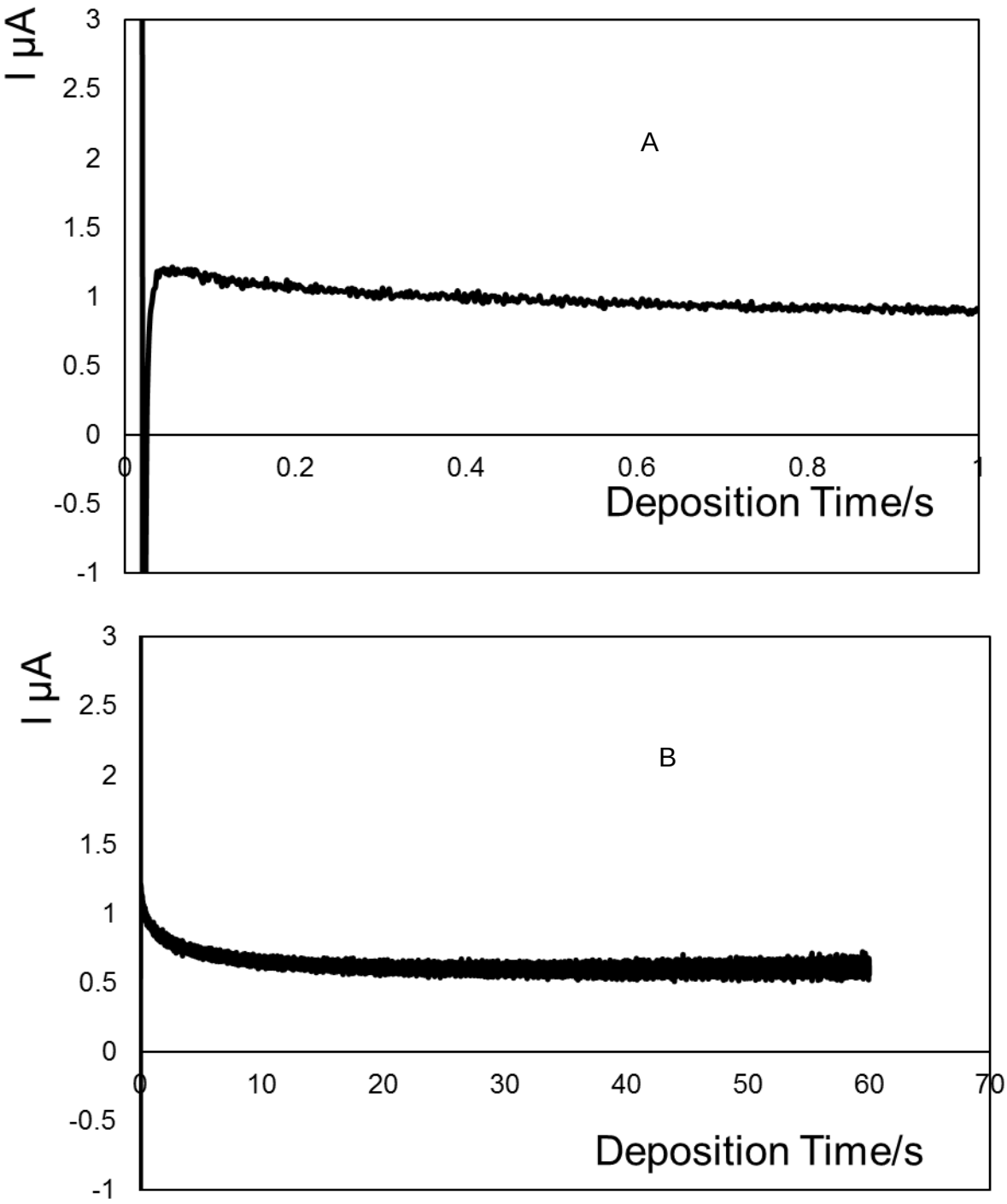


*Figure 2.3: Current transient for the double potential step deposition of platinum on a 2 mm gold disc electrode. The nucleation step was for 0.02 s at potential of -1.6 V, and a growth step for 60 s at potential of -0.2 V. Graph A: The first second of the experiment. Graph B: The full transient.*

### 2.4.4 Electrochemical deposition of silver shell on PtNPs

The aim of this step is to create a silver shell on the top surface of platinum particles.

#### 2.4.4.1 Silver Shell deposition

The silver shell was created by electrochemical deposition from a 0.1 M solution of silver nitrate in water. The electrochemical deposition is carried out using the double potential step technique, the initial step was -1.6V for 20 milliseconds, and followed by second step of 0.2 V and applied to different time intervals. The time current transient for this experiment is shown in Figure 2.4.

#### 2.4.4.2 Modified double step deposition of silver.

Double potential steps were applied to the 2 mm gold disc electrode after electrochemical deposition of platinum using the double step deposition method described in Section 2.4.3.2. The deposition solution used was 0.01 M solution of silver nitrate in 0.1 M solution of potassium nitrate. The first step was -1.2 V and growth pulse was at potential of 0.2 V for 60 s. Figure 2.5 depicts the double potential step deposition.

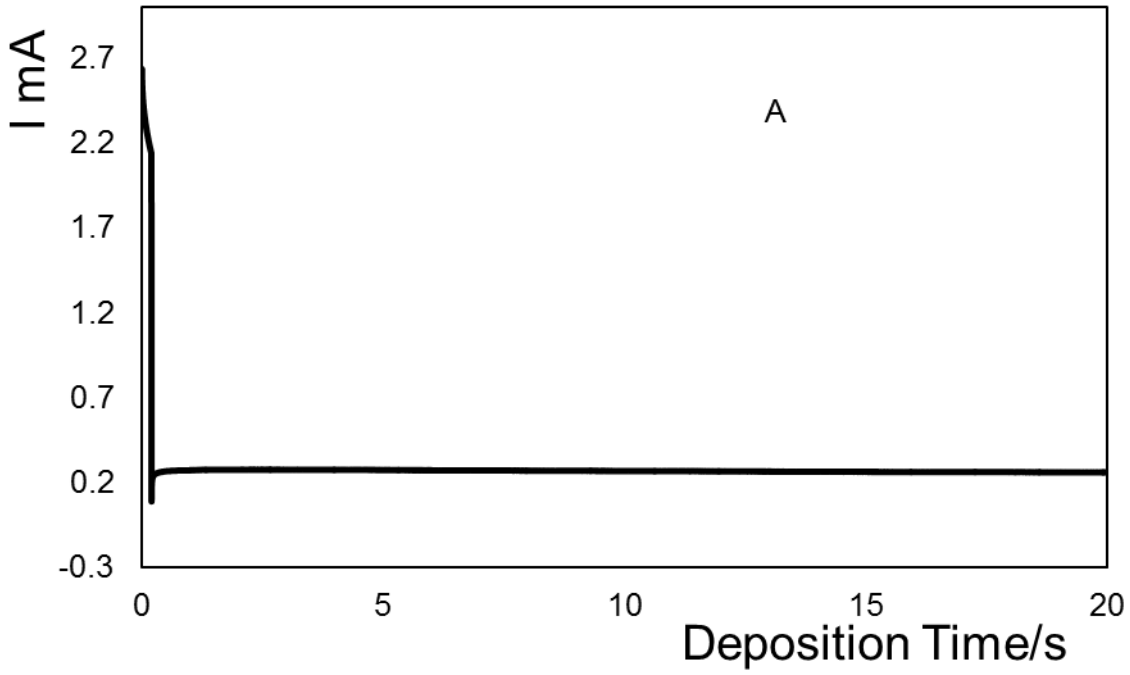


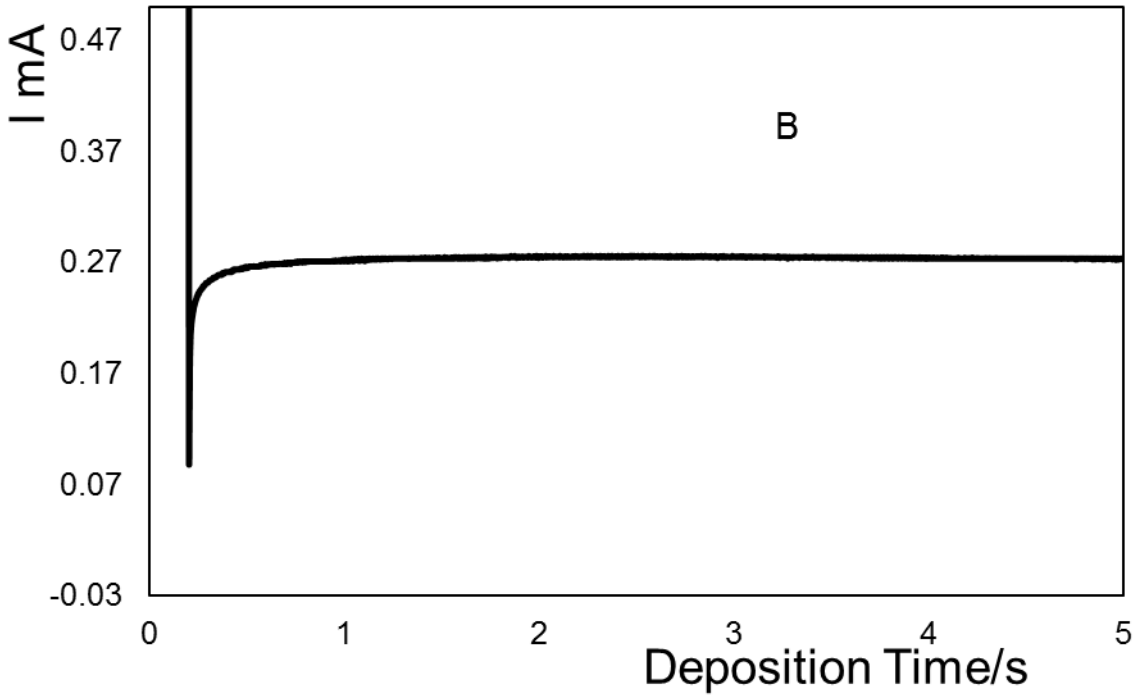


*Figure 2.4: Current transient for the double potential step deposition of silver on a 2 mm gold disc electrode modified with platinum particles using single potential step. The nucleation step was for 2 ms at potential of -1.6 V, and a growth step for variable times at potential of 0.2 V. Graph A: The first 5 seconds of the experiment. Graph B: The full transient.*

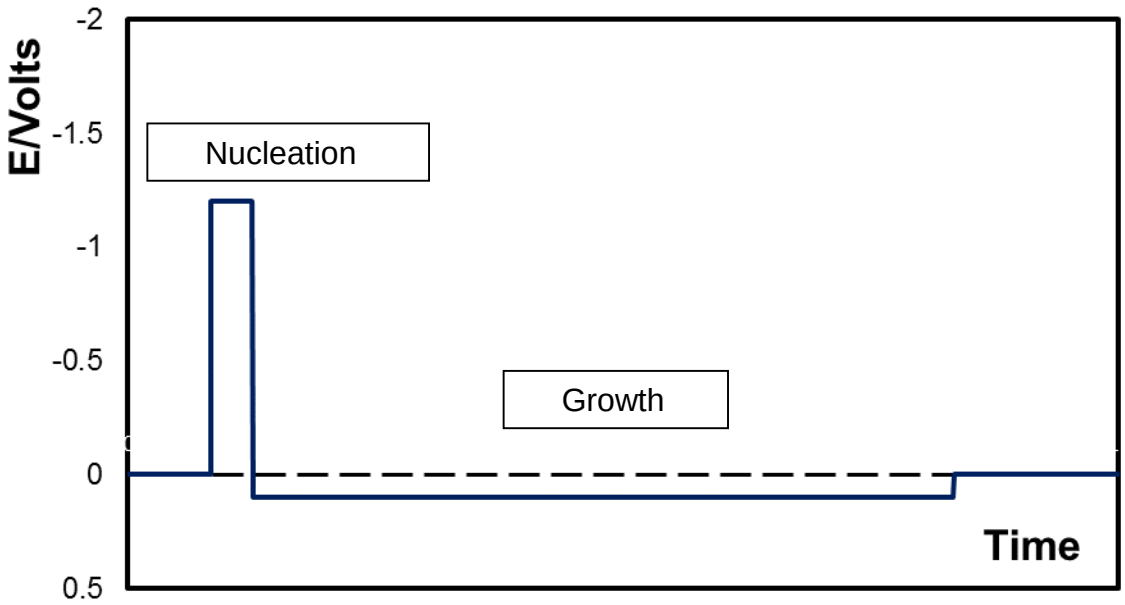


*Figure 2.5: Potential time plot for the double step potential technique used to deposit silver on top of platinum particles in Section 2.4.4.2. The nucleation step was for 1 ms at potential of -1.2 V, and a growth step for 60 s at a potential of 0.1 V.*

### 2.4.5 Attachment of probe-strand DNA

The probe strand was a 20 nucleotide long single strand thiolated on its 5' end and is complementary to the 3' end of the target DNA with the structure of (SH-5'- TA-AGT-TTC-TTC-TAA-ACA-GAC- -3' ). A 10 µM solution of the probe strand was prepared in buffer, 1 M NaCl-TE, contains 1.0 M NaCl, 10 mM Tris-HCl, and 1 mM ethylene diamine tetra acetic acid (adjusted to pH 7.0 by adding 1.0 M NaOH). The probe is allowed to self-assemble on the surface of the silver shell from the thiol terminal that forms a bond to the silver atoms[138]. This is achieved by immersing the modified electrode in the probe strand DNA solution for 7 h in 37 °C to give sufficient time for adsorption to occur. The electrode then removed from the solution, rinsed with deionized water and dried with nitrogen stream.

### 2.4.6 Desorption of platinum silver particles

After attachment of the probe DNA strand to the particles, they are ready to be desorbed and collected. Due to the mushroom shape of these particles, the stem is a nanowire with a small diameter and when subjected to a high current step this wire breaks and releases the head particles in the solution following the method used previously.[44] Another approach that can be followed by is to use a high power ultrasonicator to release the particles from the surface and mechanically snap the connection between the particle and the surface.

After functionalizing the electrode with the probe strand DNA, it is then subjected to a high current step +0.01 A for 120 s. The potential time plot is presented in Figure 2.6 where the contacting solution is 2 mL of 0.01 M $H_2SO_4$.

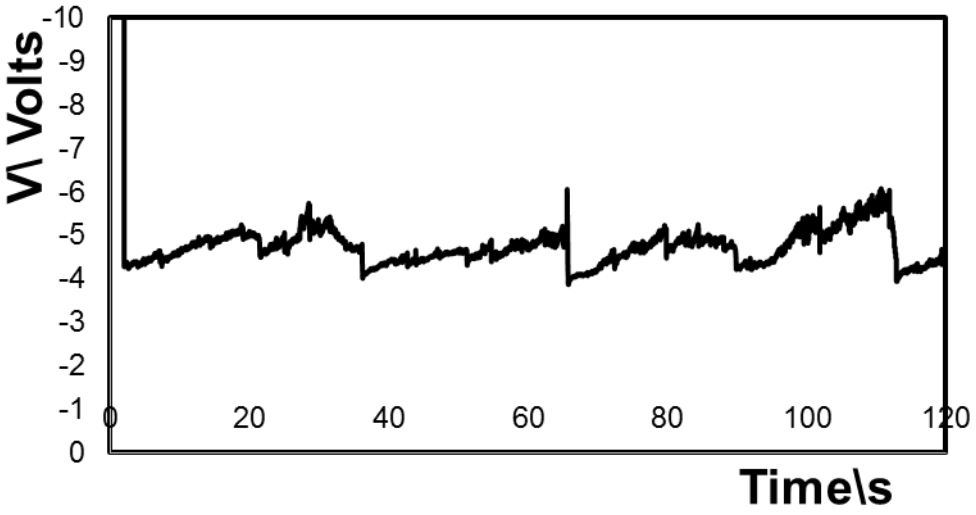


*Figure 2.6: Potential time plot for the desorption of silver coated platinum particles using current step. The applied current is +0.01 A (Reductive) for 120 s.*

## 2.5 Electrochemical Detection of DNA

The detection strategy uses the electro catalytic properties of silver and platinum particles to convert hydrogen peroxide to water and oxygen and using the associated current to measure the DNA concentration. The current magnitude is directly proportional to the number of particles immobilized on the surface. As seen in Figure 2.7, the immobilization of the particles is mediated by the target strand DNA. It connects a probe strand to a capture strand by DNA hybridization. The probe strand is bound to a silver-coated platinum particle as show in Section 2.4.6 and will be the means by which the particles attach to the surface of the electrode.

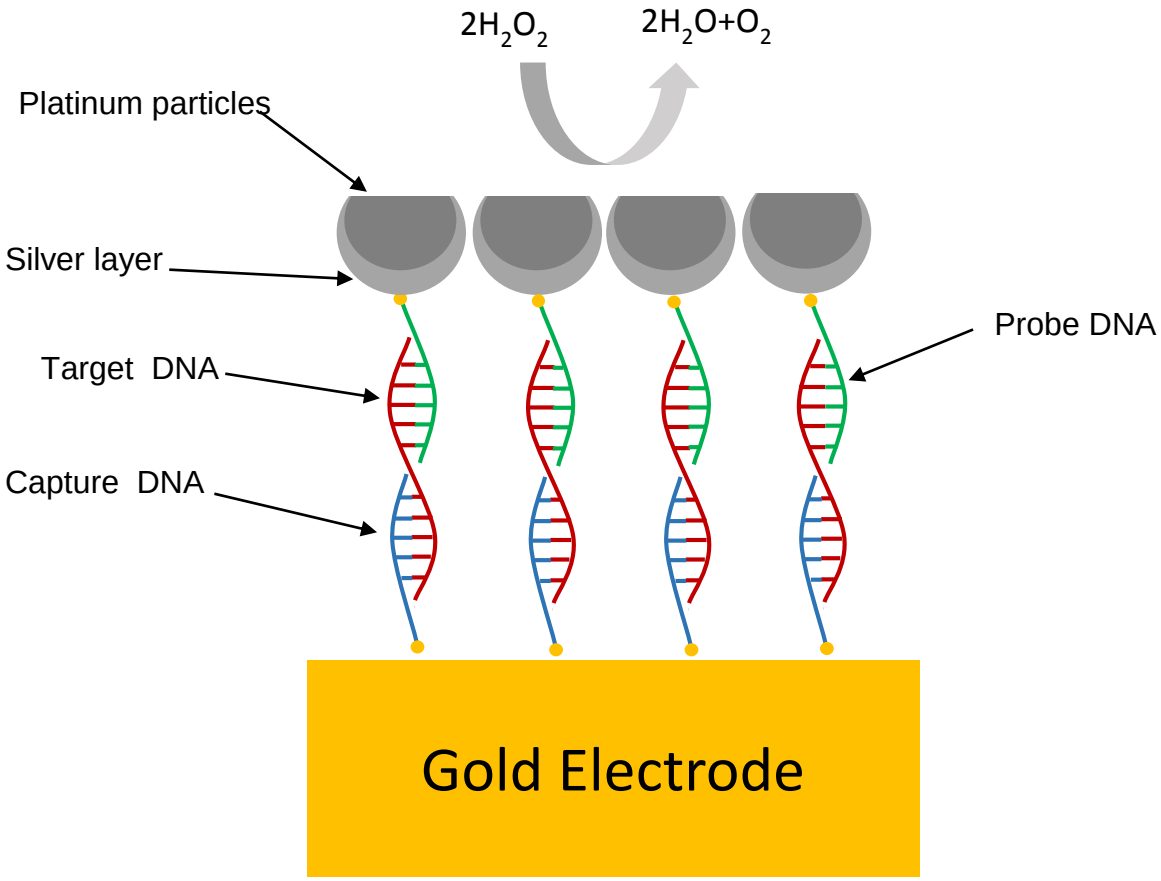


*Figure 2.7 Structure of gold electrode modified following the completion of the DNA sandwich assay where the probe strand is labelled with an electrocatalytic nanoparticle.*

### 2.5.1 Attachment of capture strand DNA.

A 10 µM solution of the capture strand was prepared in buffer, 1 M NaCl-TE, contains 1.0 M NaCl, 10 mM Tris-HCl, and 1 mM ethylene diamine tetra acetic acid (adjusted to pH 7.0 by adding 1.0 M NaOH). The capture strand DNA is allowed to self-assemble on the surface of the gold electrode surface This is achieved by immersing the cleaned gold electrode in the capture strand DNA solution for 7 h in 37 °C. It was then removed from the solution and rinsed with deionized water and dried with a nitrogen stream. 12 gold disc electrodes were modified with the capture strand DNA in this way.

### 2.5.2 Hybridization of the target strand to the capture strand DNA.

Each of the 12 electrodes was incubated in a different target strand DNA solution concentration. The concentrations range between 1 aM (Atto Molar) and 100 nM of target strand DNA. The concentrations were prepared by dilution with buffer, i.e., 1 M NaCl-TE, that contains 1.0 M NaCl, 10 mM Tris-HCl, and 1 mM ethylene diamine tetra acetic acid (adjusted to pH 7.0 by adding 1.0 M NaOH) for 90 min at 37 °C following the procedures from previous studies.[44] The electrodes were then removed and washed with deionised water and dried with nitrogen stream.

### 2.5.3 Hybridization of the probe strand DNA attached to the silver platinum particles to the immobilised target.

The purpose of this step is to attach the prepared silver-coated platinum particles to the surface by hybridization of the probe oligonucleotide to the unbound end of the target DNA which is immobilized on the electrode surface.

This is achieve by incubating the electrodes in the previously prepared nanoparticles suspension obtained from Section 2.4.6 at 37 °C for 90 min. The electrodes are then removed and washed with deionized water.

# 2.6 Immobilization of complex inside gold micro cavities

### 2.6.1 Micro cavity formation.

Nano-cavity gold films were fabricated by electrochemical deposition of gold onto a polystyrene self-assembled template on gold-coated silicon wafers, following the general procedures described by Bartlett[59]Gold-coated (400 nm thick) silicon wafers were used as a substrate as this surface is suitably flat. They were cut by means of diamond cutter to size of about 1 cm width and 2 cm length. The polystyrene spheres obtained from Bangs Laboratories, USA with a size of 5.42 µm were dispersed in water to prepare a suspension of a concentration of 1% w/v. The self-assembly of the spheres was achieved by drop casting the suspension on the gold-coated silicon wafers, leaving it overnight to dry. The drop is cast in a way that covers one-half of the wafer. The polystyrene spheres are pushed together by the surface tension of the water drop that decreases in volume upon evaporation. The result is a close packed arrangement of spheres on the gold covered silicon wafers. The wafer is then immersed in the commercially available gold plating solution TG – 25 – RTU obtained from Technic Corporation that contains approximately 12 g\L gold. The electrochemical deposition should start as soon as possible after deposition of the spheres to avoid loss of the template. A potential of -0.95 V is applied to a three-electrode set up electrochemical cell where the wafer is connected as a working electrode. This potential is

suitable to form cavities with a smooth surface, as higher potential caused the surface to be granular and rough. On the contrary, lower potentials would require significantly longer deposition time. The micro-cavities are then washed and immersed overnight in a 1 mM solution of 1-dodecanethiol in absolute ethanol. That allows the formation of a blocking monolayer on the upper surface of the micro-cavity array to confine the thiolated DNA capture strand into the interior of the cavity. The cavities are then inserted in tetrahydrofuran THF and sonicated to dissolve the spheres and expose the interior.

### 2.6.2 Immobilization of the silver coated platinum particles inside the gold micro cavity array.

The gold micro cavity array is immersed in the thiolated capture strand DNA solution for 7 h at 37 °C to allow the capture strand to self-assemble inside the micro-cavities. The cavities are then removed and washed with deionized water to remove the loosely bound DNA, then incubated in the target strand DNA solution used in Section 2.5.2. It has a concentration of 1 μM for 90 min to allow the target to hybridize with the capture strand DNA and removed from the solution, washed with deionized water and finally incubated in the desorbed silver coated platinum particles suspension that has the probe strand DNA attached to the silver coated side, and prepared as described in Section 2.4.6. for 5 h in 37 °C. It was then removed and washed with deionized water and dried with nitrogen stream. A presentation to the structure of the micro cavities array with particles immobilized inside is depicted in Figure 2.8.

Two sets of micro cavities were prepared in parallel. They were then modified with nanoparticles as described except that the type of particles used was changed. The first set were prepared using platinum particles without a silver coat and the second set with silver coated platinum particles. The aim was to compare the enhancement properties of the platinum particles and silver coating to assess whether silver deposition gave an advantage in terms of Raman signal enhancement.

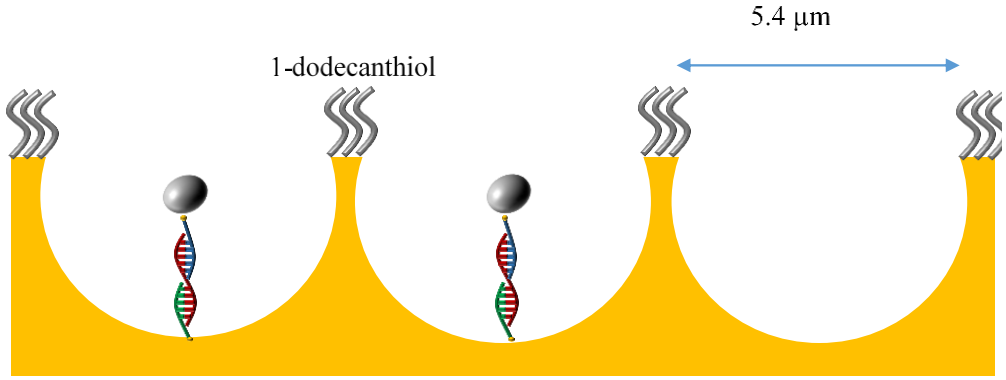


*Figure 2.8:Structure of the gold micro cavities array with capture strand DNA "green" and target strand DNA "red" and probe strand DNA "blue" and silver coated platinum particle. The top surface was modified with a dodacan-1-thiol monolayer.*

# 2.7 Results and Discussion

## 2.7.1 Electrode cleaning and dodecane thiole SAM formation and characterization.

Voltammetry in (0.1 M $H_2SO_4$) was carried out to determine the microscopic area of the freshly polished electrode. As shown in Figure 2.9, the electrode was cycled between 0.35 and 1.5 V. It shows a nearly flat region between -0.2 and 1 V. At approximately +1.1 V the formation of gold oxide monolayer begins. At about +1.5 V the onset of bulk gold oxidation is observed. To avoid further oxidation and surface roughness, the scan is reversed at +1.5. The gold oxide reduction peak (usually found at around 0.8 V) is used to calculate the surface roughness factor (ratio of the microscopic to geometric areas) from the geometric area GA, 0.0314 $cm^2$ . The calculation of electrochemical area and surface roughness factor is given below in Equation 2.1- Equation 2.3, where A is the electrochemical area, $A_p$ is the area under the peak of gold oxide monolayer reduction and R.F. is the roughness factor. A surface roughness factor less than 1.6 is considered satisfactory[44].

The integrated area under the current peak of gold oxide $A_p$ of the bare electrode was found to be 1.8 x $10^{-5}$ C corresponding to a microscopic area of 0.047 $cm^2$ and roughness factor of 1.5.

In Figure 2.10, the solid line represents the bare electrode with an $A_p$ of 1.8 x$10^{-5}$ C and measured surface area of 0.047 $cm^2$. The dashed line represents the same electrode after immersion in 1mM solution of 1-dodecanethiol in absolute ethanol for 7 h. The $A_p$ decreased to 1.3 x $10^{-6}$ C and the measured surface area dropped to 0.0033 $cm^2$ which indicates that

about 7.2% of the surface area remains exposed to the solution after deposition of the defective monolayer.

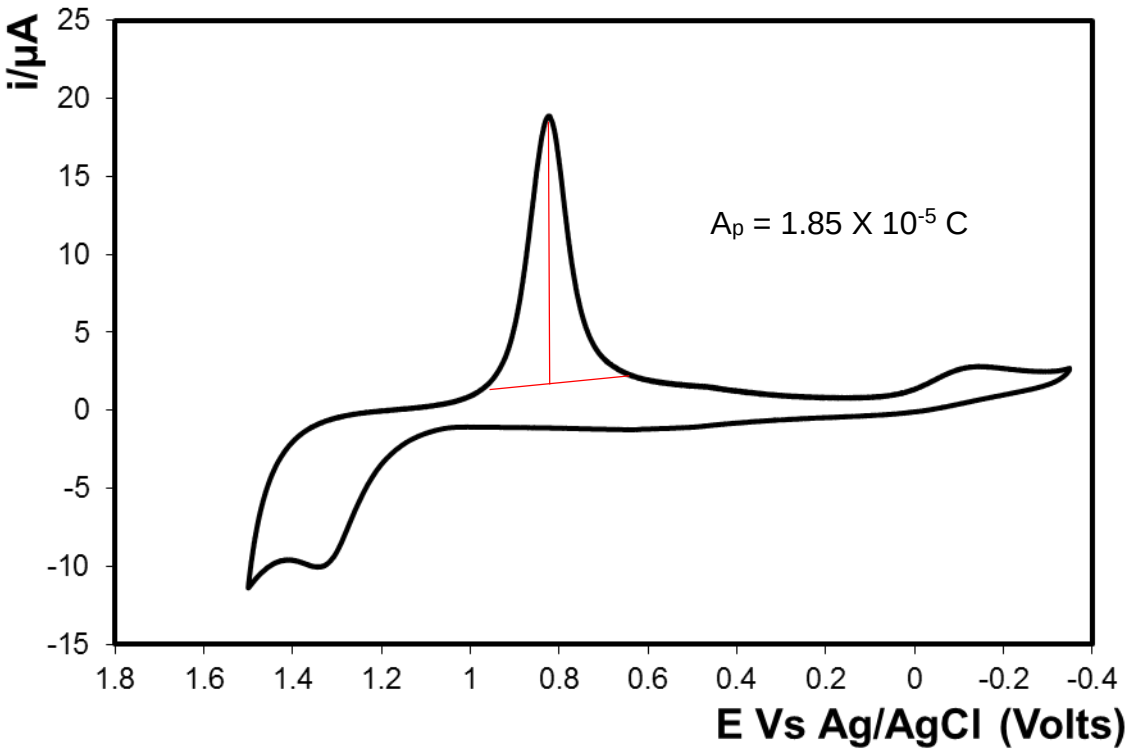


*Figure 2.9: Cyclic voltammogram of a 2 mm diameter gold electrode in 0.1 M $H_2SO_4$. The counter electrode was a platinum wire and the reference electrode was Ag/AgCl saturated in 3M KCl. The scan rate is 0.1 $Vs^{-1}$.*

*Equation 2.1* $$GA = \pi r^2$$

*Equation 2.2* $$A = \frac{A_p}{390\ \mu C.cm^{-2}}$$

*Equation 2.3* $$R.F = \frac{GA}{A}$$

The formation of self-assembled monolayers (SAMs) of alkane thiol on gold is well known to involve rapid adsorption to give a film with a high defect

density which slowly anneals to give a perfect monolayer[127] . The exposure time of the gold electrode to the solution and its concentration are just enough to form a hydrophobic 1-dodecanethiol monolayer on the top of the gold electrode with an array of well separated defects that could be used as templates for nanoparticle deposition. The size and defect density may be controlled by varying the concentration of the 1-dodecanethiol solution as well as the monolayer deposition time[127]. Figure 2.10 illustrates cyclic voltammograms before and after deposition of the defective monolayer. The area under the gold oxide reduction peak centered at approximately +0.8 V decreases by approximately 93% following monolayer deposition for 7 h, i.e., there are a substantial number of sites for metal deposition at the partially blocked surface. These voltammetric data do not allow the nature of these defects to be identified, i.e., there could be a relatively large number of small defects or a small number of relatively bigger patches of bare electrode surface. This issue will be addressed later following the electrochemical deposition of platinum in Section 2.4.3.

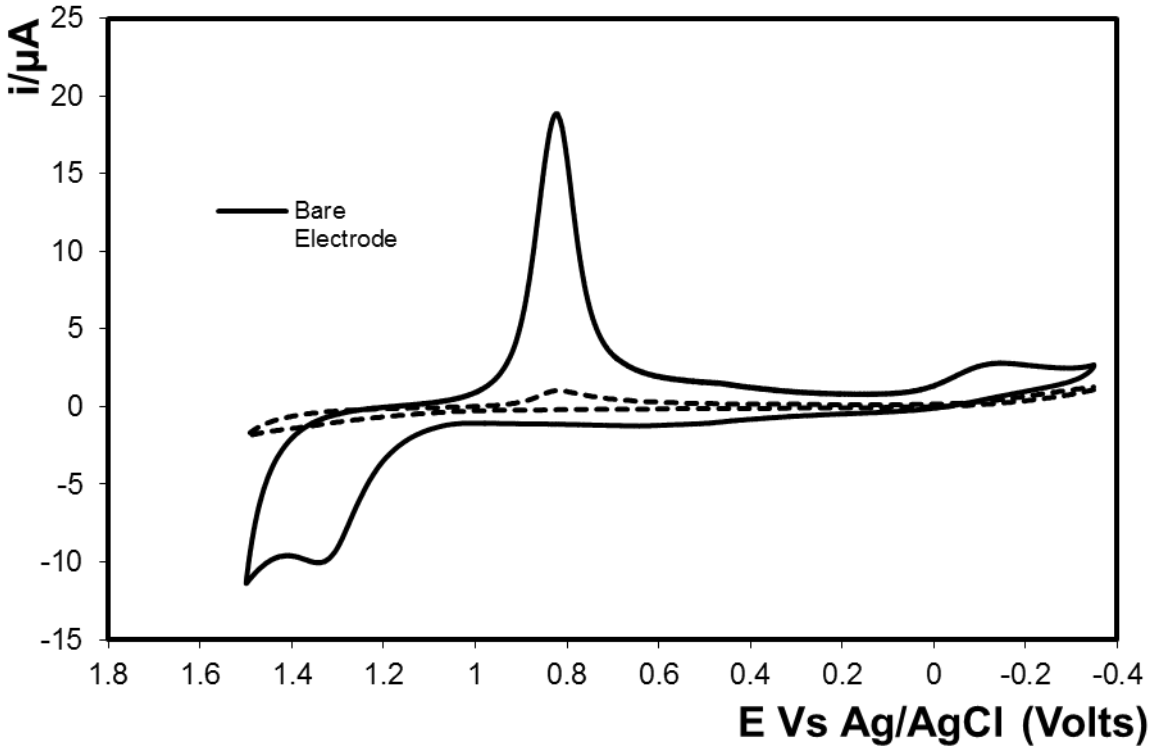


*Figure 2.10 : Cyclic voltammogram of a 2 mm diameter gold electrode before (solid) and after (dashed) the deposition of the defective monolayer of dodecan-1-thiol. In all cases the supporting electrolyte was 0.1 M $H_2SO_4$, the counter electrode was a large area platinum wire and a saturated KCl Ag/AgCl reference electrode. The scan rate is 0.1 $Vs^{-1}$.*

### 2.7.2 Characterization of electrode after platinum deposition

#### 2.7.2.1 Single step deposition:

The deposition current time transient of the Pt deposition suggests that the growth of the particle was progressive. Current-time transients were used for studying the nucleation and growth of platinum nanoparticles within the nucleation sites on the gold disc electrode. As seen in Figure 2.1

To characterize the surface modification following platinum single step deposition, cyclic voltammetry was carried out as shown in Figure 2.11 in 0.1 M $H_2SO_4$ and the area under the platinum oxide reduction peak (between 0.05 and 0.3 V vs. Ag/AgCl) increased. A large increase in current was also observed at about -0.25 V due to reduction of water. Adapting Equation 2.2 for platinum as shown in Equation 2.4 gives the available area after platinum

deposition upon integrating the area under the platinum peak. A calculated surface area of 0.015 $cm^2$ was obtained demonstrating an increased surface area after deposition of platinum from the area of the electrode modified with the dodecanethiol monolayer 0.0033 $cm^2$ which suggests a mushroom shape for the platinum particles formed.

*Equation 2.4*

$$A = \frac{A_p}{420\ \mu C.cm^{-2}}$$

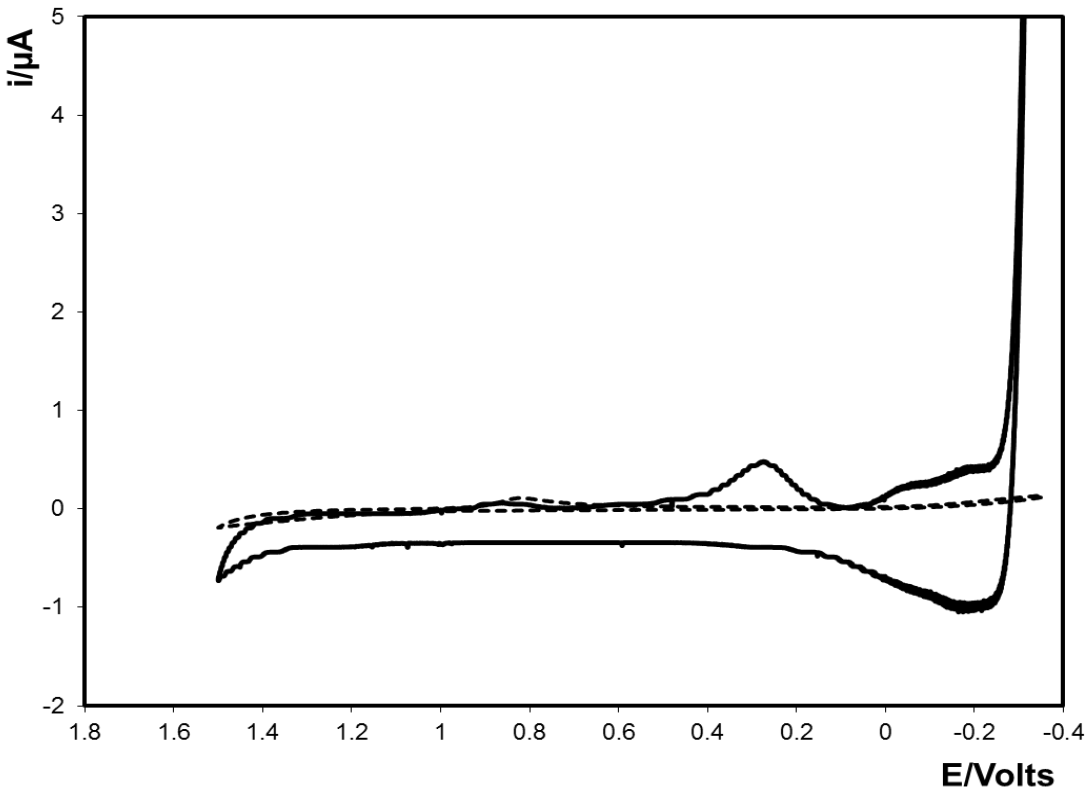


*Figure 2.11 Cyclic voltammogram of a 2 mm diameter gold electrode in 0.1 M $H_2SO_4$. Solid line: Electrode after deposition of platinum particles. Dashed: The same electrode before deposition of platinum.*

Figure 2.12 shows an SEM image for the surface after electrodeposition of platinum particles using a single potential step. Image J analysis reveals that the size of particles was 560 nm ± 124nm. The surface of the particles

was spiky which gave them star shape that can be attributed to the deposition potential used [139]. The size polydispersity was an issue with this method. In addition, the average particle size obtained is larger than what is required to create our electrochemical biosensor.

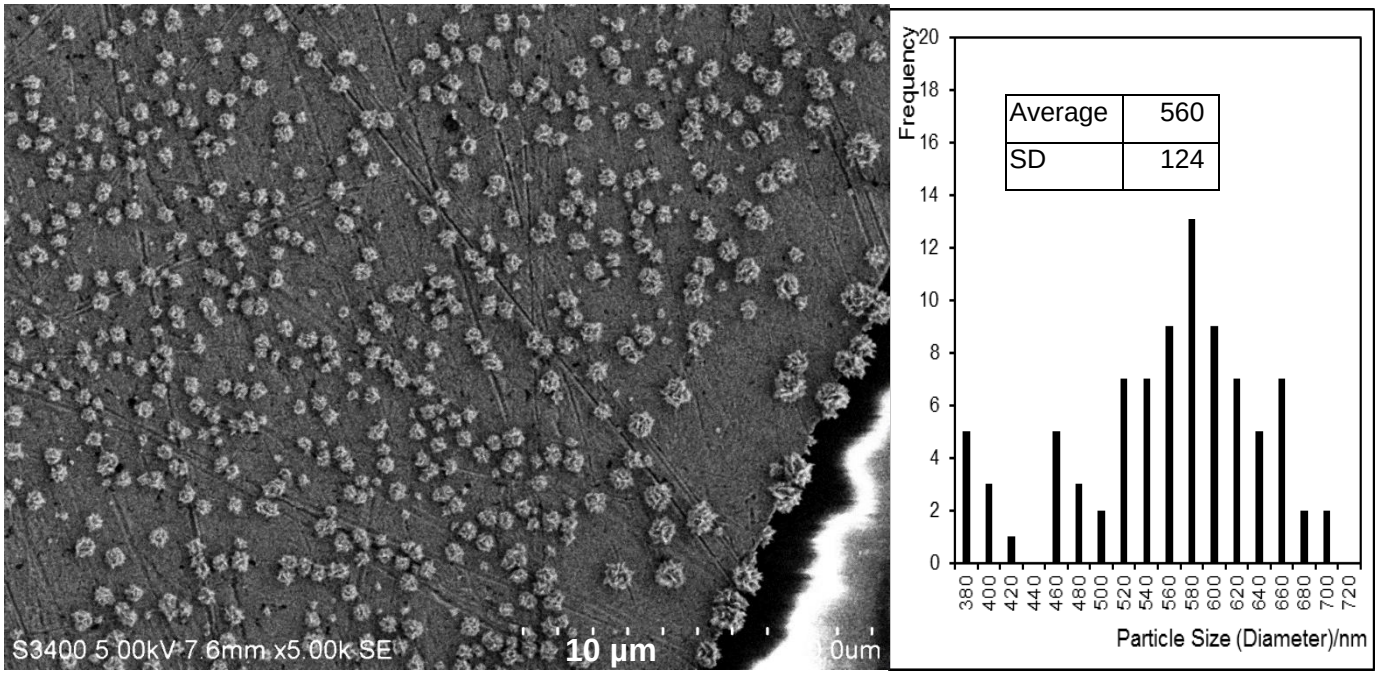


*Figure 2.12 SEM images of a gold disc electrode following deposition of the platinum particles using single potential step deposition. On the right is the size distribution produced by ImageJ. The acceleration voltage is 5 kV.*

### 2.7.2.2 Double step platinum electrodeposition

In order to achieve instantaneous nucleation without having a large driving force for growth, and to control the uniformity of the electrodeposited nanoparticles, it is necessary to separate the nucleation and growth steps. A nucleation pulse with a large overpotential is needed to achieve instantaneous nucleation, which forms nuclei on the surface of the electrode[140]. The potential is then changed to a lower potential so that these nuclei can be grown at the desired rate.

As mentioned in the literature review, to improve the size homogeneity, double potential steps or pulses technique was used for the formation of PtNPs within a self-assembled monolayer, as previously reported by our group and others[45,46]. In this technique, a large potential pulse is applied for a brief time to guarantee nucleation of platinum particles in the monolayer defects sites at the same time, and then followed by a growth phase that allows the diffusion controlled 3D growth of platinum leading to enhanced size monodispersity.

In addition, the concentration of the potassium hexachloroplatinate solution was decreased to 1 mM solution in 0.5 sulphuric acid. This produces particles with smaller size for the same deposition time.

It was established that the greatest nucleation densities were attained at 2 ms at nucleation potentials ($E_{nuc}$) negative of -1000 mV with nucleation density reducing significantly at potentials negative of -1600 mV presumably due to hydrogen evolution[141]. The optimized growth conditions were -200 mV for 60 s. Upon examining the current-time transient, a high current is associated with the high potential step is noticed. Then a sudden drop followed by a small peak and a gradual decline as shown in Figure 2.3.

Performing cyclic voltammetry on the 2 mm gold electrodes before and after dodecanethiol monolayer and platinum deposition, can give an indication about the surface area of platinum produced. It also allows the single potential step and the double potential step to be compared in terms of the available surface area after formation of particles. As shown Figure 2.13 there was an increase in the area under the peak of gold oxide reduction after applying the double step potential deposition. That might be due to the loss of the alkyl thiol monolayer after using a more negative

nucleation potential. Also we can see from the area under the platinum oxide reduction peak that the total platinum particles area is much lower than the previous experiment. This result is expected as both the time of deposition and concentration of platinum solution were reduced. One might expect that the diameter of the resulting particles would be reduced relative to the previous experiment. The area of platinum in the previous method was found to be around 0.015 $cm^2$ and with this procedures it was found to be around 0.006 $cm^2$ representing a decrease of about 50% compared to single step approach. This result can be confirmed using the Scanning electron microscopy.

Figure 2.14 presents an SEM image of the surface of a disc gold electrode after depositing the platinum particles using the double potential step procedures. Consistent with the smaller Pt area obtained from cyclic voltammetry, the particle size was reduced to 219 nm ±28 nm i.e. the double potential step technique produces smaller particles rather than producing a lower particle coverage. Moreover, there is an improved monodispersity. The particles retained the spiky surface observed with the previous method because the growth potential did not vary significantly from the first method.

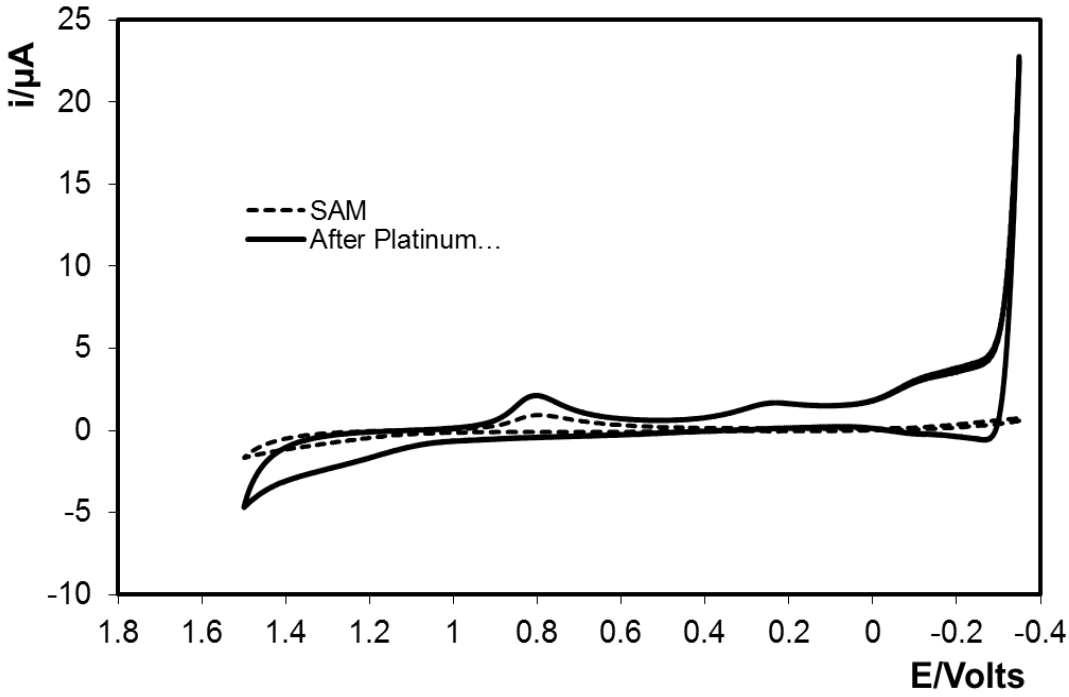


*Figure 2.13: Cyclic voltammogram of a 2 mm diameter gold electrode in 0.1 M $H_2SO_4$. Solid line: Electrode after deposition of platinum particles. The dashed line depicts the same electrode before deposition of Pt. The scan rate is 0.1 $Vs^{-1}$.*

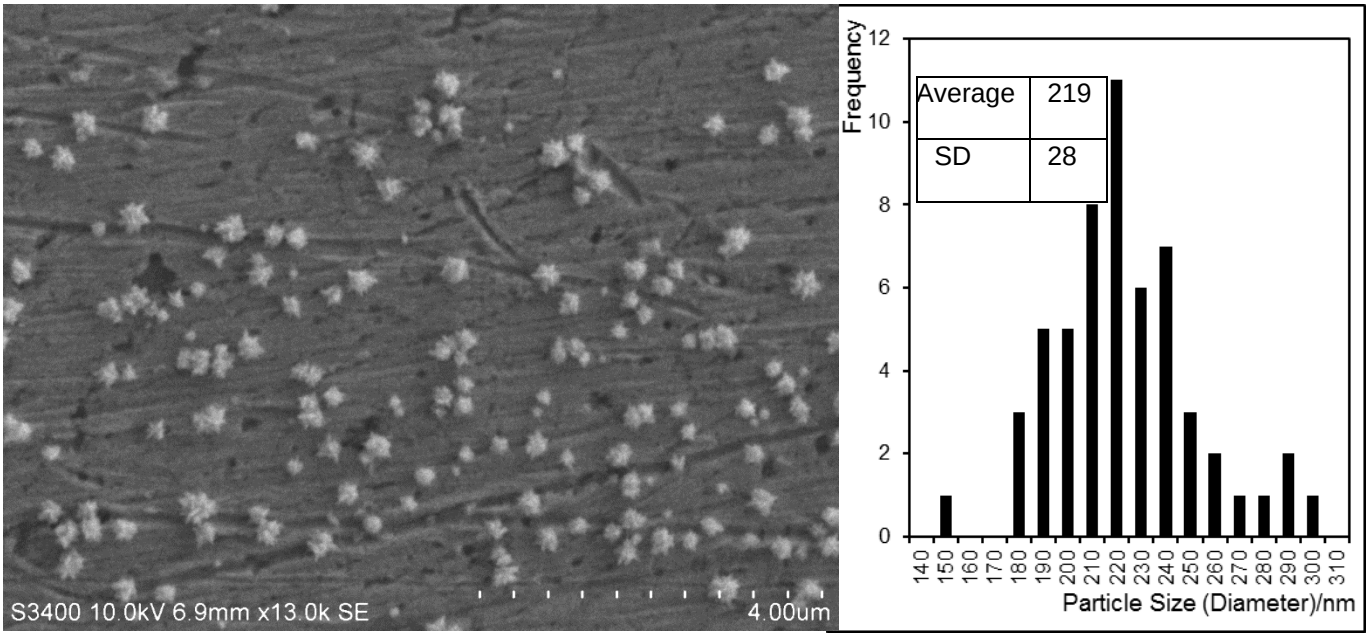


*Figure 2.14: SEM images of a gold disc electrode following deposition of the platinum partices using double potential steps deposition. The acceleration voltage is 10 kV. On the right is the size distribution histogram produced by Imagej.*

### 2.7.3 Characterization of the silver deposition

To improve the deposition of silver on the platinum particles in terms of the amount deposited and coverage, a new protocol of deposition of silver was developed. The silver electrolyte solution used was 0.1 M silver nitrate solution in a 0.1 M solution of potassium nitrate. This concentration was ten times less that the concentration used in the single step deposition to prevent deposition of excessive amount of silver. In addition, the nucleation potential was reduced from -1.6 to -1.2 V, and the growth pulse potential was changed from 0.2 to 0.1. The new double steps potential deposition is depicted in Figure 2.5. The platinum particles used for this method are the ones fabricated using the double step deposition technique of Section 2.4.3.2. The particle size was 214 ± 28 nm, the characterization of the particles obtained in this step is presented later in the results and discussion section.

After deposition of the silver coating, cyclic voltammetry was used to characterize the electrode surface. Cyclic voltammetry destroys the silver layer by oxidizing it. Figure 2.15 illustrates the cyclic voltammogram of gold disc electrode after deposition of silver shell on platinum deposited within the dodecane thiol monolayer defects. The double step potential deposition method was used to deposit both the platinum particles and the silver shell.

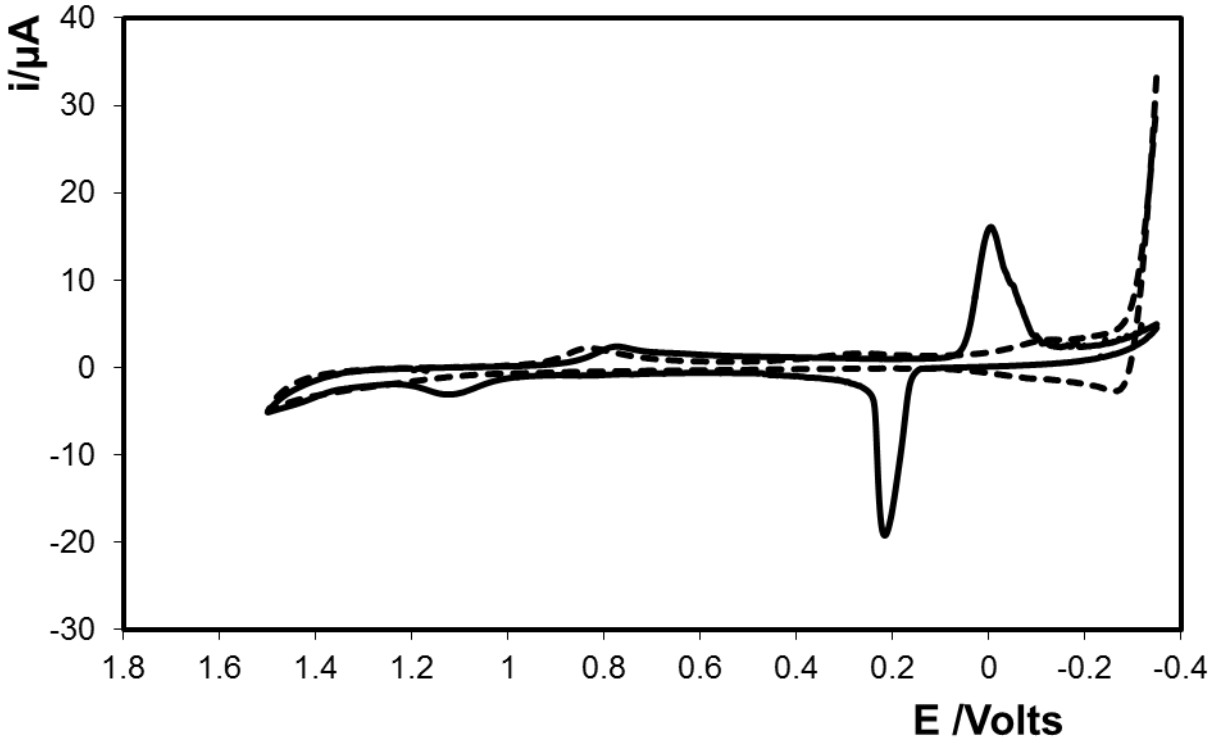


*Figure 2.15: Cyclic voltammogram of a 2 mm diameter gold electrode in 0.1 M $H_2SO_4$. Solid line: Electrode after deposition of silver on top of platinum particles. Dashed: The same electrode before deposition of silver on top of the platinum nanoparticles. The scan rate is 0.1 $Vs^{-1}$.*

The voltammogram suggests that the platinum is covered by silver, as the platinum peaks disappeared after silver deposition. The reduction and oxidation peaks of silver are much lower in area than the previous experiment which is expected due to decrease in both the concentration of the silver solution as well as the deposition potentials.

Figure 2.16 shows platinum particles of the diameter of 560 ± 124 nm covered with silver shell using the method described in Section 2.4.3.1. The EDX spectrum shows characteristics peaks for both platinum and silver. The underlying electrode is not covered by silver deposits, which suggests that the silver is selectively deposited on the platinum particles.

EDX analysis was carried out at six sites (only two are shown) and because the size of platinum particles is much bigger than the thickness of the silver shell in this sample, it can be noted that the average relative weight percent is about 7 % for the silver shell and 92% for the platinum core. The percent of silver is expected to be higher when smaller platinum particles are used.

| Element | App | Weight% | Atomic% |
|---|---|---|---|
| | Conc. | | |
| Ag L | 0.05 | 6.68 | 11.46 |
| Pt M | 1.06 | 93.32 | 88.54 |
| Totals | | 100.00 | |

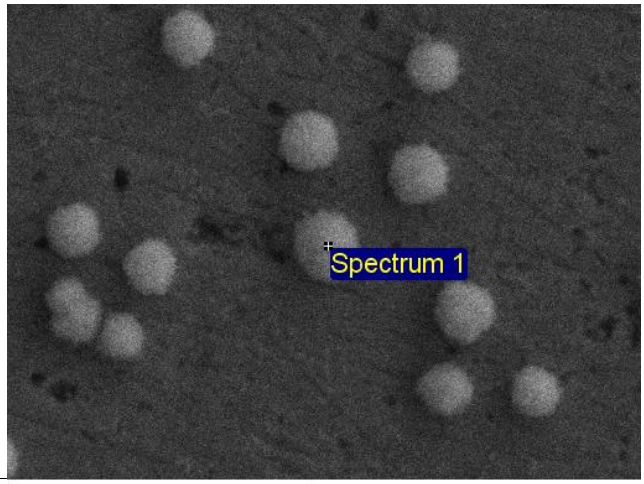


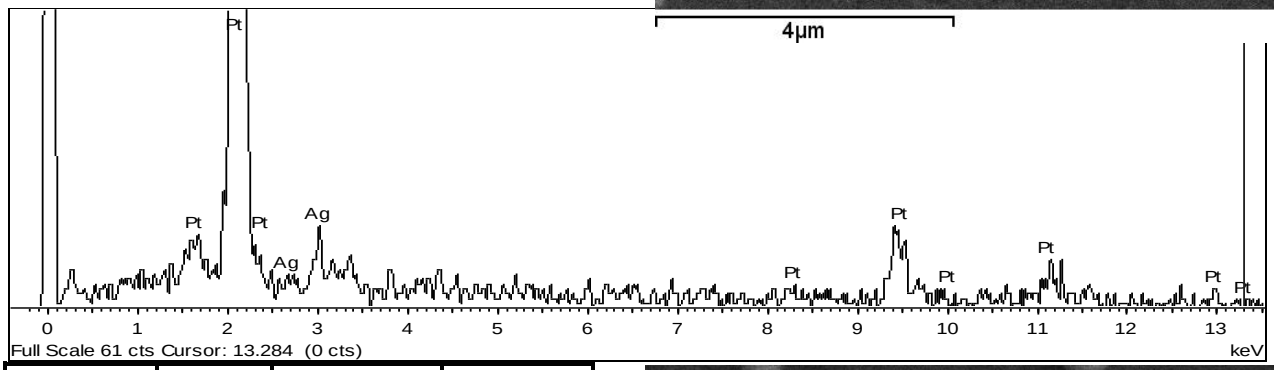


| Element | App | Weight% | Atomic% |
|---|---|---|---|
| | Conc. | | |
| Ag L | 0.12 | 8.83 | 14.91 |
| Pt M | 1.93 | 91.17 | 85.09 |
| Totals | | 100.00 | |

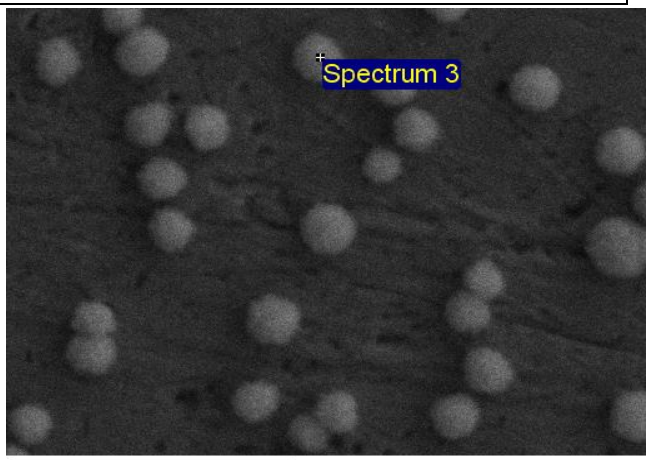


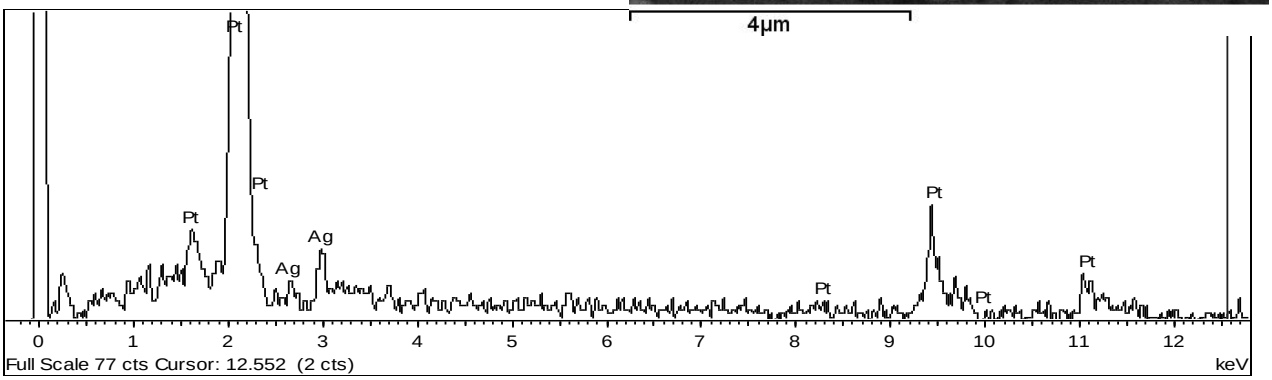


*Figure 2.16: SEM images of a gold disc electrode following deposition of the platinum partices using single potential step deposition. Then depositing silver using double potential step mentioned in 2.4.4.1. The acceleration voltage is from 10 kV. The EDX spectrum shows peaks for platinum and silver.*

### 2.7.4 Characterization of electrode surface by Raman spectroscopy:

The enhancement of the Raman signal for pyridine compounds by silver metal particles is well known[49]. Since the platinum does not produce the same enhancement as silver, a characterization of the silver deposition on top of platinum can be carried out using surface enhancement Raman spectroscopy SERS of a pyridine derivative probe molecule. The 1,2-di(4-pyridyl) ethylene (BPE) molecule displays a high intensity doublet at approximately 1600 $cm^{-1}$ and 1650 $cm^{-1}$ corresponding to pyridine ring breathing modes[132]. Two identical gold electrodes were modified as previously described and platinum particles were deposited, then a silver shell was deposited onto the platinum particles for one electrode and the other was left unmodified. The two electrodes were then immersed in a 1mM solution of 1,2-di(4-pyridyl) ethylene (BPE) in absolute ethanol. The compound is left to self-assemble on the surface of silver particles overnight, then rinsed with alcohol and dried with nitrogen stream and characterized with Raman spectroscopy using a 633 nm excitation laser.

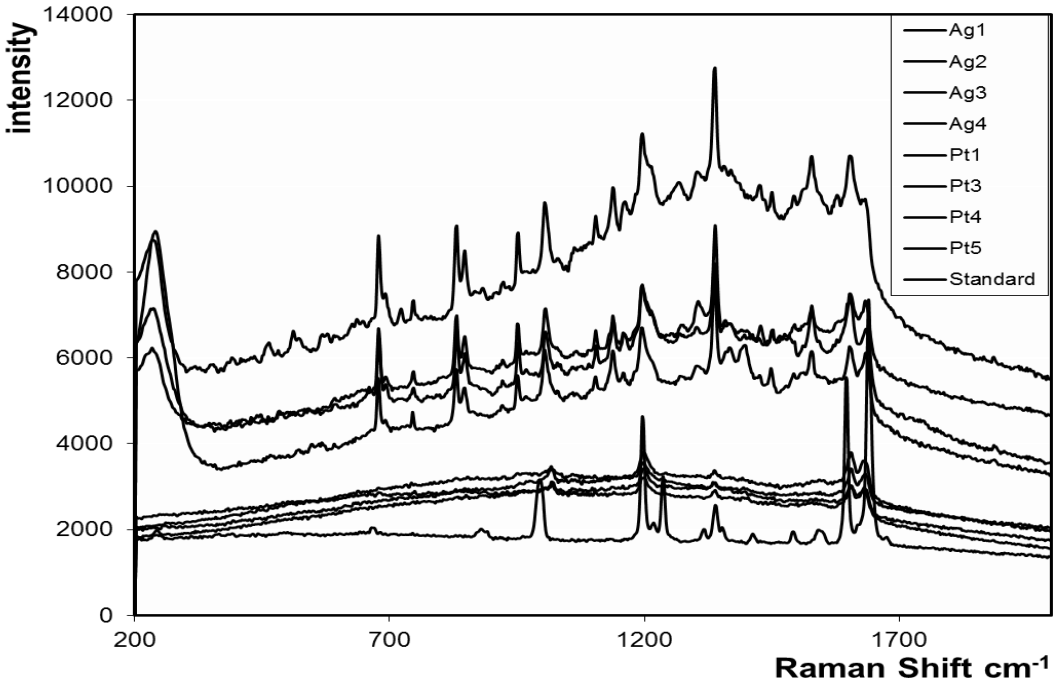


*Figure 2.17: Raman spectrum recorded of BPE on 2 mm gold disc electrode surface electrodeposited with platinum particles coated with silver shell of mean diameter of 569 nm, excitation wavelength was 633 nm. The upper four spectrums coded Ag1-4 are for silver coated platinum particles present on the same electrode, the lower four spectrums coded Pt1-4 are for uncovered platinum particles present on the same electrode, the lowest spectrum is for solid BPE on gold slide.*

In Figure 2.17 the Raman spectrum for BPE shows a significant enhancement of the Raman signature of the molecule in the case of the silver coated platinum particles compared to the uncoated platinum particles. The particle coverage of both electrodes should be the same as the same method of platinum deposition is followed. While the surface coverage of BPE maybe different on the platinum and silver surfaces, these results suggest that the surface has been modified with a silver layer that has different Raman enhancement properties than platinum. That demonstrates that the BPE monolayer is formed on the silver layer, and the planned attachment of a DNA probe strand will be through the silver layer on top of the platinum particle.

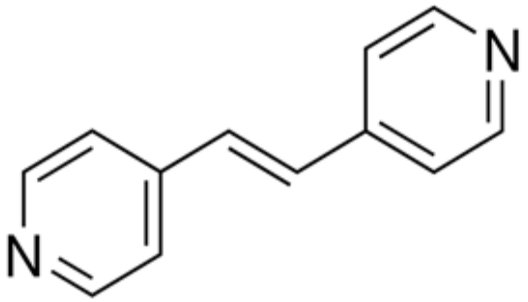


1,2-Di(4- pyridyl)ethylene

*Figure 2.18 Chemical structure if dipyridyl ethylene BPE*

### 2.7.5 Characterization of desorption step using cyclic voltammetry

The cyclic voltammogram of the electrode before desorption is compared to the same electrode after desorption using a current step in Figure 2.19. It shows that the peaks due to silver oxidation and reduction at approximately 0.2 and 0 V respectively and platinum were lost, which suggests the removal of the metals from the electrode surface. Also the area under gold oxide reduction peak at 0.8 V is much larger than that found for polished electrode. This result also suggests that the surface roughness of the gold electrode increases upon desorption of the particles.

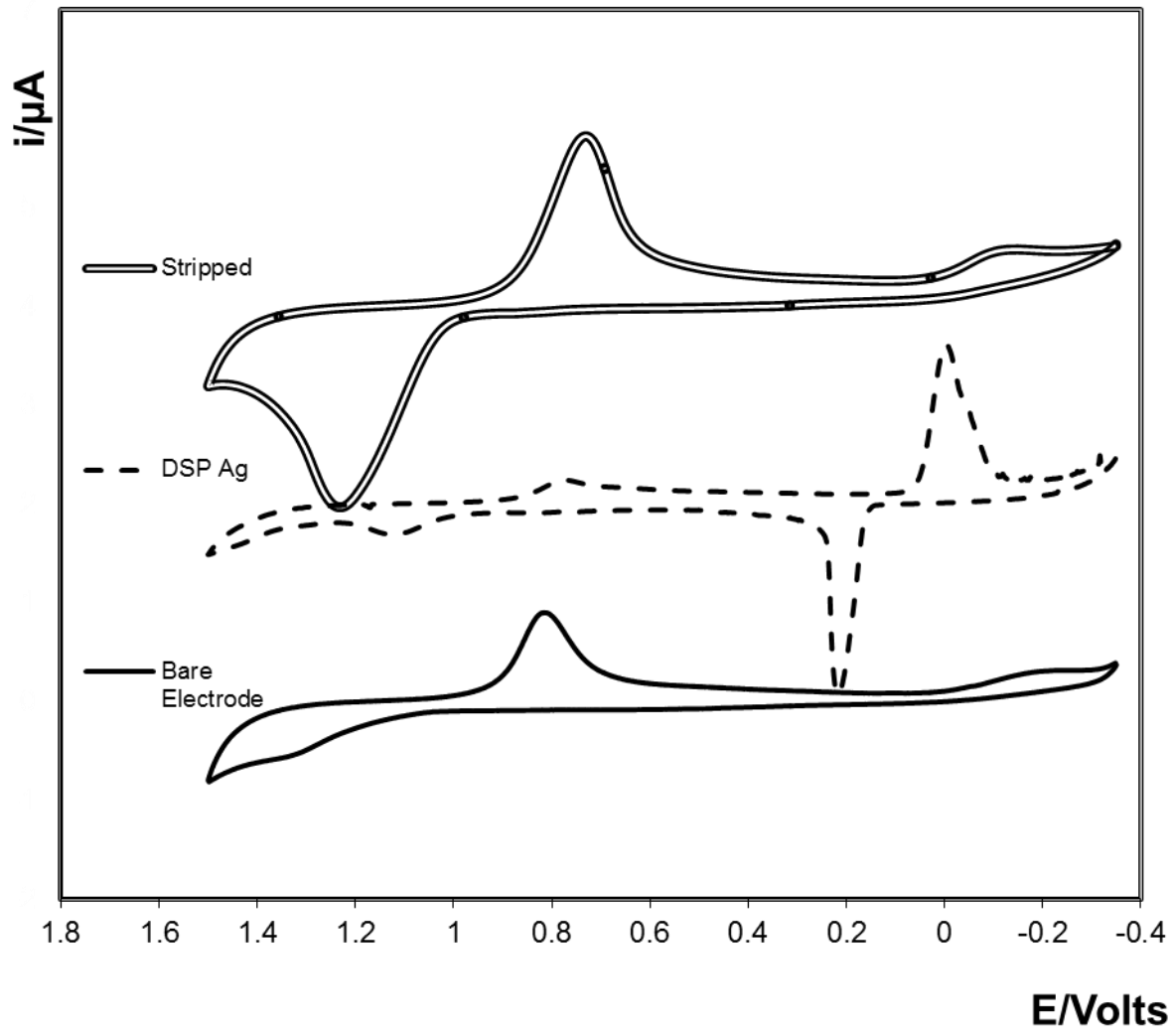


*Figure 2.19: Cyclic voltammogram of a 2 mm diameter gold electrode in 0.1 M $H_2SO_4$ . Solid line: Bare electrode . Dashed, The same electrode before stripping of particles. Double line, The same electrode after stripping by a current step. The scan rate is 100 $mVs^{-1}$.*

Another cyclic voltammetry experiment was carried out using a clean gold disc electrode using the desorbed particles suspension in 0.01 M $H_2SO_4$ solution as shown in Figure 2.20. Significantly, peaks due to silver oxidation and reduction are observed at 0.5 V and 0.35 V respectively, and a platinum reduction peak at 0.1 V. This result demonstrates that the particles have been separated from the electrode and dispersed in the electrolyte solution.

However, this experiment would be worth repeating at a glassy carbon electrode to avoid the gold peak from the underlying electrode.

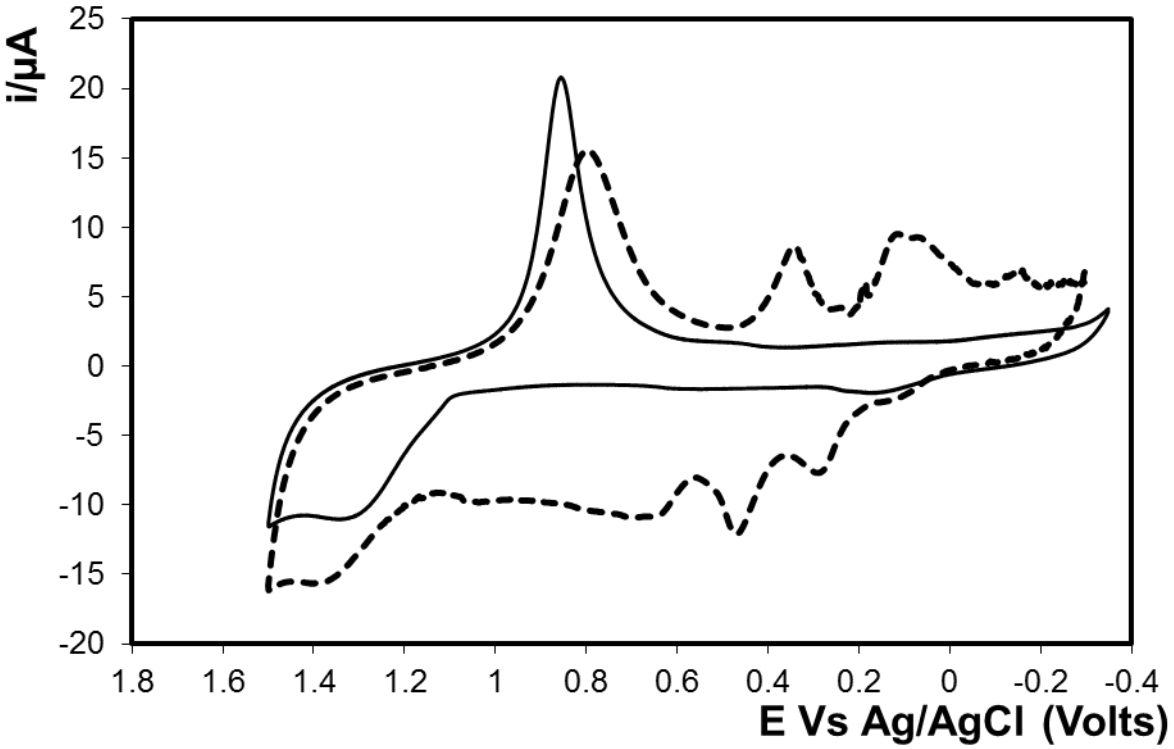


*Figure 2.20: Cyclic voltammogram of a clean and polished 2 mm diameter gold electrode. Solid: in 0.1 M $H_2SO_4$. Dashed: in desorbed silver coated platinum particle suspension in 0.01 M $H_2SO_4$ solution.*

### 2.7.6 Characterization of desorbed particles using Scanning Electron microscope (SEM) and EDX:

The particles suspension was drop-cast on an SEM stub that is covered with a double stick carbon disc, left to dry and examined using SEM. The platinum particles were grown using the single potential step deposition. As seen in Figure 2.21, the EDX spectroscopy shows clear peaks of platinum and silver for the particles confirming its core:shell composition.

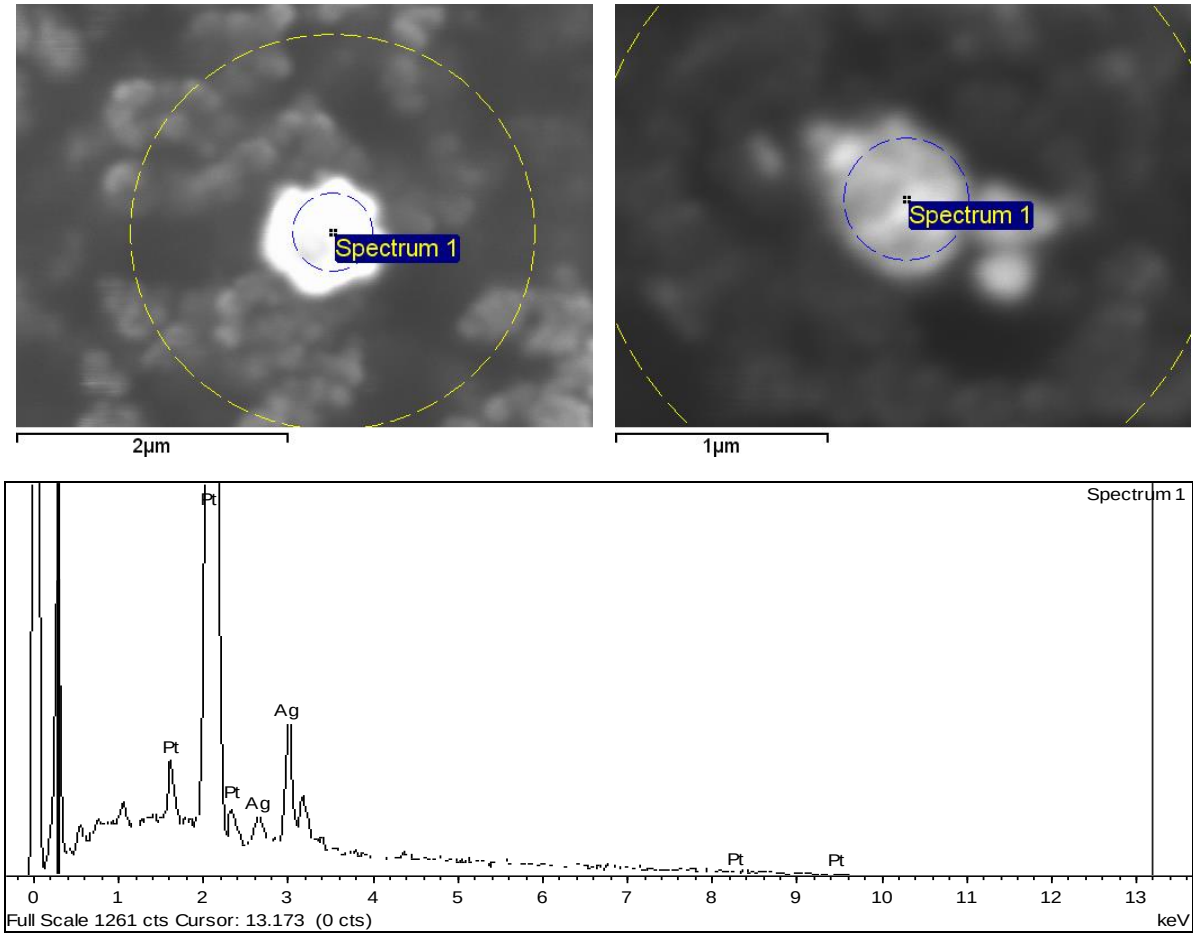


*Figure 2.21 SEM images of desorbed silver-coated platinum particles drop-cast on carbon surface. Below is the EDX spectrum showing peaks for platinum and silver.The acceleration voltage is 10 kV.*

### 2.7.7 Characterization of desorbed particles using dynamic light scattering DLS

The DLS technique was used to determine the size of the platinum particles prepared using the double potential steps described in Section 2.4.3.2. SEM imaging for the same particles showed that the diameter is 219 ±28 nm, Figure 2.22. DLS confirms this result. It also proves that particles diameter did not change dramatically upon the attachment of probe strand DNA or when desorbed. The DLS was carried out on three different samples each independently prepared and the average particle size observed was 213 ± 34 nm, which is indistinguishable from the particle size observed by SEM.

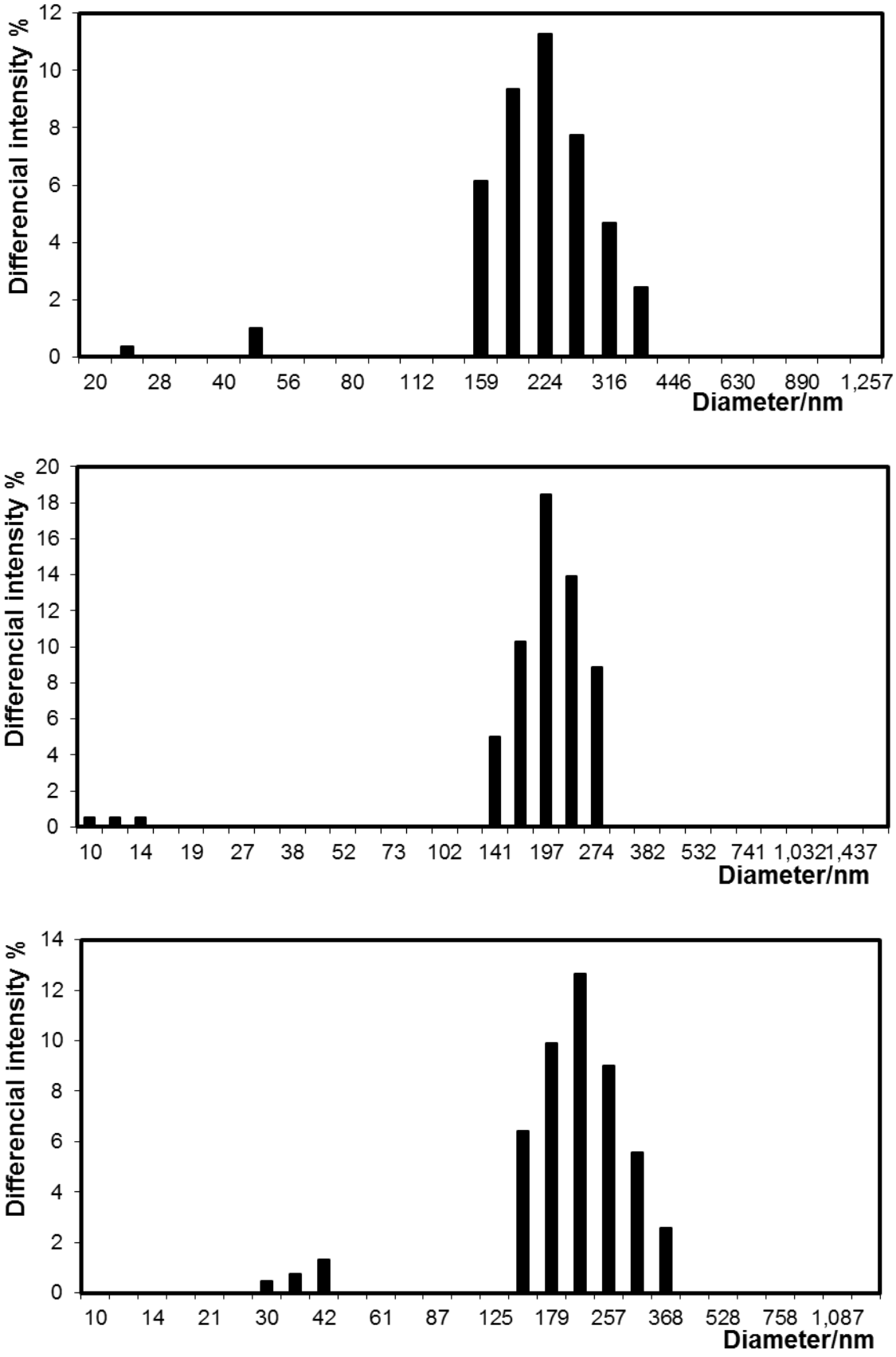


*Figure 2.22 Histogram of DLS measurements for the silver-coated platinum particles. The average of the three measurements is 213 ± 34 nm.*

## 2.8 Construction of the electrochemical biosensor and calibration curve for the DNA detection:

In this section, the analytical performance of the electrochemical biosensor is reported. The particles used in this assay are the platinum particles produced by double potential steps and asymmetrically covered with silver using the second double potential step procedure. The average particle size is 219 ± 28 nm. The target DNA used is the 41-nucleotide long single strand oligonucleotide that is exclusively found in the udder inflammation-causing organism Staphylococcus aureus mastitis. Serial dilutions of the target DNA were prepared, and different modified electrodes were used to detect the presence of the target DNA. A calibration curve is constructed and statistically analysed.

The modified electrodes were used as working electrodes in a conventional three electrode electrochemical cell. Following assembly of the capture-target-particle labelled probe DNA sequence. The electrodes were placed in a 0.01 M $H_2SO_4$ aqueous solution and the current was measured at potential of -0.250 V after equilibration for 5 min. Then, sufficient hydrogen peroxide was added to the cell to give a final concentration of 200 μM of $H_2O_2$. The current associated with peroxide reduction at the bound platinum/silver particles was measured at -0.250 V after 5 min. The analytical response was taken as the difference in current, $\Delta i$, measured before and after peroxide addition. Figure 2.23 shows the amperometric current time curve before and after the addition of hydrogen peroxide.

Figure 2.24 shows the dependence of $\Delta i$ on the log [DNA] of target DNA labelled with silver coated platinum particles. It is worth noting that the slope of the calibration curve is small. However, the dynamic range is quite large (from 1 atto mole to 100 nano mole) which suggests that the contribution of a single particle in the overall current is considerable and the arrival of few particles to the surface of the electrode provides relatively large current.

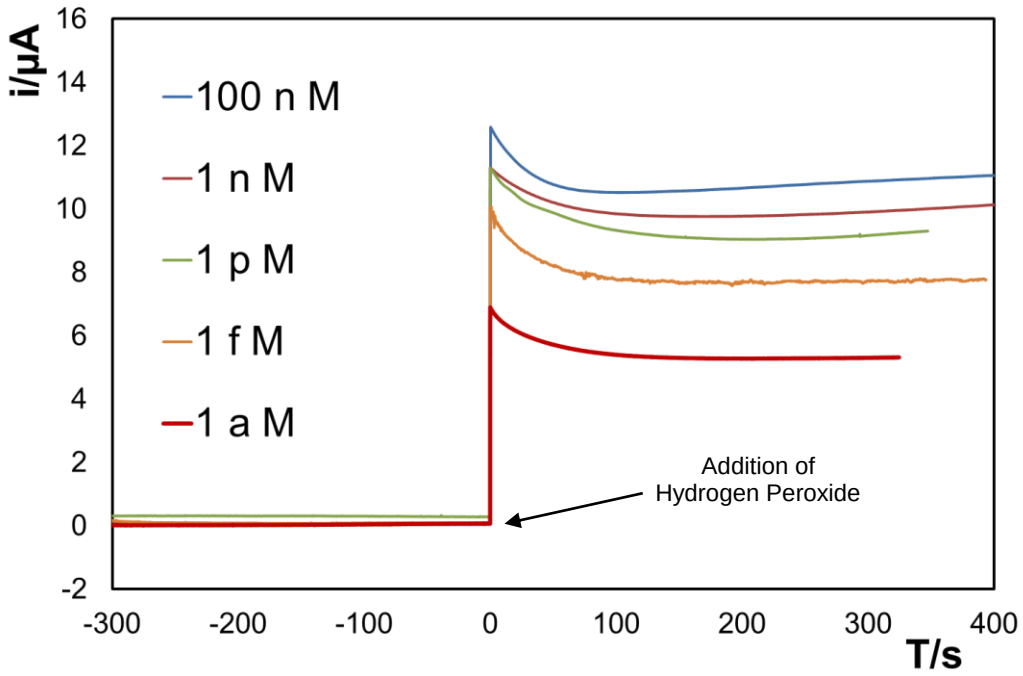


*Figure 2.23: Current transient for the amperometric detection of $H_2O_2$ reduction at potential of -0.25 V on a 2 mm gold disc electrode modified with capture-target-probe-particle complex. The target concentration was 1 aM, 1 fM, 1 pM, 1 nM and 100 nM, the arrow marks the addition of hydrogen peroxide.*

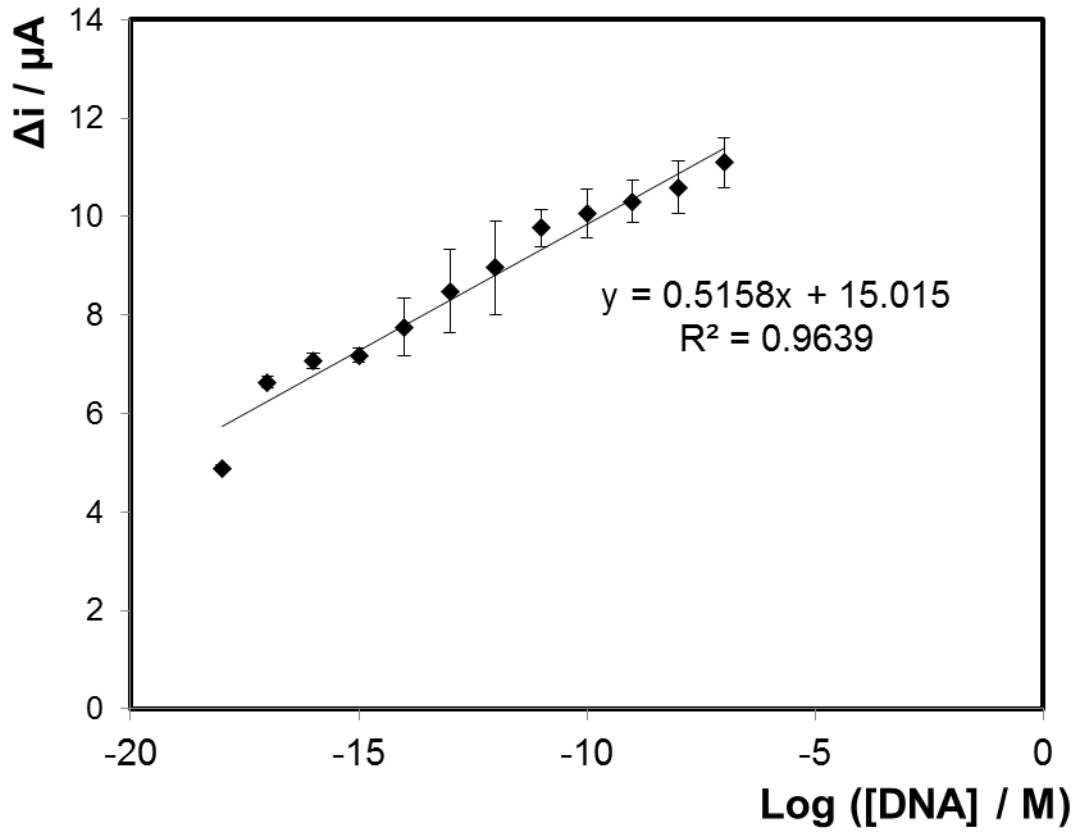


*Figure 2.24: Calibration plots for the electrochemical detection of Staph. Aureus mastitis DNA on a 2 mm diameter bare electrode following hybridization with probe DNA immobilize Ag coated Pt particles. Δi represents the difference in current before and after addition of 200 μM $H_2O_2$ at an applied potential of −0.250 V following approximately 5 min equilibration time.*

For this work, the limit of detection can be calculated as the concentration corresponding to three times the background current.

The background current was found to be 2.8 X $10^{-6}$ A, three times that current corresponds to a concentration of 1.5 x $10^{-13}$ M, (150 f M) which is considered the limit of detection.

## 2.9 Micro cavities array formation and characterization

The objective of this section is to describe the formation of the gold micro cavities and the DNA mediated immobilisation of the core-shell nanoparticles within the cavities interior, investigated specific goal is to measure the Raman enhancement factor for the nanoparticle in cavity architecture.

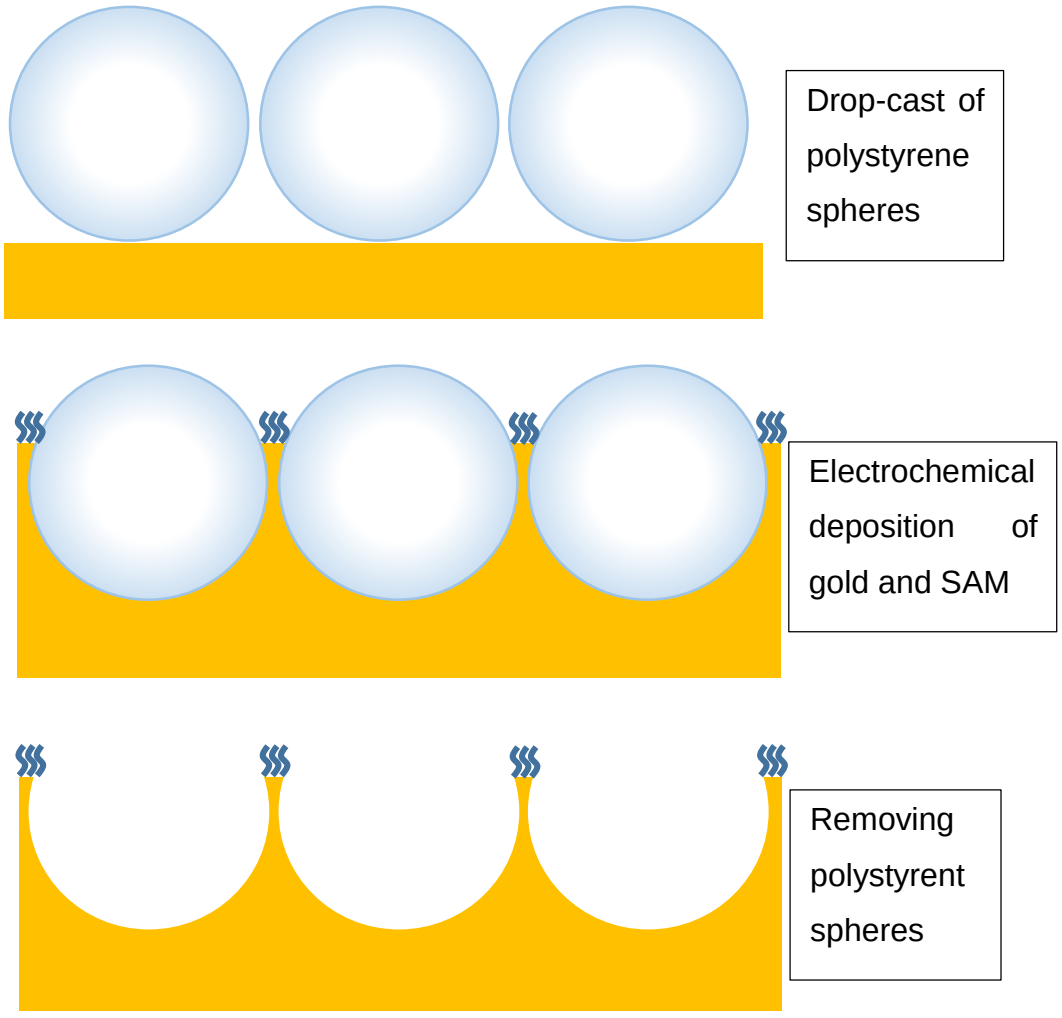


*Figure 2.25 preparation of gold microcavity array*

The current-time response during gold micro-cavity array deposition was monitored as well as the cumulative charge. The thickness of the gold deposited between the polystyrene spheres is directly proportional to the amount of charge passed during the electrochemical deposition. This quantity can be calculated using Equation 2.5

Equation 2.5 $$\mathrm{Q} = \mathrm{nFN}$$

Equation 2.6 $$\mathrm{I} = \frac{\mathrm{Q}}{\mathrm{t}}$$

Equation 2.7 $$Q = \int I.dt$$

Q is the charge passed through the cell, F is Faraday's constant (96485.34 C), equal to the charge of one mole of electrons, N is the number of moles of deposited species and n is the number of electrons involved in the redox reaction.

Since the height of the gold deposit layer should reach just above the equator (half the diameter) of the polystyrene spheres to obtain cavities with a minimum flat surface between voids. The diameter of the polystyrene spheres used was 5 µm , The a suitable height can be 3 µm.

3 µm = 3 x$10^{-4}$ cm.

The dimensions of the area of the wafer that will be covered with gold is about 1 cm length and 1cm width. The volume of gold required to be deposited is:

Height x Length x width = Volume

3 x $10^{-4}$ cm x 1 cm x 1 cm = 3 x $10^{-4}$ $cm^3$

Assuming 100% coulometric efficiency, and taking the density of gold as 19.32 g/$cm^3$ , the weight in gm of gold required to be deposited is:

Mass= Volume x Density = 3 x $10^{-4}$ $cm^3$ x 19.32 g/$cm^3$ = 5.79 x $10^{-3}$ gm.

Since the molecular weight of gold is 196.96 g/mol, Thus number of moles equals:

Number of Moles = mass/molecular weight = 5.79 x $10^{-3}$/196.96 = 2.94 x $10^{-5}$ Moles

Since Faradays Constant = 96485.34C, thus

F x moles = Q (charge) 96485.34 x 4.9 x $10^{-5}$ = 2.83 C

The deposition is continued until the cumulative charge passed through time Equation 2.7 reaches 2.83 C.

The flat surface of the deposited gold between polystyrene sphere is blocked by 1-dodecanethiol to confine the attachment of thiolated DNA capture strand to the interior of the gold cavities and prevent the non-specific binding to the upper surface. This was achieved by immersing the

cavities micro array in 1 mM solution of 1-Dodecanethiol in absolute ethanol overnight. While the templating spheres are still in place. It was then washed with ethanol and dried with nitrogen stream. The polystyrene spheres were then removed by sonicating in tetrahydrofuran, THF. The sonication is maintained for 45 – 60 min (Power, 135 W. Frequency, 24 KHz ± 6%), washed with ethanol and dried with a nitrogen stream. The preparation of the gold microcavity array is depicted in Figure 2.25.

.

### 2.9.1 Characterization of electrodeposited gold cavity.

Figure 2.26 shows a closely packed array of gold micro-cavities. The upper flat surface was modified by 1-dodecanethiol monolayer while the interior was left pristine for the next step. The sample also contained some areas where the spheres were not highly ordered or closely packed. The size of cavities matched the size of the templating spheres and no change in size was observed.

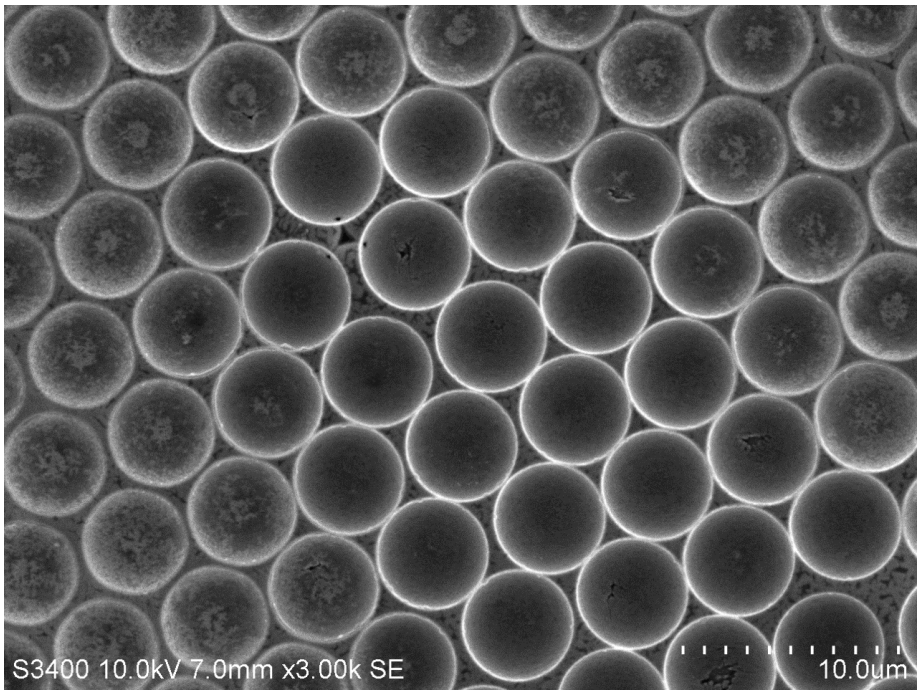


*Figure 2.26: SEM images of an array of gold micro cavities with a diameter of 5.4 µm. The acceleration voltage is from 10 kV.*

### 2.9.2 Characterization of the silver-coated platinum particles immobilized inside gold micro cavities array using SEM and EDX.

The SEM image of the micro cavities with silver coated platinum particles is shown in Figure 2.27, and pristine platinum particles in Figure 2.28. While Figure 2.27 was taken in an area where cavities are poorly close-packed, and the flat surface area is large, it is useful to demonstrate that particles are only residing selectively inside the interior of the cavities, and the surface blocking strategy was successful. Although the particle size of the suspension

used was determined by DLS and SEM and found to be 220 ± 28 nm, it appears that most of the particle that attached to the cavities were less than 200 nm but bigger sizes were also observed. In Figure 2.28 pristine platinum particles were used and the EDX spectrum does not show any silver peaks in Figure 2.27.

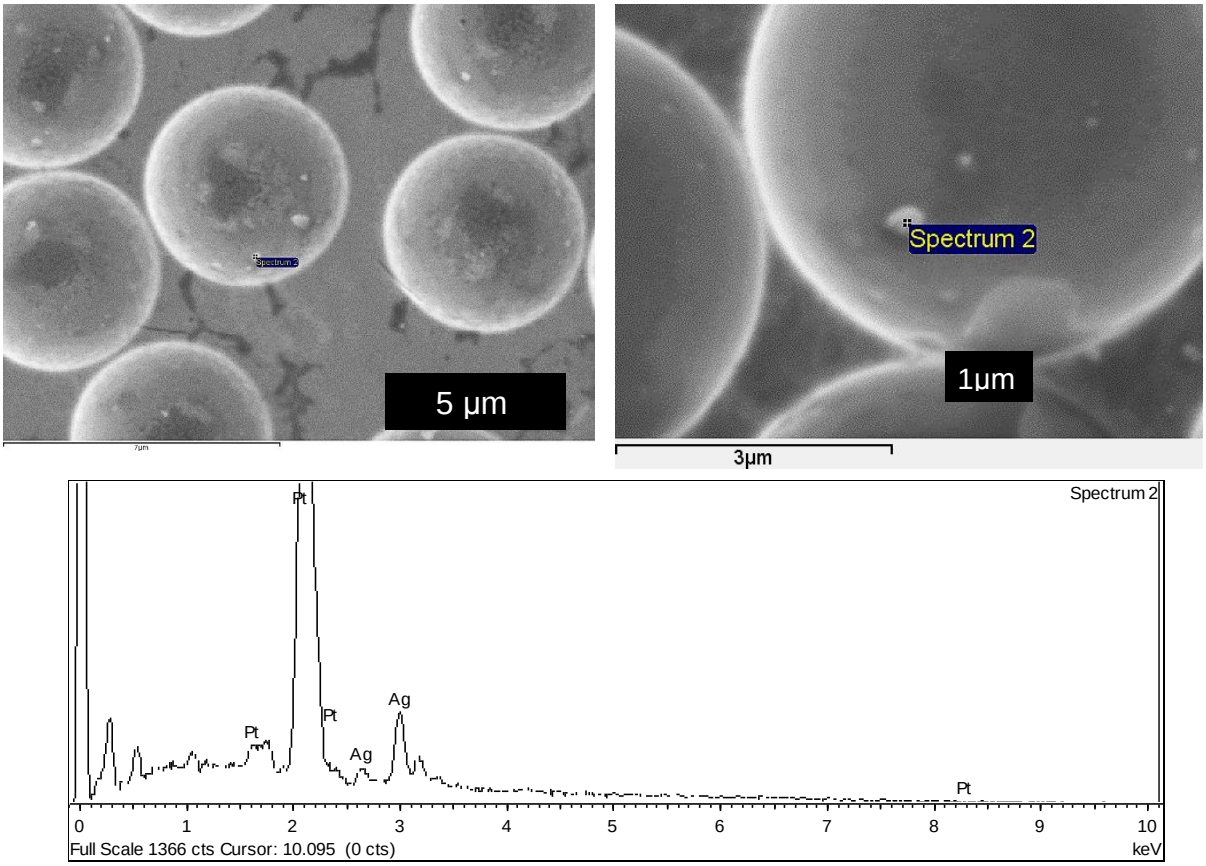


*Figure 2.27: SEM images of a gold micro cavities array diameter 5.4 µm containing DNA mediated immobilized silver coated platinum particles that can be seen inside cavities. The EDX spectrum shows that the particle contains both silver and platinum. The acceleration voltage is 10 kV.*

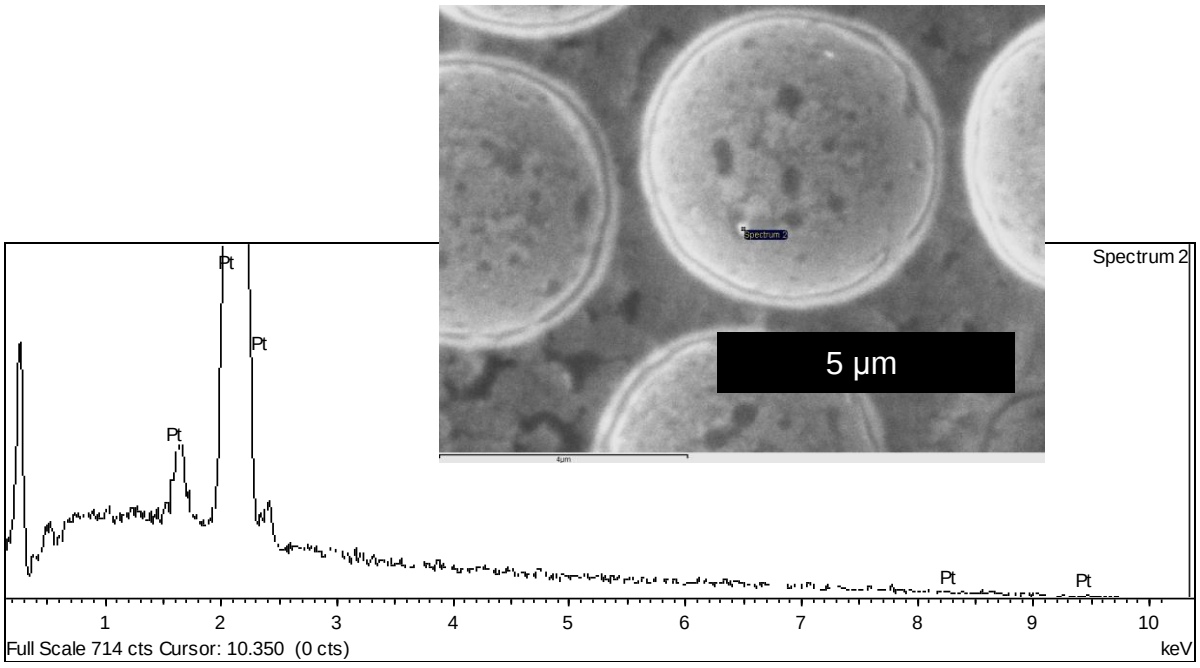


*Figure 2.28: SEM image of a gold micro cavity array diameter 5.4 µm containing DNA mediated immobilized uncoated platinum particles that can be seen inside cavities. The EDX spectrum shows that the particle contains only platinum and no peaks for silver were detected. The acceleration voltage is 10 kV.*

### 2.9.3 Characterization of the DNA mediated immobilized particles by Raman spectroscopy:

The silver coated particles are expected to enhance the Raman signal of the DNA more than the platinum particles as discussed in Section 2.7.4. The excitation wavelength of the laser used was 633 nm which was used with gold cavities in previous studies[63,142,143]. A 100 X magnification lens was used. Approximately 16 sites on the micro cavities array of platinum particles were measured by raman spectroscopy and in the case of silver-coated platinum particles approximately 30 sites were measured. Only weak spectra of DNA could be detected in case of platinum particles. On the other hand, silver coated platinum particles showed more complex and intense peaks in many sites. As shown in Figure 2.29.

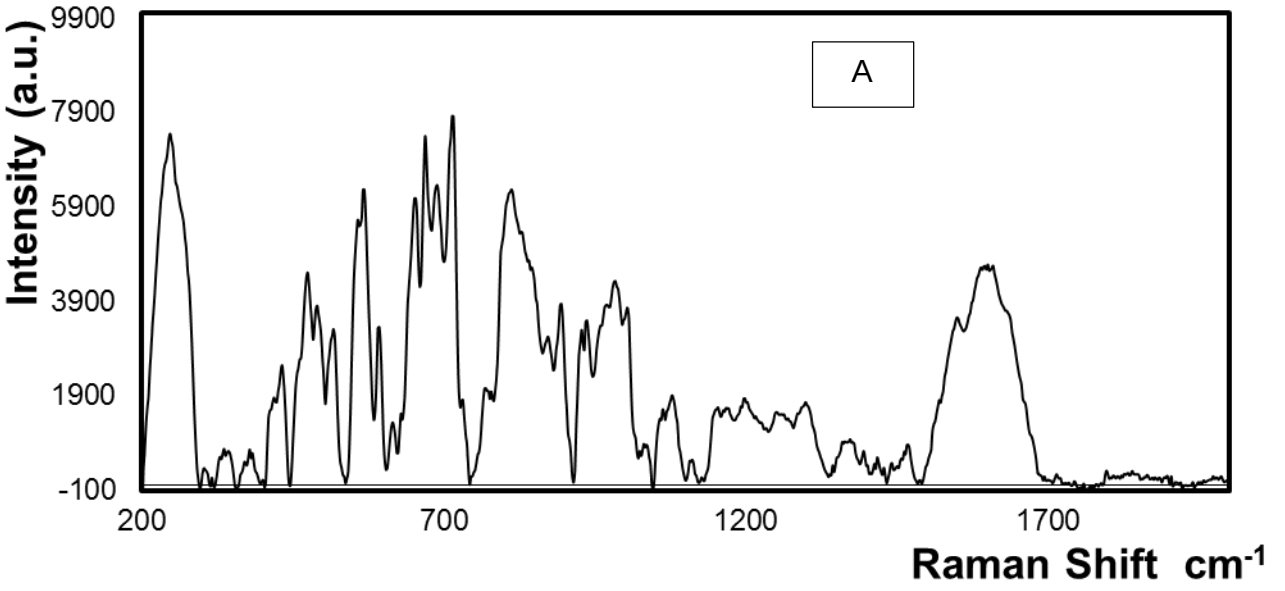
A
Intensity (a.u.)
9900
7900
5900
3900
1900
-100
200
700
1200
1700
Raman Shift cm-1

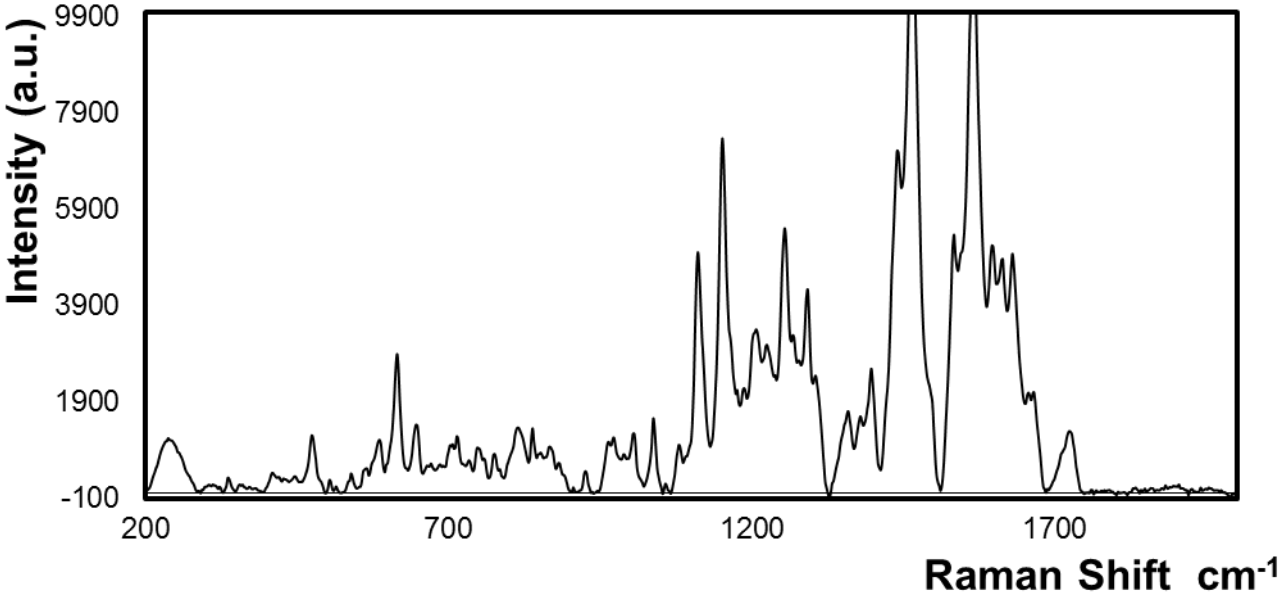
Intensity (a.u.)
9900
7900
5900
3900
1900
-100
200
700
1200
1700
Raman Shift cm-1

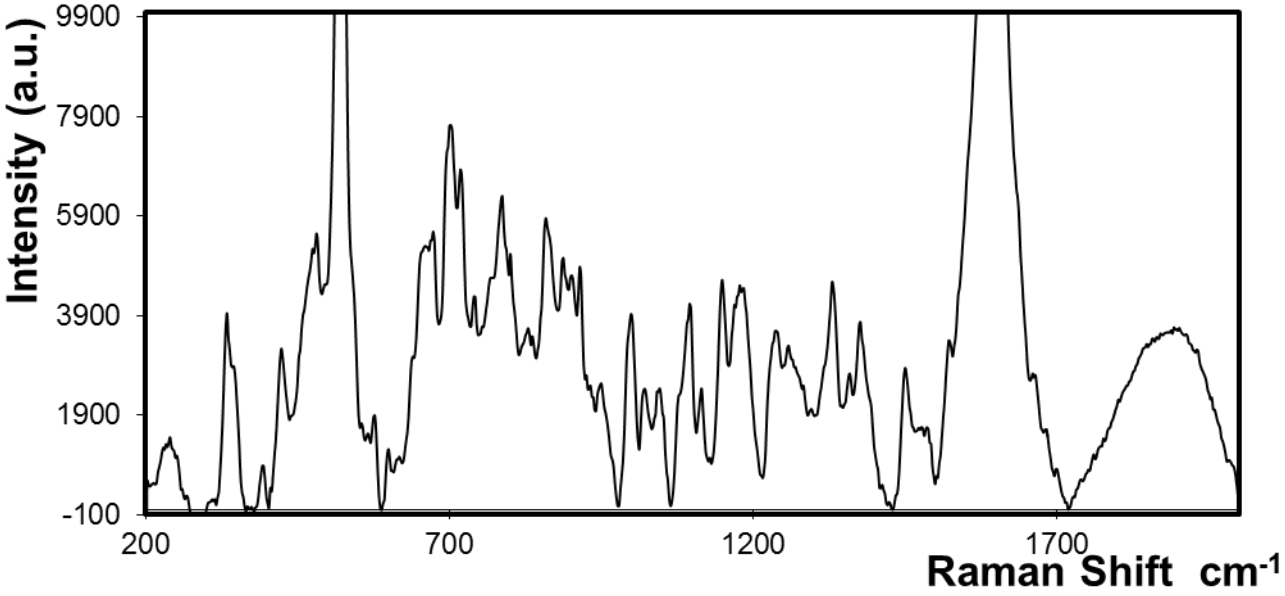
Intensity (a.u.)
9900
7900
5900
3900
1900
-100
200
700
1200
1700
Raman Shift cm-1

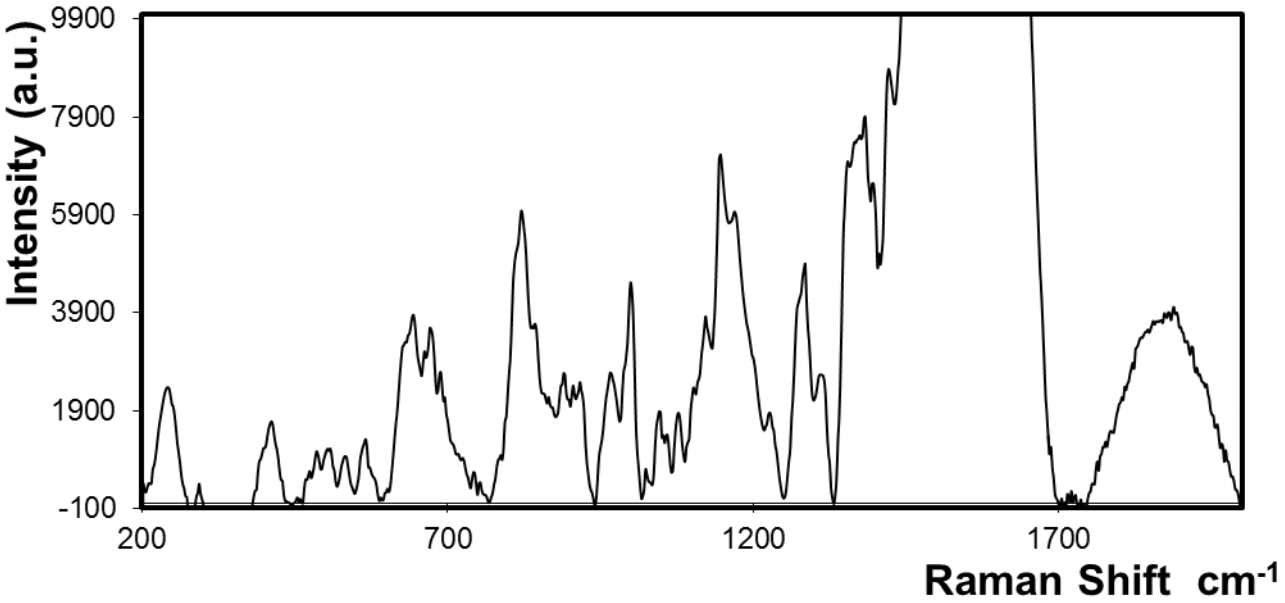
Intensity (a.u.)
9900
7900
5900
3900
1900
-100
200
700
1200
1700
Raman Shift cm-1

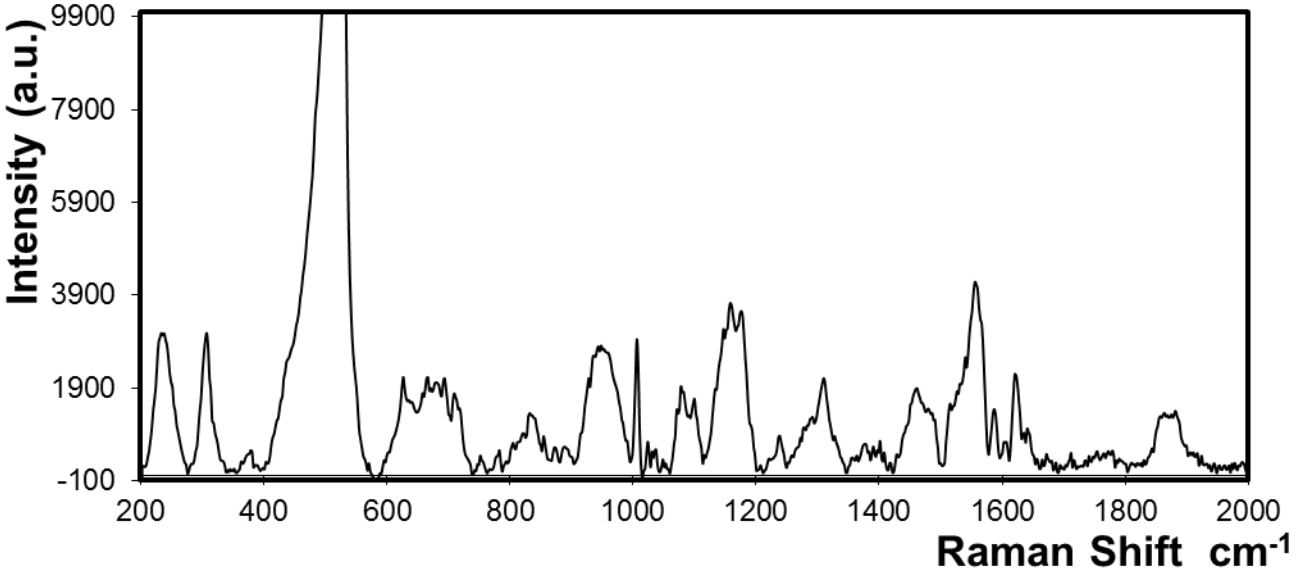
Intensity (a.u.)
9900
7900
5900
3900
1900
-100
200
400
600
800
1000
1200
1400
1600
1800
2000
Raman Shift cm-1

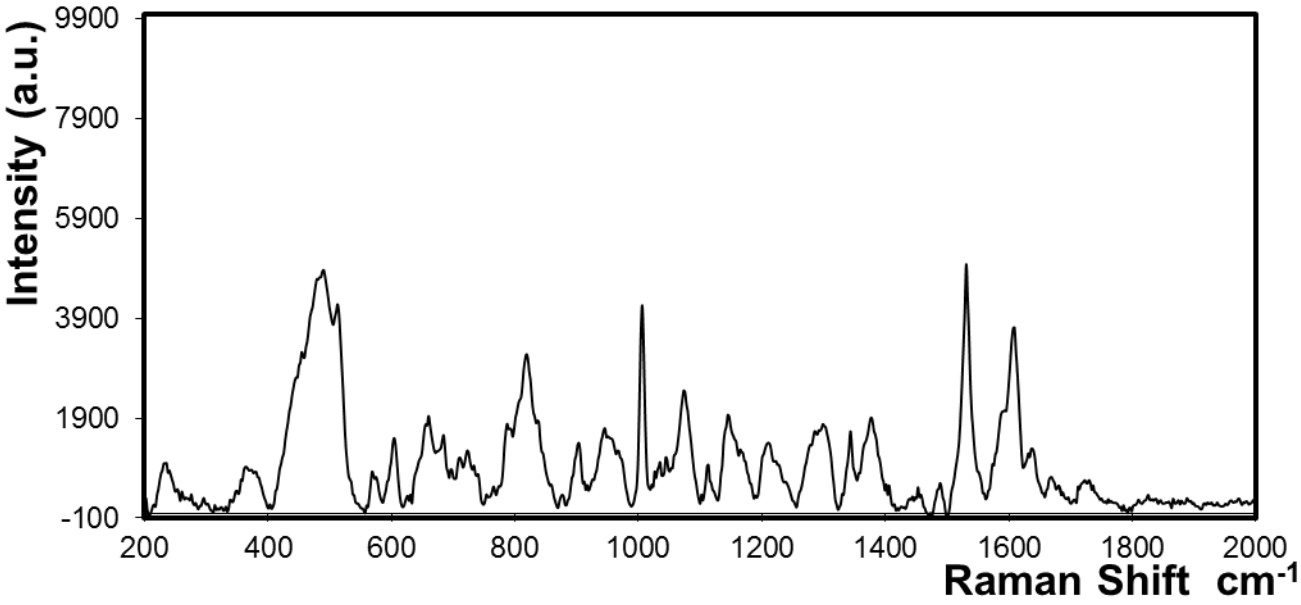
Intensity (a.u.)
9900
7900
5900
3900
1900
-100
200
400
600
800
1000
1200
1400
1600
1800
2000
Raman Shift cm-1

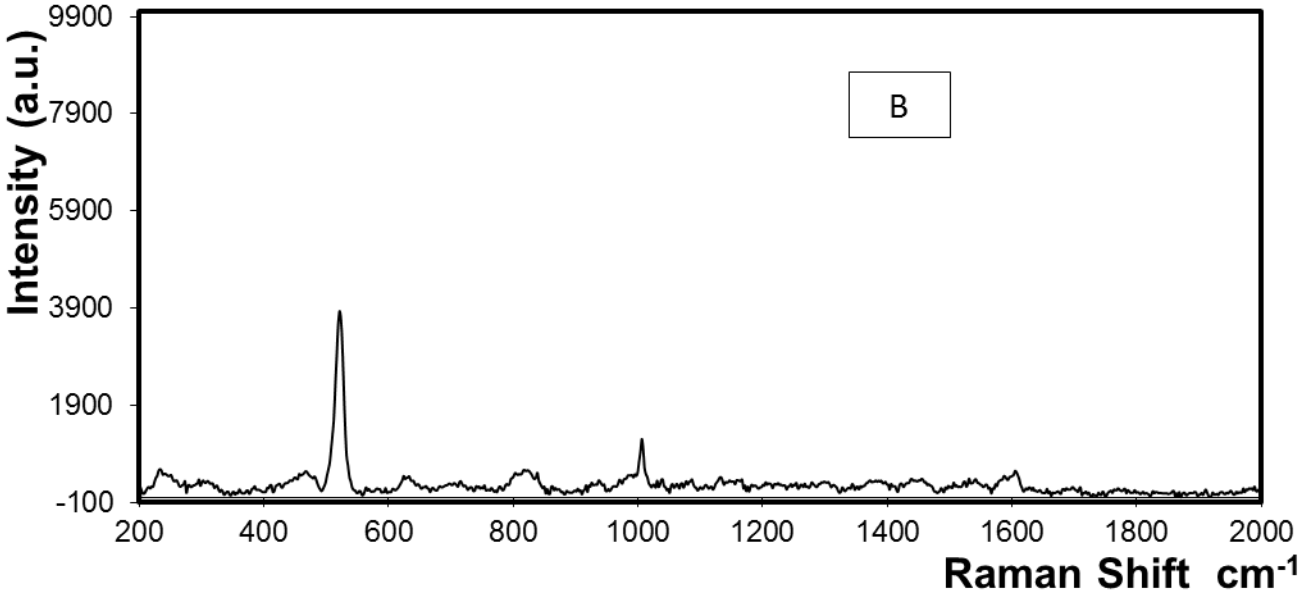
B
Intensity (a.u.)
9900
7900
5900
3900
1900
-100
200
400
600
800
1000
1200
1400
1600
1800
2000
Raman Shift cm-1

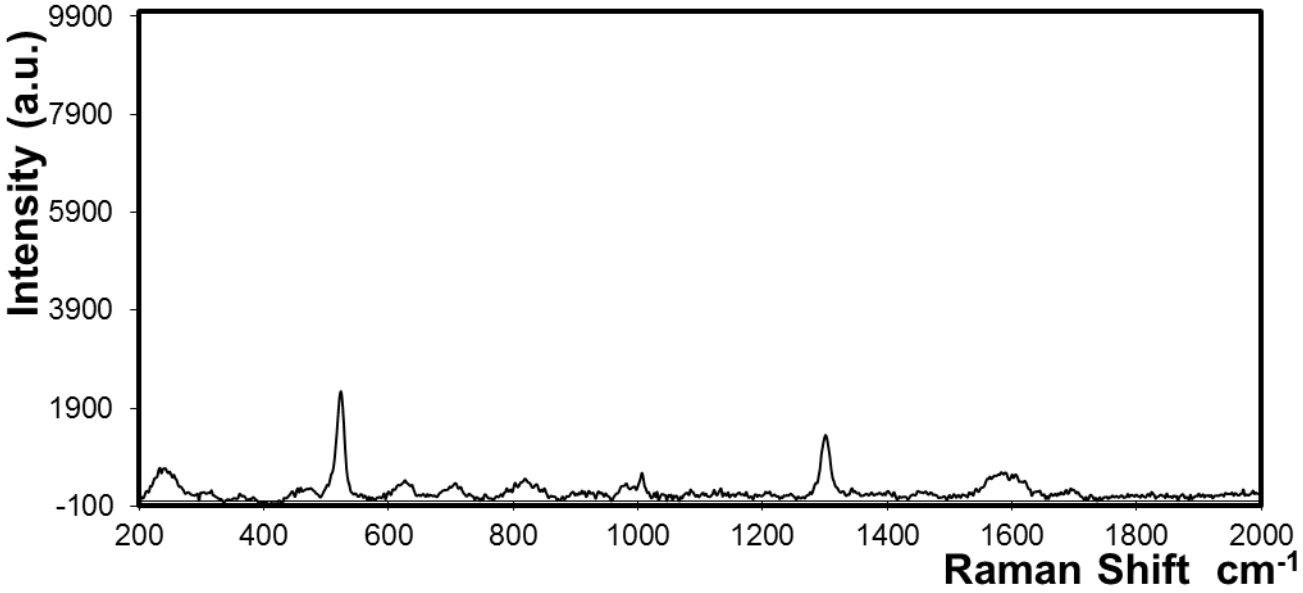
Intensity (a.u.)
9900
7900
5900
3900
1900
-100
200
400
600
800
1000
1200
1400
1600
1800
2000
Raman Shift cm-1

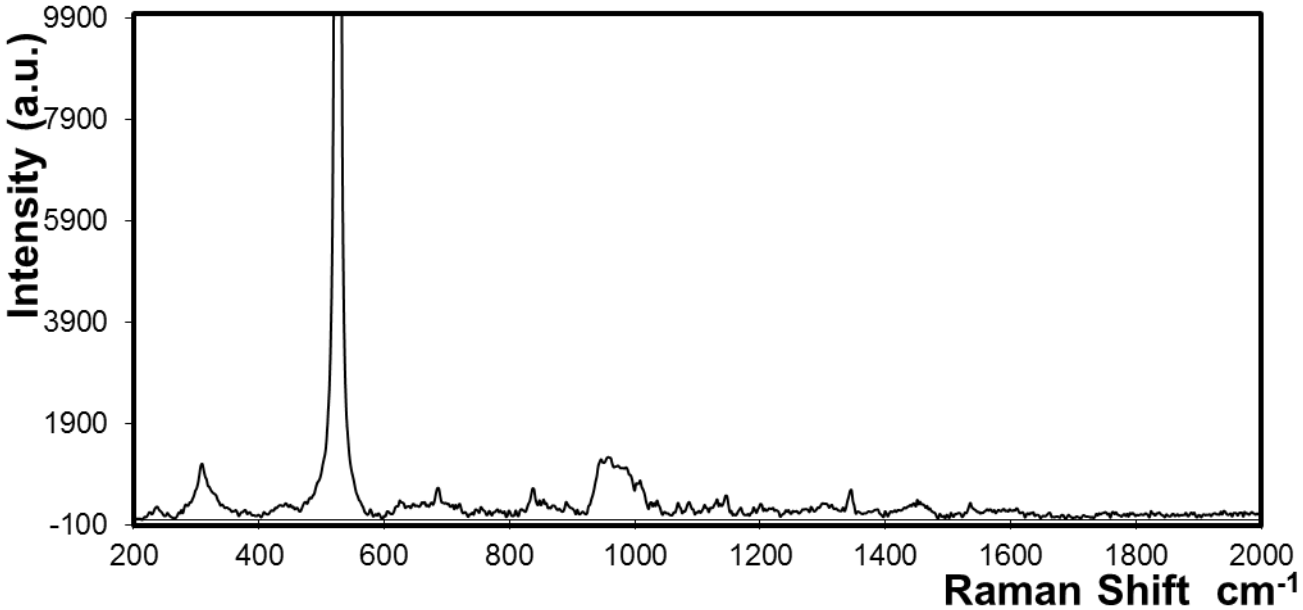
Intensity (a.u.)
9900
7900
5900
3900
1900
-100
200
400
600
800
1000
1200
1400
1600
1800
2000
Raman Shift cm-1

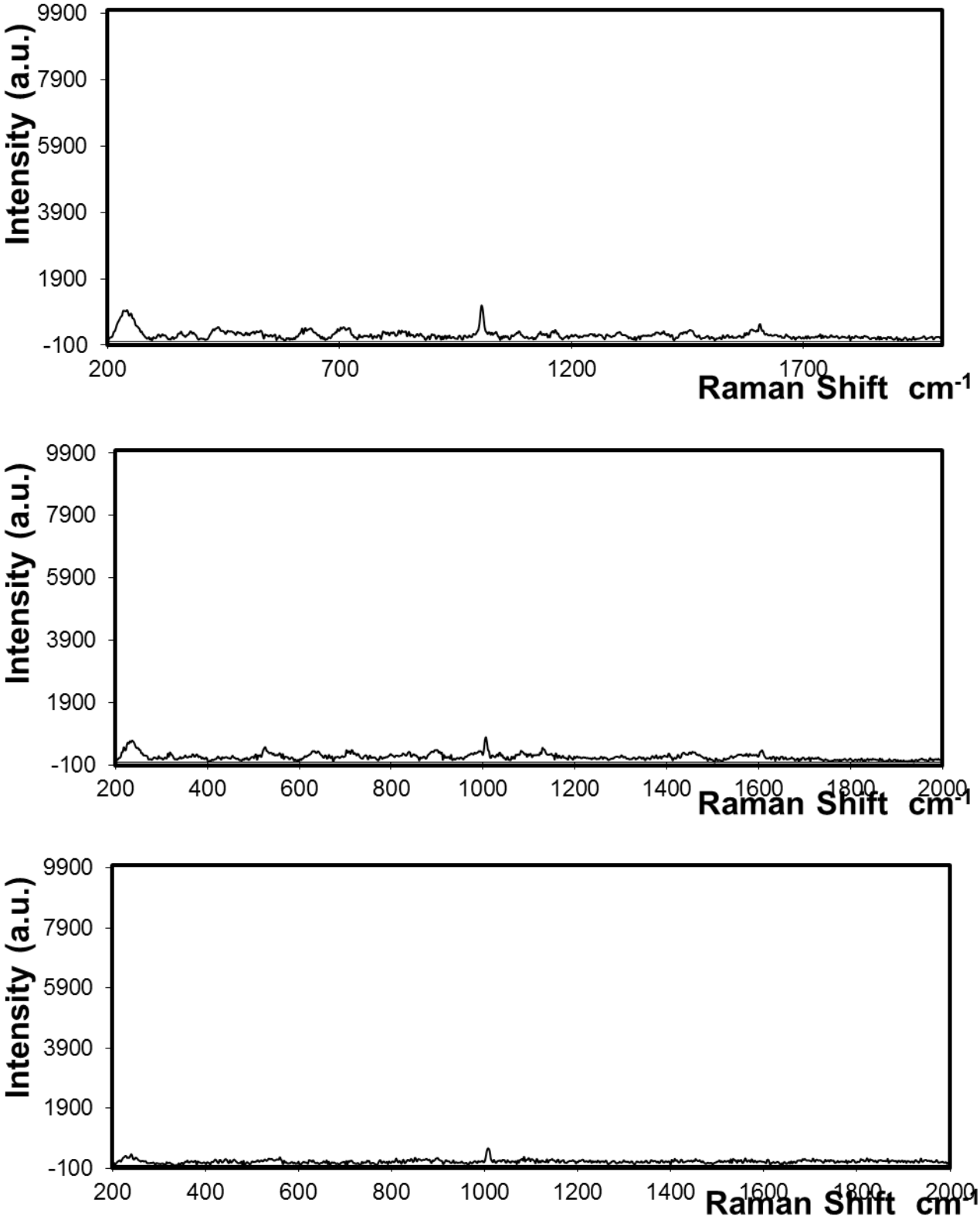


*Figure 2.29: Raman spectra recorded for DNA mediated immobilized particles within 5 µm gold micro cavities array. Group (A) represents platinum particles, Group (B) represents silver coated platinum particles. The excitation wavelength was 632 nm.*

Significantly, the spectrum obtained for both particle types was significantly different in different cavities, i.e., the inter-cavity reproducibility is not good . This behaviour most likely arises because the enhancement factor depends on the number of particles and their position inside the cavity, the incidence angle of the laser beam, particle size and silver composition. For example, some cavities were void of particles. 41% of the sites on the silver coated platinum particles showed significantly enhanced complex spectra compared to 10% in case of platinum particles, which showed weaker peaks, and less enhancement. It is not practical to determine the enhancement factor due to the uncertainty of number of particles, surface coverage and distribution of cavities and irregularity of the surface.

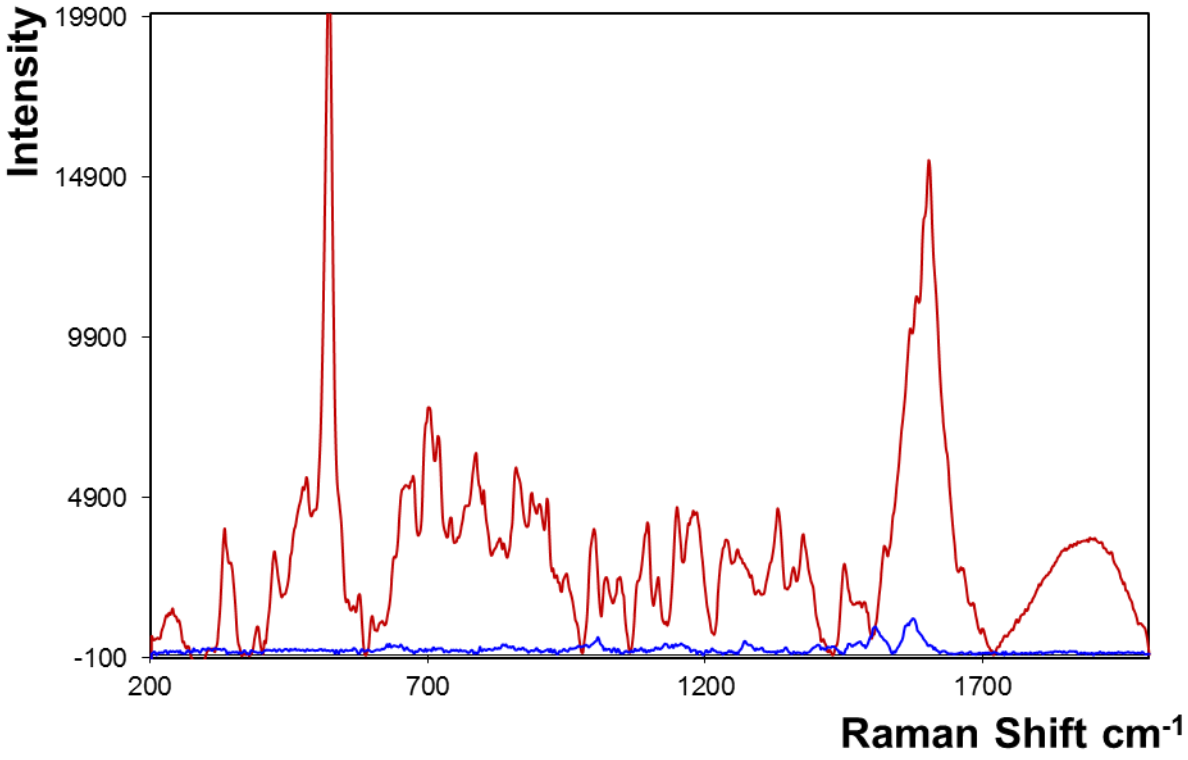


*Figure 2.30: Raman spectrum recorded for DNA mediated immobilized particles on 5 µm gold micro cavities array. Blue represents platinum particles. Red represents silver-coated platinum particles. Excitation wavelength was 632 nm.*

In Figure 2.30 two spectra showing similar peaks from the silver coated platinum and platinum particles are shown. DNA related band can be seen at 678, (ring breathing mode G) 790, (C and T ring breathing modes), 910, 1030,(N-sugar str) 1340 (A) and 1581 $cm^{-1}$.

It can be concluded from this section that the silver coat on platinum particles could show considerable enhancement for Raman scattering when compared with platinum when immobilized inside gold micro-cavity array but the magnitude of the effect cannot be quantified.

## 2.10 Conclusion

A method for producing platinum nanoparticles, that are functionalised on one side with silver, which is then functionalised with probe strand DNA oligonucleotides, has been developed. The prepared particles had diameters of 220 nm ± 30. The nanoparticles can electrocatalytically reduce hydrogen peroxide generating a significant amperometric signal in a DNA sandwich assay that allows low concentrations of target DNA to be measured quantitatively. Moreover, by performing the sandwich assay within a gold microcavity array (nanoparticle in microcavity architecture) the possibility of generating Surface Enhanced Raman Spectroscopy exists.

The target DNA belongs to Staphylococcus aureus mastitis one of the causative bacteria for udder infection in cattle, it is a 41 base oligonucleotide, The dynamic range used was between 1 aM and 100 nM. And limit of detection of $1.5 \times 10^{-13}$ M was reached.

# Chapter 3

# Molecular Modelling of Conducting DNA Analogues

"What is real? How do you define real? If you're talking about what you can feel, smell, taste and see, then ‘real’ is simply electrical signals interpreted by your brain. The world as you know exists now only as part of a neural interactive simulation, that we call the Matrix" *Morpheus, The Matrix.*

# 3 Chapter 3

## 3.1 Introduction

### 3.1.1 Conductinge Nucleic Acid

The electric conductivity of DNA has been studied extensively since it has profound implications for signaling and DNA repair in living cells[64], as well as its uses in nanoscale circuits and devices[65]. Some photophysical investigations, especially those of Barton, have suggested that under particular conditions DNA may be able to support long range electron transfer through the π-stacked nucleotides[66]. However, in the context of electrochemical measurements, DNA does not typically support fast rates of electron transfer over long sequences. This can have significant implications for detection, e.g., in nucleic acid sandwich assays involving long target sequences, >100 bases, the rate of electron transfer to a redox active label may influence the current observed thus decreasing sensitivity.

One way to enhance the conductivity[67] is to synthesise an artificial analogue of DNA that replaces the phosphate deoxyribose backbone with an electronically conducting polymer backbone. This conducting backbone could then shuttle electrons to/from the bases so as to, increase the current response and improve the sensitivity of nucleic acid based electrochemical biosensors. This chapter reports on molecular modelling of the proposed conducting DNA structures as well as their ability to bind their complementary target.

## 3.2 Experimental

### 3.2.1 Computational methods

The design of the electronically conducting DNA analogues has been informed by modelling of the proposed structures using HyperChem before attempting their synthesis. In this way, insights can be obtained on issues such as their ability to hybridise with a target and the strength of that interaction before effort is invested in synthesis. Before modelling new conducting structure, the modelling system was validated using known, naturally occurring sequences and the resulting calculated thermodynamic values compared with those found from experiment. The computation modelling is important as it gives a prediction as to which electronically conducting structure is the most promising in terms of the sensitivity and selectively that might be achieved.

### 3.2.2 Structure building

HyperChem™ Release 8.0.9 for windows was used to model the nucleic acid structures and their hybridisation. Hyperchem contains pre-designed molecular databases for polymers including saccharides and oligonucleotides. As shown in Figure 3.1, single strands of both target, probe and capture oligonucleotides were built using this database and the specific sequence of interest built up base by base from dA, Adenosine (A), dG guanine (g), dC for cytosine (C) and dT Thymidine (T)

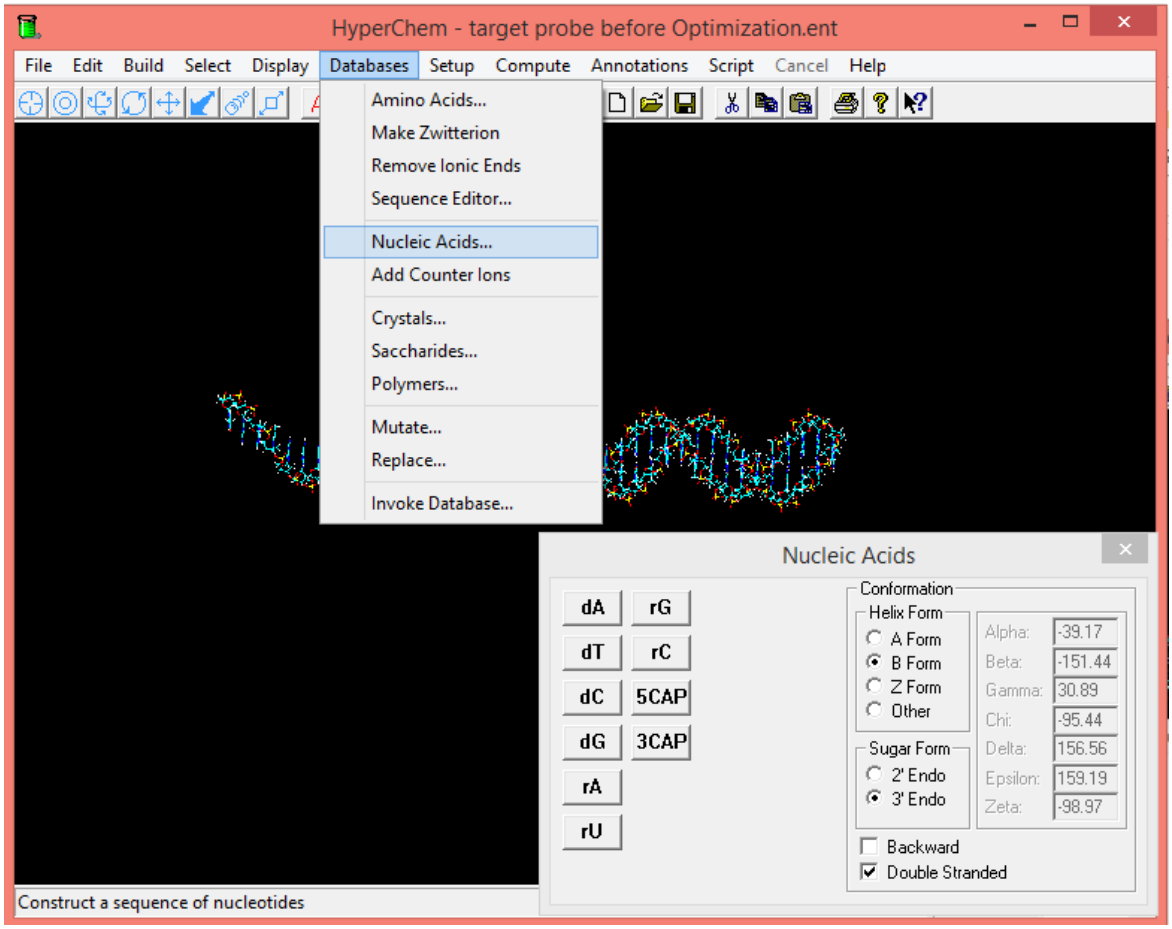


*Figure 3.1 Molecules building using Nucleic Acids database in HyperChem*

In the nucleic acid window, different helix forms are available, namely, the A, B and Z form. The B form is the most prevalent in biological systems while the A form is more common in dried samples and methylated DNA. Form B was chosen as it is the most closely related to the experimental conditions used in this work as the buffer used is at the physiological pH. There are other types of RNA nucleotides.

The three oligonucleotides involved in the Staph aureus mastitis sandwich assay, i.e., DNA target and the complementary capture and probe strands were modelled as shown in Figure 2.26 using the following sequences:

Capture: 5'- CGG-CAG-TGT-TTA-TCA -3'

Target: 5'-TGA-TAA-ACA-CTG-CCG-TTT-GAA-GTC-TGT-TTA-GAA-GAA-ACT-TA-3'

Probe: 5’- TA-AGT-TTC-TTC-TAA-ACA-GAC- -3’

The three structures were brought together and aligned to form the natural B DNA helix conformation between the target sequence, capture and probe strands as shown in Figure 3.2. To confirm the proper alignment, the inter molecular hydrogen bonds between the strands can be calculated, and the presence of three H bonds for GC pairs and two H bonds for AT pairs, confirmed as shown in Figure 3.3.

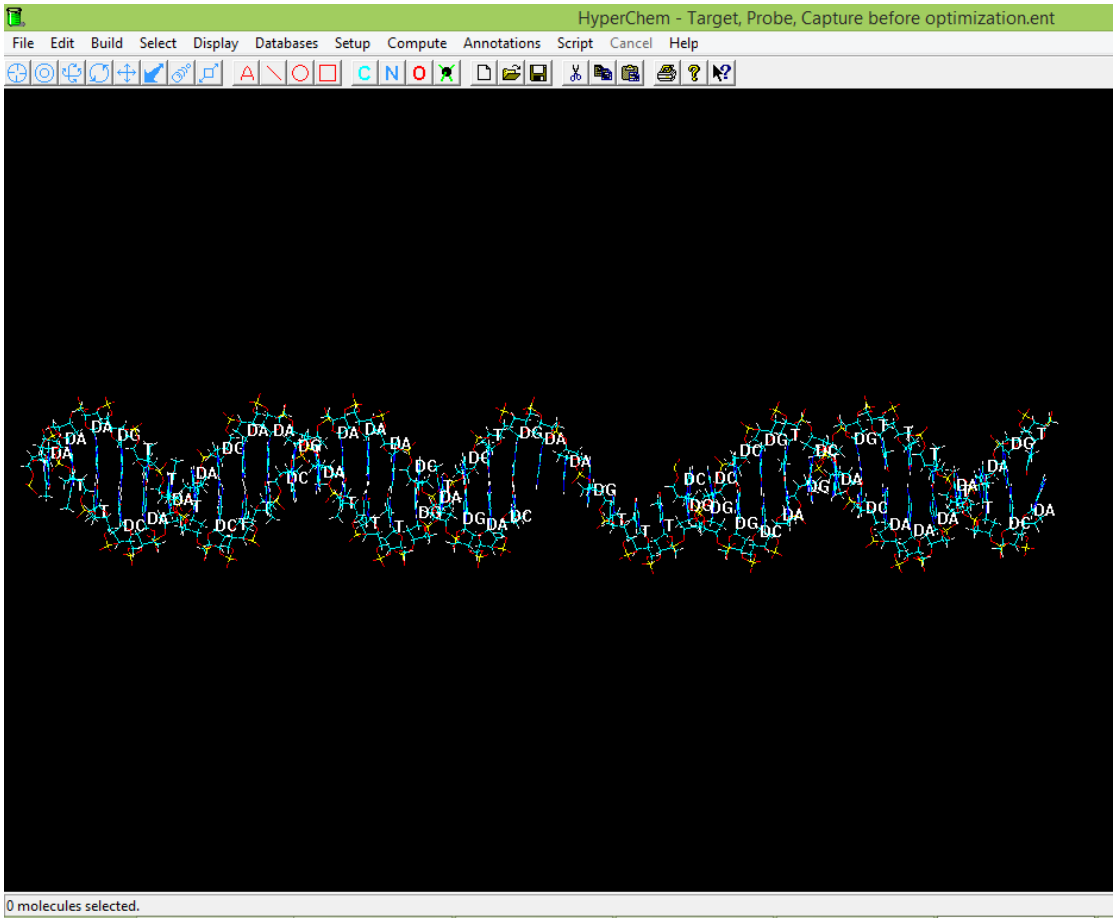


*Figure 3.2 Target strand hybridized with both capture and probe strands.*

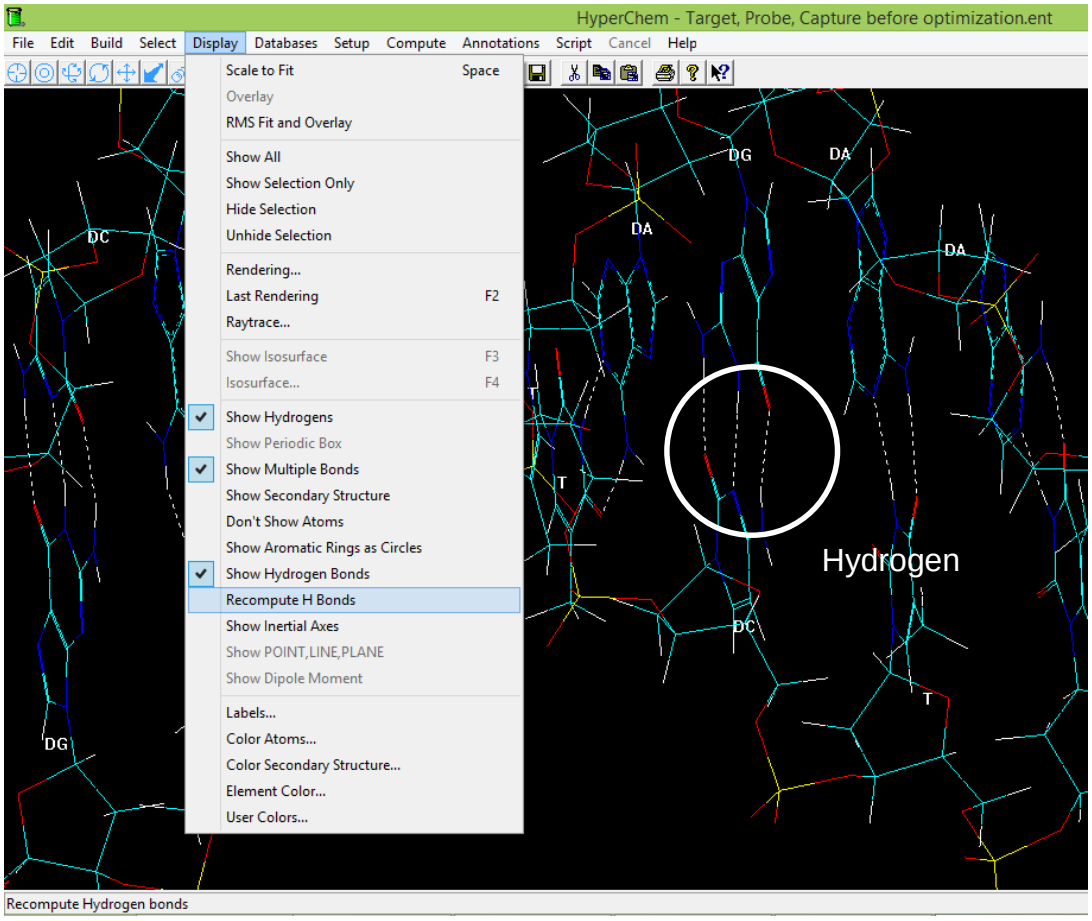


*Figure 3.3 Hybridized structures showing the computed inter-molecular hydrogen bonds.*

### 3.2.3 Geometry optimisation.

AMBER is the molecular mechanics force field method that is optimised for proteins and nucleic acids.

The Polak-Ribiere optimization algorithm was chosen and the total energy gradient is calculated as a root mean square value. The gradient (G) is the rate of change (first derivative) of total energy (E) with respect to displacement of each atom in the x, y, and z directions. The units are Kcalmol$^{-1}$. HyperChem reports this value as the geometry optimization is being optimised and for single point calculations. An RMS gradient of zero means the structure is at a local minimum or saddle point in the potential energy surface, not necessarily at the lowest energy (global minimum). It was chosen

in this work to be 0.01 Kcal $mol^{-1}$ which ensures a well optimised structure while minimising the calculation time.

### 3.2.4 Root-mean-square deviation of atomic positions, RMSD.

RMSD is an important tool to compare the match of structure between two molecules in terms of atomic position in Cartesian coordinates. During that calculation two molecules of identical *chemical* structure (number and type of atoms constituting the molecule) are superimposed on each other and the root mean square deviation of position of all of the atoms in the three dimensional space in Angstrom is calculated and summed.

### 3.2.5 Calculation of binding energy

One of the main goals of this chapter is to determine the binding energy of the different proposed conducting DNA analogues. The binding energy is related to the association constant and is considered to be a key value in determining whether the synthetic analogue can hybridise and how stable that duplex will be. After building and optimizing the fully bound structure using Hyperchem, the global energy of the system is calculated and then the two strands are separated and another step of geometry optimization is carried out. After the optimization, the global energy is calculated again and the binding energy is calculated as the difference between the energies of the free and the bound structures as shown in Figure 3.4

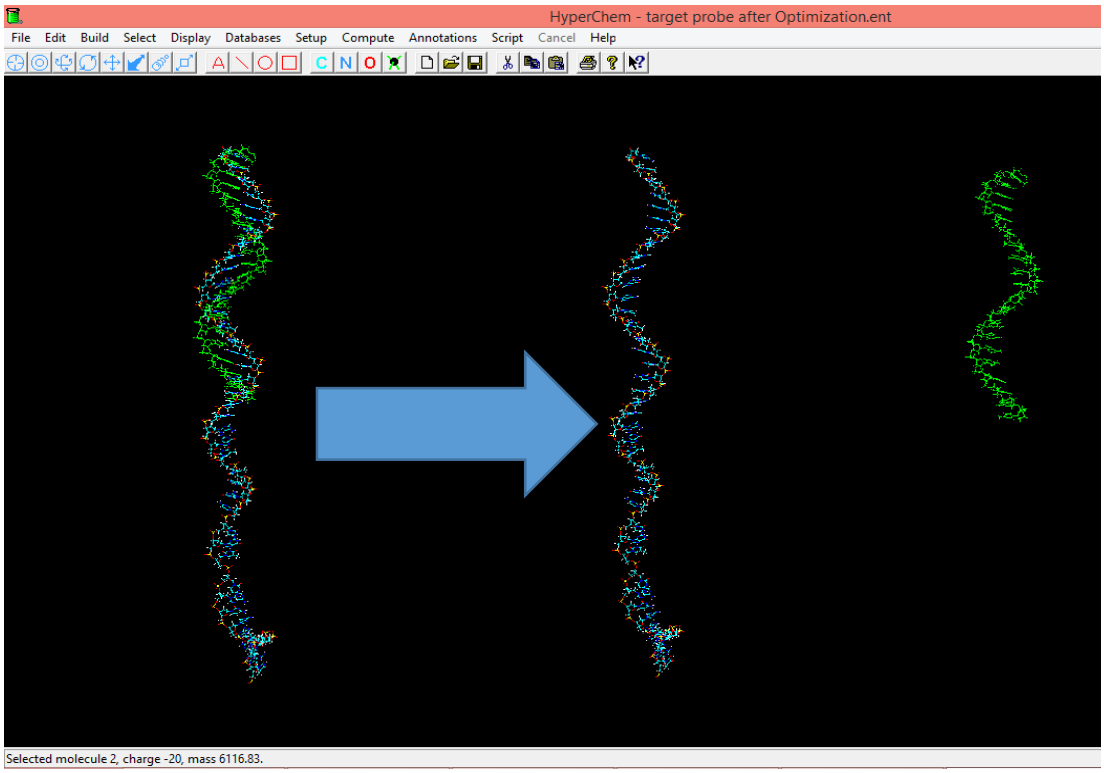


*Figure 3.4 Target strand bound to probe strand on the left, on the right the two separated strands.*

## 3.3 Validation of structure building and optimization.

In order to validate the performance of the Hyperchem structure building and optimisation using the AMBER method, previously reported and measured structures were downloaded from the Protein Data Bank (PDB) and compared to modelled structures. Energy minimization of the modelled structures was carried out both in vacuum and water as a solvent in a boundary condition “periodic box”. The evaluation of the similarity between the measured and the calculated structures is carried out using the RMSD fitting.

### 3.3.1 Two base pair mismatch DNA measured by solution NMR.

The first model was used to investigate the ability of Hyperchem to model base mismatches in the nucleic acid structure. The downloaded file “PDB ID: 2MJX”, Published by Anirban Ghosh *et al*.[144] contains 8 different measured structures. The calculated RMSD between those experimentally determined structures was found to be 3.069 Å in average. Which can be a suitable cut off reference value for RSMD

Also the structures were determined using solution NMR.

The sequence is as follows:

5'-GCGCAT**GC**TACGCG-3’

3'-CGCGTA**GC**ATGCGC -5'

The RMSD between the measured and calculated structures by solvated and non-solvated optimization methods is summarized in Table 3.

| | Solvated “Periodic box” RMSD /Å | Non Solvated RMSD /Å |
|---|---|---|
| Trial 1 | 4.866 | 4.777219 |
| Trial 2 | 5.30829 | 5.167749 |
| Trial 3 | 4.813851 | 4.901624 |
| Trial 4 | 4.967117 | 4.87682 |
| Average | 4.9888145 | 4.930853 |

*Table 3 RMSD between experimentally measured and calculated structures for solvated and non-solvated structures.*

The RMSD between the calculated structures using the two methods and the measured structure were higher than that of the RMSD between measured structures. However the difference is insignificant between the two calculate structures. Taking into account the considerable difference in

computational time, the optimization of structures was carried out in vacuum using the following modelling steps.

### 3.3.2 Fully complementary structure measured by high resolution crystallography

The second structure chosen was published by Wei *et al*.[145] with high resolution crystal structure PDB ID: 3U2N, which is different from the previous solution phase NMR method. The sequence is

CGCGAATTCGCG

GCGCTTAAGCGC

The energy minimization and RMSD fitting was carried out as described above. The modelled structures are shown in Figure 3.5 and Figure 3.6.

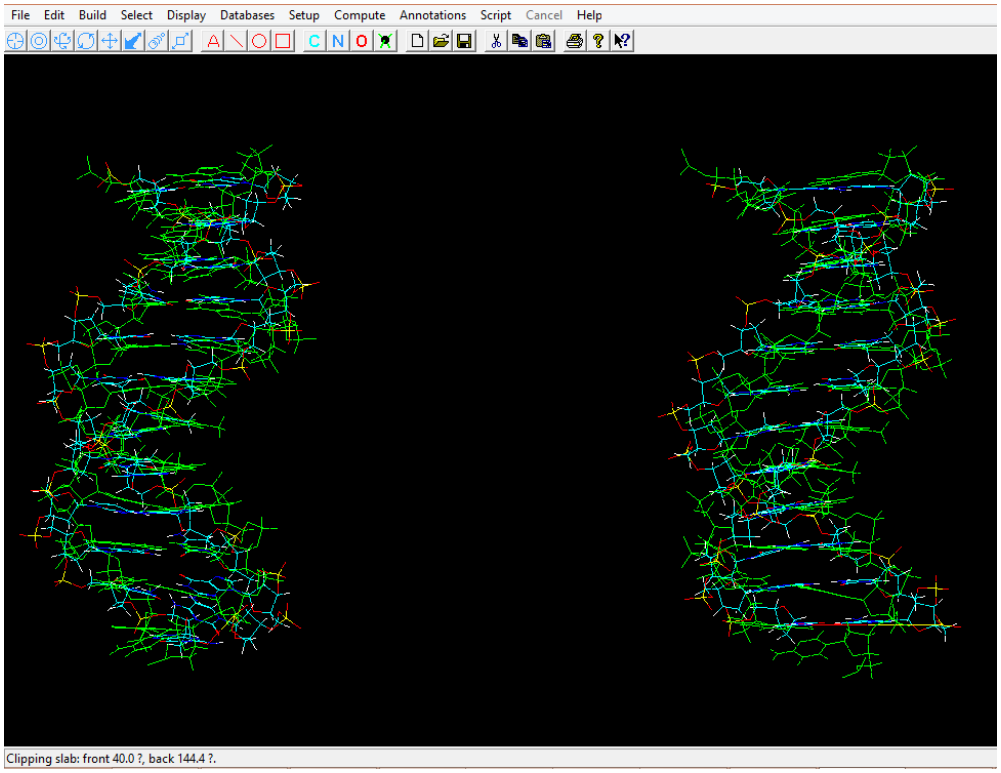


*Figure 3.5 RMSD fitting between calculated structures and measured structures.*

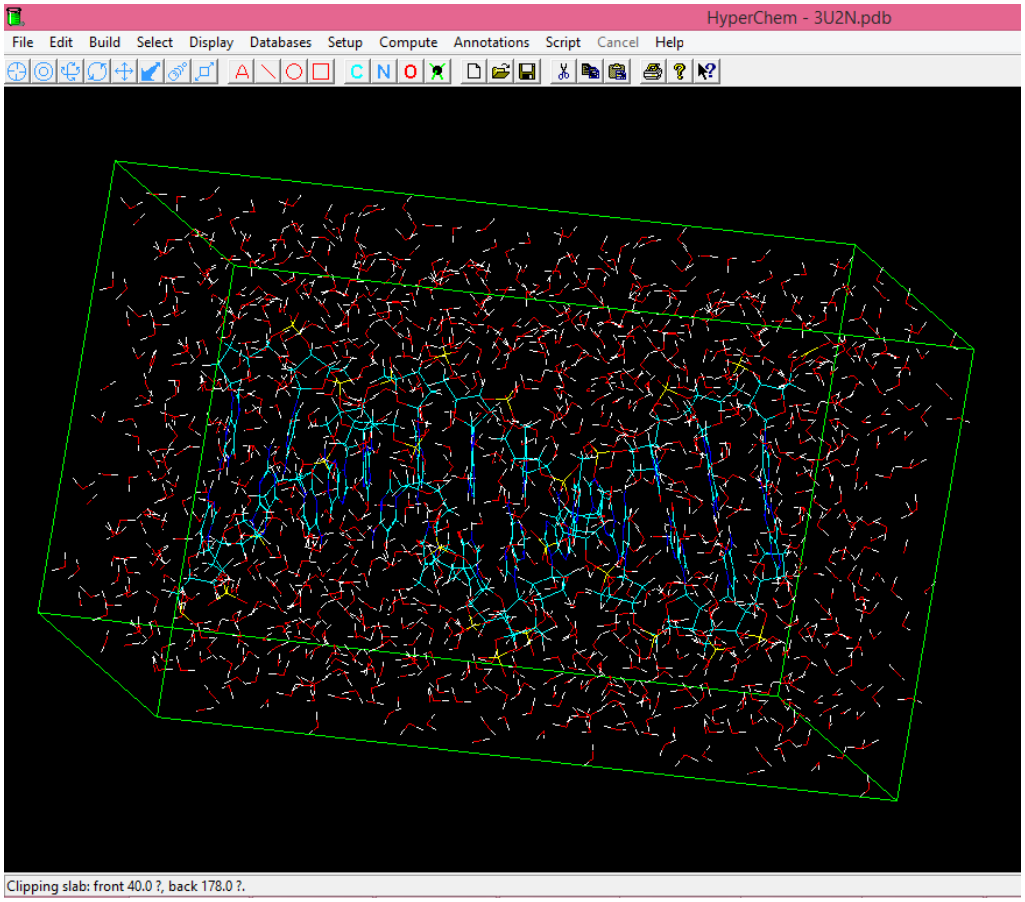


*Figure 3.6 Calculated structure optimized in water periodic box.*

In Table 4, the RMSD fitting compared between the structural similarity of measured structure and the calculated structure using vacuum and water periodic box as seen in Figure 3.6. The difference between the two values was approximately 0.5 Å. Which confirms the insignificance of the difference between the two methods in this application.

| RMSD /Å | Solvated “periodic box” Å | None solvated “Vacuum” Å |
|---|---|---|
| Trial 1 | 4.945549 | 5.503091 |
| Trial 2 | 4.856754 | 5.456743 |
| Trial 3 | 4.974343 | 5.348547 |
| Average | 4.925549 | 5.436127 |

*Table 4 Comparison of RMSD for calculated structures using either a water periodic box or vacuum, and the experimentally determined structure downloaded from PDB.*

### 3.3.3 Staph mastitis DNA modelling and validation of binding energy.

To validate the accuracy of the binding energy calculations, the results of the Hyperchem binding energy calculations (based on difference in energy between single strands and duplex forms), to the results obtained from an empirical binding energy, ΔG, calculator available at Integrated DNA Technologies’ website Oligo analyser found at https://eu.idtdna.com/calc/analyzer

The oligo analyser calculator adds the standard energies of base pairs present in the sequence and produces an overall ΔG value for each specific sequence.

As described in Section 3.2.5, the binding energies of fully complementary target strand DNA with both capture and probe strands were calculated. Also the one base pair mismatch and three base pair mismatches binding energies were calculated.

As shown in Table 5, the average energy differences between bound and free forms were calculated, and these are compared to the ΔG calculations obtained from the Oligo analyser in Table 6. These tables show that there is

a strong correlation with the maximum difference between the values obtained by the two calculation methods being 6 kcal/mol.

| ΔG in kcal/mol | Capture | | | Probe | | |
|---|---|---|---|---|---|---|
| | Bound | Separate | Difference | Bound | Separate | Difference |
| Target | -1817.72 | -1783.9 | -33.82 | -1874.5 | -1838.56 | -35.94 |
| 1 base mismatch | -1802.23 | -1778.05 | -24.18 | -1858.51 | -1844.54 | -13.97 |
| 3 base mismatch | -1782.77 | -1757.16 | -25.61 | -1882.5 | -1866.35 | -16.15 |

*Table 5 Energies of bound and separate structures and difference in energies in kcal/mol.*

| ΔG in kcal/mol | capture | | | probe | | |
|---|---|---|---|---|---|---|
| | Oligo Analyser | Hyperchem | Difference | Oligo Analyser | Hyperchem | Difference |
| Normal Target | -27.74 | -33.82 | 6.08 | -30.69 | -35.94 | 5.25 |
| 1 base mismatch | -22.86 | -24.18 | 1.32 | -14.85 | -13.97 | -0.88 |
| 3 base mismatch | -22.86 | -25.61 | 2.75 | -15.83 | -16.15 | 0.32 |

*Table 6 Average binding energies calculated using Hyperchem compared to ΔG values calculated using oligo analyser tool at https://eu.idtdna.com/calc/analyzer.*

### 3.3.4 Experimental determination of solution phase association constant.

To compare the previous theoretical calculations to the real world experimental values, the association constant between the target and capture strand was experimentally measured. The binding event was monitored using the DNA intercalating, luminescent, ruthenium dye [Ru $(bpy)_2(dppz)]^{2+}$ (bpy = 2,2'-bipyridine, dppz = dipyrido[ 3,2- a:2',3'-

c]phenazine). The luminescence of the dye switches on upon intercalation within DNA duplex. The structure of the Ru $(bpy)_2(dppz)$ dye is given below:

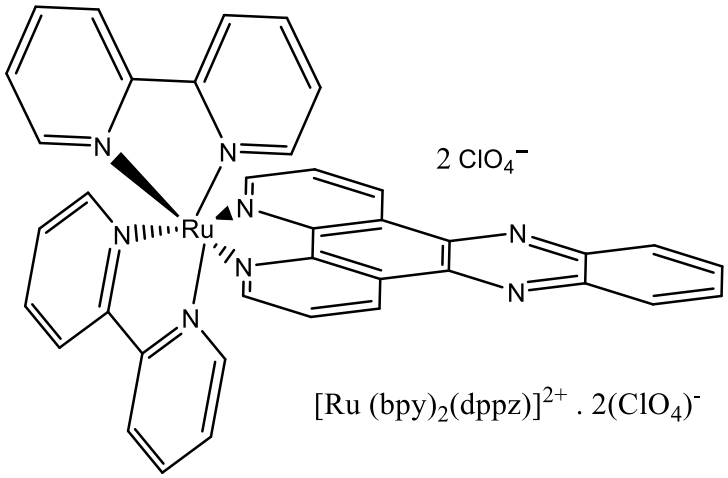


The experiment is carried out using a spectro fluorimeter and a 100 µL quartz cuvette. The excitation wavelength was at 441 nm and emission at 620 nm. The concentration of the capture strand solution was 10 µM, the target strand stock solution used was 25 µM and the $[Ru\ (bpy)_2(dppz)]^{2+}$ stock solution used was 1mM, i.e., a large excess. The experiment was carried out by transferring 50 µL of capture stock solution to the cuvette, adding 1 µL of dye stock solution and 45 µL of Tris-EDTA (TE) buffer, the final concentration of the capture strand is 5 µM and 10 µM $[Ru\ (bpy)_2(dppz)]^{2+}$ dye. The target is added as 1 µL increments of the stock solution to (which was 25 µM) increase the concentration of the target strand in the final solution by 0.25 µM upon each addition. The increase in fluorescence due to the intercalated Ru dye in the target-capture hybridized double helix is measured by recording the emission-time response as illustrated in Figure 3.7. The average intensity after attaining the equilibrium is calculated by taking the average of the values of the emission after the curve plateaus. The average is then plotted against the final target

concentration. The experiment was repeated three times as illustrated by error bars seen at Figure 3.7. The curve is then fitted using Langmuir isotherm model for reversible binding and the dissociation constant $K_d$ and association constant $K_a$ were determined. The fitting was carried out using Kaleidagraph mathematical software as seen in Figure 3.9.

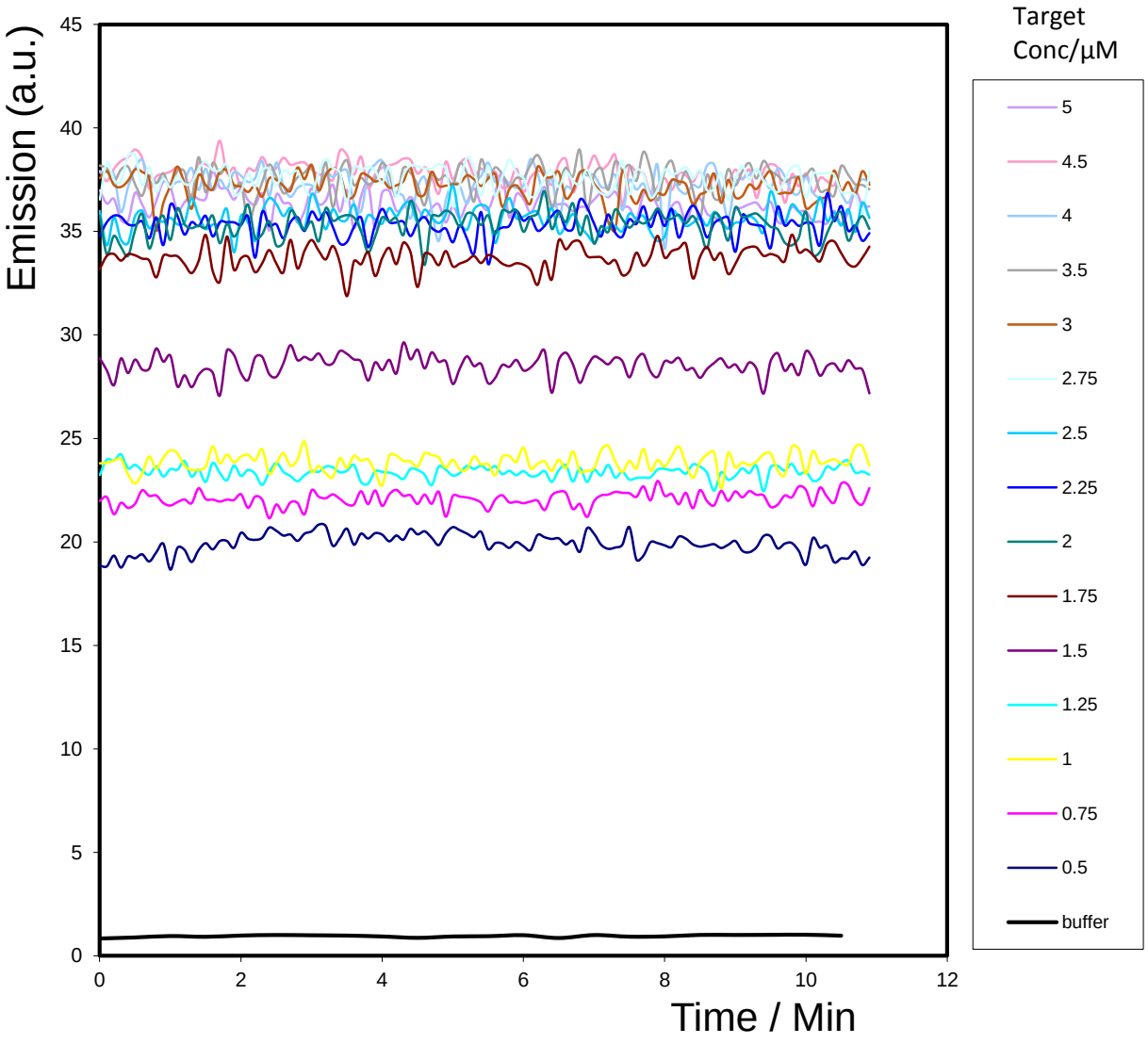


*Figure 3.7 Fluorescence time plot for addition of target strand on capture strand, the fluorescence is due to DNA intercalator Ru (bpy)$_2$(dppz) dye. The capture concentration was 5 µM and target concentration was increased by 0.25 µM upon each addition, excitation wavelength was at 441 nm and emission at 620 nm, a measurement was taken every 6 seconds for 20 min.*

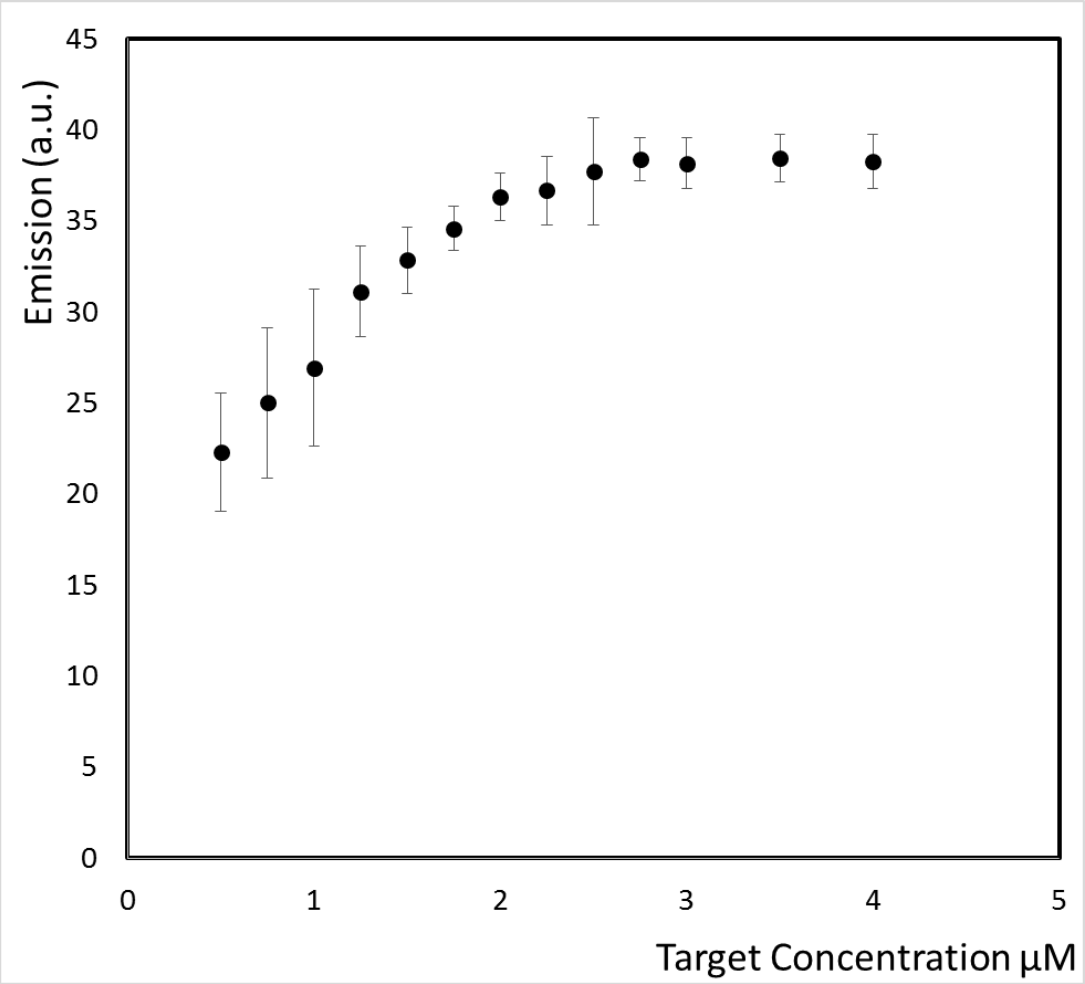


*Figure 3.8 Dependence of the emission intensity of the target concentration. Luminescent dye is the DNA intercalator Ru (bpy)$_2$(dppz). The capture concentration was 5 µM and target concentration was increased by 0.25 µM upon each addition, excitation wavelength was at 441 nm and emission at 620 nm, the average was taken to the measurements at the plateau.*

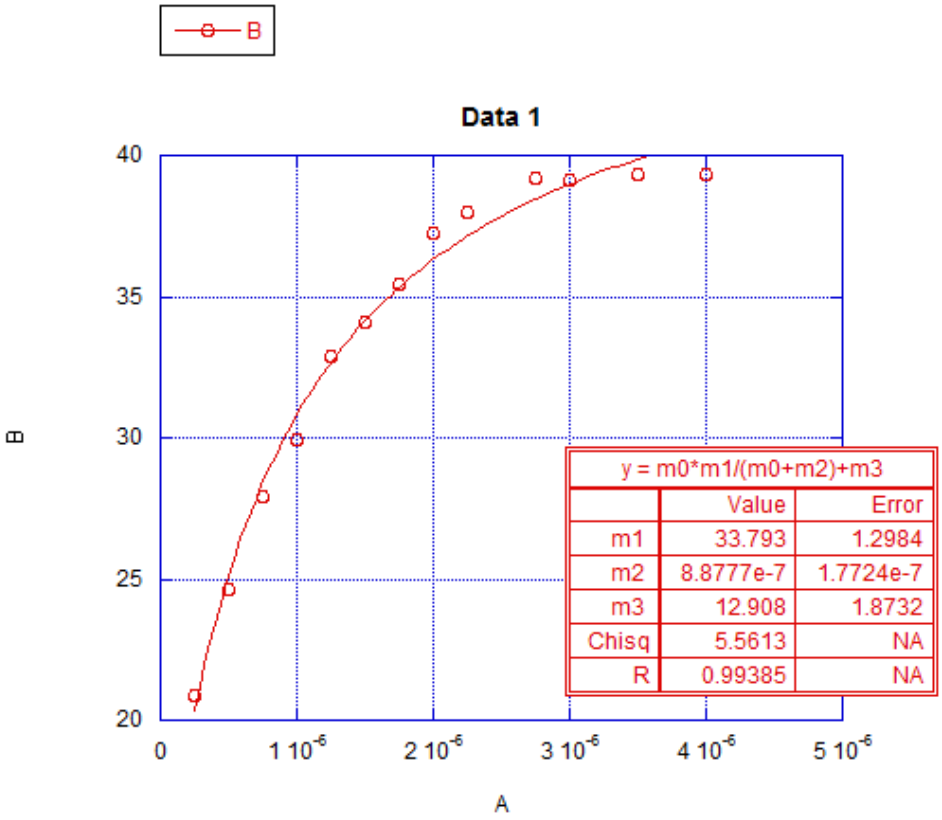


*Figure 3.9 Fitting of plot using Langmuir isotherm model, m2 is Kd. The fitting was done using Kaleidagraph mathematical software.*

The dissociation constant $K_d$ value was calculated from the fitted model to be 8.87 X $10^{-7}$, from which we can calculate the value of $K_a$, which can be used to calculate ΔG as stated in the following formula:

*Equation 8* $$\Delta G = -RT\ ln\ Ka$$

where R is the universal gas constant, T is the absolute temperature, 298° K. The value of the free energy difference, ΔG, between bound and unbound forms is 34.5 kcal/mol. The values obtained using Hyperchem and Oligoanalyzer, Section 3.3.3, were 33.8 and 27.7 kcal/mol respectively, i.e., there is reasonable agreement between the modelled and measured values for binding affinity and demonstrates the reliability of the modelling system used.

## 3.4 Design of different DNA analogues with potentially conducting backbones.

As mentioned in the introduction, the aim of this chapter is to design and test the binding efficiency of different nucleic acid analogues that have a backbone composed of a conducting polymer. The backbone is not the only part of the molecule that should be considered, since the linker that connects the nucleotide bases to the backbone can also greatly affect the binding energy and the overall configuration of the structure. The design was carried out on Hyperchem molecular modelling software following the previously discussed method in the structure building Section 3.2.2., and the binding affinity between the proposed structures and the natural DNA complementary strand was calculated following the procedures explained in 3.2.5.

An efficient way to model the different artificial nucleic acid structure was to modify a natural fully hybridized DNA double strand and replace the phosphate deoxyribose backbone of one of the strands with the proposed conducting polymer. It is theoretically possible to design two single strands and allow the program to try to reach the global minimum of energy, but that is not practically possible. The energy minimization algorithm will only look for the nearest minima to the current structure. The global minimum might need conformational changes to the structure that might not be readily attainable because it lies beyond a local minimum that the program would not efficiently identify. Therefore, the best way is to start from the nearest possible point to the fully hybridised structure and minimising the total energy from there. After identifying a minimum, the two strands are moved apart to a point where they do not interact with each other, and another energy minimization step is carried out to get the energy minimum of the free strands.

The sequence used for modelling is as follows :

CGATATCGCGATATCG

GCTATAGCGCTATAGC

The sequence was used to model the natural DNA and the conductive polymers analogues in order to compare them in terms of binding energies.

Three conducting polymers were chosen to be incorporated in the structure as a backbone. Namely, polypyrrole, polythiophene and polyaniline. The nucleotides were attached to the backbone by means of ester or amide bond which is synthetically accessible. The side chain was chosen to be either two or three atoms long as longer or shorter linkers rendered the structure unstable as discussed previously in the literature review[76]. The length of the linker can affect the degree of freedom of the nucleotides to rotate and accommodate less energetic conformations while binding to the complementary DNA strand. In this work, an amide link was chosen due to its ease of preparation and the activating nature of amino group attached to aromatic system is unlikely to adversely affect the electrochemical polymerization. The three membered linker is composed of an amide bond and a methylene group extension on the nucleotide side. This linker is the same used in peptide nucleic acid “PNA” and it is known that PNA exhibits more favourable binding properties over natural DNA[81] as discussed previously.

### 3.4.1 Native DNA sequence and building of conductive analogues

The natural DNA sequence was modelled and the energy minimized structure for the bound and separate structures was determined. As shown in Figure 3.10 the fully bound structure which represents the desired global

energy surface minimum point was used as a template for building the designed synthetic structures. The energy difference between the bound and separate structures is also used as a bench mark to compare other binding energies to the natural DNA molecule.

The building of DNA analogues is carried out by deleting the phosphate sugar backbone of the DNA, and replacing them with the monomers of the polymer as near as possible to the original position of the deleted deoxyribose sugar. The orientation is adjusted manually and the monomer is connected to the nucleotide vial the linker. The monomers are then connected to each other and energy minimization step is carried out to obtain the calculated structure and energy.

| DNA | Bound | Separate | ΔG kcal/mol |
|---|---|---|---|
| 1 | -1007 | -905 | -102 |
| 2 | -1009 | -904 | -105 |
| 3 | -1008 | -907 | -101 |
| | | **Average** | -102.667 |
| | | **SD** | 2.081666 |

*Table 7 DNA binding energy calculations. Values in kcal/mol.*

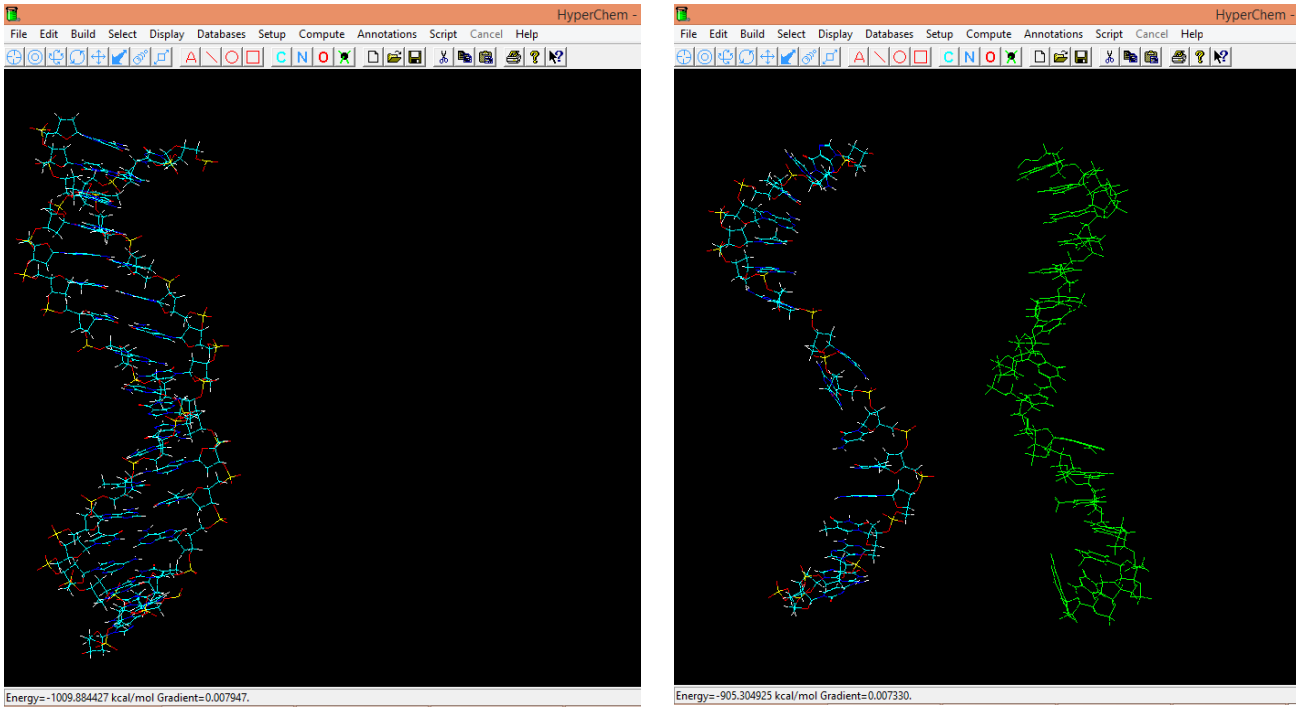


*Figure 3.10 Natural DNA sequence in bound and separate forms.*

### 3.4.2 Polythiophene based analogues

Polythiophene is composed of monomers of thiophene connected directly to one another without a connecting atom. In this synthetic analogue, there are only three atoms separating each nucleotide. This short length is expected to increase rigidity and perhaps reduce the ability of the strand to take the helical shape of DNA.

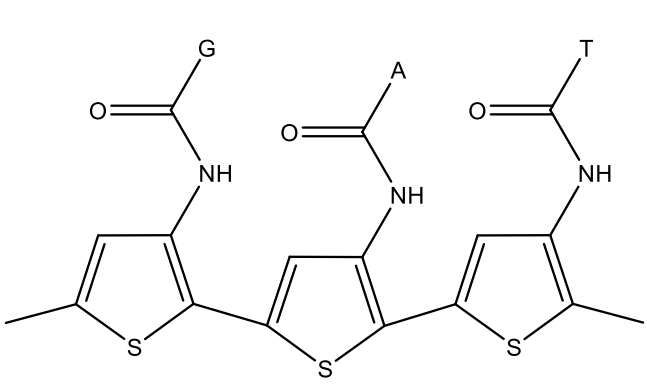


Polythiophene with two atoms long scaffold

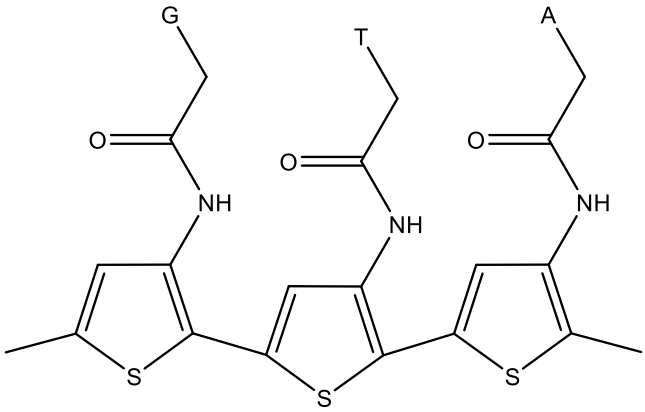


Polythiophene with three atoms long scaffold

*Figure 3.11 Chemical structure of Polythiophene-based analogues.*

Figure 3.12 shows the bound and separate structure of polythiophene analogue with complementary DNA strand, with three atoms long linker and Figure 3.13 shows the analogue with the short, two atoms, linker. As shown in Table 8, the polymer forms a poor helical structure with DNA and the binding energy is remarkably lower than the native DNA. This behaviour can be attributed to the relatively strained structure.

Generally, the analogue with three atoms long linker showed slightly greater binding energy. It was obvious from the shape of the separate strands after geometry optimization and energy minimization that the polythiophene based analogues did not fold to form any coiled structures. That is also can be attributed to the relative inflexibility of the polythiophene backbone that renders these conformations less energetically favourable.

| **Polythiophene long linker** | **Bound** | **Separate** | **ΔG kcal/mol** |
|---|---|---|---|
| 1 | -173 | -54 | -119 |
| 2 | -153 | -66 | -87 |
| 3 | -172 | -69 | -103 |
| | | Average | -103 |
| | | SD | 16 |
| **Polythiophene short linker** | **Bound** | **Separate** | **ΔG kcal/mol** |
| 1 | -98 | -5 | -93 |
| 2 | -91 | -7 | -84 |
| 3 | -102 | -11 | -91 |
| | | **Average** | -89 |
| | | **SD** | 4.7 |

*Table 8 Polythiophene-based analogues binding calculations*

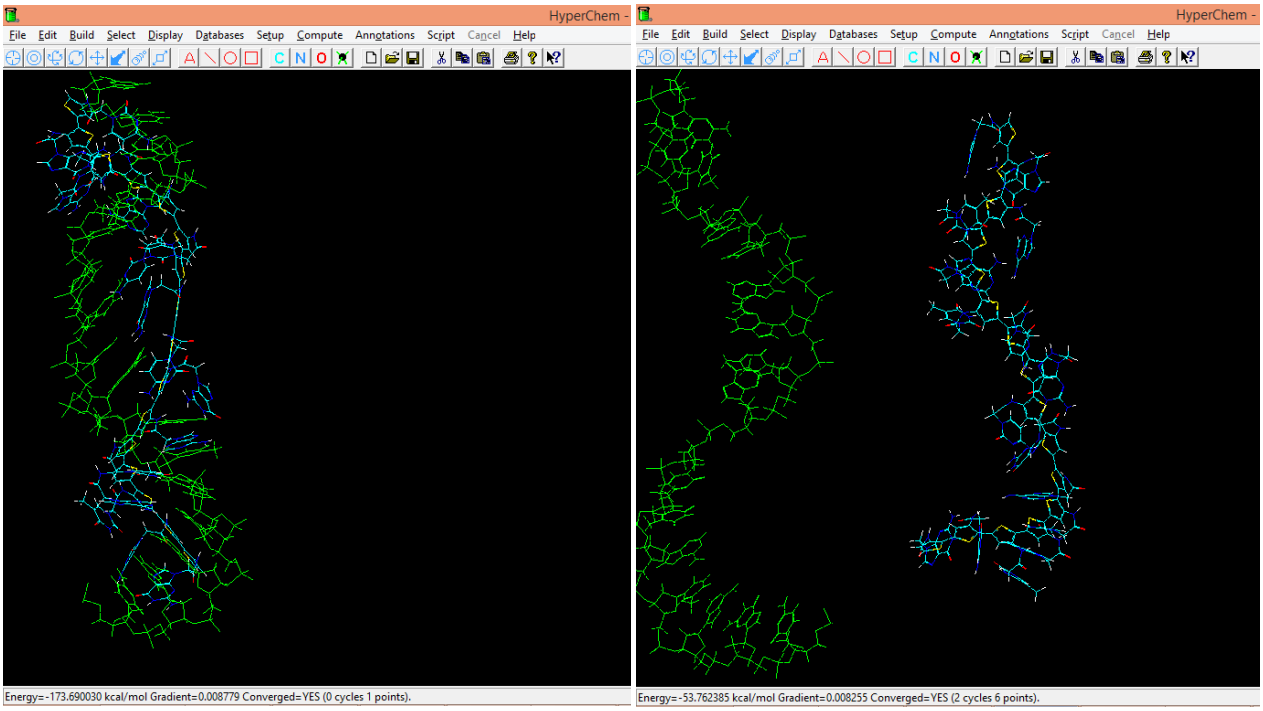


*Figure 3.12 polythiophene based analogue with three atoms linker in bound and separate forms.*

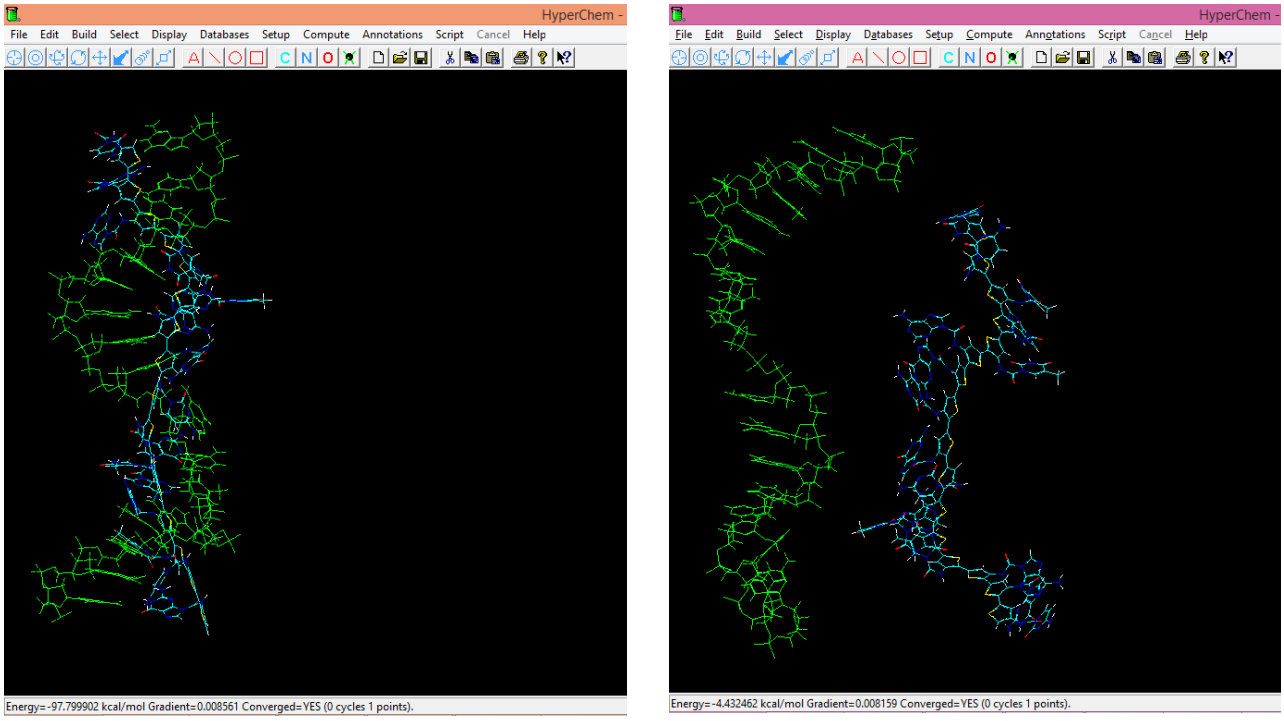


*Figure 3.13 Polythiophene based analogue with two atoms linker (short) in bound and separate forms.*

### 3.4.3 Polypyrrole based analogues

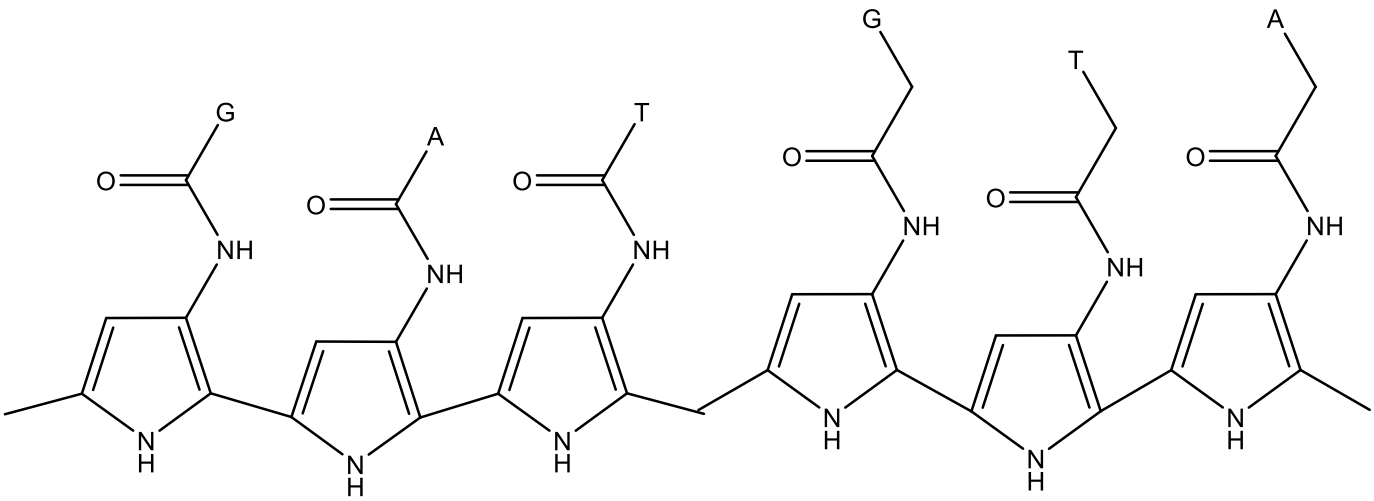


*Figure 3.14 Chemical structure of polypyrrole based polymers.*

Polypyrrole is composed of polymerized pyrrole rings. Pyrrole is a five membered ring like polythiophene and its DNA analogue structure is expected to suffer from shortness. The proposed structures are shown below with two and three atoms long linker connecting the different nucleotides to the backbone.

Figure 3.15 and Figure 3.16, the structure of polypyrrole analogue with two (referred to as short linker) and three atoms linker (referred to as long linker) respectively are shown bound to a normal DNA complementary strand and separate. It is obvious that the native B form double helix of DNA symmetry is distorted by the polypyrrole strand.

In Table 9 the calculated binding energy is shown. As found with the polythiophene analogue, the helical structure is distorted especially in the case of the short linker, again, this analogue has less binding energy than the natural DNA. This behaviour is expected because this analogue shares similar structural dimensions as polythiophene which is the smaller distance between nucleotides compared to the natural DNA.

The analogue with three atoms long linker showed more binding energy. As in the case of polythiophene, the inflexibility of the polypyrrole backbone renders the coiled conformation less energetically favourable.

| Polypyrolle long linker | Bound | Separate | ΔG kcal/mol |
|---|---|---|---|
| 1 | -206 | -45 | -161 |
| 2 | -230 | -54 | -176 |
| 3 | -217 | -66 | -151 |
| | | **Average** | -162.6 |
| | | **SD** | 12.5 |
| **Polypyrrole short linker** | **Bound** | **Separate** | **ΔG kcal/mol** |
| 1 | -105 | -19 | -86 |
| 2 | -96 | -7 | -89 |
| 3 | -85 | -11 | -74 |
| | | **Average** | -83 |
| | | **SD** | 7.937254 |

*Table 9 polypyrrole-based analogues binding calculations*

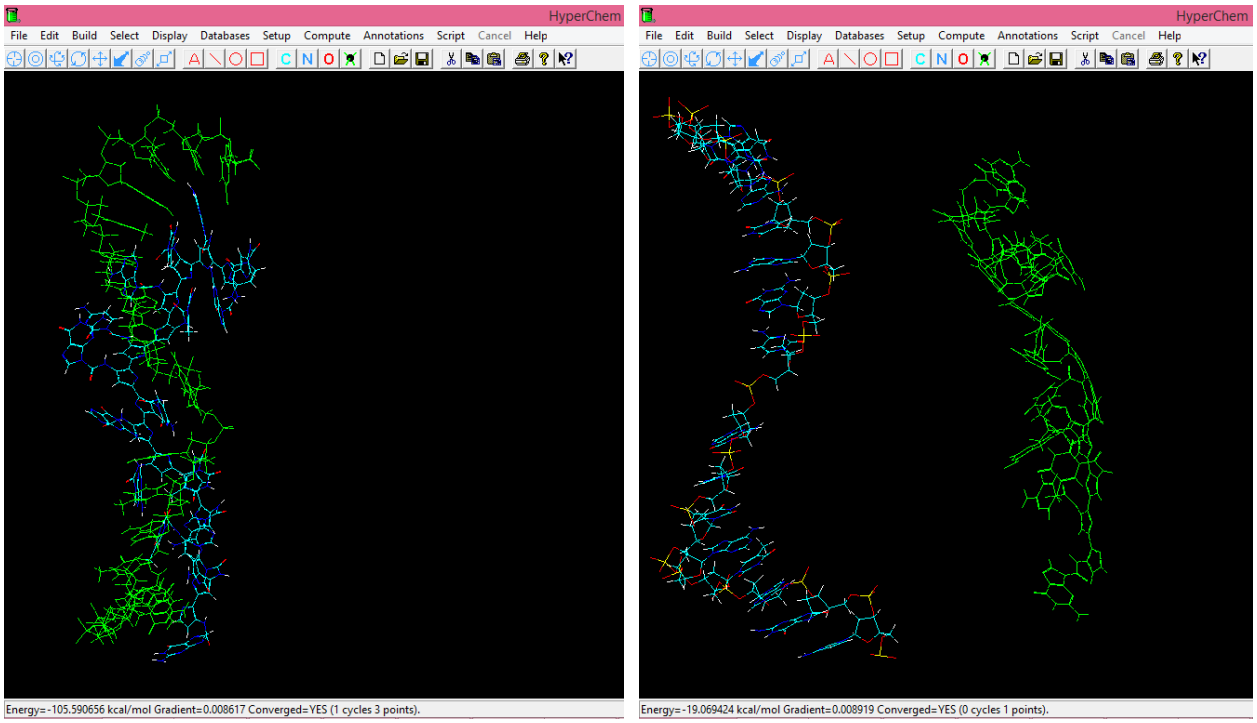


*Figure 3.15 Polypyrolle analogue with short linker bound and separate.*

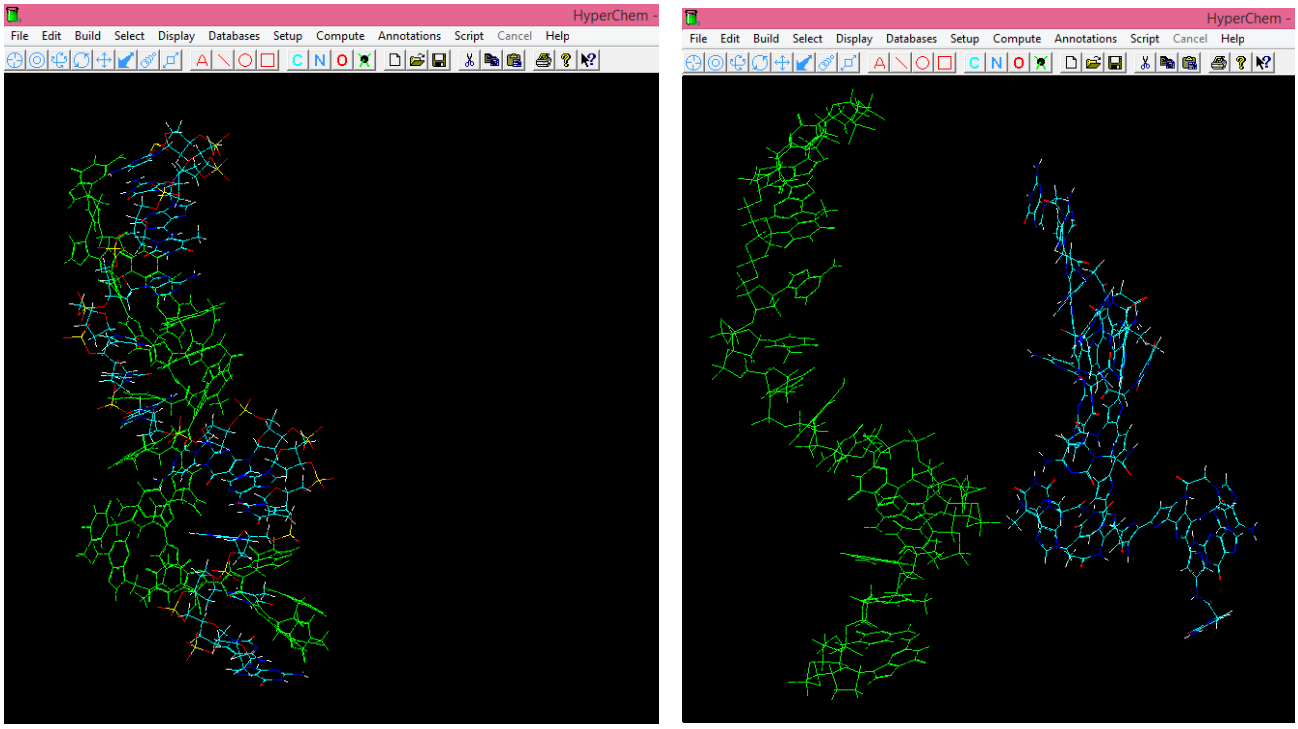


*Figure 3.16 Polypyrolle analogue with long linker bound and separate.*

To test the effect of adding a spacer group between the polypyrrole monomers so as to allow a greater distance between nucleotides, the structure of an extended polypyrrole-like polymer composed of amino pyrrole monomers was investigated as illustrated Figure 3.17.

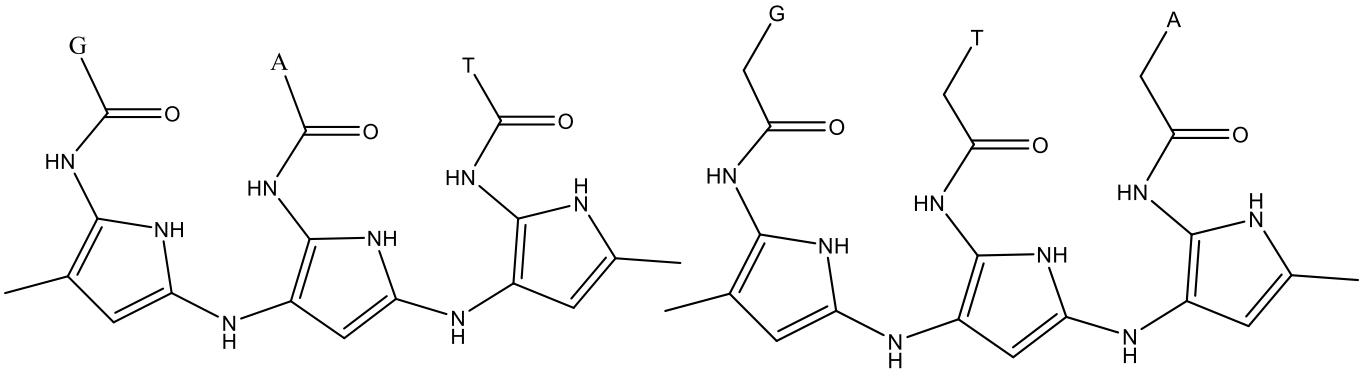


Polypyrrole like polymer with two atoms long scaffold

Polypyrrole like polymer with three atoms long scaffold

*Figure 3.17 Structure of the extended polypyrrole-like polymer "Polyaminopyrrole" with long and short linker.*

Figure 3.17 shows the extended polypyrrole analogue with two atoms long linker (referred to as short linker). The helical structure of the bound strands is obvious, however, the polymer is strained which is apparent from the value of calculated energy value which is less negative compared to the long linker, (-83 and -232 kcal/mol respectively). The structure of the separated strand changed significantly upon energy minimisation and folded to form a nearly globular structure. These intramolecular hydrogen bonds are again easier to form in case of the long linker due to the higher degree of rotational freedom. The short linker analogue is more constrained and less able to form a coiled structure. In Table 10, the calculation of binding energy shows that the average energy difference between the bound and separate forms is significantly more negative in case of the long linker.

| **Polyaminopyrrole Long linker** | **Bound** | **Separate** | **ΔG kcal/mol** |
|---|---|---|---|
| 1 | -378 | -151 | -227 |
| 2 | -385 | -135 | -250 |
| 3 | -374 | -155 | -219 |
| | | **Average** | -232 |
| | | **SD** | 16.09348 |
| **Polyaminopyrrole Short linker** | **Bound** | **Separate** | **ΔG kcal/mol** |
| 1 | -139 | -52 | -87 |
| 2 | -137 | -58 | -79 |
| 3 | -154 | -71 | -83 |
| | | **Average** | -83 |
| | | **SD** | 4 |

*Table 10 Binding energies for the polyaminopyrrole based analogues. All values are in kcal/mol.*

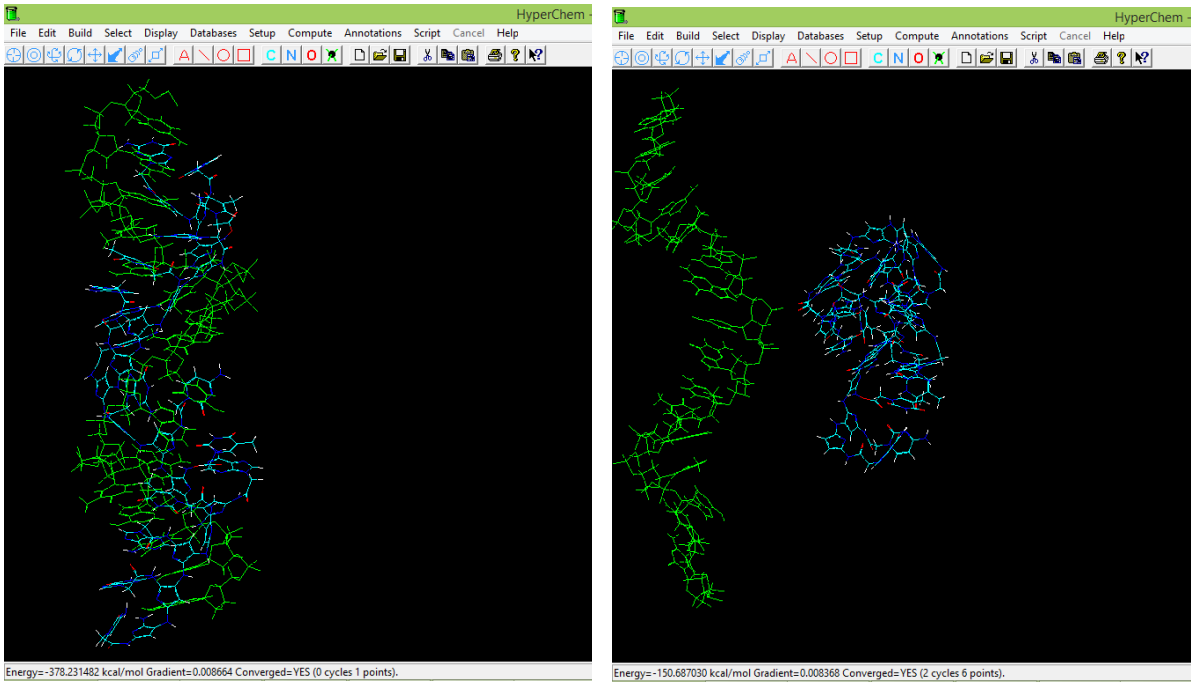


*Figure 3.18 Polyaminopyrrole with three atoms linker (long) in the bound and separate forms.*

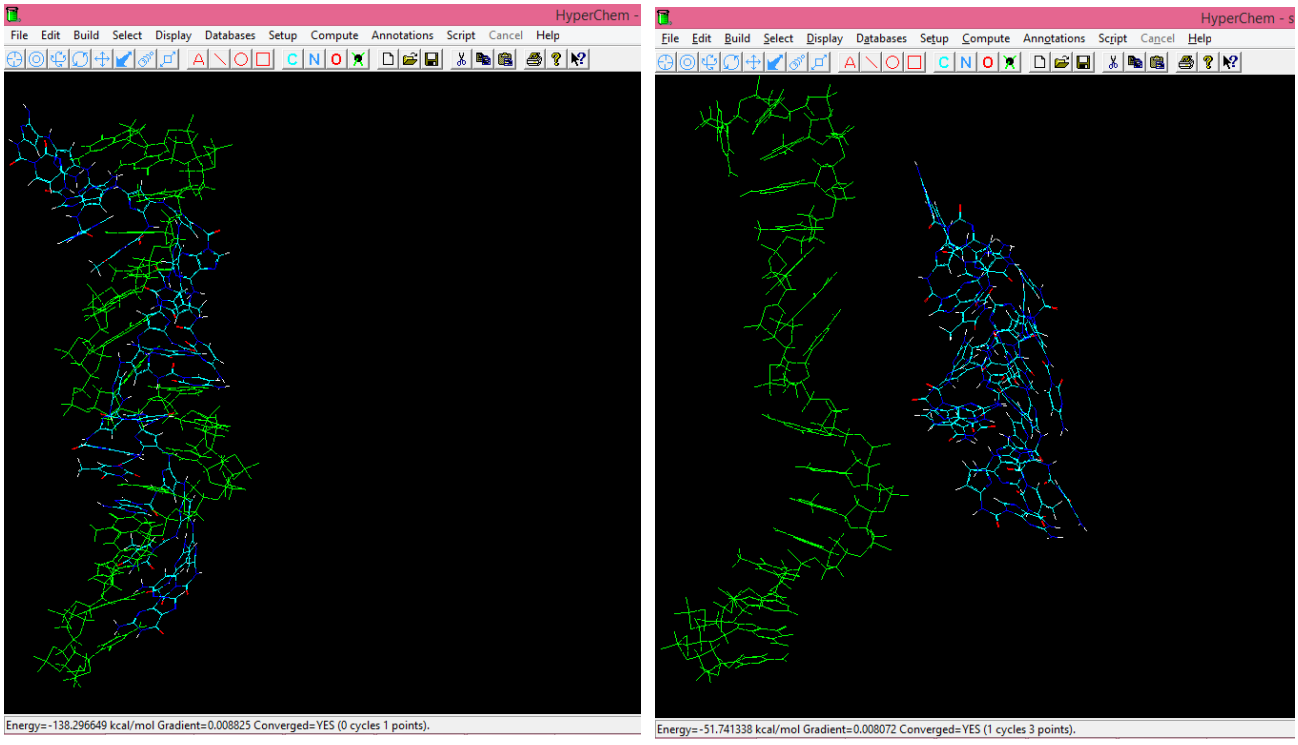


*Figure 3.19 Polyaminopyrrole with the short linker in bound and separated forms.*

### 3.4.4 Polyaniline based analogues

Polyaniline is composed of monomers of aniline. From a structural point of view, it is composed of a six membered rings that are separated by a nitrogen atom and it provides four atoms separation between adjacent nucleotides, which is the case in natural DNA, RNA and the successful analogue PNA.

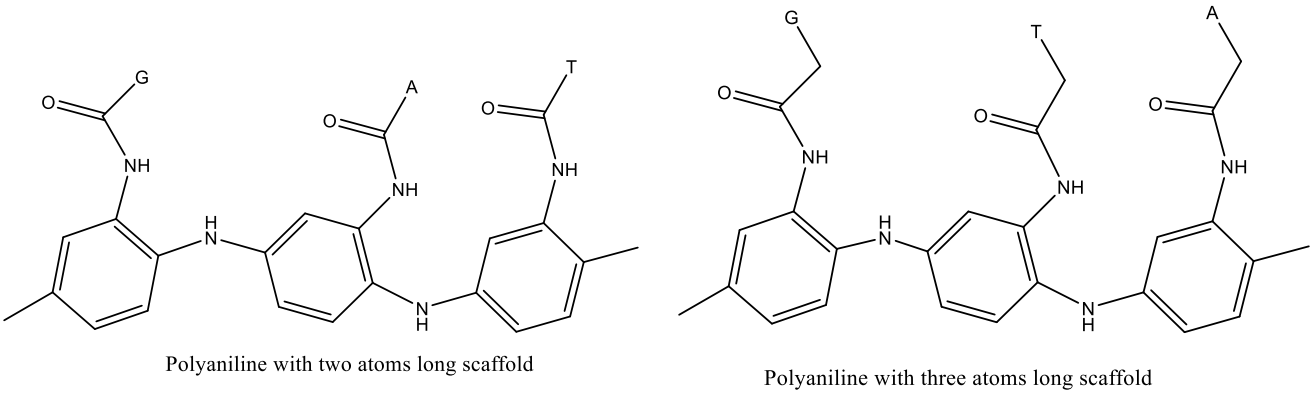


*Figure 3.20 Chemical structure of polyaniline with long and short linker.*

The structures of the long and short linkers are shown in Figure 3.21 and Figure 3.22, respectively. It can be seen that the double helix structure is well formed. The polyaniline backbone moved during the simulation towards the backbone of the complementary strand DNA and align itself parallel to it as it lacks the negative charge that causes repulsion between natural DNA strands. The structure with short linker considerably shows less favourable binding energy than the analogue with long linker.

As shown in Table 11, the binding energy is slightly more favourable than that of polyaminopyrrole analogues and considerably more favourable than polypyrrole and polythiophene analogues.

The following section contains a summary and overall conclusions of modelling of the different DNA analogues and compares the calculated values.

| Polyaniline long linker | Bound | Separate | ΔG kcal/mol |
|---|---|---|---|
| | -436 | -210 | -226 |
| | -503 | -278 | -225 |
| | -533 | -279 | -254 |
| | | **Average** | -235 |
| | | **SD** | 16.4 |
| **Polyaniline short linker** | **Bound** | **Separate** | **ΔG kcal/mol** |
| | -284 | -181 | -103 |
| | -302 | -191 | -111 |
| | -315 | -183 | -132 |
| | | **Average** | -115.3 |
| | | **SD** | 14.9 |

*Table 11 Binding energies for polyaniline-based analogues all values are in kcal/mol.*

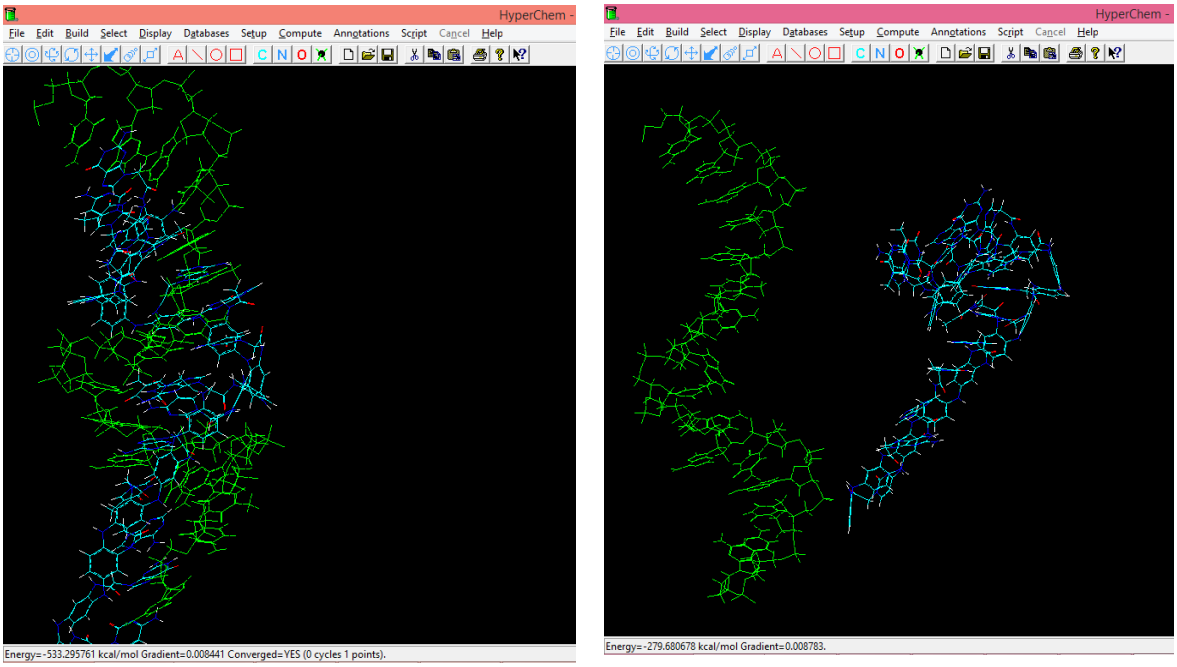


*Figure 3.21 Polyaniline based analogue with three atoms linker (long) in bound and separate forms.*

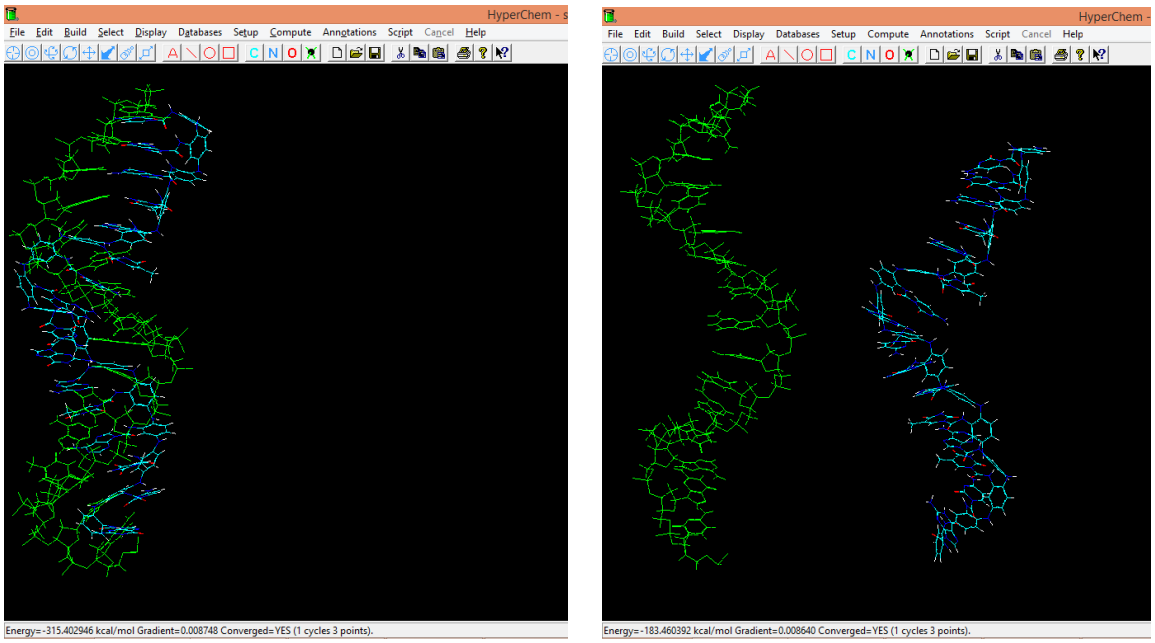


*Figure 3.22 Polyaniline based analogue with two atoms linker (short) in bound and separate forms.*

### 3.4.5 Summary and conclusion of modelling

In this chapter different structures were proposed as candidates for producing an electrically conducting nucleic acid analogue. The proposed compounds were modelled and the binding energy with normal DNA was calculated. The modelling was carried out at least three times for each molecule and the average and standard deviation of the results was calculated.

As shown in Table 12, polyaniline with a three atom long linker was found to have the most favourable binding energy. This behaviour arises because the separation between nucleotides is similar to that of naturally occurring DNA and the polymer is relatively flexible allowing rotation around the secondary amine bonds connecting benzene rings together, which is not the case for the polypyrrole and polythiophene based materials. Also the three

atom long linker that resembles that of the PNA is more energetically favourable.

Based on this modelling information, choosing the polyaniline based polymer seemed to be reasonable. In the following chapter, the synthesis and characterization of this compound is discussed in detail.

| Backbone | Number or atoms in linker | Average ΔG kcal/mol | SD |
|---|---|---|---|
| **DNA** | NA | -102 | 2. |
| **Polythiophene** | 2 | -89.3 | 4 |
| | 3 | -103 | 16 |
| **Polypyrrole** | 2 | -83 | 7 |
| | 3 | -162 | 12 |
| **Polyaminopyrrole** | 2 | -83 | 4 |
| | 3 | -253 | 27 |
| **polyaniline** | 2 | -106 | 4 |
| | 3 | -235 | 16 |

*Table 12 Comparison between calculated binding energies of modelled analogues.*

# Chapter 4

# Synthesis and Characterization of Conducting Nucleic Acid Analogue

"If you can dream it, you can do it." *Walt Disney*

# 4 Chapter 4: Synthesis and characterization of conducting nucleic acid analogue

## 4.1 Introduction

As discussed earlier in the thesis, the rate of electron transfer to a remote, redox active label can influence the current response observed. One strategy to mitigate this effect is to synthetically replace the backbone of the capture strand DNA with an electronically conducting analogue. The Hyperchem molecular modelling suggests that this ought to be possible using a range of monomers and that the resulting polymer should preserve the ability of the covalently attached bases to hybridise with the target.

This chapter reports on the synthesis and characterisation of the conducting nucleic acid analogue using electrochemical polymerization. Details are provided regarding the preparation of the electrode, the new step-wise growth strategy for producing the conducting polymer backbone and its characterization. Finally, results for the ability of the synthetic analogue to bind natural DNA are discussed. The electrochemical behaviour of the analogue is presented and its performance within assays compared with that achieved using a natural capture strand.

In the previous chapter, the design and modelling of different candidates was discussed. The proposed conjugated conductive polymers are polyaniline, polypyrrole, polythiophene. As described in detail in the previous chapter, polyaniline was chosen to be the backbone since the calculations showed that its binding to DNA is energetically favourable and it can be prepared relatively easily using electrochemical polymerisation. However,

electrochemical polymerization is normally used to produce long chains of homogenous polymers. To address this issue, a modified step-wise addition of a single monomer unit by electrochemical polymerization so as to control the structure of a heterogeneous oligomer chain at the single monomer level was developed. In this strategy, a different nucleotide-bound monomer can be added according to the sequence desired, to produce a specifically coded polymer that is complementary to the target nucleic acid sequence of interest.

After synthesizing the conductive capture strand, a complementary DNA target sequence is allowed to bind to it. The binding was investigated by tagging the DNA with a fluorescent dye and a nanoparticle that allows electrochemical detection of the binding.

## 4.2 Materials and instrumentations

4amino thiophenol 4ATP, butane-1-thiol, 3-(tert-Butoxycarbonylamino)aniline, lithium perchlorate, Acetonitrile, N-tBoc aniline, Trifluoroacetic acid (TFA) and absolute ethanol were purchased from Sigma Aldrich and were of analytical grade. Thymine acetic acid was purchased from Polyorganic Inc. Gold coated 200 nm thick silicon wafers were obtained from Tyndall National Institute. A gold colloidal solution containing 56.8 µg per mL gold particles with a diameter of 250 nm was purchased from BBI Solutions.

All electrochemical experiments were carried out in a conventional three-electrode cell at a temperature 22±2°C using a CH Instruments Model 660 electrochemical workstation. The working electrode was a 1 x 0.5 cm planar gold-coated silicon wafer. A large area platinum wire acted as the counter electrode. Potentials are quoted with respect to a silver /silver chloride

(Ag/AgCl) reference electrode (3 M KCl). All solutions were deoxygenated thoroughly using nitrogen prior to use and a blanket of nitrogen was maintained over the solution during all experiments. Unless stated otherwise, the scan rate in all experiments was 0.1 $Vs^{-1}$. SEM images were taken using a Hitachi S3000N scanning electron microscope at an accelerating voltage of 5-30 kV.

## 4.3 Experimental

### 4.3.1 Synthesis of Boc-protected aniline

The synthesis illustrated in Figure 4.1, weight of 0.218 g (1 mmol) of Di-tert-butyl dicarbonate was dissolved in 50 mL deionized water, stirred and 0.093 g (1 mmol) of aniline were added. The mixture was left to stir for 4 h. The crystals which fall out spontaneously were collected and washed with water and dried under nitrogen. The yield was calculated to be 62%.

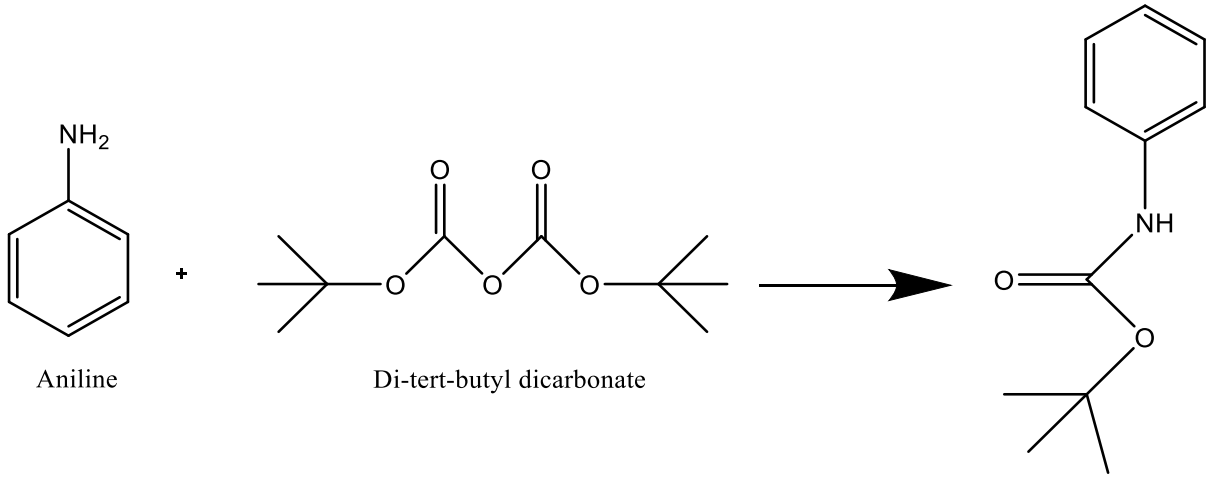


Figure 4.1 Synthesis scheme of N-Boc aniline.

### 4.3.2 Synthesis of thymine derivative:

The synthetic scheme of thymine derivative is shown in Figure 4.2:

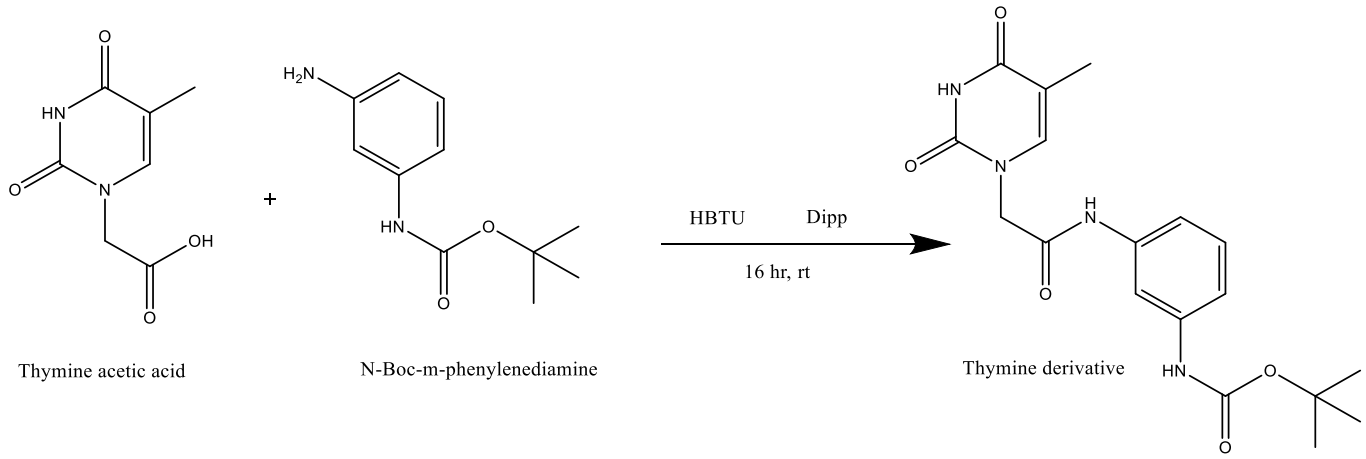


*Figure 4.2 Synthesis scheme of thymine derivative.*

The compound was synthesized using the standard procedures of HBTU coupling (O-(Benzotriazol-1-yl)-N,N,N′,N′-tetramethyluronium hexafluorophosphate) 0.046 g (0.25 mmol) of thymine acetic acid were dissolved in 15 mL of dimethyl formamide DMF in a round bottom flask, with stirring, 3 equivalents 0.096 g (0.75 mmol) of the organic base N,N diisopropylethylamine was added. After the complete dissolution of the thymine acetic acid, 0.19 g of HBTU were added (0.5 mmol, 2 equivalent). Following stirring for 30 min, 0.062 g (0.3 mmol, 1.2 equivalent)of N-Boc-m-phenylenediamine was added. The mixture was left with stirring at room temperature for 16 h. After the reaction was complete, the mixture was crashed out in a cold saturated aqueous solution of NaCl. The precipitate was then filtered and washed twice with 10 mL of chloroform, then dried under nitrogen. The yield was calculated to be 60%.

### 4.3.3 Modification of electrode surface

Before the stepwise polymer growth, the electrodes were covered with a monolayer of 4-Aminothiohenol (4ATP), i.e., a thiolated derivative of aniline that can attach to gold and at the same time has the aniline function group that can undergo electrochemical polymerization with aniline derivative monomers in solution.

To characterize the 4ATP monolayer and the mixed monolayer of 4ATP and Butane-1-thiole, reductive desorption by LSV was used. Gold disc electrodes were used after cleaning and polishing using 0.3 µm diameter alumina and washing with deionized water then ethanol. One electrode was modified by a monolayer of 4ATP by immersing the electrode in 2 mM solution of 4ATP in absolute alcohol overnight. The second electrode was modified by a monolayer of butane-1-thiol by immersion in 20 mM solution of butane-1-thiol solution in absolute ethanol and the third electrode was immersed in a mixed solution with a concentration of 2 mM of 4ATP and 20 mM butane-1-thiol. The three electrodes were left in the solutions overnight for 16 h and then taken out and washed with ethanol and deionized water. In the LSV experiment, the electrolyte used was aqueous 1 M KOH solution. The potential was swept from -0.2 to -1.5 V and the scan rate was 0.1 $Vs^{-1}$.

### 4.3.4 Single monomer electrochemical polymerization of aniline and thymine derivative.

After the-self-assembly of the mixed monolayer that is composed of 4ATP and butane-1-thiol the electrode was cycled between -0.35 V and 1.1 V and the scan rate was 0.1 $Vs^{-1}$ and number of cycles is 3. The electrolyte was 1mM solution of N-Boc, aniline dissolved in 0.1 M solution of $LiClO_4$ in acetonitrile.

The electrochemical polymerization of thymine derivative of t-Boc protected aniline is carried out using the same cyclic voltammetry procedures followed for the N-Boc aniline single monomer electrochemical polymerization. Thymine derivative of aniline that was synthesized in Section 4.3.2 was used. The electrodes used in this experiments are gold coated silicon wafers, cut in rectangular shape with 0.5 cm wide and 2 cm long, the electrodes are immersed in the electrolyte solution so that about 1 cm is contacting the solution, which gives electrode area of approximately 0.5 $cm^2$. The electrolyte solution was 0.5 mM solution of the thymine derivative of aniline in an acetonitrile solution of 0.1 M $LiClO_4$.

### 4.3.5 Amperometry

After the single monomer electrochemical polymerization the potential was stepped to +0.900V and the current measured as a function of time over 40 s to make sure all the surface bound molecules were coupled. Figure 4.3 shows the current-time transient for the oxidative polymerization of N-Boc-aniline using the amperometric i-t technique.

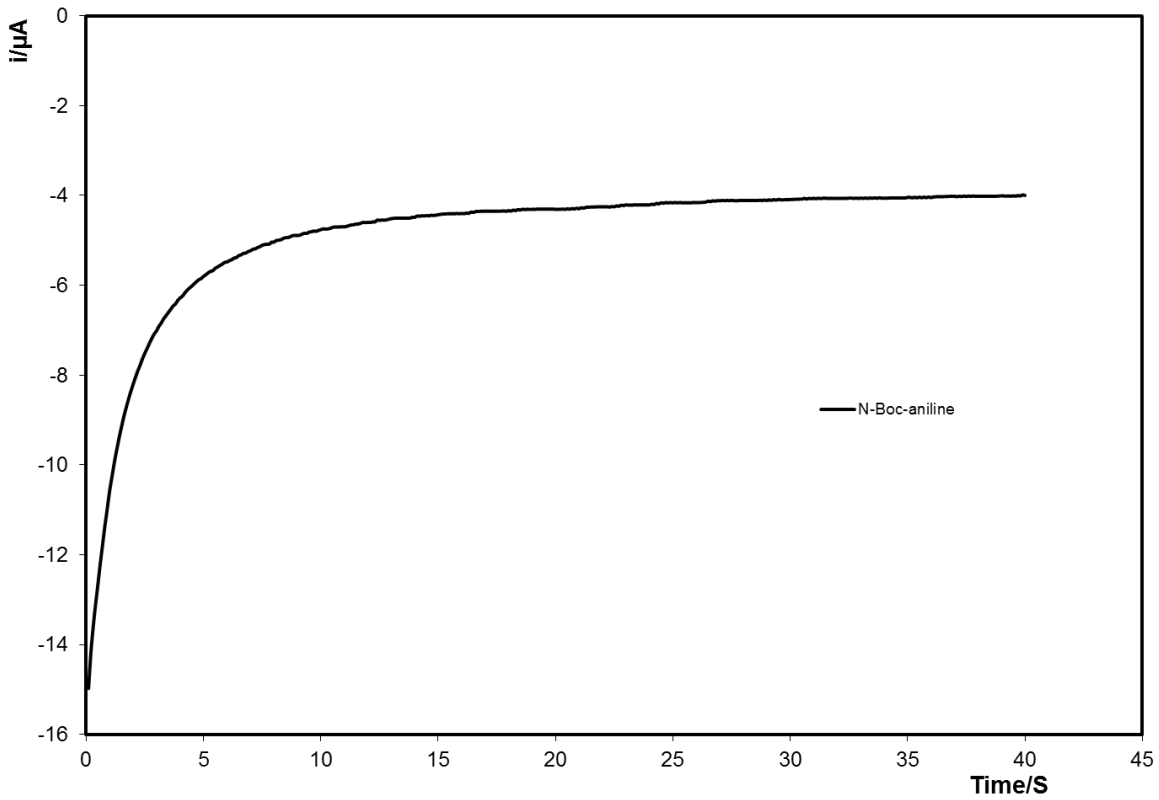


*Figure 4.3 Amperometric i-t transient for one unit electrochemical coupling. Electrode was 0.5 cm$^2$ gold-coated silicon wafer electrodes modified with a mixed monolayer of 4ATP and butane-1-thiol in 1mM solution of N-tBoc,protected aniline dissolved in 0.1 M solution of $LiClO_4$ in acetonitrile, potential step was at 0.9 V for 40 s.*

### 4.3.6 Deprotection by Trifluoroacetic acid TFA

After carrying out the oxidative coupling of the surface bound 4ATP with a single monomer of the N-Boc-aniline, the electrodes were then washed with acetonitrile and immersed in 100% TFA for 30 min to completely cleave the protecting tBoc group. The electrodes are then removed from the TFA, washed with acetonitrile and then dried in a nitrogen stream.

### 4.3.7 Attachment of gold particles.

Three gold coated silicon wafer electrodes were functionalized with a mixed monolayer of 4ATP and butane-1-thiol as described previously. The number of discrete monomer addition cycles, or elongation cycles were carried out to the three electrodes were as follows: Electrode 1 has three

coupled monomers, Electrode 2 has four coupled monomers and Electrode 3 has five coupled monomers and all were protected by tBoc i.e. before the protection step by TFA. The electrodes were then washed with acetonitrile and water, then placed in plastic vials so as the gold-covered side is facing upwards and 1 mL of a gold nanoparticle suspension (d = 250 nm) was added, and left for 1 h. The wafers then were removed and washed with water for 60 s to remove non-specifically bound gold particles. The electrodes were then attached to aluminium stubs and examined using SEM.

The wafers then were recovered from the aluminium stubs and immersed in 100% TFA for 30 min to deprotect the tBoc group, washed with acetonitrile then water then again placed in plastic vials so as the gold-covered side is facing upwards and 1 mL of a gold nanoparticle suspension (d = 250 nm) was added, and left for 1 h. The wafers then were removed and washed with water for 60 s to remove non-specifically bound gold particles. The electrodes were then attached again to aluminium stubs and examined using SEM to see the effect of deprotection on the gold attachment.

# 4.4 Results and discussion

### 4.4.1 Synthesis of thymine derivative of aniline

Amide bond formation is one of the basic and most important reactions in organic chemistry and biology[146]. An amide bond is formed between a carboxylic acid group and an amino and a molecule of water is lost and the bond is formed between nitrogen atom and the carbon of the carbonyl group of the carboxylic acid. During the development of peptide synthesis, many coupling agents were developed to activate the carboxylic acid and increase the yield and efficiency of the amide coupling reactions[147].

HBTU, or N,N,N′,N′-Tetramethyl-O-(1H-benzotriazol-1-yl)uronium hexafluorophosphate, O-(Benzotriazol-1-yl)-N,N,N′,N′-tetramethyluronium hexafluorophosphat, was first discovered in 1975 and used as a coupling agent in amide bond formation efficiently and produced a good yield without racemization[148]. The chemical structure of HBTU is shown in Figure 4.4.

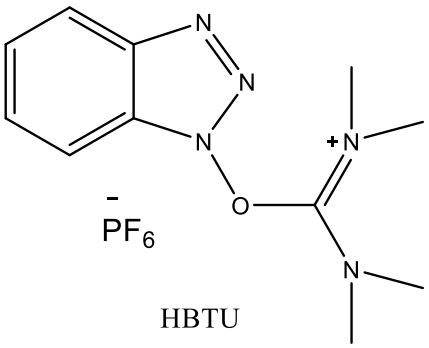


O-(Benzotriazol-1-yl)-N,N,N',N'-tetramethyluronium hexafluorophosphate

*Figure 4.4 Chemical structure of HBTU.*

The mechanism of reaction of HBTU involves the use of a tertiary base to deprotonate the carboxylic acid for example diisopropylamine.

The aniline derivative that is used in this synthesis is N-Boc-m-phenylenediamine. The free amino group is in the meta position from the t-Boc protected amino group. The aromatic diamines has been used before in electrochemical polymerization to produce polymers with a side functionality that allows modification and adding sidechains. A very detailed review was written by Xin-Gui Li *et al*. describing preparation of polymers from different phenylenediamine isomers [149]. m-phenylenediamine has been used alone and copolymerized with aniline[150]. In the current work, the facile electrochemical polymerization of phenylenediamine and the t-Boc protection was utilised to control the process and allow step wise elongation of the chain to control the type of monomer added. That is why one of the amino group of the m-phenylenediamine is protected by the t-Boc protecting group and the chemical structure is shown is Figure 4.5.

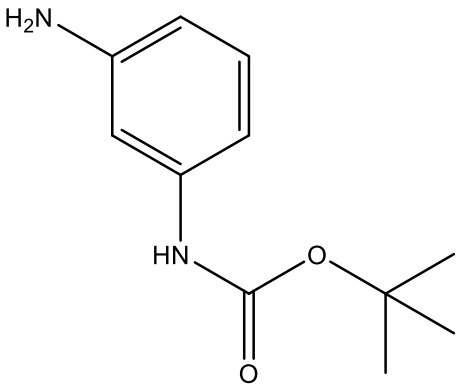


*tert*-butyl (3-aminophenyl)carbamate
N-Boc-m-phenylenediamine

*Figure 4.5 Chemical structure of N-Boc-m-phenylenediamine.*

Thymine is one of the pyrimidine nucleotides, it forms a two hydrogen bonds with the adenine nucleotide during DNA hybridization. It is replaced in RNA with Uracil[151]. The thymine derivative of aniline is synthesized by means

of amide coupling of thymine acetic acid derivative with a free amino group of N-t-Boc phenylene diamine. The thymine acetic acid derivative is the same compound used to synthesize thymine monomer in peptide nucleic acid PNA after reacting with glycine which form the backbone. The chemical structure is shown in Figure 4.6.

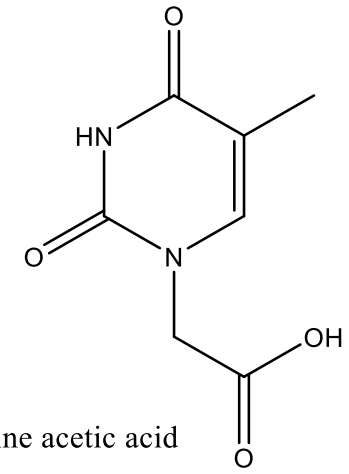


Thymine acetic acid

2-(5-methyl-2,4-dioxo-3,4-dihydropyrimidin-1(2*H*)-yl)acetic acid

*Figure 4.6 Chemical structure of thymine acetic acid.*

The $^{1}$H-NMR spectrum of the prepared compound was carried out in dimethylsulfoxide DMSO.

$^{1}$H NMR (400 MHz, DMSO):

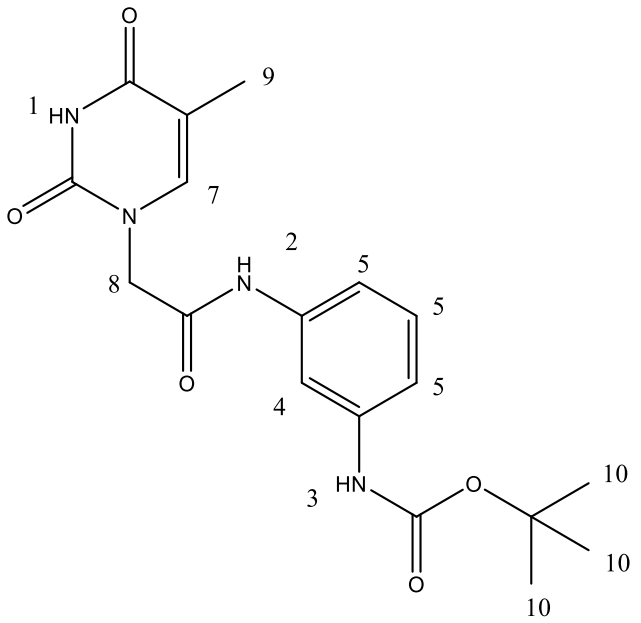


Hydrogen numbering in T aniline derivative

| number | ppm | integration | shape |
|---|---|---|---|
| 1 | 11.351 | 1 | s |
| 2 | 10.238 | 1 | s |
| 3 | 9.394 | 1 | s |
| 4 | 7.817 | 1 | s |
| 5 | 7.509 | 1 | s |
| 6 | 7.152 | 3 | m |
| 7 | 4.471 | 2 | s |
| 8 | 1.76 | 3 | s |
| 9 | 1.468 | 9 | s |

*Table 13 $^{1}$H NMR peak assignment table (400 MHz in DMSO)*

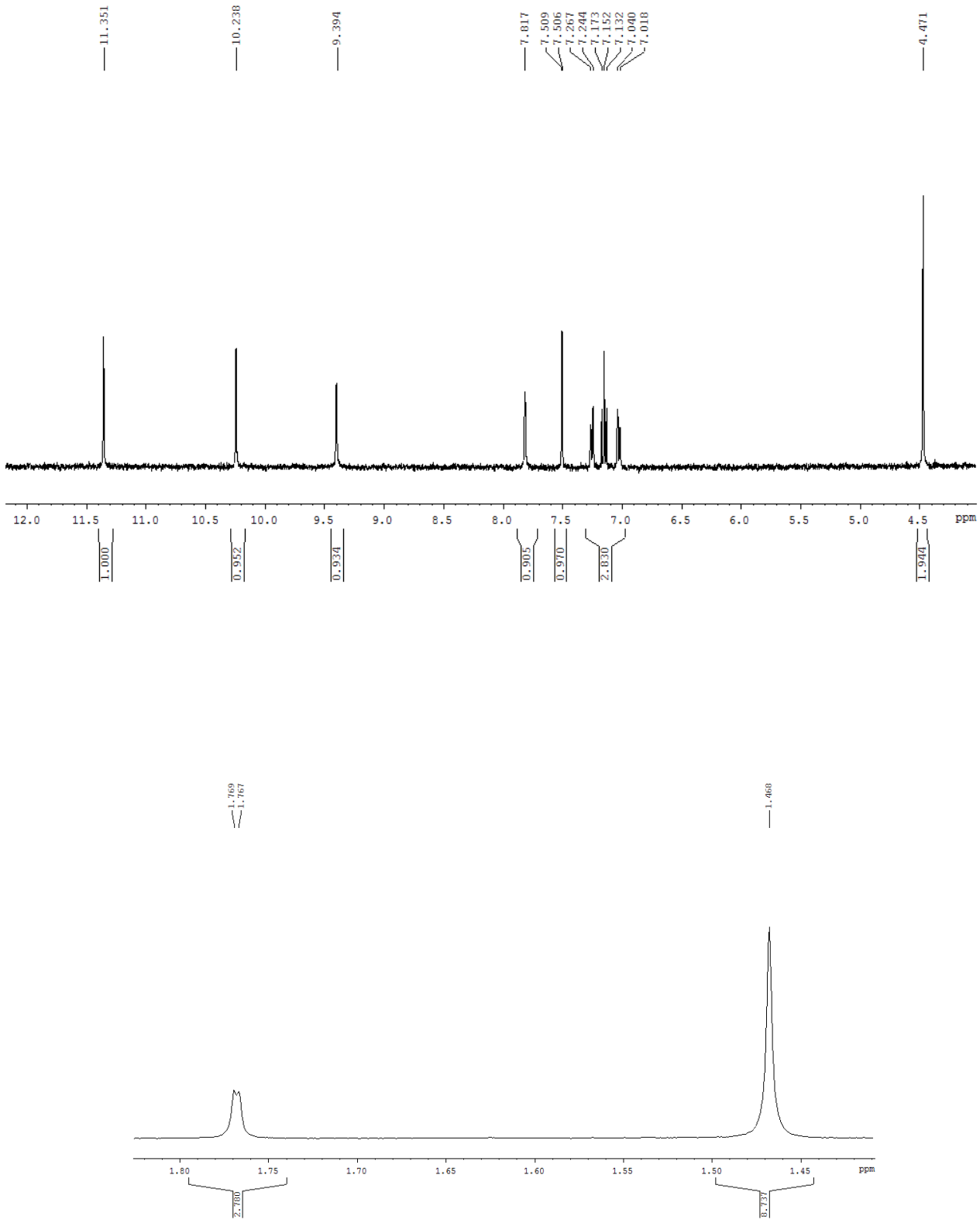


*Figure 4.7 NMR peaks for Thymine aniline derivative.*

### 4.4.2 4-aminothiophenol 4ATP monolayer formation

The compound that was investigated as the anchoring monolayer is 4-aminobenzenethiol or 4-aminothiophenol (4ATP) shown in Figure 4.8. The thiol and amino groups are in para position and that allows the amino group to be readily available for further polymerization steps.

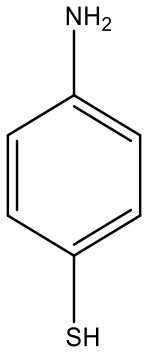


4-aminobenzenethiol
4-aminothiophenol

*Figure 4.8 Chemical structure of 4-aminothiophenol (4ATP).*

The electrochemical properties of 4ATP self-assembled monolayers were studied by Lukkar et[152] al using cyclic voltammetry in perchlorate electrolyte. They found that an oxidation of 4ATP occurs at approximately 0.5 V when adjacent 4ATP molecule couple form di and oligo aniline. A similar result was obtained in our experiment upon functionalization of 2 mm gold disc electrode with a monolayer of 4ATP. In Figure 4.9, cyclic voltammetry of the gold disc electrode shows two oxidation peaks. Peak A represents the oxidation of the 4-aminothiophenol molecule to the delocalization-stabilized radical cation that remains attached to the surface. This radical cation attacks the adjacent molecule to form a dimer. This dimer can undergo a hydrolytic cleavage of the imine moiety to give the corresponding surface-bound quinone mono-imine compound which gives rise to peak B in Figure 4.9.

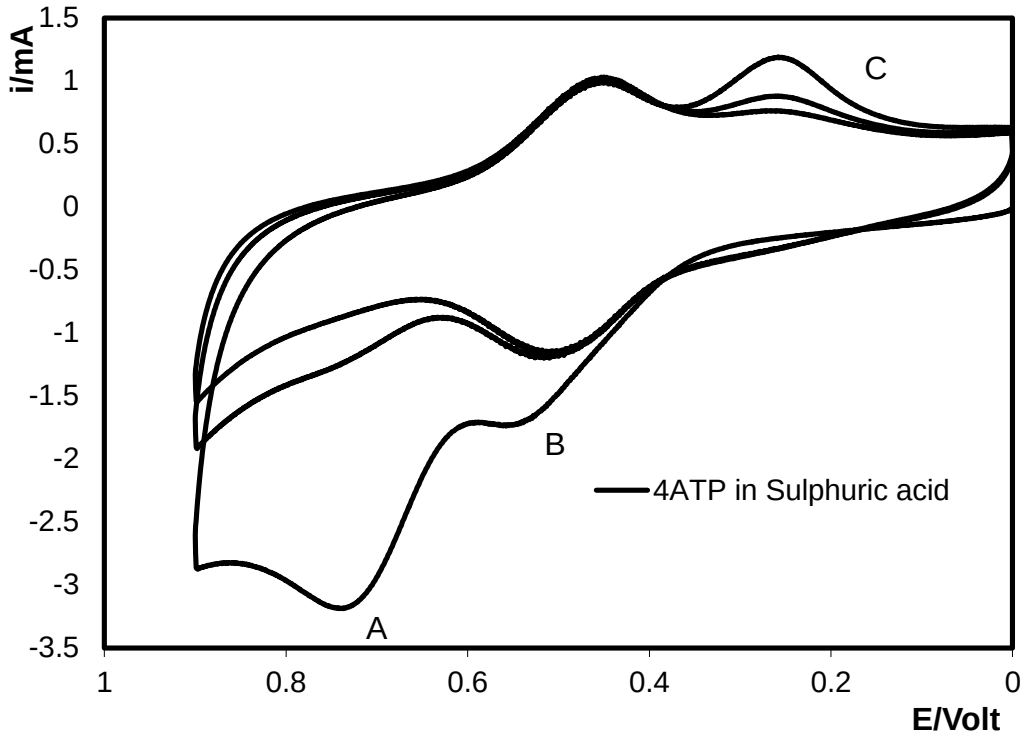


*Figure 4.9 Cyclic voltammetry for a 2 mm diameter gold disc electrode modified with a self-assembled monolayer of 4ATP. The electrolyte used was aqueous 0.1 $H_2SO_4$ and the scan rate was 0.1 $Vs^{-1}$*

Lateral coupling of the 4ATP adsorbates is not desirable. One way to minimize such side interactions is to prepare a monolayer of 4ATP mixed with an inert molecule that works as a spacer between adjacent 4ATP molecules thus decreasing the chance of having adjacent molecules couple. The choice of the molecule and preparation of the mixed monolayers is discussed in the next section.

### 4.4.3 Mixed monolayer self-assembly.

Alkane thiols can form well organised monolayers whose properties depend on the alkane chain length. The fact that alkane thiols are relatively electrochemically inert, apart from reductive desorption, makes them a good candidate to function as a spacer molecule between the 4ATP adsorbates.

In this way the density of nucleation sites for the growth of the conducting capture strand oligo can be controlled. The alkane thiol spacer has been selected so that it is  long enough to prevent lateral reaction between two 4ATP molecules but short enough to allow the aniline monomers in solution approach the amino group of the surface immobilized 4ATP and polymerise. As shown in Figure 4.10 the length of 4ATP is comparable to the length of the butane-1-thiole spacer.

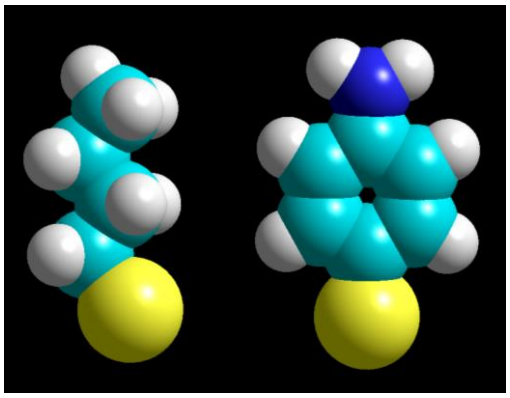

*Figure 4.10 Length comparison between 4aminothiophenol on the right, and butane-1-thiol on the left. Modelled using Hyperchem.*

#### 4.4.3.1 LSV of mixed Monolayer.

**Error! Reference source not found.** shows the LSV responses obtained for each of the three types of thiol monolayer formed. All three monolayers show a well-defined reduction peak at approximately -1.15 V corresponding to reductive desorption.  Specifically, the 4ATP shows a reduction peak at -1.15V and the butane-1-thiol at -1.12 V.

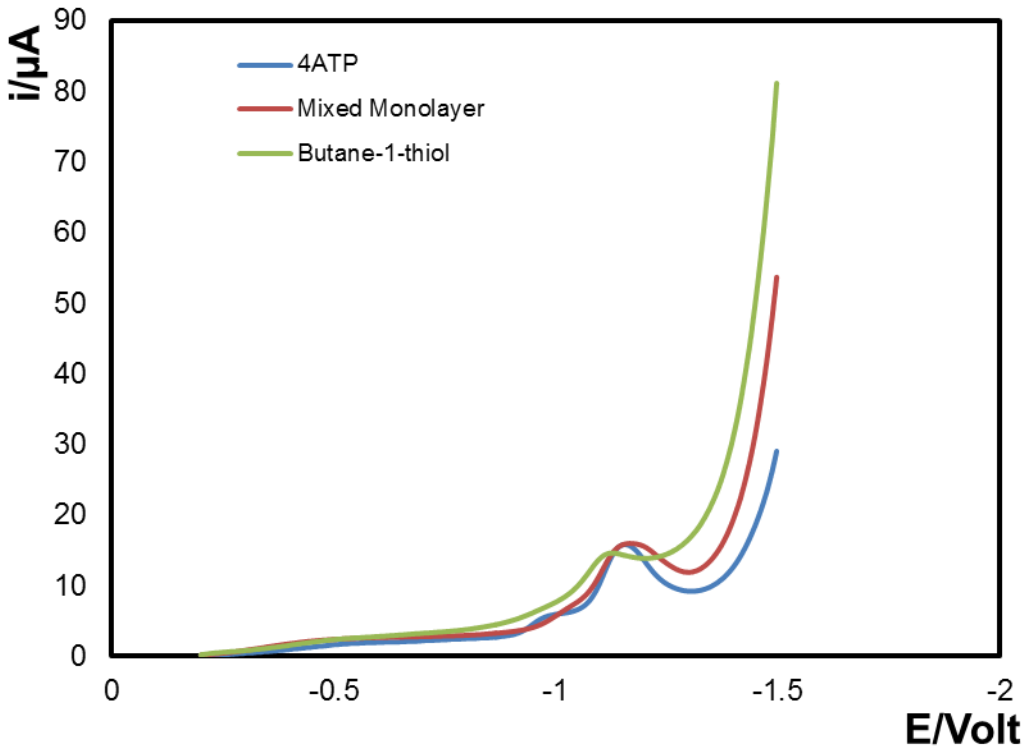


*Figure 4.11 Linear sweep voltammetry in 1M KOH solution. The first electrode was covered with a pure monolayer of 4ATP and the second with a pure monolayer of butane-1-thiol, and the third with mixed monolayer. The potential swept from -0.2 to -1.5 V Scan rate was 0.1 $Vs^{-1}$.*

As expected on the basis of single component monolayer responses, the mixed monolayer did not show two distinct peaks which would allow their relative mole fractions to be estimated[153]. The mixed monolayer voltammogram shows a single peak at -1.17 V which indicates that the strength of the thiol-gold bonds is similar for the two compounds and desorption is not influenced by their co-adsorption. The total charge passed under the peak of 4ATP following exhaustive desorption was 7.4 µC, 2.8 µC for butane-1-thiol and 7.7 µC for the mixed monolayer. These values are consistent with the surface concentrations of 4ATP and the butane-1-thiol being similar despite the concentration of the solution of butane-1-thiol is 10 times the concentration of the 4ATP.

The cyclic voltammograms in **Error! Reference source not found.** show the effect of adding butane-1-thiol to the 4ATP monolayer, it is evident that the peak B which is associated with the dimer which is the product of coupling of two adjacent 4ATP molecule has lower current and overall area, indicating that effective separation is provided by the butane-1-thiol.

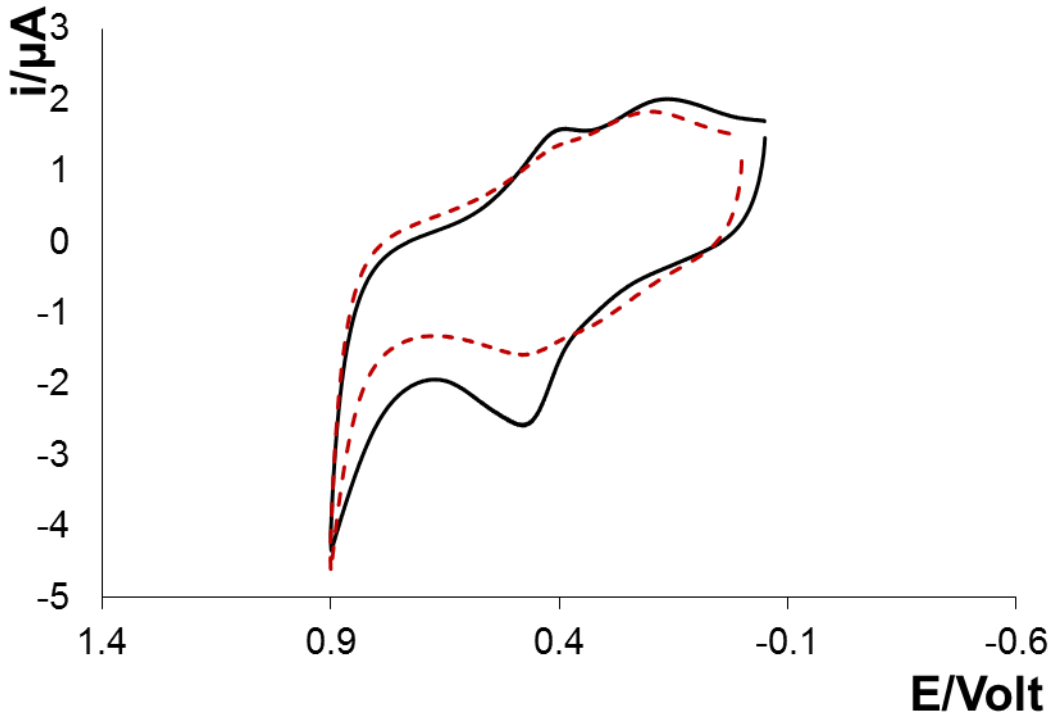


*Figure 4.12 Cyclic voltammetry for gold disc electrode covered with a monolayer of 4ATP (solid) and mixed monolayer of 4ATP and butane-1-thiol (dashed) solution was in 0.1M $H_2SO_4$, between 0.9V and -0.1V scan rate 0.1 $Vs^{-1}$.*

## 4.5 Stepwise addition of aniline monomers.

The stepwise coupling of monomers is needed because the designed nucleic acid analogue will eventually have different nucleotides connected in series to form a specifically coded sequence that is complementary to a target strand DNA or RNA. In the previous section the formation of the mixed monolayer was explained and the characterization of the electrochemical properties was discussed. The 4ATP is the polymerization starting point and

the linker that anchors the synthesized polymer to the electrode surface via the thiol-gold bond. Adding of a spacer molecule between the 4ATP helps preventing the in-plane polymerisation of adjacent 4ATP molecules and limit the electrochemical coupling process between 4ATP molecules. The protection of the amino group on the monomers prevents the uncontrolled polymerisation of more than one monomer as the incoming aniline or its derivative molecule is protected/blocked. The activation of the chain for further addition of another monomer can be attained by deprotecting the terminal amino group. The type of the added monomer can change by changing the composition of the electrolyte solution. Preparing four different electrolyte solutions contain four different derivatives of aniline, for example thymine, adenine, cytosine or guanine derivatives can enable a predesigned polyaniline nucleic acid analogue that is complementary to a specific target sequence to be synthesized. This process closely resembles the solid phase synthesis of PNA described in the literature review. However, the use of electrochemical oxidative coupling in highly controlled synthesis has not been described before to the best of our knowledge.

In order to examine the possibility of adding a single monomer to the polyaniline chain, the first compound tested was the N-Boc-aniline and compared to unprotected aniline. The Boc-protected aniline prepared in Section 4.3.1 was used. Cyclic voltammetry was used to characterize the electrochemical polymerization process. An amperometric technique was used to complete the electrochemical polymerization step.

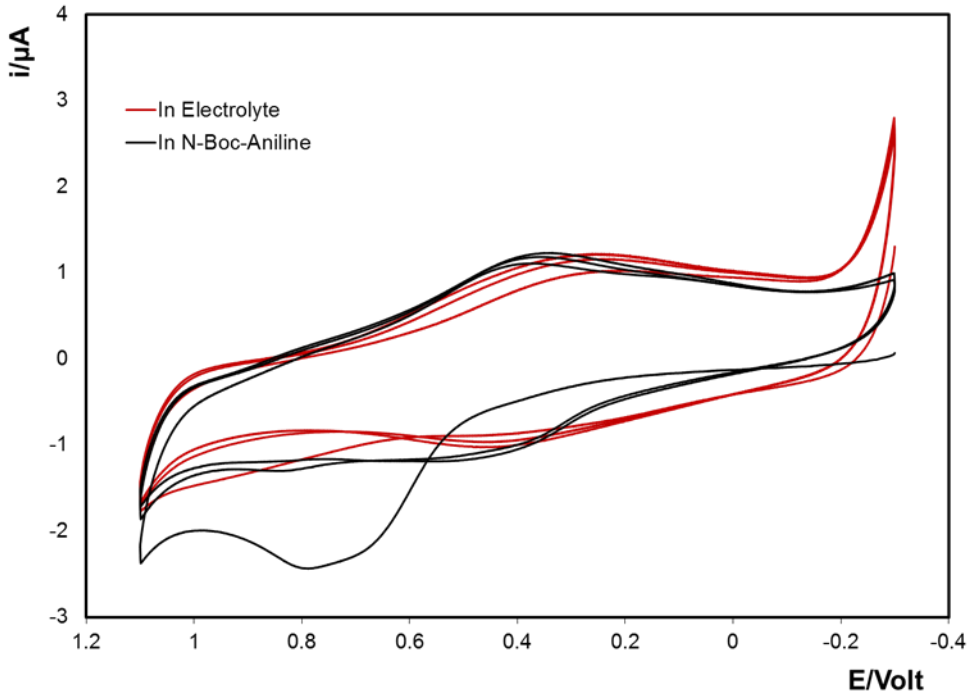


*Figure 4.13 cyclic voltammograms of 2 mm gold disc electrodes modified with a mixed monolayer of 4ATP and butane-1-thiol in: (red) 0.1 M solution of $LiClO_4$ solution in acetonitrile. And (black) 1mM solution of N-Boc-aniline in 0.1 M solution of $LiClO_4$ in acetonitrile. The scan rate was 0.1 $Vs^{-1}$.*

As illustrated in Figure 4.13, the two voltammograms were carried out using identical 2 mm gold disc electrodes modified with a mixed SAM of butan-1-thiol and 4ATP. One of the electrodes (the red voltammogram) was cycled in 0.1 M solution of $LiClO_4$ in acetonitrile (the electrolyte without dissolved monomer) and is considered a control experiment. And the second electrode (the black voltammogram) was cycled in 1mM solution of N-Boc-aniline in 0.1 M solution of $LiClO_4$ in acetonitrile. The control electrode showed a small increase in current at about 0.8 V to form a nearly flat peak. This oxidative current can be attributed to the residual in-plane polymerisation of the 4ATP. While at the same potential in the black voltammogram of the electrode cycled in the 1mM solution of N-Boc-aniline, an oxidation peak is clearly visible. This peak appeared as large irreversible

peak in the first cycle, and in the second and third cycle, it diminished in height and area.

Upon increasing the concentration of the N-Boc-aniline in the solution to 5 mM solution, the peak increased in height and area on the first scan relative to the 1 mM concentration. Figure 4.14 compares the voltammograms of the modified electrodes in N-Boc-Aniline solution and unprotected aniline solution, the peak appears at the same potential to that observed for the electropolymerisation of unprotected/blocked aniline. However, in the case of unprotected aniline a very large current is observed and a well-defined peak is not observed indicating efficient formation of an electropolymerised conducting film. In case of the protected N-Boc-aniline solution, polymerisation cannot occur since the monomer is protected and only a single unit can be added and a well-defined peak is observed whose shape is consistent with a redox process involving a surface confined reactant. Also from Figure 4.14 peaks due to oxidation and reduction of polyaniline can be observed at 0.1 V and 0.2 respectively.

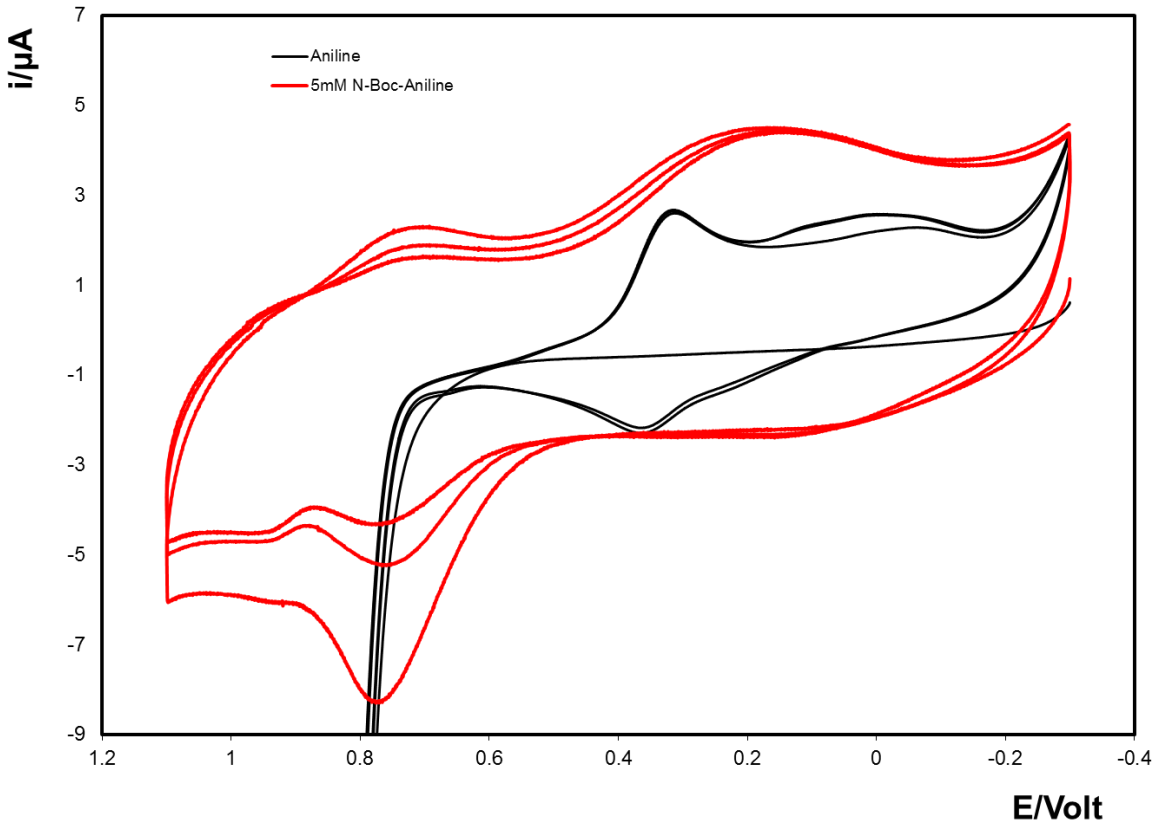


*Figure 4.14 Cyclic voltammograms of gold disc electrode modified with a mixed monolayer of 4ATP and butane-1-thiol (Black) in 0.1 M solution of aniline in 0.1 M solution of $LiClO_4$ solution in acetonitrile. And (red) in 5mM solution of N-Boc-aniline in 0.1 M solution of $LiClO_4$ in acetonitrile. The scan rate was 0.1 $Vs^{-1}$.*

### 4.5.1 Amperometric i-t curve

As seen in the cyclic voltammetry, the area of the oxidation peak of aniline decreases in the second and further in the third cycles. The fact that a peak current is observed on the second scan suggests incomplete oxidation of all of the surface-bound 4ATP molecules, i.e., a fraction remains unreacted after the first cycle. In order to guarantee a complete coupling for all the surface bound anilines with monomer molecules in the solution, an amperometric step is applied for 40 s at 0.9 V (which is positive to the oxidation peak potential).

It is obvious from the current time transient in Figure 4.3 that the current starts from a large negative value then drops to reach a steady state after

about 20 s. That can be explained by the saturation of the surface with monomers and dropping the oxidation current to a minimum steady state value.

### 4.5.2 Repeating the polymerization cycle.

The cycle of adding single monomer to the chain using electrochemical oxidative coupling, deprotecting the terminal amino group with TFA then re-immersing in the monomer solution was repeated several times so as to build up the structure one unit at a time. The electrodes used in this experiment were 0.5 $cm^2$ gold coated silicon wafer electrodes.

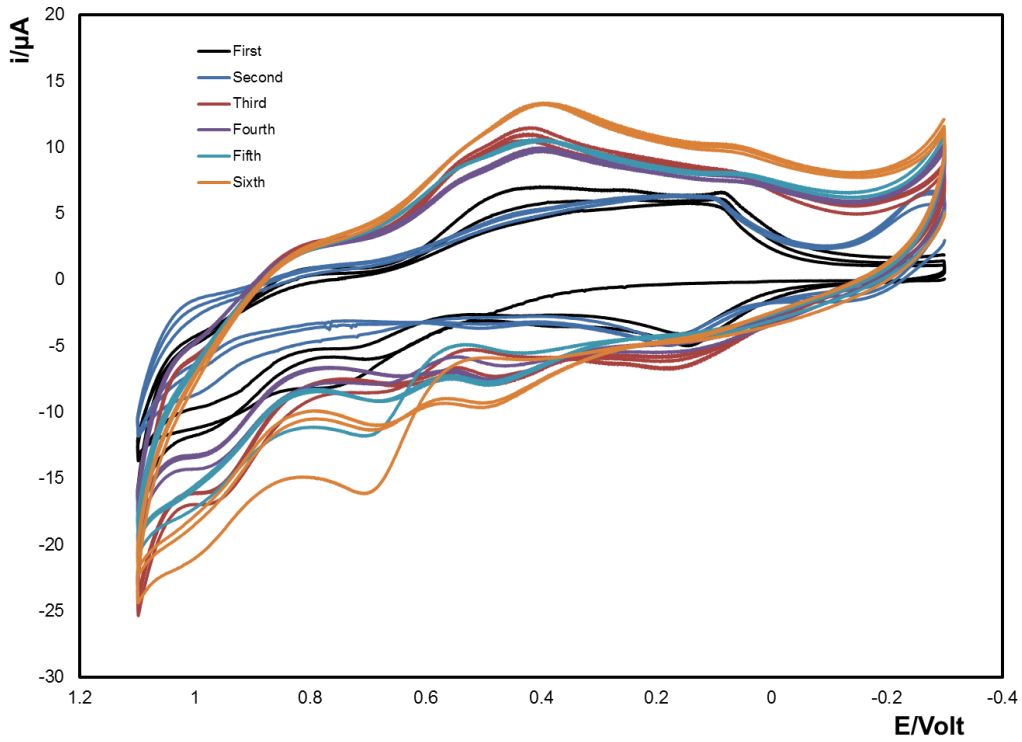


*Figure 4.15 Six cycles of adding N-Boc-aniline then deprotecting. Cyclic voltammograms of 0.5 $cm^2$ gold-coated silicon wafer electrodes modified with a mixed monolayer of 4ATP and butane-1-thiol in 1mM solution of N-Boc, aniline dissolved in 0.1 M solution of $LiClO_4$ in acetonitrile, potential swept between -0.35 and 1.1 V for three cycles and the scan rate was 0.1 $Vs^{-1}$.*

In Figure 4.15, five cyclic voltammograms showing five elongation/single monomer deposition cycles that were carried out using a 5mM solution of N-Boc-aniline solution in 0.1 M $LiClO_4$ solution in acetonitrile.

It can be noted that the difference between the positive and negative current increases with each elongation cycle at the potential used which was 0.9 V. That can be explained by the increase in the double layer capacitance at the electrode surface. This increase in capacitance is unlikely to come from changes in the effective dielectric constant at the electrode surface but rather suggest that the effective area of the electrode is increasing as the number of cycles increases, i.e., the electrodeposited film is electronically conducting to some degree.

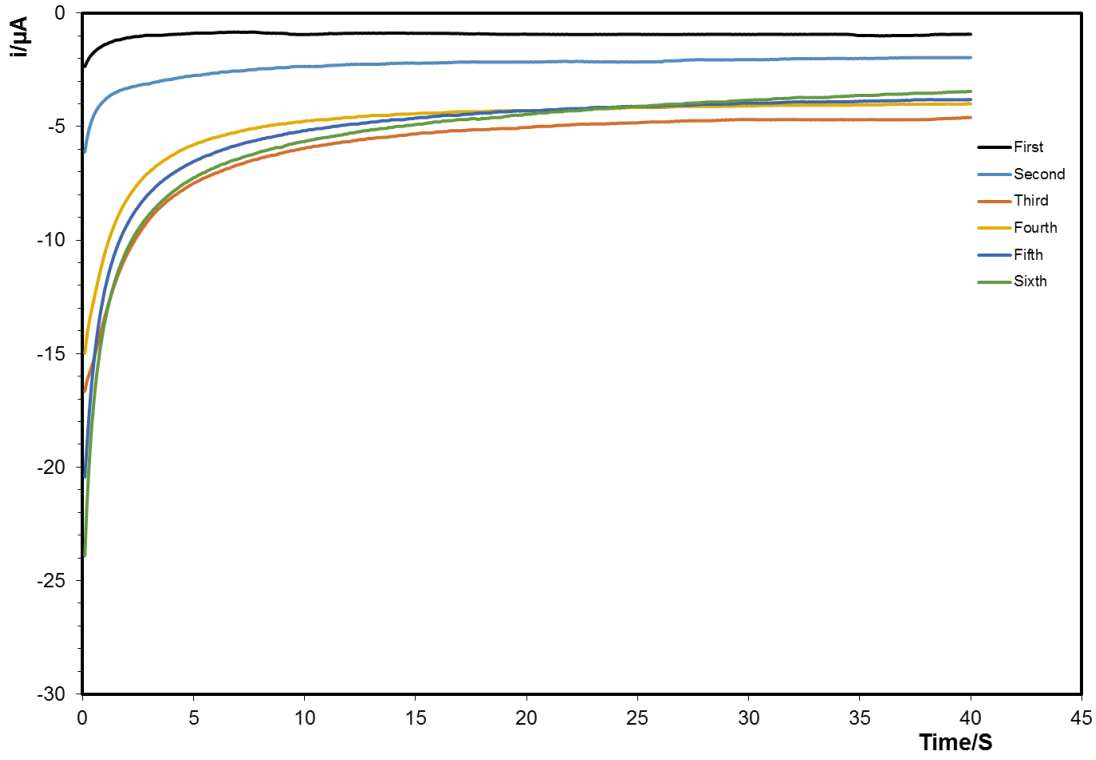


*Figure 4.16 Amperometric i-t transient for six cycles of polymer elongation. Electrode was 0.5 $cm^2$ gold-coated silicon wafer electrodes modified with a mixed monolayer of 4ATP and butane-1-thiol in 1mM solution of N-Boc, aniline dissolved in 0.1 M solution of $LiClO_4$ in acetonitrile, potential step was at 0.9 V for 40 s.*

Figure 4.16 shows the amperometric current time transient of six cycles of polymer elongation following the voltammetry shown in Figure 4.15. The potential step was at 0.9 V. The value of the initial current increases as the cycle number increase as expected from an increase in the effective area of

the electrode as the conducting backbone is deposited. Significantly, the steady state current increases with increasing cycle number which is consistent with the behaviour expected for an array of nano/microelectrodes, i.e., each monomer coupling site, where the diffusion fields do not overlap. The steady state current increases with each cycle because the polymer chain increases by a monomer unit during each cycle. Figure 4.17 depicts the whole cycle of the electrochemical polymerisation of one unite of the polymer.

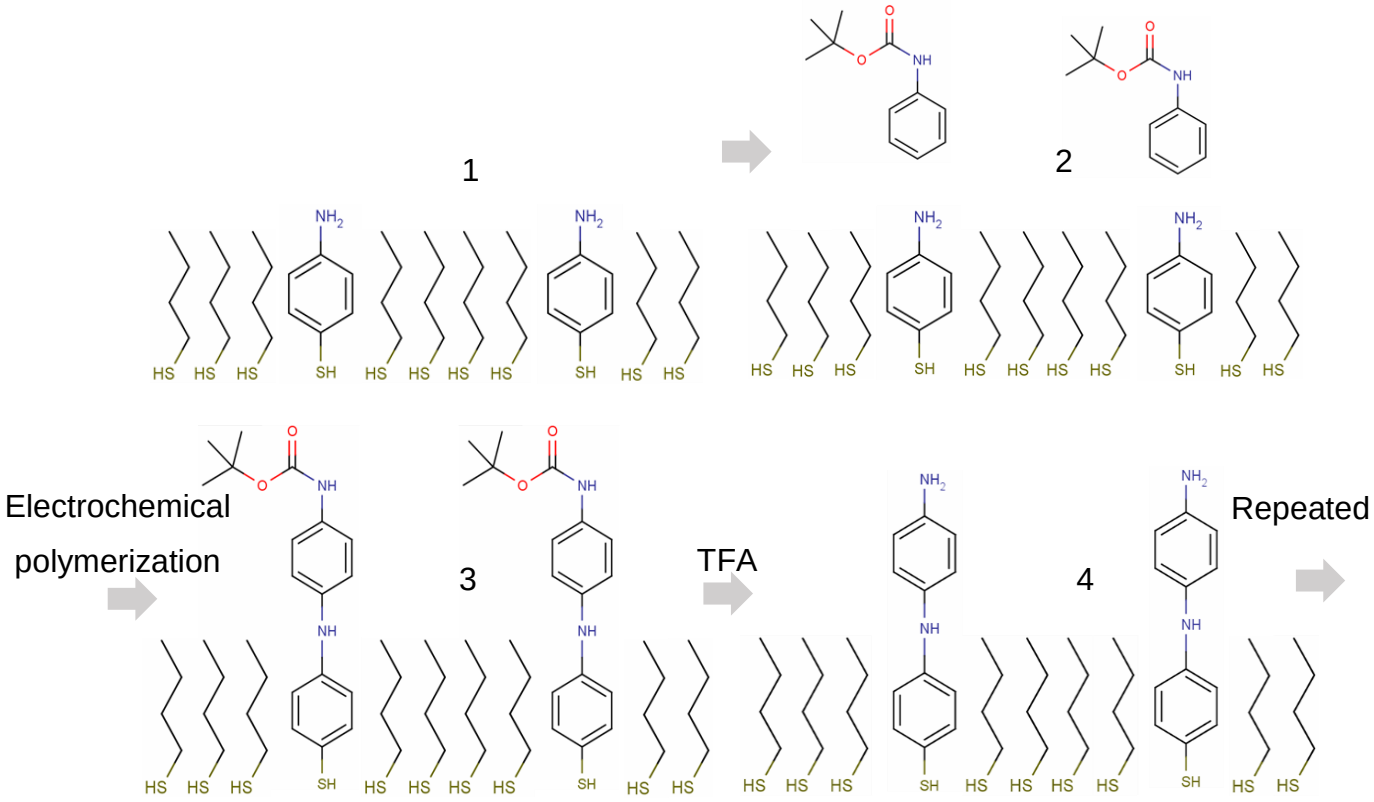


*Figure 4.17 The four steps of one cycle of stepwise electrochemical polymerization of aniline. Step1: attachment of mixed SAM on electrode surface. Step2: electrode surface in the t-Boc protected aniline before the electrochemical polymerization step. Step3: electrode surface after the electrochemical polymerization of one monomer. Step4: after deprotection of the t-Boc group using TFA.*

## 4.6 Stepwise growing of Thymine derivative polyaniline.

The same procedures are repeated again using the thymine derivative of the Boc-protected aniline (T-aniline) as a polymerization monomer.

As seen in Figure 4.18, the cyclic voltammetry of growing of six units of T-aniline shows an increase in the peak current and electrode capacitance with cycle number which is comparable to that observed using aniline and the oxidation peak in the first scan in the cyclic voltammetry is still larger than the following scans. Figure 4.19 shows the current-time transient of the amperometric steps and it also closely resembles the results obtained with the N-Boc-aniline.

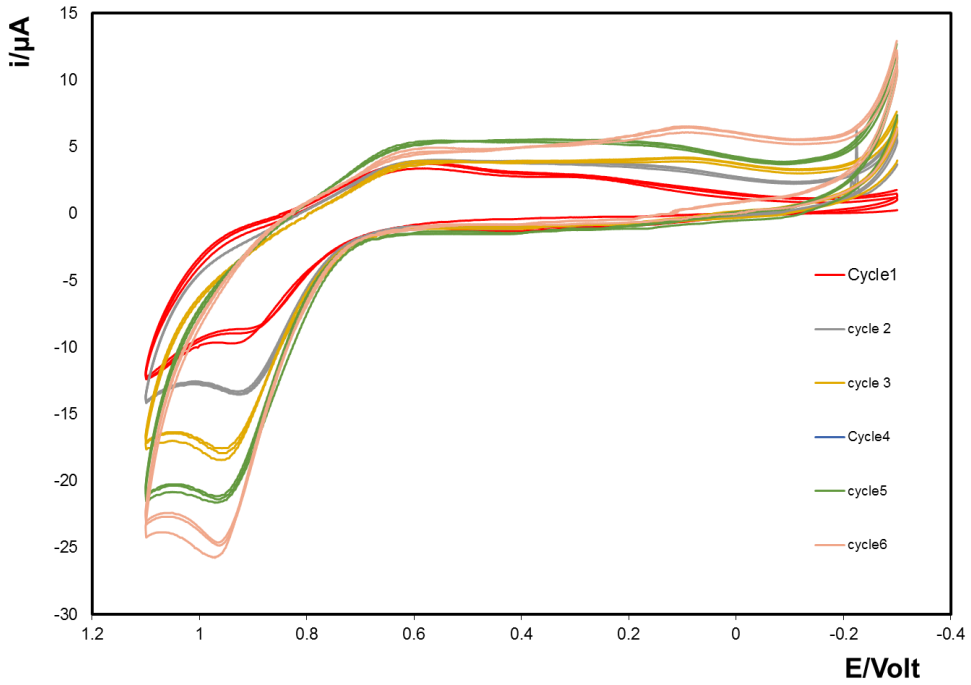


*Figure 4.18 Cyclic voltammetry of six cycles of adding T-aniline derivative then deprotecting. Elelcrode was 0.5 $cm^2$ gold-coated silicon wafer modified with a mixed monolayer of 4ATP and butane-1-thiol in 1mM solution of N-Boc, aniline dissolved in 0.1 M solution of $LiClO_4$ in acetonitrile, potential swept between -0.35 and 1.1 V for three cycles and the scan rate was 0.1 $Vs^{-1}$.*

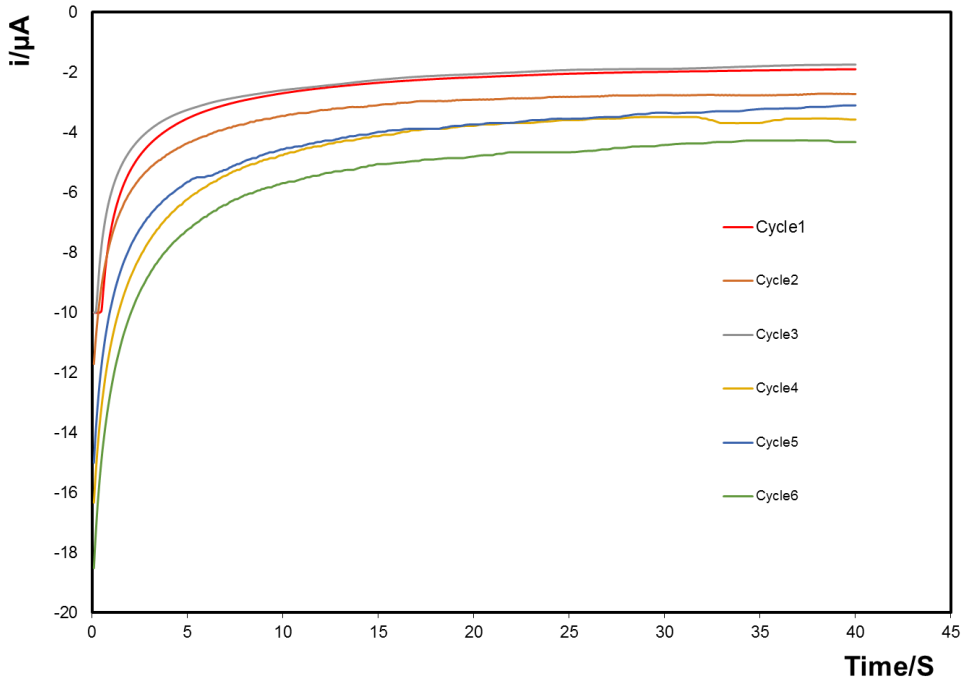


*Figure 4.19 Amperometric i-t transient for six cycles of adding T-aniline derivative then deprotecting. Electrode was 0.5 $cm^2$ gold-coated silicon wafer electrodes modified with a mixed monolayer of 4ATP and butane-1-thiol in 1mM solution of N-Boc, aniline dissolved in 0.1 M solution of $LiClO_4$ in acetonitrile, potential step was at 0.9 V for 40 s.*

## 4.7 Characterization of stepwise growth using gold particles attachment.

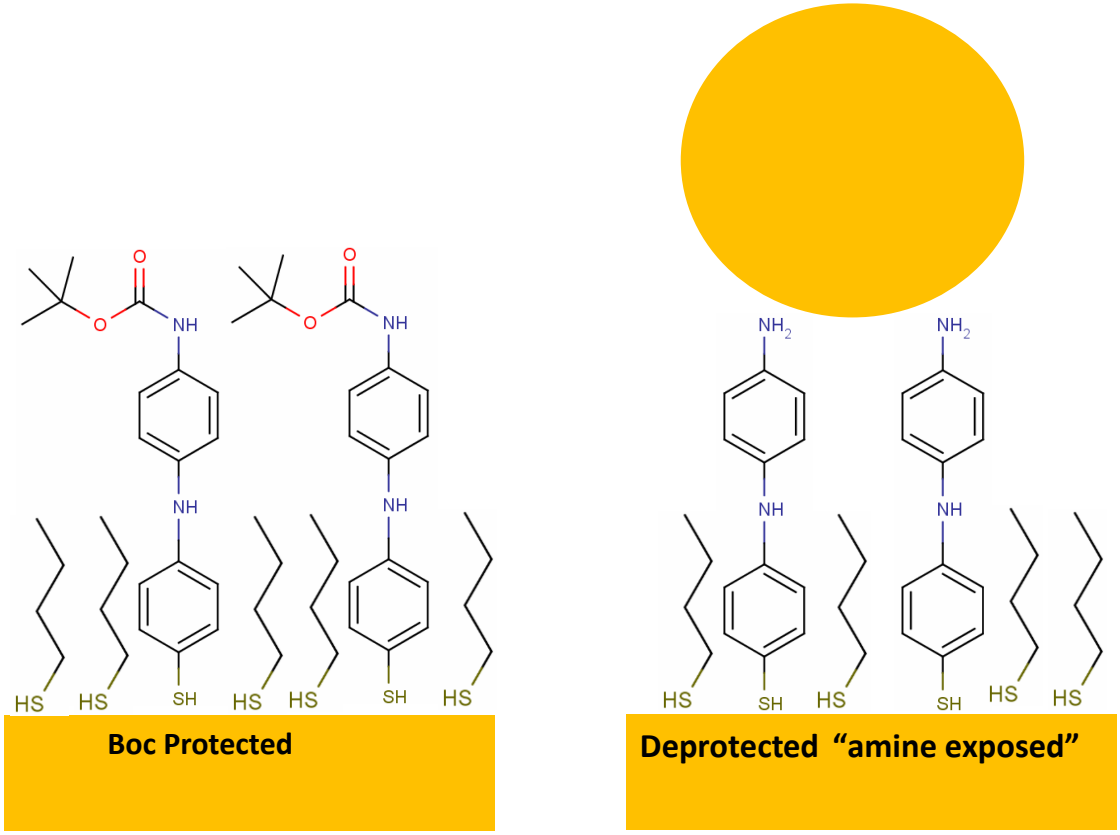


*Figure 4.20 Immobilization of gold nanoparticles on the modified electrode surface.*

As discussed in the literature review, the amino group can form a stable bond with metal atoms[154,155]. This property can be used here to characterize the nature of the electrode surface in each step of the polymer elongation cycle. After the electrochemical coupling of the aniline derivative, the terminal amino group is still protected by the t-Boc group. This protecting group will block the amino group from forming a bond with metallic nanoparticles. After the deprotection step using TFA, the amino group is exposed to the bulk of the solution and can bind a gold nanoparticle immobilizing it on the electrode surface. The ability of the electrode to immobilize gold particles was investigated at different stages of the elongation process using SEM.

As shown in Figure 4.22, the particles count was carried out by ImageJ software. The average number of particles across the entire electrode surface was 370 before the aniline is deprotected and this increases to 4570 particles following deprotection, i.e., there are approximately 12 times more particles immobilised on the deprotected surface. This result suggests that electrochemical cycling does not trigger deprotection to any great extent.

Also in Figure 4.22 it can be noted that the electrode surface before immobilization of particles shows a smooth organic film that is not observed in case of an unmodified gold-coated silicon wafer. The electrodes are covered with a five unites long polymer. Figure 4.21 shows calculated length of a polyaniline unit using HyperChem which was found to be 5.6 Å (0.56 nm). That suggests that a five units long layer of polymer with t-Boc protection should be close to 3 nm thick. The surface of the electrode does not show any large growth of polyaniline fibres or particles. That suggests that the growth was homogenous throughout the surface and forming a thin layer with no significant roughness detectable with the SEM resolution.

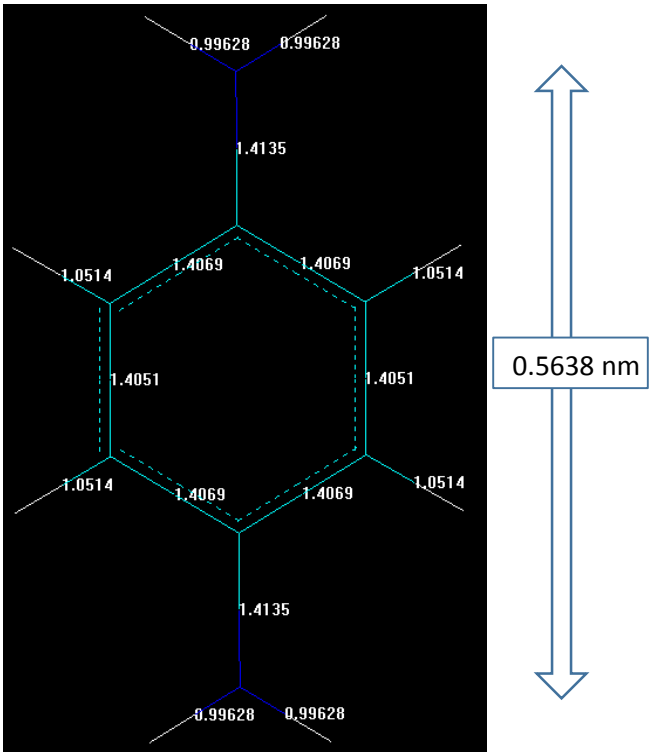


*Figure 4.21 Calculated bond lengths and the overall length of one unit of polyaniline optimised by Hyperchem.*

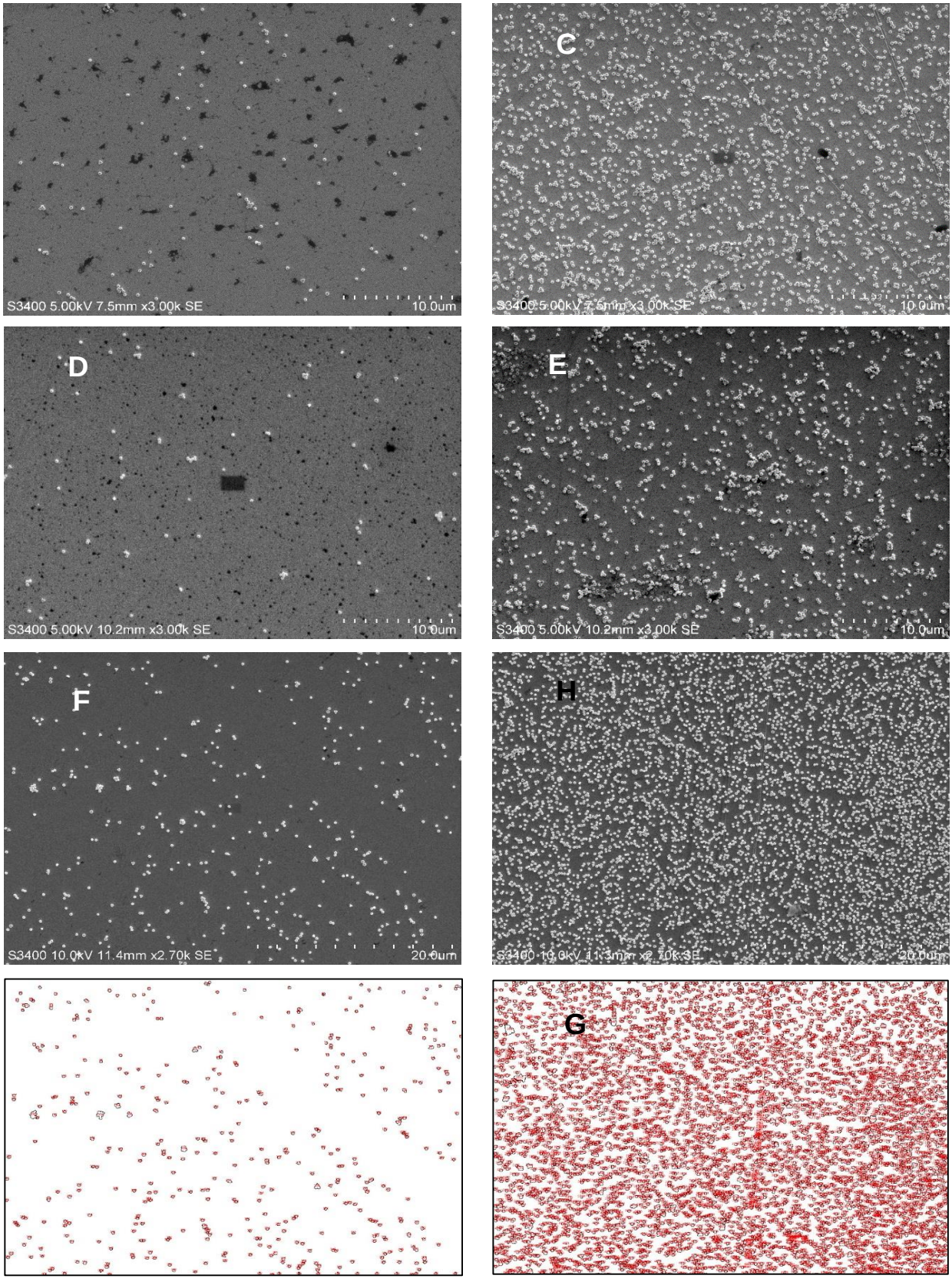


*Figure 4.22 SEM images for electrode surface after immobilization of gold particles. A,B represent electrode 1 before and after deprotection respectively. C,D, electrode 2 before and after deprotection. E and F, electrode 3 before and after deprotection. G and H are ImageJ particles count for electrode 3. At 5-10 kV.*

## 4.8 Assessment of polyaniline nucleic acid binding with DNA complementary strand.

The ultimate goal of the current work is to create an electronically conducting nucleic acid analogue which can bind to natural DNA strands. The DNA binding is crucial in the construction a DNA electrochemical biosensor, since without binding affinity to the capture strand, the target sequence will not attach. Also, the binding kinetics are important. Having a high association rate constant means that high concentrations of the target sequence will bind to the electrode surface in shorter times. The time needed to attain a steady state surface concentration at the kinetic equilibrium will directly influence the time taken from sample to answer.

Detection of DNA binding can be done via different ways. In this section, two different ways to confirm binding were described and information about the kinetics and equilibrium association constant of this binding was obtained.

### 4.8.1 6-fam labeled DNA binding.

A 6-Fam labeled DNA strand was purchased from Sigma Aldrich, which has the following sequence:

6Fam-3’ AAAAAAAAAAAAAAAAAAA 5’

i.e., it comprises 20 adenosine bases. The solution used was a 10 μM of the 6-Fam tagged DNA strand in TE buffer that is complementary to the artificial capture strand on the surface assembled using the stepwise electrochemical deposition approach. The chemical structure of 6-Fam is shown in Figure 4.25. A complementary structure of thymine derivative aniline was prepared following the method described in Section 4.6. The

number of monomers prepared was 15 by applying 15 cycles of polymer elongation. Control samples were prepared from N-Boc-aniline, that contains the backbone without the nucleotides. Figure 4.23 and Figure 4.24 shows the 15 cyclic voltammograms of the stepwise coupling of N-Boc-aniline and thymine derivative of aniline respectively. Three electrodes of the test and control electrodes were prepared. The electrodes were incubated in the DNA solution at 37°C for 7 h. The electrodes were then withdrawn and washed with deionized water to remove the loosely bound oligos.

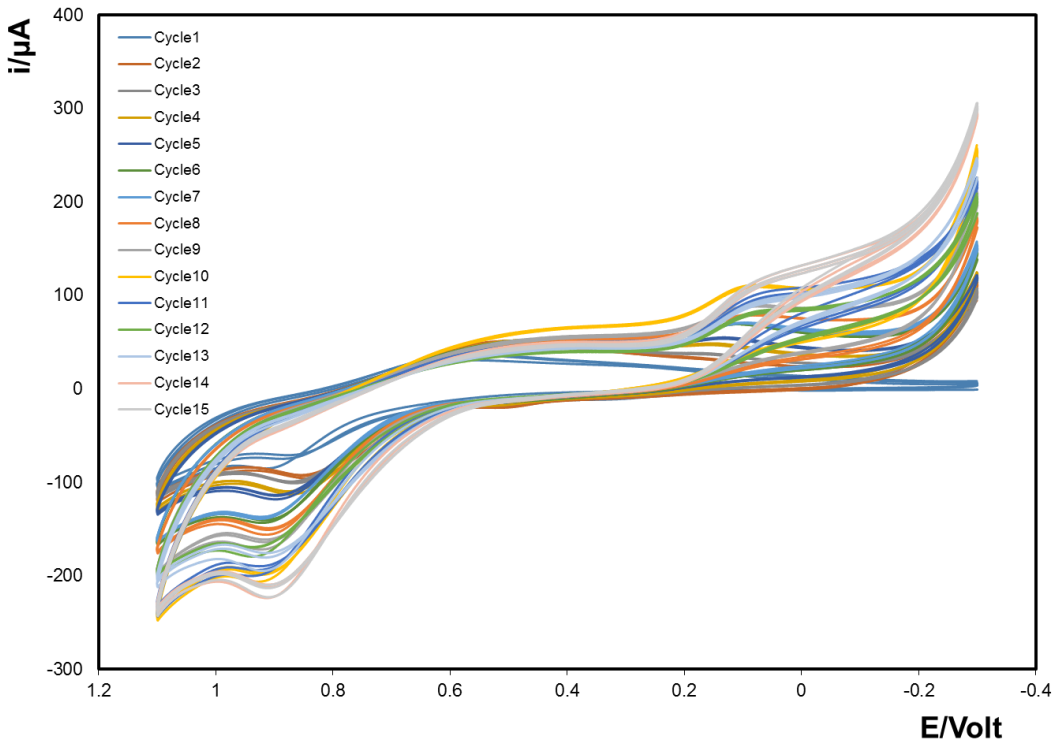


*Figure 4.23 Cyclic voltammetry of fifteen cycles of adding aniline and then deprotecting. Electrode was 0.5 $cm^2$ gold-coated silicon wafer modified with a mixed monolayer of 4ATP and butane-1-thiol in 1mM solution of N-Boc, aniline dissolved in 0.1 M solution of $LiClO_4$ in acetonitrile, the potential was swept between -0.35 and 1.1 V for three cycles and the scan rate was 0.1 $Vs^{-1}$.*

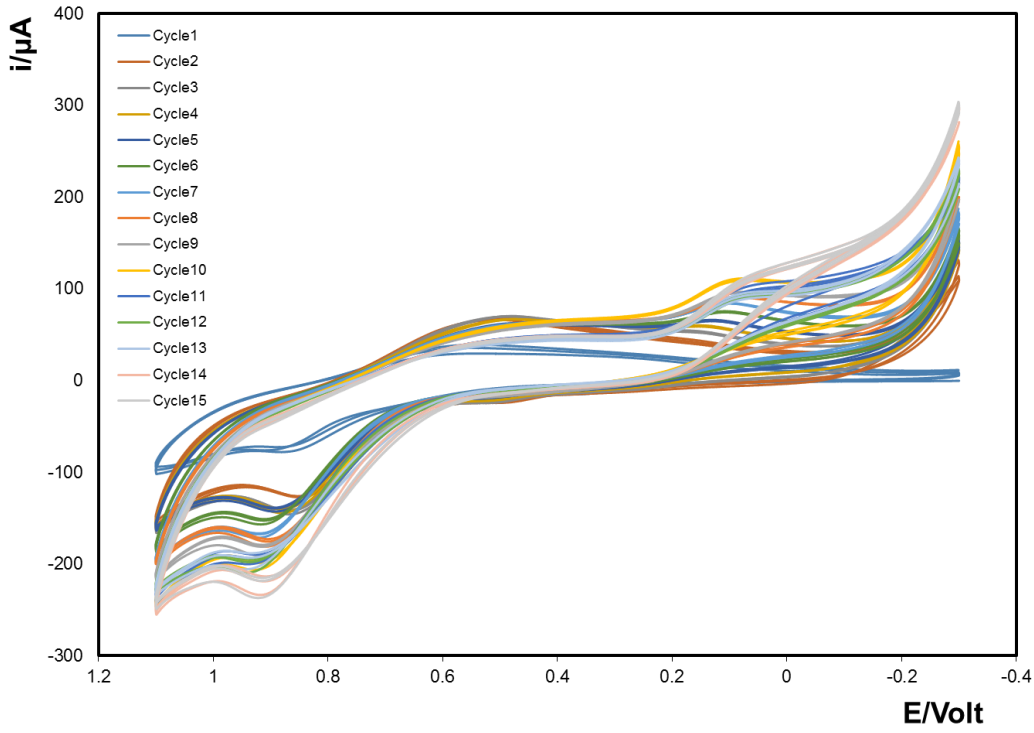


*Figure 4.24 Cyclic voltammetry of six cycles of adding T-aniline derivative then deprotecting. Electrodes was 0.5 $cm^2$ gold-coated silicon wafer modified with a mixed monolayer of 4ATP and butane-1-thiol in 1mM solution of N-Boc, aniline dissolved in 0.1 M solution of $LiClO_4$ in acetonitrile, potential swept between -0.35 and 1.1 V for three cycles and the scan rate was 0.1 $Vs^{-1}$.*

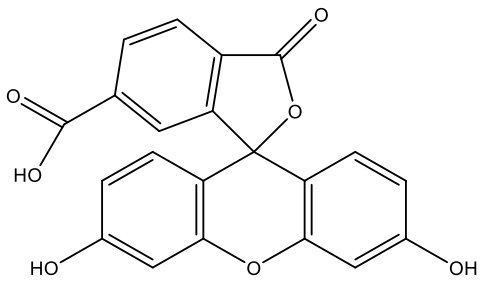


6-Fam

*Figure 4.25 Chemical structure of 6-fam.*

Figure 4.26 shows the voltammogram of an electrode modified with 15 monomers of thymine aniline derivative (PA-T) and an electrode modified with 15 monomers of aniline (PA). The latter electrode is used as a negative control. The cyclic voltammograms were carried out in 0.1 M solution of $H_2SO_4$. At about 0.06 V, a sharp reduction peak and its corresponding oxidation peak at about 0.25 V are visible in the PA-T sample. Those peaks

are not detectable in the voltammogram of the polyaniline modified electrode.

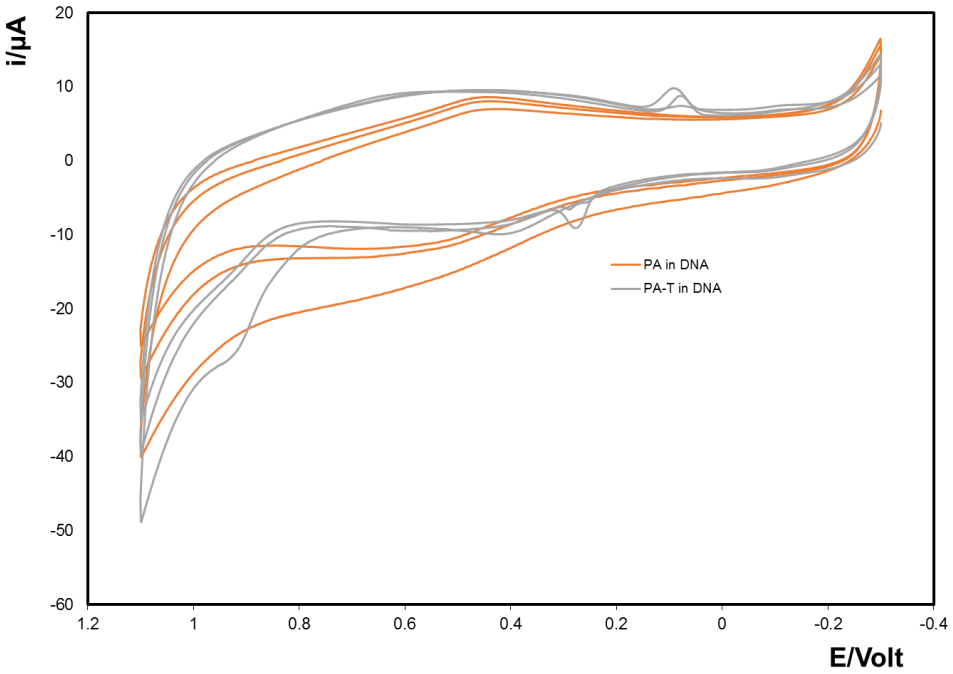


*Figure 4.26 Cyclic voltammogram of negative control (polyaniline chain) and sample (Poly Thymine-aniline derivative) after incubation with 6-Fam tagged complementary strand DNA. Aqueous 0.1M $H_2SO_4$ was used as contacting solution and scan rate was 0.1$Vs^{-1}$.*

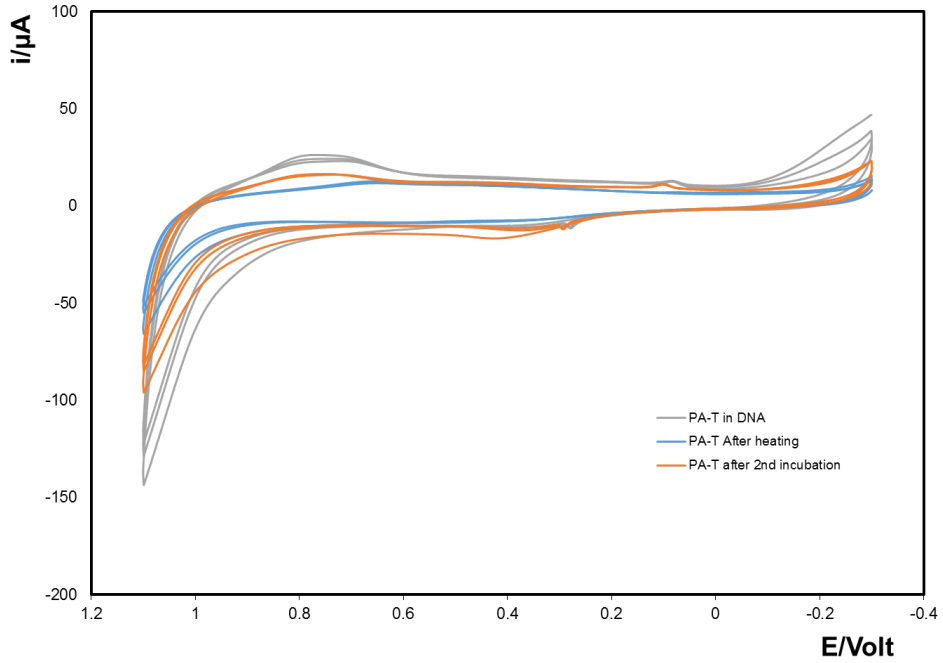


*Figure 4.27 Cyclic voltammogram of sample (Poly Thymine-aniline derivative) after incubation with 6-Fam tagged complementary strand DNA. Then after heating at 70°C for an 1 h and then after second incubation. Aqueous 0.1M $H_2SO_4$ was used as contacting solution and scan rate was 0.1$Vs^{-1}$.*

In order to further investigate the nature and origin of these unexpected peaks, the PA-T electrode was heated in deionized water to 70°C while stirring for an 1 h then rinsed with DW.

In Figure 4.27, the voltammogram of an electrode covered with the PA-T polymer is shown after incubation in the 6-Fam tagged complementary strand DNA, after heating and then after a second incubation. It was found that the redox couple appeared after the first incubation, disappeared after heating then reappeared again after the second incubation. In another experiment, the PA-T electrode was incubated in TE buffer and did not show the same peaks. These results strongly suggest that these peaks are associated with the 6-Fam tagged DNA binding to the electrode surface.

In Figure 4.28 the area under the reduction peak of this redox couple was calculated and the associated charge was found to be $A_p$= 2.4 X $10^{-6}$ C.

Using the following formula:

$$\Gamma = \frac{C}{F \times 2 \times A}$$

where $\Gamma$ is surface concentration in mol $cm^{-2}$, C is the charge in coulombs and obtained from the area under curve of the reduction peak, F is Faraday constant equals 96 485 C $mole^{-1}$ and A is the area of the electrode taken as 0.5 $cm^2$.

The surface coverage obtained, 2.6 $X10^{-11}$ mol $cm^{-2}$ corresponds to approximately 1.5$X10^{13}$ Oligos $cm^{-2}$

Comparing this value of surface coverage to theoretical value[129] = 5.8$X10^{12}$ Oligos/$cm^2$, and taking into account the uncertainty in the electrode areas and background capacitance charging, it appears that a monolayer of oligonucleotides is formed.

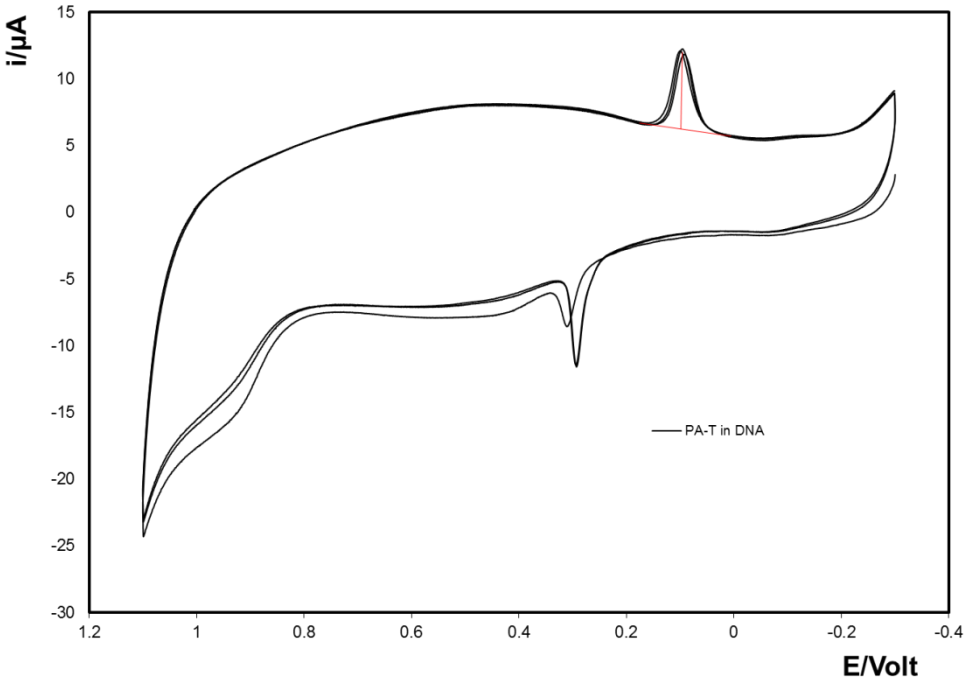


*Figure 4.28 Cyclic voltammogram of sample (Poly Thymine-aniline derivative) after incubation with 6-Fam tagged complementary strand DNA. Aqueous 0.1M $H_2SO_4$ was used as contacting solution and scan rate was 0.1Vs$^{-1}$.*

### 4.8.2 Platinum particles attached to DNA

Platinum is also a potentially useful label to probe the assembly of the synthetic capture strand since it is electrocatalytic.

The complementary strand of DNA was a thiolated oligonucleotide composed of a 20 base long chain of Adenosine nucleotides with the following sequence:

HS-C6-5'AAAAAAAAAAAAAAAAAAA3'

Platinum particles of 50 nm diameter were used and functionalized with the thiolated oligonucleotides by adding 1 µl of 100 µM solution to a 0.1 mg mL$^{-1}$ suspension of platinum particles. This concentration was used so that a close packed monolayer of the probe strand DNA could be assembled on the nanoparticle surface. This is important to reduce the available surface on the platinum particles to attach non-specifically to any free terminal amino group of the synthetic nucleic acid.

The test samples were prepared on gold coated silicon wafers with an area of approximately 0.5 $cm^2$ that was modified with thymine derivative chain of 15 monomer and in the last step, the terminal amino group was left protected with the t-Boc group so as to reduce the nonspecific binding of platinum particles. The preparation of those electrodes followed the procedures discussed in Section 4.6. The control samples were prepared using the same substrates as the test samples but where the “capture” strand comprises 15 monomers of aniline only, i.e., nucleic acid free, and the terminal amino group was left protected as in the case of the synthetic DNA samples.

Four test and control electrodes were incubated in the DNA functionalized platinum particles suspension at room temperature for 7 hours. They were then withdrawn and rinsed with deionised water to remove any non-specifically bound nanoparticles. The electrodes were used as the working electrode in a three electrode electrochemical cell. The electrolyte was 0.1 M $H_2SO_4$ solution in water. Amperometry was used to measure the current against time. Prior to peroxide addition, the system was left for 5 min to equilibrate and then enough $H_2O_2$ solution was added to give a concentration of 200 μM in the electrolyte solution. The current was then recorded for approximately another 5 min. The difference in the current before and after addition of $H_2O_2$ was determined. The experiment was carried out in duplicate and Figure 20 shows the corresponding calibration curve. This figure shows that there is a linear correlation between the concentration of the DNA-covered particles in suspension and the magnitude of the catalytic current for both the thymine derivative and the nucleic acid base system. However, the sensitivity for the thymine derivative is significantly higher (approximately 6x) indicating that while there is some non-specific binding capture-probe

complementarity is important in controlling the surface coverage of the platinum nanoparticles.

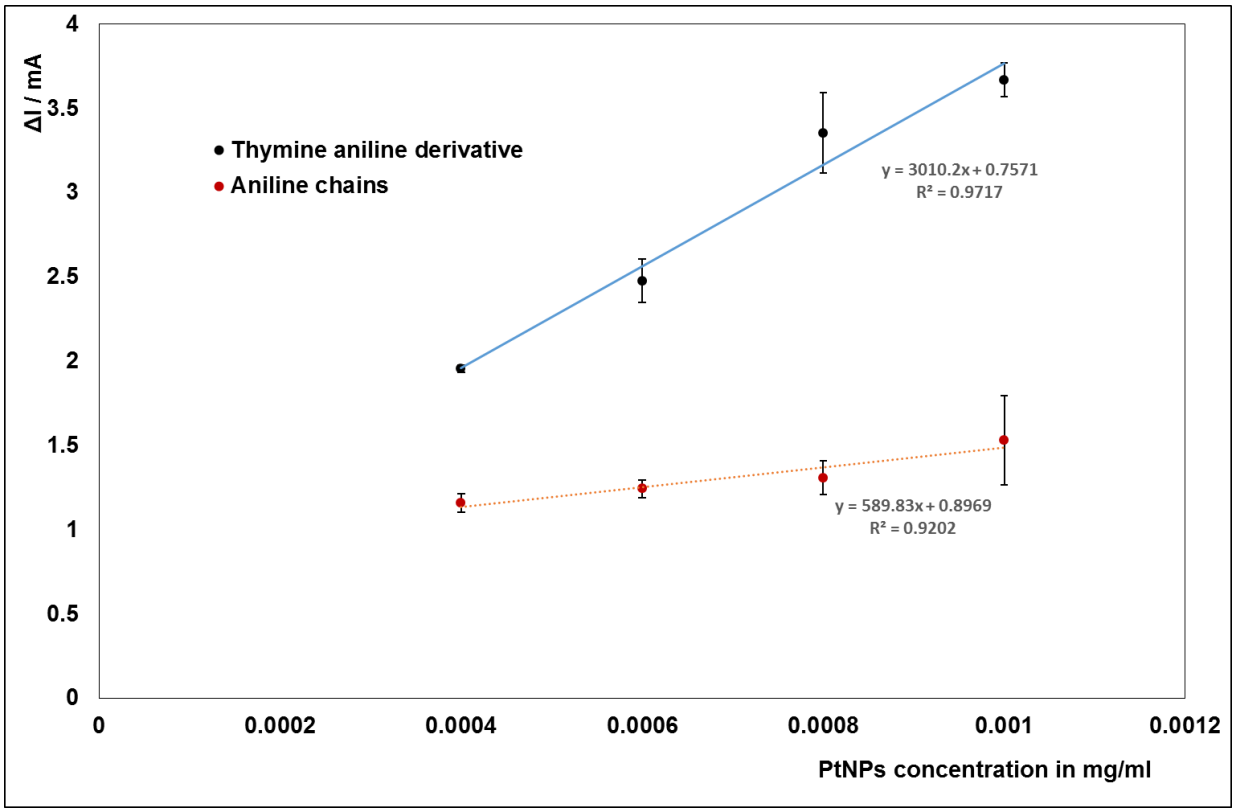


*Figure 4.29 Calibration plot for electrochemical catalysis of platinum particles immobilized via DNA bound to surface grown complementary conducting polymer. Δi represents the difference in current before and after addition of 200 μM $H_2O_2$ at an applied potential of −0.250 V following approximately 5 min equilibration time.*

Non-specific binding was observed previously in the SEM of gold particles attached to the electrode surface before deprotection as shown in Figure 4.22. And from the graph, it is obvious that the non-specific binding increases with the increased concentration of particles which is expected.

To convert the value of this experiment to the molar scale, the highest concentration used in this calibration curve was 0.001 mg/mL which is approximately equivalent to 1.6 $X10^{11}$ particles per litre. That is equivalent to about 250 fM concentration of bound DNA and the lowest concentration 0.004 mg/mL is equivalent to about 100 fM.

The electrocatalytic current density due to platinum particles tethered to the electrode surface by the conductive nucleic acid analogue can be compared to that of the current density for nanoparticles bound using naturally occurring DNA sequences. In the chapter on DNA mediated particles attachment, the current for the 100 fM was 8 µA and the area of the electrode was 0.0314 $cm^2$ the current density J can be calculated from the following formula:

$$J = \frac{I}{A}$$

where I is current and A is area. J was found to be 248 µA $cm^2$. Where the particles are bound by the conducting nucleic acid the current due to the 100 fM concentration of particles was 2 mA (2000 µA) and the electrode surface area was 0.5 $cm^2$ giving a current density of 4000 µA/$cm^2$. This significant 16 fold increase in current gives an indication about the ability of the conductive analogue to improve the amperometric signal in DNA nanoparticles sandwich assays

## 4.9 STM measurement of single molecule conductance

The electrochemical scanning tunnelling microscopy STM is a technique used to study the electrochemical and electron transfer properties at molecular level. It involves making an electrical connection to a single molecule by an STM tip and measuring the electric charge transport characteristics. The microscope is able to detect ultra-low currents (~ pA).

Scanning tunnelling microscope was used to probe the single molecule conductivity of the synthetic DNA analogue. The single molecule conductance and apparent length were both measured and the distribution of the adsorbates on the surface investigated.

### 4.9.1 Preparation of substrates

Arrandee™ substrates were used[156], they are made of gold-coated glass slides of a square shape of an area of approximately 0.25 $cm^2$. Before the use in electrochemical deposition the substrates are annealed to create an atomically flat surface by placing them into a hydrogen flame until dark red glowing is observed. The substrates are then removed from the flame and let to cool down for 30 s. Care should be taken not to overheat the substrate. This procedure is repeated two to three times to make sure that the atomically flat Au(111) terraces are formed.

### 4.9.2 Mixed monolayer assembly

The electrochemical deposition was carried out in the same way described previously. The substrates were immersed in the solution of the mixed monolayer with a concentration of 2 mM of 4ATP and 20 mM butane-1-thiol. The substrates then were left in the solution overnight for 16 h and then taken out and washed with ethanol and acetonitrile.

### 4.9.3 Stepwise electrochemical polymerization

The substrates modified with the mixed monolayer then were cycled in 5mM solution of the thymine derivative of aniline in 0.1 M $LiClO_4$ solution in acetonitrile, between -0.35 V and 1.1 V and the scan rate was 0.1 $Vs^{-1}$ for three cycles.

After the cyclic voltammetry, an amperometric step was applied at a potential of +0.900V for 40 s.

The substrates were then immersed in TFA 100% for 30 mins to deprotect the t-Boc group.

The cyclic voltammetry and amperometry were repeated 5 times to prepare a 5 units long polymer.

### 4.9.4 STM measurements

The STM measurements were conducted in collaboration with Tim Albrecht group from the Imperial College London. Four samples were examined with the break junction STM technique . The applied voltage bias, $V_{bias}$, was 0.3, 0.5, 0.7 and 0.9 V and the current set point $I_{sp}$ was in the range of 20 to 60 nA. Gold and platinum-iridium tips were used. The measurement was carried out in air and at room temperature.

### 4.9.5 Results and discussion

Figure 4.30 illustrates STM measurements of the Arrandee substrates after annealing and shows that atomically flat terraces approximately 100 nm deep are obtained. These terraces are essential for measuring single molecule conductivity and their presence indicates that the annealing process has been successful.

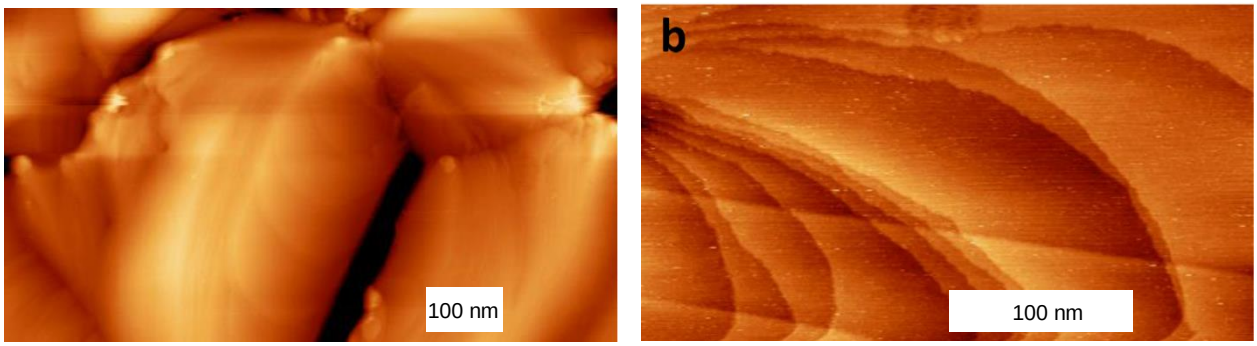


*Figure 4.30 STM images of Arrandee Au substrate after $H_2$ annealing showing atomically flat Au(111) terraces of about 100 nm width.*

A mixed SAM was adsorbed as previously described and then 5 units of the thymine derivative aniline were electrochemically polymerized.

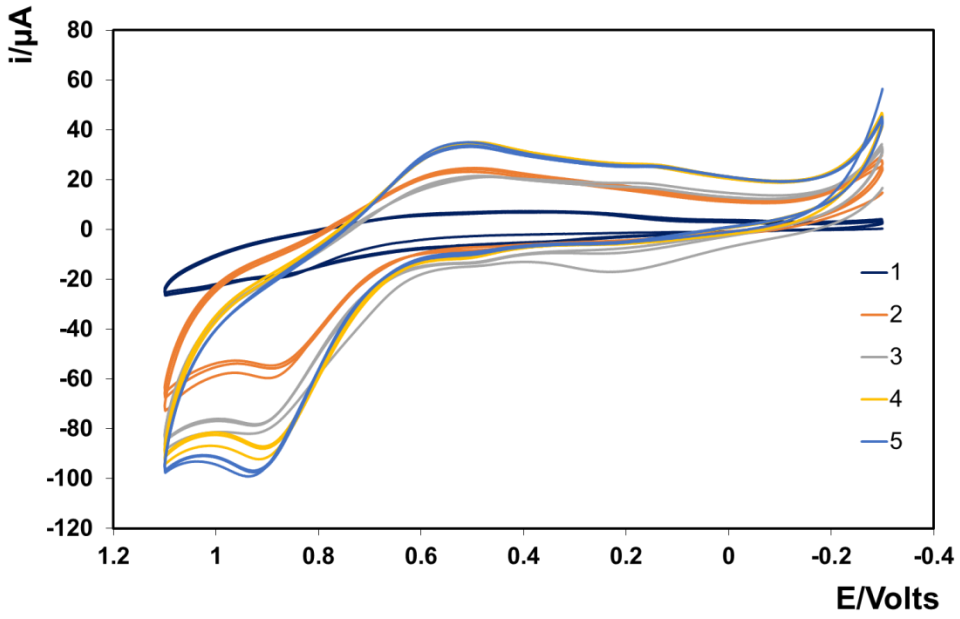


*Figure 4.31 Five cycles of adding aniline and then deprotecting. Cyclic voltammograms of 0.25 $cm^2$ gold-coated glass substrate modified with a mixed monolayer of 4ATP and butane-1-thiol in 5mM solution of thymine analogue of aniline dissolved in 0.1 M solution of $LiClO_4$ in acetonitrile, the potential swept between -0.35 and 1.1 V for three cycles and the scan rate was 0.1 $Vs^{-1}$.*

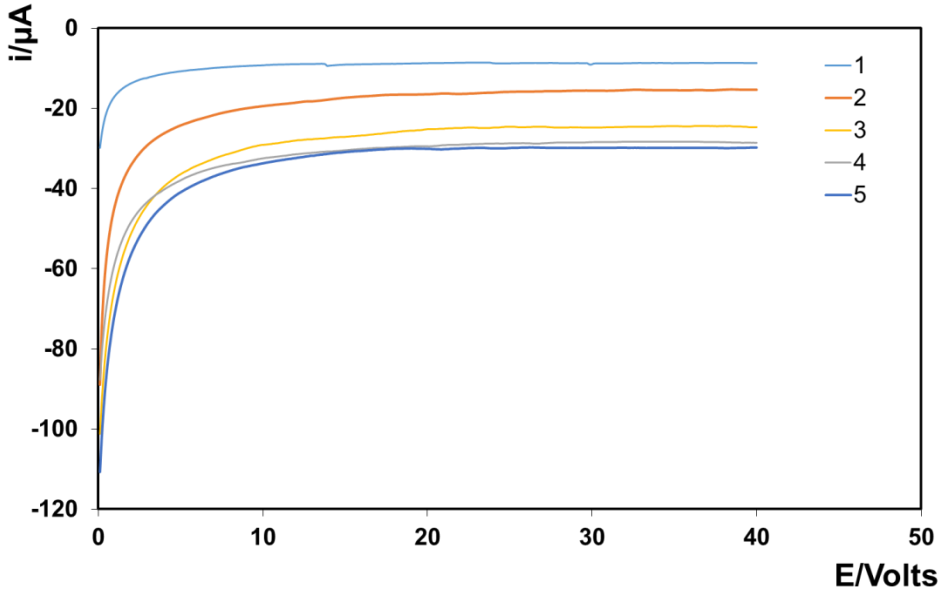


*Figure 4.32 Amperometric i-t transient for six cycles of adding T-aniline derivative then deprotecting. Electrode was 0.25 $cm^2$ gold-coated glass substrate modified with a mixed monolayer of 4ATP and butane-1-thiol in 5mM solution thymine analogue of aniline in 0.1 M solution of $LiClO_4$ in acetonitrile, potential step was at 0.9 V for 40 s.*

Figure 4.31 shows the cyclic voltammetry and Figure 4.32 shows the amperometry of the five steps of the electrochemical polymerisation of the T-aniline polymer. The same features and properties are observed on the Arrandee electrodes as those discussed previously for polycrystalline gold electrodes.

### 4.9.6 STM measurement of the synthetic DNA analogue

The STM can give information about electrical and morphological aspects of the synthetic DNA analogue. Imaging of the topography and the electrical conductance properties were carried out and discussed in the following sections.

#### 4.9.6.1 Surface topography

The footprint of a natural DNA is known in the literature[129] to be approximately 18 $nm^2$, i.e. an attached DNA molecule covers a circular area of 18 $nm^2$ on the electrode surface with a diameter of approximately 4.8 nm. The footprint of the synthetic polymer it expected to be in the same range.

Figure 4.33 shows the STM measurement of the substrate that shows regions of an organized monolayer that is separated by a distance of about 5 nm.

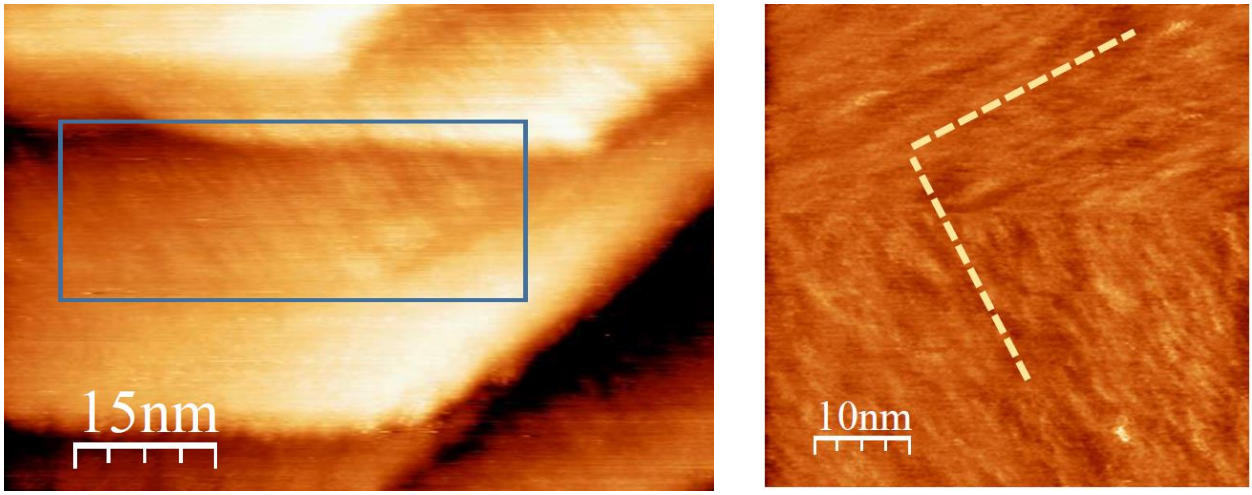


*Figure 4.33 STM image of gold substrate modified with 5 units long polymer on the left: flat of monolayer where the adsorbates are separated by approximately 5nm (see square on the image). On the right, 90° rotation of the sample to confirm the direction of the terrace.*

### 4.9.7 Single molecule conductance and length

As discussed earlier in Section 4.7, the length single unit of the polyaniline is approximately 0.57 nm, thus the length of the 5 units polymer is expected to be in the range between 2.5-3 nm.

The results of the break junction experiment conducted on the flat terraces are shown in Figure 4.34. The experiment shows clear single molecule conductance events. Most of the terraces showed a chain length between 2.5 and 3 nm (the length of the horizontal part of the terrace) is the expected for a five units long polymer. In only a few cases the length was measured between 5-6 nm which is consistent with coupling of more than one unit in a single deposition cycle, e.g., due to uncontrolled loss of a protecting group. These results demonstrate that the stepwise polymerization technique is providing a high degree of control over the length of the polymerized chains, which is crucial especially when a specifically coded polymer, i.e., nucleic acid analogues is desired.

However, despite the similarities in length, the current values obtained from the break junction experiment showed a wide distribution. From Figure 4.34, most of the terraces showed a plateau between 2 and 4 nA but some the range was from 0.5 to 6 nA. The average value was 3 nA ± 1.8 which shows that the standard deviation is significant.

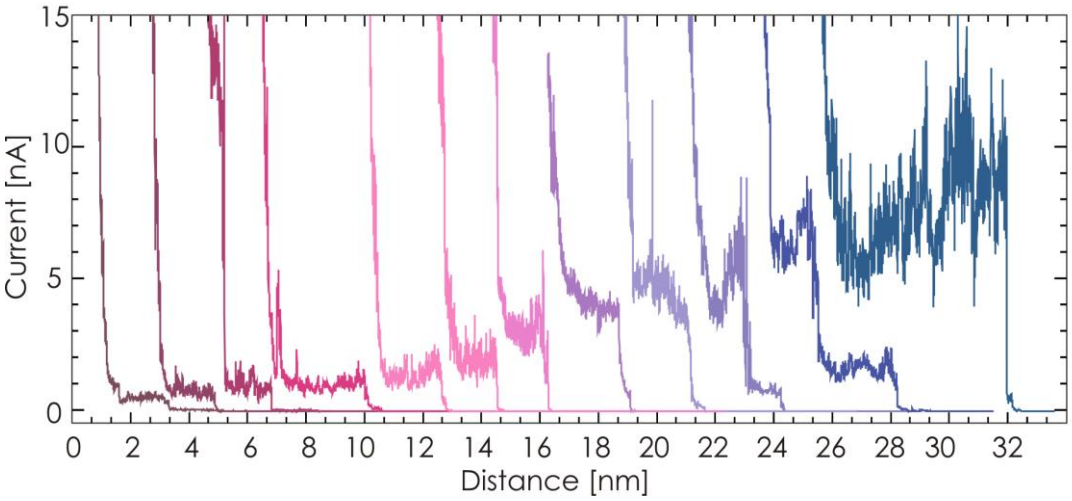


*Figure 4.34 Break junction traces of the conducting DNA analogue ($V_{bias}$ = 0.3V,I sp = 20 nA). The plateau length is approximately 2 -3 nm, just in a few cases is approaching 6nm (see the last blue trace). $I_s$ value 3 nA in average but the values range from 1 to 5 nA.*

The break junction experiment was repeated for four different voltage biases. The terraces were sorted and the values of $I_s$ against the counts per terrace were plotted, which is shown in the histogram in Figure 4.35. A peak at approximately 3 nA is detected at $V_{bias}$ of 0.3 V. A small peak is also apparent at 10 nA. Although the height and the shape of the peaks do not allow for the Gaussian fitting analysis and elucidation of the number of conducting molecules associated with each peak, the value of the conductance can be calculated and compared to previously reported values for a similar system.

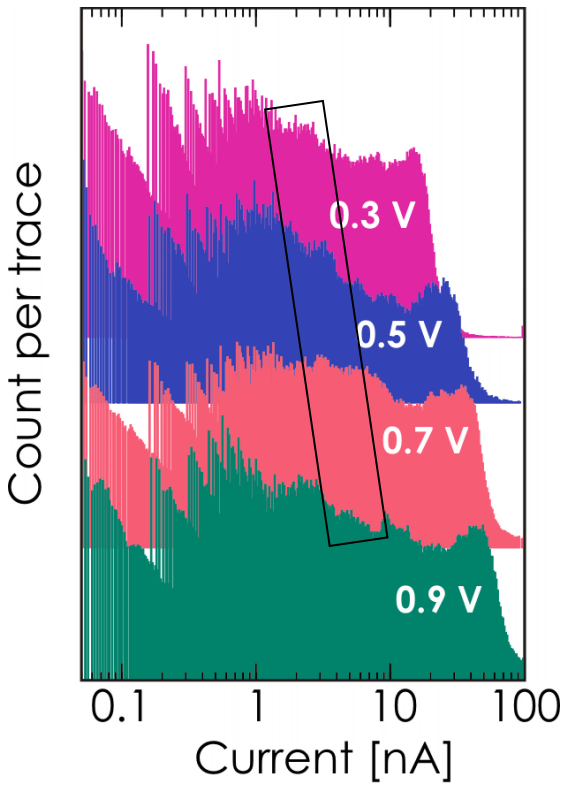


*Figure 4.35 $I_s$ current histograms after sorting for break junction terraces at different $V_{bias}$ values. A peak is detectable at approximately 3 nA at 0.3 $V_{bias}$ (marked by a black box).*

The current value for the detected peak 3 nA can be converted to conductance value using the formula: $G = I_s/V_{bias}$. The value obtained is 10 nS. As discussed in the literature review, the previously reported values for polyaniline single molecule conductance was 0.32 ± 0.03 nS for leucoemeraldine and 5.3 ± 0.4 nS for emeraldine salt in a hepta-aniline oligomer. This value can be due to two molecules conductance.

### 4.9.8 Conclusion

STM measurements provide valuable information and characterization for the deposited conducting DNA analogue. The electrode surface imagining showed the formation of ordered monolayer of the polymers with the expected dimensions. The single molecule conductance showed that the length of the polymer is within the expected length and the conductivity

measurement proves that there are conductance events, although a typical value for conductance or current was not determined.

# Chapter 5

# Conclusion and Future Work

"Science never solves a problem without creating ten more." *George Bernard Shaw*.

# 5 Chapter 5

## 5.1 Conclusion

This thesis reports on DNA electrochemical biosensors that utilize nanoparticle based sandwich assays for the detection of target DNA sequences.

A method for producing platinum nanoparticles, that are functionalised on one side with silver, which is then functionalised with probe strand DNA oligonucleotides, has been developed. Moreover, by performing the sandwich assay within a gold microcavity array (nanoparticle in microcavity architecture) the possibility of generating Surface Enhanced Raman Spectroscopy exists.

The assay has been applied to the detection of Staphylococcus aureus mastitis one of the causative bacteria for udder infection in cattle, it is a 41 base oligonucleotide, The dynamic range used was between 1 aM and 100 nM and a limit of detection of $1.5 \times 10^{-13}$ M was achieved.

Beyond the development of engineered nanoparticles for use as high sensitivity, multi-mode (electrochemistry and Raman spectroscopy) a second aspect of the thesis was the development of conducting capture strands that would enhance the rate of electron transfer from the electrode to the bound nanoparticle. Modified DNA analogues were designed and modelled. A polyaniline (PANI) based conductive nucleic acid analogue was identified as the optimum conducting. Then it was electrochemically synthesized and its binding to natural DNA was assessed. The PANI-NA was synthesized using a novel stepwise electrochemical polymerization method and characterized using electrochemical techniques and nanoparticles attachment and STM

measurement. Finally, the current generated by electrocatalytic reduction of hydrogen peroxide was measured as a function of the target concentration. The measurement of current densities of the electrodes modified with a PANI-NA capture strand immobilizing electrocatalytic nanoparticles was found to be 16 times the current densities obtained with DNA capture strand at similar concentrations.

## 5.2 Future work

Although the Raman enhancement was observed from the core-shell particles, but the optimisation of the architecture can be further tuned in terms of the composition and the size of core and shell. The electrochemical deposition method provided a robust way to fabricate a well-controlled structure.

Also the position of the particles inside the cavities is believed to be a factor in the enhancement. Directing the particles attachment into certain position inside the cavities by selectively depositing capture strand DNA the desired spots can control the position and the modes of enhancement and give more uniform spectra. Also different sizes of the cavities can be tried.

To utilize the electrochemical properties of the conductive DNA developed in this work, the other nucleotides monomers need to be chemically synthesized to allow a specifically coded nucleic acid analogue to be prepared that is complementary to real targets that are important for disease detection and diagnosis.

The prepared PANI nucleic analogue showed promising electrochemical properties. Thymine was the only nucleotide analogue that was synthesized. The next step should be the synthesis of the other nucleotide analogues to prepare a sequenced polymer that can bind real DNA samples.

The stepwise polymerization procedures is an interesting process that can be automated by designing an automatic synthesizer that allows quick and facile production of PANI-NA sequences and modified sequences in a way resembles the conventional DNA and PNA synthesizers. Which will allow producing different analogues and modified backbones.

The t-Boc protecting group for the stepwise electrochemical polymerization procedures can also be replaced by a group that does not need strong acids like TFA. In this study, the t-Boc cleavage required 30 min immersion in TFA. A reductively cleaved protecting group can provide a very interesting alternative. Applying a reductive potential to the polymer will deprotect the terminal amino group while and oxidative potential will attach the following monomer. And the stepwise elongation can be carried out much quicker by applying a simple cyclic voltammetry or alternative oxidative and reducing steps.

The charge transfer can be improved by trying different dopants to the PANI-NA analogue. Side chain modification of the aniline backbone can provide a means to attach groups that can act as self-dopant can improve the charge transfer and hence the conductivity. Other electrochemical or luminescent probes can also be attached to the backbone.

# 6 References


1. Oliver, N.; Toumazou, C.; Cass, A.; Johnston, D. Glucose sensors: a review of current and emerging technology. *Diabetic Med.* **2009***, 26*, 197-210.

2. Ozer, J.; Ratner, M.; Shaw, M.; Bailey, W.; Schomaker, S. The current state of serum biomarkers of hepatotoxicity. *Toxicology* **2008***, 245*, 194-205.

3. Abelev, G.; Eraiser, T. In *In Cellular aspects of alpha-fetoprotein reexpression in tumors;* Seminars in cancer biology; Elsevier: 1999; Vol. 9, pp 95-107.

4. Metzker, M. L. Sequencing technologies—the next generation. *Nature reviews genetics* **2010***, 11*, 31-46.

5. Gonzaga-Jauregui, C.; Lupski, J. R.; Gibbs, R. A. Human genome sequencing in health and disease. *Annu. Rev. Med.* **2012***, 63*, 35-61.

6. Schwarzenbach, H.; Hoon, D. S.; Pantel, K. Cell-free nucleic acids as biomarkers in cancer patients. *Nature Reviews Cancer* **2011***, 11*, 426-437.

7. Zhang, X.; Zhang, Z.; Dai, F.; Shi, B.; Chen, L.; Zhang, X.; Zang, G.; Zhang, J.; Chen, X.; Qian, F. Comparison of circulating, hepatocyte specific messenger RNA and microRNA as biomarkers for chronic hepatitis B and C. *PloS one* **2014***, 9*, e92112.

8. Creemers, E. E.; Tijsen, A. J.; Pinto, Y. M. Circulating microRNAs: novel biomarkers and extracellular communicators in cardiovascular disease? *Circ. Res.* **2012***, 110*, 483-495.

9. Wei, F.; Lillehoj, P. B.; Ho, C. DNA diagnostics: nanotechnology-enhanced electrochemical detection of nucleic acids. *Pediatr. Res.* **2010***, 67*, 458-468.

10. Niemz, A.; Ferguson, T. M.; Boyle, D. S. Point-of-care nucleic acid testing for infectious diseases. *Trends Biotechnol.* **2011***, 29*, 240-250.

11. Gillespie, B. E.; Oliver, S. P. Simultaneous Detection of Mastitis Pathogens, Staphylococcus aureus, Streptococcus uberis, and Streptococcus agalactiae by Multiplex Real-Time Polymerase Chain Reaction. *J. Dairy Sci.* **2005***, 88*, 3510-3518.

12. Syring, C.; Boss, R.; Reist, M.; Bodmer, M.; Hummerjohann, J.; Gehrig, P.; Graber, H. U. Bovine mastitis: The diagnostic properties of a PCR-based assay to monitor the Staphylococcus aureus genotype B status of a herd, using bulk tank milk. *J. Dairy Sci.* **2012***, 95*, 3674-3682.

13. Charman, N.; Dyson, R.; Hodge, A.; Robertson, N.; Chaplin, S. In *In A survey of mastitis pathogens in the south-eastern Australian dairy industry;* Proceedings of Countdown Symposium 2012; 2012; , pp 18-22.

14. Seegers, H.; Fourichon, C.; Beaudeau, F. Production effects related to mastitis and mastitis economics in dairy cattle herds. *Vet. Res.* **2003***, 34*, 475-491.

15. Huijps, K.; Lam, T. J.; Hogeveen, H. Costs of mastitis: facts and perception. *J. Dairy Res.* **2008***, 75*, 113-120.

16. Kulkarni, A. G.; Kaliwal, B. BOVINE MASTITIS: A REVIEW. **2013**.

17. Viguier, C.; Arora, S.; Gilmartin, N.; Welbeck, K.; O'Kennedy, R. Mastitis detection: current trends and future perspectives. *Trends Biotechnol.* **2009***, 27*, 486-493.

18. Fox, L.; Adams, D. The Ability of the Enzyme-Linked Immunosorbent Assay to Detect Antibody against Staphylococcus aureus in Milk following Experimental Intramammary Infection. *Journal of Veterinary Medicine, Series B* **2000***, 47*, 517-526.

19. Norberg, E. Electrical conductivity of milk as a phenotypic and genetic indicator of bovine mastitis: A review. *Livest. Prod. Sci.* **2005***, 96*, 129-139.

20. Schukken, Y. H.; Wilson, D. J.; Welcome, F.; Garrison-Tikofsky, L.; Gonzalez, R. N. Monitoring udder health and milk quality using somatic cell counts. *Vet. Res.* **2003***, 34*, 579-596.

21. Hovinen, M.; Aisla, A.; Pyörälä, S. Accuracy and reliability of mastitis detection with electrical conductivity and milk colour measurement in automatic milking. *Acta Agriculturae Scand Section A* **2006***, 56*, 121-127.

22. Hettinga, K.; Van Valenberg, H.; Lam, T.; Van Hooijdonk, A. Detection of mastitis pathogens by analysis of volatile bacterial metabolites. *J. Dairy Sci.* **2008***, 91*, 3834-3839.

23. Åkerstedt, M.; Björck, L.; Persson Waller, K.; Sternesjö, Å Biosensor assay for determination of haptoglobin in bovine milk. *J. Dairy Res.* **2006***, 73*, 299-305.

24. Viguier, C.; Arora, S.; Gilmartin, N.; Welbeck, K.; O'Kennedy, R. Mastitis detection: current trends and future perspectives. *Trends Biotechnol.* **2009***, 27*, 486-493.

25. Thévenot, D. R.; Toth, K.; Durst, R. A.; Wilson, G. S. Electrochemical biosensors: recommended definitions and classification. *Biosensors and Bioelectronics* **2001***, 16*, 121-131.

26. Liu, A.; Wang, K.; Weng, S.; Lei, Y.; Lin, L.; Chen, W.; Lin, X.; Chen, Y. Development of electrochemical DNA biosensors. *TrAC Trends in Analytical Chemistry* **2012***, 37*, 101-111.

27. Wang, J. Electrochemical nucleic acid biosensors. *Anal. Chim. Acta* **2002***, 469*, 63-71.

28. Lereau, M.; Fournier-Wirth, C.; Mayen, J.; Farre, C.; Meyer, A.; Dugas, V.; Cantaloube, J.; Chaix, C.; Vasseur, J.; Morvan, F. Development of innovative and versatile polythiol probes for use on ELOSA or electrochemical biosensors: application in hepatitis C virus genotyping. *Anal. Chem.* **2013***, 85*, 9204-9212.

29. Hamidi-Asl, E.; Palchetti, I.; Hasheminejad, E.; Mascini, M. A review on the electrochemical biosensors for determination of microRNAs. *Talanta* **2013***, 115*, 74-83.

30. Chen, A.; Chatterjee, S. Nanomaterials based electrochemical sensors for biomedical applications. *Chem. Soc. Rev.* **2013***, 42*, 5425-5438.

31. Turner, A. P. Biosensors: sense and sensibility. *Chem. Soc. Rev.* **2013***, 42*, 3184-3196.

32. Bora, U.; Sett, A.; Singh, D. Nucleic Acid Based Biosensors for Clinical Applications. *Biosens J* **2013***, 1*, 104.

33. Bastús, N. G.; Merkoçi, F.; Piella, J.; Puntes, V. Synthesis of highly monodisperse citrate-stabilized silver nanoparticles of up to 200 nm: kinetic control and catalytic properties. *Chemistry of Materials* **2014***, 26*, 2836-2846.

34. Lee, N.; Yoo, D.; Ling, D.; Cho, M. H.; Hyeon, T.; Cheon, J. Iron Oxide Based Nanoparticles for Multimodal Imaging and Magnetoresponsive Therapy. *Chem. Rev.* **2015***, 115*, 10637-10689.

35. Saha, K.; Agasti, S. S.; Kim, C.; Li, X.; Rotello, V. M. Gold nanoparticles in chemical and biological sensing. *Chem. Rev.* **2012***, 112*, 2739-2779.

36. Starowicz, Z.; Lipiński, M.; Socha, R.; Berent, K.; Kulesza, G.; Ozga, P. Photochemical silver nanoparticles deposition on sol–gel TiO2 for plasmonic properties utilization. *J. Sol Gel Sci. Technol.* **2015***, 73*, 563-571.

37. Peng, Z.; Yang, H. Designer platinum nanoparticles: Control of shape, composition in alloy, nanostructure and electrocatalytic property. *Nano Today* **2009***, 4*, 143-164.

38. Chen, A.; Holt-Hindle, P. Platinum-based nanostructured materials: synthesis, properties, and applications. *Chem. Rev.* **2010***, 110*, 3767-3804.

39. Wang, J. Electrochemical biosensing based on noble metal nanoparticles. *Microchimica Acta* **2012***, 177*, 245-270.

40. Zhou, H.; Chen, H.; Luo, S.; Chen, J.; Wei, W.; Kuang, Y. Glucose biosensor based on platinum microparticles dispersed in nano-fibrous polyaniline. *Biosensors and Bioelectronics* **2005***, 20*, 1305-1311.

41. Qiaocui, S.; Tuzhi, P.; Yunu, Z.; Yang, C. F. An Electrochemical Biosensor with Cholesterol Oxidase/Sol-Gel Film on a Nanoplatinum/Carbon Nanotube Electrode. *Electroanalysis* **2005***, 17*, 857-861.

42. Yang, G.; Yuan, R.; Chai, Y. A high-sensitive amperometric hydrogen peroxide biosensor based on the immobilization of hemoglobin on gold colloid/l-cysteine/gold colloid/nanoparticles Pt–chitosan composite film-modified platinum disk electrode. *Colloids and Surfaces B: Biointerfaces* **2008***, 61*, 93-100.

43. Polsky, R.; Gill, R.; Kaganovsky, L.; Willner, I. Nucleic acid-functionalized Pt nanoparticles: catalytic labels for the amplified electrochemical detection of biomolecules. *Anal. Chem.* **2006***, 78*, 2268-2271.

44. Spain, E.; Brennan, E.; McArdle, H.; Keyes, T. E.; Forster, R. J. High Sensitivity DNA Detection Based on Regioselectively Decorated Electrocatalytic Nanoparticles. *Anal. Chem.* **2012***, 84*, 6471-6476.

45. Spain, E.; McArdle, H.; Keyes, T. E.; Forster, R. J. Detection of sub-femtomolar DNA based on double potential electrodeposition of electrocatalytic platinum nanoparticles. *Analyst* **2013***, 138*, 4340-4344.

46. Bouzek, K.; Mangold, K.; Jüttner, K. Platinum distribution and electrocatalytic properties of modified polypyrrole films. *Electrochim. Acta* **2001***, 46*, 661-670.

47. Wang, J.; Polsky, R.; Xu, D. Silver-enhanced colloidal gold electrochemical stripping detection of DNA hybridization. *Langmuir* **2001***, 17*, 5739-5741.

48. Zhang, Y.; Zhang, K.; Ma, H. Electrochemical DNA biosensor based on silver nanoparticles/poly (3-(3-pyridyl) acrylic acid)/carbon nanotubes modified electrode. *Anal. Biochem.* **2009***, 387*, 13-19.

49. Lee, P.; Meisel, D. Adsorption and surface-enhanced Raman of dyes on silver and gold sols. *J. Phys. Chem.* **1982***, 86*, 3391-3395.

50. Kneipp, K.; Flemming, J. Surface enhanced Raman scattering (SERS) of nucleic acids adsrobed on colloidal silver particles. *J. Mol. Struct.* **1986***, 145*, 173-179.

51. Kneipp, K.; Kneipp, H.; Kartha, V. B.; Manoharan, R.; Deinum, G.; Itzkan, I.; Dasari, R. R.; Feld, M. S. Detection and identification of a single DNA

base molecule using surface-enhanced Raman scattering (SERS). *Physical Review E* **1998**, *57*, R6281.

52. Bell, S. E.; Sirimuthu, N. M. Surface-enhanced Raman spectroscopy (SERS) for sub-micromolar detection of DNA/RNA mononucleotides. *J. Am. Chem. Soc.* **2006**, *128*, 15580-15581.

53. Cao, Y. C.; Jin, R.; Mirkin, C. A. Nanoparticles with Raman spectroscopic fingerprints for DNA and RNA detection. *Science* **2002**, *297*, 1536-1540.

54. Braun, G.; Lee, S. J.; Dante, M.; Nguyen, T.; Moskovits, M.; Reich, N. Surface-enhanced Raman spectroscopy for DNA detection by nanoparticle assembly onto smooth metal films. *J. Am. Chem. Soc.* **2007**, *129*, 6378-6379.

55. Wu, L.; Wang, Z.; Zong, S.; Huang, Z.; Zhang, P.; Cui, Y. A SERS-based immunoassay with highly increased sensitivity using gold/silver core-shell nanorods. *Biosensors and Bioelectronics* **2012**, *38*, 94-99.

56. MinháTran, T. SERS spectroscopy and SERS imaging of Shewanella oneidensis using silver nanoparticles and nanowires. *Chemical Communications* **2011**, *47*, 4129-4131.

57. Rycenga, M.; Cobley, C. M.; Zeng, J.; Li, W.; Moran, C. H.; Zhang, Q.; Qin, D.; Xia, Y. Controlling the synthesis and assembly of silver nanostructures for plasmonic applications. *Chem. Rev.* **2011**, *111*, 3669-3712.

58. Kelf, T.; Sugawara, Y.; Cole, R.; Baumberg, J.; Abdelsalam, M.; Cintra, S.; Mahajan, S.; Russell, A.; Bartlett, P. Localized and delocalized plasmons in metallic nanovoids. *Physical Review B* **2006**, *74*, 245415.

59. Bartlett, P.; Baumberg, J.; Birkin, P. R.; Ghanem, M.; Netti, M. Highly ordered macroporous gold and platinum films formed by electrochemical deposition through templates assembled from submicron diameter monodisperse polystyrene spheres. *Chemistry of Materials* **2002**, *14*, 2199-2208.

60. Gamero, M.; Sosna, M.; Pariente, F.; Lorenzo, E.; Bartlett, P.; Alonso, C. Influence of macroporous gold support and its functionalization on lactate oxidase-based biosensors response. *Talanta* **2012**, *94*, 328-334.

61. Cole, R. M.; Baumberg, J. J.; García de Abajo, F Javier; Mahajan, S.; Abdelsalam, M.; Bartlett, P. N. Understanding plasmons in nanoscale voids. *Nano Letters* **2007**, *7*, 2094-2100.

62. Lordan, F.; Rice, J. H.; Jose, B.; Forster, R. J.; Keyes, T. E. Effect of Cavity Architecture on the Surface-Enhanced Emission from Site-Selective Nanostructured Cavity Arrays. *The Journal of Physical Chemistry C* **2012**, *116*, 1784-1788.

63. Mallon, C. T.; Spain, E.; Keyes, T. E.; Forster, R. J. DNA mediated immobilisation of electrocatalytic platinum nanoparticles in gold nanocavity arrays. *Chemical Communications* **2013***, 49*, 1380-1382.

64. Sontz, P. A.; Muren, N. B.; Barton, J. K. DNA charge transport for sensing and signaling. *Acc. Chem. Res.* **2012***, 45*, 1792-1800.

65. Houlton, A.; Watson, S. M. DNA-based nanowires. Towards bottom-up nanoscale electronics. *Annual Reports Section" A"(Inorganic Chemistry)* **2011***, 107*, 21-42.

66. Slinker, J. D.; Muren, N. B.; Renfrew, S. E.; Barton, J. K. DNA charge transport over 34 nm. *Nature chemistry* **2011***, 3*, 228-233.

67. Chen, S. T.; Yau, S. L. In *In Real-Time STM Imaging of the Reversibility of Polyaniline's Conformation in Response to Potential Modulation of Au (111) Electrode;* Meeting Abstracts; The Electrochemical Society: 2013; , pp 190-190.

68. Watson, J. D.; Crick, F. H. Molecular structure of nucleic acids. *Nature* **1953***, 171*, 737-738.

69. Burge, S.; Parkinson, G. N.; Hazel, P.; Todd, A. K.; Neidle, S. Quadruplex DNA: sequence, topology and structure. *Nucleic Acids Res.* **2006***, 34*, 5402-5415.

70. Hélène, C. DNA recognition: Reading the minor groove. *Nature* **1998***, 391*, 436-438.

71. Bustamante, C.; Bryant, Z.; Smith, S. B. Ten years of tension: single-molecule DNA mechanics. *Nature* **2003***, 421*, 423-427.

72. Bennett, C. F.; Swayze, E. E. RNA targeting therapeutics: molecular mechanisms of antisense oligonucleotides as a therapeutic platform. *Annu. Rev. Pharmacol. Toxicol.* **2010***, 50*, 259-293.

73. De Clercq, E.; Eckstein, E.; Merigan, T. C. Interferon induction increased through chemical modification of a synthetic polyribonucleotide. *Science* **1969***, 165*, 1137-1139.

74. Nicholson, A. W.; Niebling, K. R.; McOsker, P. L.; Robertson, H. D. Accurate in vitro cleavage by RNase III of phosphorothioate-substituted RNA processing signals in bacteriophage T7 early mRNA. *Nucleic Acids Res.* **1988***, 16*, 1577-1591.

75. Lee, R. G.; Crosby, J.; Baker, B. F.; Graham, M. J.; Crooke, R. M. Antisense technology: an emerging platform for cardiovascular disease therapeutics. *Journal of cardiovascular translational research* **2013***, 6*, 969-980.

76. Freier, S. M.; Altmann, K. H. The ups and downs of nucleic acid duplex stability: structure-stability studies on chemically-modified DNA:RNA duplexes. *Nucleic Acids Res.* **1997***, 25*, 4429-4443.

77. Schtz, R.; Cantin, M.; Roberts, C.; Greiner, B.; Uhlmann, E.; Leumann, C. Olefinic Peptide Nucleic Acids (OPAs): New Aspects of the Molecular Recognition of DNA by PNA*. **2000**.

78. Koshkin, A. A.; Singh, S. K.; Nielsen, P.; Rajwanshi, V. K.; Kumar, R.; Meldgaard, M.; Olsen, C. E.; Wengel, J. LNA (Locked Nucleic Acids): Synthesis of the adenine, cytosine, guanine, 5-methylcytosine, thymine and uracil bicyclonucleoside monomers, oligomerisation, and unprecedented nucleic acid recognition. *Tetrahedron* **1998***, 54*, 3607-3630.

79. Singh, S.; Koshkin, A. LNA (locked nucleic acids): synthesis and high-affinity nucleic acid recognition. *Chemical communications* **1998**, 455-456.

80. Nielsen, P. E.; Egholm, M.; Berg, R. H.; Buchardt, O. Sequence-selective recognition of DNA by strand displacement with a thymine-substituted polyamide. *Science* **1991***, 254*, 1497-1500.

81. Egholm, M.; Buchardt, O.; Christensen, L.; Behrens, C.; Freier, S. M.; Driver, D. A.; Berg, R. H.; Kim, S. K.; Norden, B.; Nielsen, P. E. PNA hybridizes to complementary oligonucleotides obeying the Watson Crick hydrogen-bonding rules. **1993**.

82. Dueholm, K. L.; Egholm, M.; Behrens, C.; Christensen, L.; Hansen, H. F.; Vulpius, T.; Petersen, K. H.; Berg, R. H.; Nielsen, P. E.; Buchardt, O. Synthesis of peptide nucleic acid monomers containing the four natural nucleobases: thymine, cytosine, adenine, and guanine and their oligomerization. *J. Org. Chem.* **1994***, 59*, 5767-5773.

83. Christensen, L.; Fitzpatrick, R.; Gildea, B.; Petersen, K. H.; Hansen, H. F.; Koch, T.; Egholm, M.; Buchardt, O.; Nielsen, P. E.; Coull, J. Solid-phase synthesis of peptide nucleic acids. *Journal of Peptide Science* **1995***, 1*, 175-183.

84. Thomson, S. A.; Josey, J. A.; Cadilla, R.; Gaul, M. D.; Hassman, C. F.; Luzzio, M. J.; Pipe, A. J.; Reed, K. L.; Ricca, D. J.; Wiethe, R. W. Fmoc mediated synthesis of peptide nucleic acids. *Tetrahedron* **1995***, 51*, 6179-6194.

85. Sugiyama, T.; Kittaka, A.; Takemoto, Y.; Takayama, H.; Kuroda, R. Synthesis of PNA using a Fmoc/Boc protecting group strategy. *Nucleic Acids Res. Suppl.* **2002***, (2)*, 145-146.

86. Tsantrizos, Y. S.; Lunetta, J. F.; Boyd, M.; Fader, L. D.; Wilson, M. Stereoselective Synthesis of a Thymine Derivative of (S)-2-Hydroxy-4-(2-aminophenyl) butanoic Acid. A Novel Building Block for the Synthesis

of Aromatic Peptidic Nucleic Acid Oligomers1. *J. Org. Chem.* **1997***, 62*, 5451-5457.

87. Fader, L. D.; Boyd, M.; Tsantrizos, Y. S. Backbone modifications of aromatic peptide nucleic acid (APNA) monomers and their hybridization properties with DNA and RNA. *J. Org. Chem.* **2001***, 66*, 3372-3379.

88. Fader, L. D.; Myers, E. L.; Tsantrizos, Y. S. Synthesis of novel analogs of aromatic peptide nucleic acids (APNAs) with modified conformational and electrostatic properties. *Tetrahedron* **2004***, 60*, 2235-2246.

89. Wallace, G. G.; Teasdale, P. R.; Spinks, G. M.; Kane-Maguire, L. A. *Conductive electroactive polymers: intelligent polymer systems;* CRC press: 2003; .

90. Shirakawa, H.; Louis, E. J.; MacDiarmid, A. G.; Chiang, C. K.; Heeger, A. J. Synthesis of electrically conducting organic polymers: halogen derivatives of polyacetylene,(CH) x. *Journal of the Chemical Society, Chemical Communications* **1977**, 578-580.

91. Skotheim, T. A.; Reynolds, J. *Conjugated polymers: theory, synthesis, properties, and characterization;* CRC press: 2007; .

92. Deshpande, P. P.; Jadhav, N. G.; Gelling, V. J.; Sazou, D. Conducting polymers for corrosion protection: a review. *Journal of Coatings Technology and Research* **2014***, 11*, 473-494.

93. Grgur, B. N. Metal| polypyrrole battery with the air regenerated positive electrode. *J. Power Sources* **2014***, 272*, 1053-1060.

94. Li, G.; Zhu, R.; Yang, Y. Polymer solar cells. *Nature Photonics* **2012***, 6*, 153-161.

95. Sirringhaus, H.; Tessler, N.; Friend, R. H. Integrated optoelectronic devices based on conjugated polymers. *Science* **1998***, 280*, 1741-1744.

96. Sandhu, P. K.; Singla, S. OLED–An Imminent Technology.

97. Otero, T.; Martinez, J.; Arias-Pardilla, J. Biomimetic electrochemistry from conducting polymers. A review: artificial muscles, smart membranes, smart drug delivery and computer/neuron interfaces. *Electrochim. Acta* **2012***, 84*, 112-128.

98. Stafström, S.; Bredas, J.; Epstein, A.; Woo, H.; Tanner, D.; Huang, W.; MacDiarmid, A. Polaron lattice in highly conducting polyaniline: theoretical and optical studies. *Phys. Rev. Lett.* **1987***, 59*, 1464.

99. Guimard, N. K.; Gomez, N.; Schmidt, C. E. Conducting polymers in biomedical engineering. *Progress in Polymer Science* **2007***, 32*, 876-921.

100. Matsushita, M.; Kuramitz, H.; Tanaka, S. Electrochemical oxidation for low concentration of aniline in neutral pH medium: application to the removal of aniline based on the electrochemical polymerization on a carbon fiber. *Environ. Sci. Technol.* **2005***, 39*, 3805-3810.

101. Tiwari, A. Synthesis and characterization of pH switching electrical conducting biopolymer hybrids for sensor applications. *Journal of Polymer Research* **2008***, 15*, 337-342.

102. Chowdhury, P.; Saha, B. Potassium dichromate initiated polymerization of aniline. *Indian J. Chem. Technol.* **2005***, 12*, 671-675.

103. Wang, Y.; Jing, X.; Kong, J. Polyaniline nanofibers prepared with hydrogen peroxide as oxidant. *Synth. Met.* **2007***, 157*, 269-275.

104. Rao, C. R.; Vijayan, M. Ruthenium (II)-mediated synthesis of conducting polyaniline (PAni): A novel route for PAni–RuO 2 composite. *Synth. Met.* **2008***, 158*, 516-519.

105. Teshima, K.; Yamada, K.; Kobayashi, N.; Hirohashi, R. Photopolymerization of aniline with a tris (2, 2′-bipyridyl) ruthenium complex–methylviologen polymer bilayer electrode system. *Chemical Communications* **1996**, 829-830.

106. Jin, Z.; Su, Y.; Duan, Y. A novel method for polyaniline synthesis with the immobilized horseradish peroxidase enzyme. *Synth. Met.* **2001***, 122*, 237-242.

107. Zhang, J.; Kuznetsov, A. M.; Medvedev, I. G.; Chi, Q.; Albrecht, T.; Jensen, P. S.; Ulstrup, J. Single-molecule electron transfer in electrochemical environments. *Chem. Rev.* **2008***, 108*, 2737-2791.

108. Chen, F.; Hihath, J.; Huang, Z.; Li, X.; Tao, N. Measurement of single-molecule conductance. *Annu. Rev. Phys. Chem.* **2007***, 58*, 535-564.

109. Xiao, X.; Xu, B.; Tao, N. J. Measurement of single molecule conductance: Benzenedithiol and benzenedimethanethiol. *Nano Letters* **2004***, 4*, 267-271.

110. Xu, B.; Tao, N. J. Measurement of single-molecule resistance by repeated formation of molecular junctions. *Science* **2003***, 301*, 1221-1223.

111. Chen, F.; He, J.; Nuckolls, C.; Roberts, T.; Klare, J. E.; Lindsay, S. A molecular switch based on potential-induced changes of oxidation state. *Nano letters* **2005***, 5*, 503-506.

112. Young, D. *Computational chemistry: a practical guide for applying techniques to real world problems;* John Wiley & Sons: 2004; .

113. Mohamadi, F.; Richards, N. G.; Guida, W. C.; Liskamp, R.; Lipton, M.; Caufield, C.; Chang, G.; Hendrickson, T.; Still, W. C. MacroModel—an

integrated software system for modeling organic and bioorganic molecules using molecular mechanics. *Journal of Computational Chemistry* **1990***, 11*, 440-467.

114. Ponder, J. W.; Richards, F. M. An efficient Newton-like method for molecular mechanics energy minimization of large molecules. *Journal of Computational Chemistry* **1987***, 8*, 1016-1024.

115. Case, D. A.; Cheatham, T. E.; Darden, T.; Gohlke, H.; Luo, R.; Merz, K. M.; Onufriev, A.; Simmerling, C.; Wang, B.; Woods, R. J. The Amber biomolecular simulation programs. *Journal of computational chemistry* **2005***, 26*, 1668-1688.

116. Cheatham, T. E.; Young, M. A. Molecular dynamics simulation of nucleic acids: Successes, limitations, and promise*. *Biopolymers* **2000***, 56*, 232-256.

117. Maiorov, V. N.; Crippen, G. M. Significance of root-mean-square deviation in comparing three-dimensional structures of globular proteins. *J. Mol. Biol.* **1994***, 235*, 625-634.

118. Qiu, P.; Qin, L.; Sorrentino, R.; Greene, J.; Wang, L.; Dismutase, S.; Cioni, P.; Pesce, A.; della Rocca, B.; Castelli, S. A Model for Statistical Significance of Local Similarities in Structure. *Structure , 1549*, 1557.

119. Reva, B. A.; Finkelstein, A. V.; Skolnick, J. What is the probability of a chance prediction of a protein structure with an rmsd of 6 å? *Folding and Design* **1998***, 3*, 141-147.

120. Compton, R. G.; Banks, C. E. *Understanding voltammetry;* World Scientific: 2007; .

121. Bain, C. D.; Troughton, E. B.; Tao, Y. T.; Evall, J.; Whitesides, G. M.; Nuzzo, R. G. Formation of monolayer films by the spontaneous assembly of organic thiols from solution onto gold. *J. Am. Chem. Soc.* **1989***, 111*, 321-335.

122. Lim, M. S.; Feng, K.; Chen, X.; Wu, N.; Raman, A.; Nightingale, J.; Gawalt, E. S.; Korakakis, D.; Hornak, L. A.; Timperman, A. T. Adsorption and desorption of stearic acid self-assembled monolayers on aluminum oxide. *Langmuir* **2007***, 23*, 2444-2452.

123. Fadeev, A. Y.; Helmy, R.; Marcinko, S. Self-assembled monolayers of organosilicon hydrides supported on titanium, zirconium, and hafnium dioxides. *Langmuir* **2002***, 18*, 7521-7529.

124. Ulman, A. Formation and structure of self-assembled monolayers. *Chem. Rev.* **1996***, 96*, 1533-1554.

125. Bain, C. D.; Evall, J.; Whitesides, G. M. Formation of monolayers by the coadsorption of thiols on gold: variation in the head group, tail group, and solvent. *J. Am. Chem. Soc.* **1989***, 111*, 7155-7164.

126. Paik, W.; Eu, S.; Lee, K.; Chon, S.; Kim, M. Electrochemical reactions in adsorption of organosulfur molecules on gold and silver: Potential dependent adsorption. *Langmuir* **2000***, 16*, 10198-10205.

127. Love, J. C.; Estroff, L. A.; Kriebel, J. K.; Nuzzo, R. G.; Whitesides, G. M. Self-assembled monolayers of thiolates on metals as a form of nanotechnology. *Chem. Rev.* **2005***, 105*, 1103-1170.

128. Herne, T. M.; Tarlov, M. J. Characterization of DNA probes immobilized on gold surfaces. *J. Am. Chem. Soc.* **1997***, 119*, 8916-8920.

129. Hill, H. D.; Millstone, J. E.; Banholzer, M. J.; Mirkin, C. A. The role radius of curvature plays in thiolated oligonucleotide loading on gold nanoparticles. *ACS nano* **2009***, 3*, 418-424.

130. Steel, A.; Levicky, R.; Herne, T.; Tarlov, M. J. Immobilization of nucleic acids at solid surfaces: effect of oligonucleotide length on layer assembly. *Biophys. J.* **2000***, 79*, 975-981.

131. Ferraro, J. R. *Introductory raman spectroscopy;* Academic press: 2003; .

132. Fleischmann, M.; Hendra, P.; McQuillan, A. Raman spectra of pyridine adsorbed at a silver electrode. *Chemical Physics Letters* **1974***, 26*, 163-166.

133. Campion, A.; Kambhampati, P. Surface-enhanced Raman scattering. *Chem. Soc. Rev.* **1998***, 27*, 241-250.

134. Sharma, B.; Frontiera, R. R.; Henry, A.; Ringe, E.; Van Duyne, R. P. SERS: materials, applications, and the future. *Materials today* **2012***, 15*, 16-25.

135. McNay, G.; Eustace, D.; Smith, W. E.; Faulds, K.; Graham, D. Surface-enhanced Raman scattering (SERS) and surface-enhanced resonance Raman scattering (SERRS): a review of applications. *Appl. Spectrosc.* **2011***, 65*, 825-837.

136. Orendorff, C. J.; Gole, A.; Sau, T. K.; Murphy, C. J. Surface-enhanced Raman spectroscopy of self-assembled monolayers: sandwich architecture and nanoparticle shape dependence. *Anal. Chem.* **2005***, 77*, 3261-3266.

137. Kelly, K. L.; Coronado, E.; Zhao, L. L.; Schatz, G. C. The optical properties of metal nanoparticles: the influence of size, shape, and dielectric environment. *The Journal of Physical Chemistry B* **2003***, 107*, 668-677.

138. Lee, J.; Lytton-Jean, A. K.; Hurst, S. J.; Mirkin, C. A. Silver nanoparticle-oligonucleotide conjugates based on DNA with triple cyclic disulfide moieties. *Nano letters* **2007***, 7*, 2112-2115.

139. Liu, J.; Hu, W.; Zhong, C.; Cheng, Y. F. Surfactant-free electrochemical synthesis of hierarchical platinum particle electrocatalysts for oxidation of ammonia. *J. Power Sources* **2013***, 223*, 165-174.

140. Zoval, J.; Lee, J.; Gorer, S.; Penner, R. Electrochemical preparation of platinum nanocrystallites with size selectivity on basal plane oriented graphite surfaces. *The Journal of Physical Chemistry B* **1998***, 102*, 1166-1175.

141. Spain, E.; McArdle, H.; Keyes, T. E.; Forster, R. J. Detection of sub-femtomolar DNA based on double potential electrodeposition of electrocatalytic platinum nanoparticles. *Analyst* **2013***, 138*, 4340-4344.

142. Cintra, S.; Abdelsalam, M. E.; Bartlett, P. N.; Baumberg, J. J.; Kelf, T. A.; Sugawara, Y.; Russell, A. E. Sculpted substrates for SERS. *Faraday Discuss.* **2006***, 132*, 191-199.

143. Lordan, F.; Rice, J. H.; Jose, B.; Forster, R. J.; Keyes, T. E. Site selective surface enhanced Raman on nanostructured cavities. *Appl. Phys. Lett.* **2011***, 99*, 033104.

144. Ghosh, A.; Kar, R. K.; Krishnamoorthy, J.; Chatterjee, S.; Bhunia, A. Double GC: GC Mismatch in dsDNA Enhances Local Dynamics Retaining the DNA Footprint: A High-Resolution NMR Study. *ChemMedChem* **2014***, 9*, 2059-2064.

145. Wei, D.; Wilson, W. D.; Neidle, S. Small-molecule binding to the DNA minor groove is mediated by a conserved water cluster. *J. Am. Chem. Soc.* **2013***, 135*, 1369-1377.

146. Valeur, E.; Bradley, M. Amide bond formation: beyond the myth of coupling reagents. *Chem. Soc. Rev.* **2009***, 38*, 606-631.

147. El-Faham, A.; Albericio, F. Peptide coupling reagents, more than a letter soup. *Chem. Rev.* **2011***, 111*, 6557-6602.

148. Knorr, R.; Trzeciak, A.; Bannwarth, W.; Gillessen, D. New coupling reagents in peptide chemistry. *Tetrahedron Lett.* **1989***, 30*, 1927-1930.

149. Li, X.; Huang, M.; Duan, W.; Yang, Y. Novel multifunctional polymers from aromatic diamines by oxidative polymerizations. *Chem. Rev.* **2002***, 102*, 2925-3030.

150. Si, S.; Xu, Y.; Nie, L.; Yao, S. Electrochemical quartz crystal microbalance study on electropolymerization of m-phenylenediamine: effects of aniline and polyaniline. *Electrochim. Acta* **1995***, 40*, 2715-2721.

151. McClellan, A. The significance of hydrogen bonds in biological structures. *J. Chem. Educ.* **1967***, 44*, 547.

152. Lukkari, J.; Kleemola, K.; Meretoja, M.; Ollonqvist, T.; Kankare, J. Electrochemical post-self-assembly transformation of 4-aminothiophenol monolayers on gold electrodes. *Langmuir* **1998***, 14*, 1705-1715.

153. Kakiuchi, T.; Usui, H.; Hobara, D.; Yamamoto, M. Voltammetric properties of the reductive desorption of alkanethiol self-assembled monolayers from a metal surface. *Langmuir* **2002***, 18*, 5231-5238.

154. Suh, J.; Moskovits, M. Surface-enhanced Raman spectroscopy of amino acids and nucleotide bases adsorbed on silver. *J. Am. Chem. Soc.* **1986***, 108*, 4711-4718.

155. Preuss, M.; Schmidt, W.; Bechstedt, F. Coulombic amino group-metal bonding: Adsorption of adenine on Cu (110). *Phys. Rev. Lett.* **2005***, 94*, 236102.

156. Lee, Y.; Chang, C.; Yau, S.; Fan, L.; Yang, Y.; Yang, L. O.; Itaya, K. Conformations of polyaniline molecules adsorbed on Au (111) probed by in situ STM and ex situ XPS and NEXAFS. *J. Am. Chem. Soc.* **2009***, 131*, 6468-6474.